International Journal of Antennas and Propagation

Advanced Simulation Methods of Antennas and Radio Propagation for 5G and Beyond Communications Systems

Lead Guest Editor: Marko Sonkki
Guest Editors: Eva Antonino-Daviu, Danping He, and Sami Myllymäki

Advanced Simulation Methods of Antennas and Radio Propagation for 5G and Beyond Communications Systems

International Journal of Antennas and Propagation

Advanced Simulation Methods of Antennas and Radio Propagation for 5G and Beyond Communications Systems

Lead Guest Editor: Marko Sonkki
Guest Editors: Eva Antonino-Daviu, Danping He, and Sami Myllymäki

Chief Editor

Editorial Board

Contents

Advanced Simulation Methods of Antennas and Radio Propagation for 5G and Beyond Communications Systems
Marko Sonkki, Eva Antonino-Daviu, Danping He, and Sami Myllymäki
Editorial (3 pages), Article ID 4387494, Volume 2020 (2020)

OTA Testing for Massive MIMO Devices Using Cascaded APM Networks and Channel Emulators
Lijian Xin, Yong Li, Hao Sun, and Xiang Zhang
Research Article (14 pages), Article ID 6901383, Volume 2019 (2019)

A General 3D Nonstationary Vehicle-to-Vehicle Channel Model Allowing 3D Arbitrary Trajectory and 3D-Shaped Antenna Array
Qiuming Zhu, Weidong Li, Ying Yang, Dazhuan Xu, Weizhi Zhong, and Xiaomin Chen
Research Article (12 pages), Article ID 8708762, Volume 2019 (2019)

Compact Wideband Circularly Polarized Antenna with Symmetric Parasitic Rectangular Patches for Ka-Band Applications
Rongling Jian, Yueyun Chen, and Taohua Chen
Research Article (8 pages), Article ID 2071895, Volume 2019 (2019)

Outdoor-to-Indoor Channel Measurement and Coverage Analysis for 5G Typical Spectrums
Zhimeng Zhong, Jianyao Zhao, and Chao Li
Research Article (10 pages), Article ID 3981678, Volume 2019 (2019)

Continuously Frequency-Tunable Horn Filtennas Based on Dual-Post Resonators
Andreia A. C. Alves, Luis G. da Silva, Evandro C. Vilas Boas, Danilo H. Spadoti, and S. Arismar Cerqueira Jr.
Research Article (12 pages), Article ID 6529343, Volume 2019 (2019)

Vehicular Channel in Urban Environments at 23 GHz for Flexible Access Common Spectrum Application
Longhe Wang, Bo Ai, Jingya Yang, Hao Qiu, Wanqiao Wang, and Ke Guan
Research Article (13 pages), Article ID 5425703, Volume 2019 (2019)

Channel Characteristics of High-Speed Railway Station Based on Ray-Tracing Simulation at 5G mmWave Band
Lei Xiong, Haiyang Miao, Bo Ai, Tutun Juhana, and Adit Kurniawan
Research Article (10 pages), Article ID 3137583, Volume 2019 (2019)

A Wideband Differential-Fed Microstrip Patch Antenna Based on Radiation of Three Resonant Modes
Taohua Chen, Yueyun Chen, and Rongling Jian
Research Article (7 pages), Article ID 4656141, Volume 2019 (2019)

Hindawi
International Journal of Antennas and Propagation
Volume 2020, Article ID 4387494, 3 pages
https://doi.org/10.1155/2020/4387494

Editorial

Advanced Simulation Methods of Antennas and Radio Propagation for 5G and Beyond Communications Systems

Marko Sonkki,[1] **Eva Antonino-Daviu**,[2] **Danping He**,[3] **and Sami Myllymäki**[4]

[1]*Centre for Wireless Communications, University of Oulu, Oulu, Finland*
[2]*Electromagnetic Radiation Group, Universidad Politecnica de Valencia, Valencia, Spain*
[3]*State Key Lab of Rail Traffic and Control Safety, Beijing Jiaotong University, Beijing, China*
[4]*Microelectronics Research Unit, University of Oulu, Oulu, Finland*

Correspondence should be addressed to Marko Sonkki; marko.sonkki@gmail.com

Received 17 February 2020; Accepted 18 February 2020; Published 27 June 2020

Nowadays, high data rates can be provided by optical fibres as defined in the IEEE 802.3ba-2010 standard. The question is how to bring such a data rate over a wireless link between an indoor base station and a mobile device where 1000-fold growth data transfer is expected till 2020 [1] and 5000-fold growth by the year 2030 [2]. The IEEE 802.11.n standard for wireless local area networks (WLANs) can provide data rates up to 600 MBit/s, whereas the IEEE 802.11ac D standard defines data rates up to 7 GBit/s. For future wireless communications systems (5G and beyond), more than 100 GBit/s data rates are desired, giving huge challenges for the systems' design. These kinds of data speeds have been so far demonstrated only in laboratory conditions [3].

Wireless networks beyond 5G (fifth-generation) and 6G (sixth-generation) are expected to provide a performance targeting up to Tbps data rates. It is supporting a large scale of novel usage scenarios and applications with high reliability, almost zero response time, and higher frequencies. Virtual presence, 3D printing, cyber physical systems, intelligent transport, and Industry 4.0 are only a few examples of several possible use cases in order to enhance scalability, flexibility, and efficient resource allocation. These approaches do not tackle the fundamental performance limitations such as the available bandwidth, transmission and processing delay, cost, and energy consumption. To break these barriers in networks beyond 5G, resources, technologies, and research towards new technological concepts, components, architectures, and systems concepts are needed. Hence, innovative joint-investigation, assessment, and design of theoretical models, aligned and supported by experimental parameter evaluation/estimation and validation, are required.

In the future, the access to high-speed Internet is a crucial advantage in the global competition for industry sites and highly qualified human resources. Terahertz (THz) links, as a wireless backhaul extension of the optical fiber [4], are important to guarantee high-speed Internet access everywhere. Moreover, the increasing number of mobile and fixed users in the private, industrial, and service sectors will require hundreds of Gbps communications between cell towers (backhaul) or between cell towers and remote radio heads (fronthaul).

As the application scenarios and requirements are more diverse in the 5G and beyond communications than before, not only the sub-6 GHz spectrum but also higher frequency bands including millimetre wave (mm-Wave) and THz bands are key enablers to satisfy the increasing data rate demands. Therefore, tremendous funding has been and will be investigating in this area. Researchers are active in sharing their knowledge to push the related technologies forward.

Accurate channel characterization and modelling are fundamental to evaluate the designed technologies and system performance. The evaluation of multiple-input multiple-output (MIMO) technology, various mobilities, propagation environments, and frequency bands are making this work more and more challenging [5]. The researchers are making efforts on both deterministic and stochastic channel models that support spatial consistency, dual mobility, and various propagation mechanisms. Ray tracing-(RT-) based deterministic modelling approach has demonstrated the advantage in predicting time-varying channel

and MIMO channel for various frequency bands. The computational complexity and the utility of RT have been optimized by many efforts [6]. Stochastic models such as 3GPP-based QuaDRiGa (QUAsi Deterministic RadIo channel GenerAtor) model and COST2100 model support time-varying simulation like MIMO simulation as well. They are useful in non-site-specific statistical evaluation.

On the contrary, new 2D materials [7] and artificial materials [8] on mm-Wave and sub-THz wave together with new packaging and fabrication methods, components, and structures are becoming most commonly used on-chip packaged antenna arrays perspective. In addition, beyond small antenna arrays, there are massive matrix structures such as plasmonic antenna arrays [9] utilizing millions elements enabling together with 2D materials and artificial materials opening available new kind of THz electronic packaging alternatives.

Moreover, new advanced antenna systems, such as very large antenna arrays, will be required to overcome the very high path loss over the radio channel. The antennas in an mm-Wave and THz band need to support a very large bandwidth from several GHz up to a few THz [9], for example, sub-THz band communication systems at 300. GHz can provide a relative bandwidth of 10% at the centre frequency, i.e., in the order of 30 GHz.

The very large bandwidth opens the door to a variety of applications, which demand ultrahigh data rates, and allows the development of novel applications in classical networking scenarios as well as in new nanoscale communication approach. Some of these applications can already be foreseen, and others will undoubtedly emerge as technology progresses [10].

As the next generation wireless communication devices rely on MIMO technology to provide enhanced data rates, the antenna design becomes even more challenging task in any communication scenario. The theory of characteristic modes (TCM) provides some insight into the design and analysis of complex antenna systems. Characteristic modes are a set of orthogonal real modes that can be computed numerically for open electromagnetic problems. Since they are obtained in the absence of excitation, the radiating potential of any structure can be evaluated prior to the selection of excitation method. TCM is also finding its way into the design of antennas for a variety of modern applications, such as RFID, cognitive radio, UWB systems, full-duplex communications, Internet of Things (IoT), but also to a massive-MIMO antenna design by allowing to excite different modes in a single element, and, thus, decreasing the size of an array with a sophisticated feed network [11].

This special issue collects eight papers concerning various aspects of 5G and beyond system approaches. Two papers deal with radio channel measurement and modelling and two channel characterization by using ray tracing, while three papers are concerned with antennas and one with OTA (over-the-air) test measurements by combining radio channel and antenna topics together under the system level.

One paper dealing with OTA measurements for the 5G systems written by Xin et al. proposes OTA test setup for mm-Wave massive MIMO equipment using the cascaded amplitude and phase modulation (APM) network and channel emulator. Compared with the existing test setup with mechanical switch, the test setup enables more accurate reconstruction of the radio channel environment under the multiprobe anechoic chamber (MPAC) setup without increasing the number of channel emulators (CEs) allowing a lower cost test system. The constructed MPAC testing setup for mm-Wave and massive MIMO equipment is composed of an anechoic chamber, a sectored probe wall containing a number of probes, an APM network, a fading channel emulator, and a user emulator (UE), and the simulation results are compared with the test setup.

Two papers are focusing on RT at mm-Waves, where the first one is written by Xiong et al. The paper studies wireless channel characteristics of the three-dimensional (3D) model of high-speed railway station (HSR) at the 37.0–42.5 GHz band. Key parameters such as path-loss exponent, shadow fading factor, delay spread, Rician K-factor, angular spread, power angle spectrum, and spatial correlation are extracted and investigated. These channel characteristics are proposed for the selection of antenna arrays and the design of future 5G communication networks in the railway environment.

The other ray tracing paper written by Wang et al. discusses the characteristics of vehicle-to-infrastructure (V2I) channels simulated and extracted for the urban environment in Seoul. Simulations at the 23 GHz band with 1 GHz bandwidth in a realistic V2I urban environment are performed by a calibrated RT simulator to complement these missing characteristics, e.g., directionality and blockage. The path loss, shadow factor, Rician K-factor, root-mean-square (RMS) delay spread, and angular spreads are characterized from the calibrated RT simulation results, which gives a better understanding of the propagation channel for designing vehicular radio technologies and a communication system in a similar environment. The extracted parameters can be input to the channel generator, like QuaDRiGa or Metis, to generate similar channels, which can be used to evaluate or verify the performance of the system- or link-level design.

Two papers are related to channel measurements and characterization. The first paper, written by Zhu et al., develops a general 3D nonstationary vehicle-to-vehicle (V2V) channel model, which is based on the traditional geometry-based stochastic models (GBSMs) and the twin-cluster approach. In contrast to the traditional models, the new model is characterized by 3D scattering environments, 3D antenna arrays, and 3D arbitrary trajectories of both terminals and scatterers with provided channel parameters. The statistical properties, i.e., spatial-temporal correlation function (STCF) and Doppler power spectrum density (DPSD) are delivered a well. Simulation results demonstrated that the proposed model agrees with the theoretical and measured results, which verifies the theoretical derivations and channel model.

The other channel measurement paper is written by Zhong et al. where measurements are performed on the outdoor-to-indoor (O2I) propagation channels at 3.5, 4.9, and 28 GHz simultaneously by using a multiband channel sounder. The captured path loss distribution and angular power arrival profiles were presented with measured penetration loss at 28 GHz through different kinds of glass windows. The glass windows presented in the paper

introduced the penetration loss of 3 to 12 dB which was considered acceptable for mm-Wave O2I coverage. The low-emissivity (low-E) windows, assumed to be used more in the future, introduced 10 dB additional loss compared to glass window. The measurement results will help to analyse the O2I coverage at mm-Waves, which is important when designing and developing the future 5G network.

Finally, three antenna papers are focusing on 5G systems, which two are for mm-Wave and one for 6 GHz by exciting multiple modes. The first mm-Wave paper is written by Jian et al., and it is focusing on wideband circularly polarized (CP) microstrip antenna consisting a central patch and a microstrip line radiator. The CP radiation is achieved by loading a rectangular slot on the ground plane. To improve the 3 dB axial ratio bandwidth (ARBW), two symmetric parasitic rectangular patches, paralleled to a central patch and a slit, are positioned to load the central patch. The measured impedance bandwidth for of the proposed antenna is from 22.8 to 33.8 GHz, and the simulation result shows that the 3 dB ARBW is from 28.77 to 33.5 GHz within the impedance bandwidth. The peak gain of the antenna is approximately 5 dBic within 3 dB ARBW.

Another mm-Wave antenna written by Alves et al. presents a concept and development of two mechanically frequency-tunable horn filtennas (filter antenna). The design relies on the integration of a horn antenna with a mechanically tunable filter based on dual-post resonators. The proposed filtennas were manufactured and experimentally characterized. Measurements show that both filtennas have a tuning ratio approximately 1.37 with continuous adjustment. The first prototype operates from 2.56 to 3.50 GHz, whereas the second one has the bandwidth from 17.4 to 24.0 GHz. In addition, the higher frequency filtenna has been implemented in a 5.0-meter reach indoor environment, using a 16-QAM signal at 24 GHz. The configuration results, in terms of a root-mean-square error vector magnitude (EVMRMS) and antenna radiation efficiency, are 3.69% and 97.0%, respectively.

The third antenna paper written by Chen et al. presents a wideband differential-fed multimode microstrip patch antenna at 4.75–6.75 GHz band. Two symmetrical rectangular slots are cut on the radiating patch where the zero-current position of the TM30 mode excites another resonant slot mode. In addition, the slot length is enlarged to decrease the frequency of the slot mode with little effect on the TM30 mode. To further expand the impedance bandwidth, the width of the patch is reduced to increase the frequency of the TM12 mode, while having little influence on the TM30 and the slot modes. Additionally, a pair of small rectangular strips is adopted on the top of the feeding probes to achieve good impedance matching. Based on the arrangements, a broadband microstrip patch antenna with three in-band minima could be realized. The results show that the −10 dB impedance bandwidth of the antenna is extended to 35.8% with a stable radiation pattern.

Conflicts of Interest

The editors declare that they have no conflicts of interest regarding the publication of this special issue.

Acknowledgments

The guest editorial team would like to thank all the authors for their interest of selecting this special issue to publish their research results.

Marko Sonkki
Eva Antonino-Daviu
Danping He
Sami Myllymäki

References

[1] A. Osseiran, V. Braun, T. Hidekazu et al., "The foundation of the mobile and wireless communications system for 2020 and beyond: challenges, enablers and technology solutions," in *Proceedings of the IEEE 77th Vehicular Technology Conference (VTC Spring)*, pp. 1–5, Dresden, Germany, June 2013.

[2] European Project ICT-317669-METIS, "Deliverable D 8.4 METIS final project report," 2015, https://www.metis2020.com/documents/deliverables/.

[3] J. Vieira, K. Nieman, Z. Miers et al., "A flexible 100-antenna testbed for massive MIMO," in *Proceedings of the IEEE International Workshop Massive MIMO: Theory Practice*, pp. 287–293, Austin, TX, USA, December 2014.

[4] S.-H. Yang, M. R. Hashemi, C. W. Berry, and M. Jarrahi, "7.5% optical-to-terahertz conversion efficiency offered by photoconductive emitters with three-dimensional plasmonic contact electrodes," *IEEE Transactions on Terahertz Science and Technology*, vol. 4, no. 5, pp. 575–581, 2014.

[5] C.-X. Wang, J. Bian, J. Sun, W. Zhang, and M. Zhang, "A survey of 5G Channel measurements and models," *IEEE Communications Surveys & Tutorials*, vol. 20, no. 4, pp. 3142–3168, 2018.

[6] D. He, B. Ai, K. Guan, L. Wang, Z. Zhong, and T. Kürner, "The design and applications of high-performance ray-tracing simulation platform for 5G and beyond wireless communications: a tutorial," *IEEE Communications Surveys & Tutorials*, vol. 21, no. 1, pp. 10–27, 2019.

[7] E. Dadrasnia, H. Lamela, M. B. Kuppam, F. Garet, and J.-L. Coutaz, "Determination of the DC electrical conductivity of multiwalled carbon nanotube films and graphene layers from noncontact time-domain terahertz measurements," *Advances in Condensed Matter Physics*, vol. 2014, Article ID 370619, 6 pages, 2014.

[8] D. Ramaccia, A. Epstein, M. Barbuto, and S. Rudolph, "Metamaterials, metasurfaces, and artificial dielectrics: theory and applications to the next-generation telecommunication platforms," *International Journal of Antennas and Propagation*, vol. 2017, Article ID 4312542, 2 pages, 2017.

[9] I. F. Akyildiz and J. M. Jornet, "Realizing ultra-massive mimo (1024 × 1024) communication in the (0.06–10) terahertz band," *Nano Communication Networks*, vol. 8, pp. 46–54, 2016.

[10] I. F. Akyildiz, J. M. Jornet, and C. Han, "Terahertz band: next frontier for wireless communications," *Physical Communication*, vol. 12, pp. 16–32, 2014.

[11] D. Manteuffel and R. Martens, "Compact multimode multielement antenna for indoor UWB massive MIMO," *IEEE Transactions on Antennas and Propagation*, vol. 64, no. 7, pp. 2689–2697, 2016.

Hindawi
International Journal of Antennas and Propagation
Volume 2019, Article ID 6901383, 14 pages
https://doi.org/10.1155/2019/6901383

Research Article

OTA Testing for Massive MIMO Devices Using Cascaded APM Networks and Channel Emulators

Lijian Xin,[1] **Yong Li**,[1] **Hao Sun**,[1] **and Xiang Zhang**[2]

[1]*Key Laboratory of Universal Wireless Communications (Ministry of Education), Beijing University of Posts and Telecommunications, Beijing 100876, China*
[2]*China Academy of Information and Communications Technology, Beijing 100191, China*

Correspondence should be addressed to Xiang Zhang; zhangxiang1@caict.ac.cn

Received 6 May 2019; Revised 17 July 2019; Accepted 13 September 2019; Published 12 November 2019

Guest Editor: Danping He

This paper proposes an over-the-air (OTA) testing setup for millimeter-wave (mmWave) massive multiple-input multiple-output (MIMO) equipment using cascaded amplitude and phase modulation (APM) network and channel emulator. Compared with the existing test setup with mechanical switch, the proposed testing setup enables more accurate reconstruction of the radio channel environment under the multiprobe anechoic chamber (MPAC) setup without increasing the number of channel emulators (CEs) to control the system cost. The constructed MPAC testing setup for mmWave and massive MIMO equipment is composed of an anechoic chamber, a sectored probe wall containing a number of probes, an APM network, a fading channel emulator, and a user emulator (UE). In this paper, the structural model and the performance advantages of the proposed radiated testing setup are described, and a fully connected APM network for radiated testing is more prominent than the existing switch. Moreover, the angular spectrum is selected as the performance metric for the reconstructed channel. The ability of the proposed system to reconstruct the power angular spectrum (PAS) of the target channel is studied under both static and dynamic channel models, which can reflect the performance of beamforming procedures of the massive MIMO antenna arrays, e.g., beam acquisition, tracking, and refinement. The simulation results for angular spectrum support the superiority of the proposed OTA testing setup. Furthermore, the simulations for average channel capacity also show that radiated testing setup using cascaded APM network and channel emulator is valid.

1. Introduction

Due to the large amount of available spectrum in the millimeter-wave (mmWave) band, mmWave communication has become an important technology in 5G cellular communication systems. Compared with sub-6 GHz communication, mmWave channel has higher penetration losses and energy losses due to scattering, thereby resulting in high sparseness and specular reflection of the channel [1]; thus, the signal is subject to higher pathloss and transmission congestion at mmWave bands. In order to overcome pathloss and maintain high signal power, the signal-to-interference-plus-noise ratio (SINR) should have a larger value, which means that mmWave antenna should have a higher gain. The antenna array can be used to improve the reliability of the communication link and compensate for severe pathloss to increase SINR [2]. Fortunately, the wavelength for the mmWave frequency is shorter, and the actual size of the mmWave antenna is smaller than the antenna size in sub-6 GHz. Therefore, massive multiple-input multiple-output (MIMO) antenna system can be configured with more antennas to increase signal power. It is well known that massive MIMO is one of the key technologies in 5G communication, and evaluating the performances of both antennas and baseband parts is significant for the design and development of mmWave massive MIMO devices. Given the evaluation demands of the mmWave equipment in the future, the test for controllable antenna systems is an unprecedented task.

For sub-6 GHz antenna systems, conducted testing is used to test devices typically. However, there are two main reasons why the conducted testing is no longer suitable for the mmWave antenna system [3]. Firstly, the mmWave system with tens or hundreds of antennas is a highly integrated unit. Therefore, given the system cost, size, and design difficulties, it is no longer applicable to test mmWave antenna devices using radio frequency (RF) cable. Secondly, the beamforming capability of the base station (BS) should be taken into account for the mmWave test. It is expected that the best beam will be found at both ends of the link during the link establishment process and then aligned continuously under time-variant radio channel conditions. For example, when one or both ends of a link are moving, beam acquisition and beam alignment are key features for mmWave device test. However, conducted testing ignores the beam features of massive MIMO devices. Therefore, given the infeasibility of conducted testing, mmWave devices should be performed through radiated testing in which the radiated antennas are used as the interface directly.

Recently, for the mmWave massive MIMO antenna testing, a three-dimensional (3D) sectored multiprobe anechoic chamber (MPAC) setup is proposed [4]. The MPAC OTA testing setup for the massive MIMO equipment is composed of an anechoic chamber which can shield external interference signals and absorb reflected waves, a sectored probe wall which can place a large number of probes, a switch system (mechanical relay switch: the key parameters, e.g., switching speed, insertion loss, isolation, cost, crosstalk, and lifetime, are dependent on the manufacturing technology of the switch), a channel emulator, and an user emulator. The procedure of the massive MIMO OTA testing and the configuration of the sectored OTA setup are detailed in [5].

In order to test the beam acquisition and beam tracking of mmWave massive MIMO equipment, a dynamic channel environment needs to be reproduced [6]. The reasons are as follows. Firstly, the antenna array and beamformer are important parts of the mmWave devices, and the beamforming is indispensable in the link establishment process. Therefore, the test for the adaptive beamforming requires the dynamic radio channel urgently. Secondly, the link distance in a massive MIMO system may be short, and small motions may significantly change the channel propagation conditions, causing rapid changes of the power amplitude observed by different multipath components. As mentioned above, the mmWave dynamic channel needs to be reconstructed in the MPAC setup.

In the existing OTA testing systems, it is assumed that the switch configuration is completely free and can be switched at every considered moment without any distortion [6]. However, the dynamic environment has strict performance requirements for mechanical relay switches. The performance of the mechanical relay switch was tested for high-performance reconfigurable RF circuits in [7]. There are some major problems in using mechanical relay switches. Firstly, from low frequency to high frequency, the switch isolation is reduced, and the insertion loss of the device is increased significantly, which may increase the noise of the system directly and affect the performance of the relay switches at high frequencies. Secondly, during the switching of mechanical relay switches, any idle open transmission line can resonate in the microwave range, and the resonance can reflect electrical energy to a source of the operating RF, thereby damaging it. For systems operating at 26 GHz or higher frequencies, the above damage will be more severe due to the greatly reduced isolation [7]. Thirdly, the service life of the mechanical switch is short, and its components are sensitive to vibration. Longer service life requires more robust actuators and drive linkages which require that magnetic efficiency and mechanical rigidity are optimized. Last but not least, the mechanical switch can only use a subset of probes on the probe wall at each channel time sample, which wastes hardware resources and could not improve the performance of the MPAC. Therefore, in order to test mmWave massive MIMO devices accurately, higher technical requirements are put forward for the design of switches. Given the shortcomings of the mechanical relay switch, a new system structure is required and applied to the mmWave massive MIMO OTA testing system.

In view of the above drawbacks of the current mmWave OTA testing system with switches, this paper proposes the amplitude and phase modulation (APM) network, which is fully connected and digital, to replace the mechanical switch in the MPAC setup. Therefore, the MPAC testing setup with a cascaded APM network and channel emulator (CE) model is presented in this paper. The inputs of the APM network are connected to the outputs of the CE, and the outputs of the APM network are connected to the probes. The main advantages of the OTA testing setup with the cascaded model are as follows:

(i) Firstly, given the reduced channel isolation of the switch from low to high frequencies, the channels of the fully connected APM network are independent of each other. In addition, there is no distortion of the mechanical relay switch mentioned above when reconstructing the dynamic channel using digital APM network. In addition, the update speed of the APM network can be synchronized with the sampling rate of the channel emulator. Furthermore, the APM network has an automatic verification function to balance the amplitude and phase deviation caused by different RF lines.

(ii) Secondly, the digital APM network can use all the probes placed on the probe wall at each sampling time of the dynamic channel, rather than a subset of the probes as in the case of the switch, thereby making full use of hardware resources and improving the accuracy of the emulated channel. Therefore, using the OTA testing setup with a cascaded model, the channel reconstruction capability can be improved greatly without increasing the number of channel emulators in the MPAC setup.

However, nothing is perfect. Potential practical challenges of the APM network will be discussed in the summary of simulation results, such as resolution of phase shifters

(=word length), step size, and accuracy of analogue attenuators. In the future work, we will examine the influence of the above nonideal factors on channel reconstruction.

From the above descriptions, it is not difficult to find that the APM network's structure is simpler than that of the channel emulator and can only modulate the amplitude and phase of the radio frequency signals. In addition, considering a digital real-time control for APM structure, the APM network is the same as the channel emulator when generating impulse response of a single cluster. However, given the multiple clusters for a geometry-based stochastic channel model (GSCM), the APM network is powerless due to its simple structure. Therefore, the channel emulator cannot be fully replaced by the APM network, and the cost of simple APM network is lower than that of complex channel emulator. When reconstructing GSCM (multiple clusters) or generating mmWave channel, we need to add number of channel emulators to reconstruct the spatial characteristics of the target channel more accurately. Despite the APM network performance advantages described above, it is also expected to improve the accuracy of the reconstructed channel and greatly reduce test costs. Moreover, APM network is very convenient to adjust the amplitude and phase by loading data files which can be obtained in the sequel.

The notation used in this paper is as follows. Section 2 presents the structure of the APM network and the OTA testing system with a cascaded model. Section 3 details the MPAC setup with APM network for massive MIMO devices, and specific implementation process is analysed and summarized. The angular spectrum and the average channel capacity are selected as the performance metrics for the reconstructed channel. Numerical results and simulation comparisons are given in Section 4. Finally, conclusions are drawn in Section 5.

2. OTA Testing Setup Model

In the MPAC OTA testing setup, the relationship between the geometric test area and the accuracy of the reconstructed radio channel is a key issue. Using prefaded signals synthesis (PFS) technology, the purpose is to select proper probes and configure the optimal weights to reconstruct the spatial characteristics in the test area [8], so that the target PAS and the discrete PAS are as similar as possible. In the OTA testing for massive MIMO devices, the device under test (DUT) usually has larger antenna radius and higher beam resolution. Thus, more active probes are needed to recreate the target channel. The relation between the number of probes and the radius of the test area is given in [9], which indicates that increasing the number of probes can reconstruct the target channel more accurately within a given test area. Traditionally, each probe is connected to an output of the channel emulator, and adding probes means more channel emulator resources, which will greatly increase the overall cost of the OTA testing setup. Inspired by this, the paper proposes the MPAC testing setup using cascaded APM network and CE to achieve the same effect of the multiple channel emulators, improving the performance of the testing system and controlling the overall system cost.

2.1. Structure and Performance of the APM Network. Figure 1 shows physical map (output A ports and input B ports; the amplitude and the phase of each link can be updated) of the APM network. As shown in Figure 2, the fully connected structure of the APM network (Figure 2(a)) is very different from the mechanical switch (Figure 2(b)) which selects the output ports through switching at each time. Each output port connected to probe A_k, $k = 1, 2, \ldots, K$, and each input port connected to channel emulator B_p, $p = 1, 2, \ldots, P$, are cross-connected. That is, each output port of the APM network is superimposed by all input signals. The amplitude and the phase of each internal link can be updated at each sampling time and can be controlled by loading the amplitude and phase which can be set to either complex or real numbers.

Compared with mechanical switches, the main advantages of APM networks can be summarized as follows: Firstly, cross-connected links between the inputs and outputs are independent of each other, and their weights can be adjusted digitally. In addition, there is no resonance problem that may occur in the switching process of the switch. Secondly, amplitudes and phases of the fully connected links take effect within 1 millisecond quickly. The digital switching process only needs to change the amplitudes and phases of the RF channels, and there is no disturbance problem which has been described for the mechanical switching process of the switch. Thirdly, the switch and the additional RF lines may cause amplitude and phase errors of different probe links. However, the APM network has the ability of autocalibration to balance errors caused by the RF lines. Last but not least, clock calibration is another important function of the APM network. Due to the faster response time compared with the switch, the APM network can synchronize with the channel emulator, and the weights inside the APM network can be adjusted precisely in the reconstructing process of the dynamic channel.

2.2. MPAC Setup with a Cascaded Model. Components of the proposed MPAC OTA testing setup are shown in Figure 3. Unlike the testing setup of the 2D OTA ring structure, the DUT is placed at the edge of the anechoic chamber so that the space of the chamber can be utilized fully to control system costs. The DUT is placed in the center of the test area, and the distance from each point on the sectored probe wall to the test area center is equal. The fully connected APM network which can adjust the amplitude and phase of each internal link replaces the original switch device. In the uplink communication system, the K outputs of the APM network are connected to K probes, and P inputs of the APM network are connected to P outputs of the fading channel emulators ($K > P$). The end of MPAC OTA testing setup is the user emulator.

It is worth noting that the mechanical switch uses a subset of all probes to emulate a static or dynamic channel. The number of probes used to synthesize the cluster is determined by the P outputs of the CE. That is, $(K - P)$ probes are idle, and therefore, the probe resources are wasted. In addition, the APM network which adjusts the

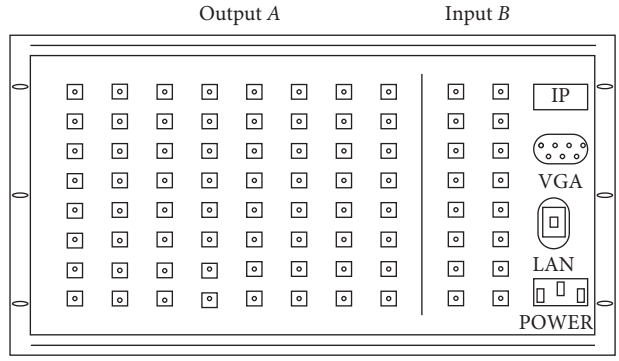

Figure 1: A physical map of the APM network equipment.

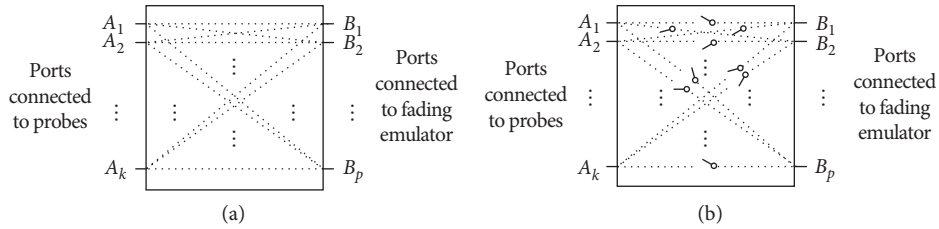

Figure 2: Internal connection structure of the (a) APM network and (b) the switch.

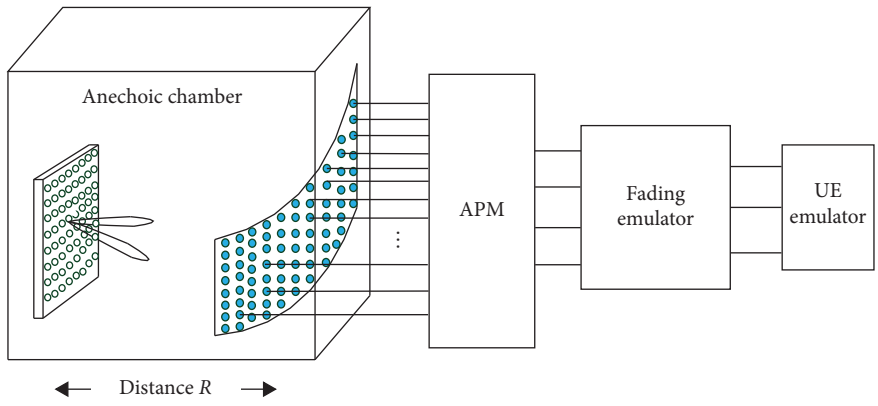

Figure 3: MPAC setup with cascaded APM network and CE for the massive MIMO BS.

frequency band signals has simpler structure and lower cost than the channel emulator. The OTA testing system using cascaded APM network and CE in Figure 3 can achieve the effect of multiple channel emulators and control the cost of the testing system. Based on the above descriptions, the APM network will have better performance than the switch system in OTA testing for mmWave massive MIMO devices.

In summary, the APM network can not only overcome the structural defects of the mechanical switch described above but also improve the testing performance of the OTA setup. The outputs of the CE and the probes used for channel reconstruction are no longer one-to-one mapping, but P-to-K. Adjusting the link parameters of the APM network properly and increasing the number of probes installed on the probe wall appropriately, the reconstructed channel can be obtained accurately. The specific implementation process and performance analysis will be detailed in Section 3. The effectiveness of the proposed MPAC setup for reconstructing the static channel model and dynamic channel model is verified in Section 4.

3. Implementation Process of the Cascaded MPAC OTA Setup

In the OTA testing system, spatial correlation can be used to evaluate the reconstructed radio channel [10]. However, there are several major problems using spatial correlation to evaluate reconstructed mmWave channels. Firstly, spatial correlation is used as a statistical measure of the similarity of the received signals, without comparing continuous angular spectrum and emulated angular spectrum synthesized by probes directly. In this process, if the number of sampling points' test area is finite and the specific parameters of the PAS are not considered, such as angular spread (AS) and

azimuth angle of arrival (AoA), two completely different angular spectrums may result in similar spatial correlation [10]. Secondly, for the sub-6 GHz OTA testing system, the spatial correlation is used to estimate the reconstruction of the channel directly. However, the mmWave massive MIMO systems are more directive and the channel is highly sparse and specular; therefore, spatial correlation function might be less relevant to determine OTA system performance [6]. Finally, the mmWave massive MIMO antennas have the beamforming capability, which should be studied when testing the performance of the DUT. Therefore, the selected evaluation metrics need to emphasize the performance of the beam, e.g., beam acquisition, tracking, refinement, and recovery [6]. Based on the above description, angular spectrum is selected as the test metric in the sequel.

3.1. Power Angular Spectrum

3.1.1. Target Power Angular Spectrum. Suppose that there is a virtual planar antenna array in the test area, which consists of M antenna elements. Using the classical Bartlett beamformer under a given geometry antenna array, the angular spectrum can be obtained by scanning the signal power in each DoA through spatial filtering [11]. Therefore, the target angular spectrum can be calculated for the reference channel model using the following equation [12]:

$$P(\Psi) = \mathbf{a}^H(\Psi)\left[\oint \mathbf{e}(\Phi)P(\Phi)\mathbf{e}^H(\Phi)\mathrm{d}\Phi\right]\mathbf{a}(\Psi), \tag{1}$$

where $\mathbf{a}(\Psi)$ is the normalized steering vector for spatial direction Ψ which consists of the azimuth ϕ and the elevation θ. Assuming the ideal far-field conditions, the expression of the steering vector is $\mathbf{a}(\Psi) = [(1/\sqrt{M})\exp(j(2\pi/\lambda)((\overrightarrow{op_\Psi}\cdot\overrightarrow{oa_1})/|\overrightarrow{op_\Psi}|)), (1/\sqrt{M})\ \exp(j(2\pi/\lambda)((\overrightarrow{op_\Psi}\cdot\overrightarrow{oa_2})/|\overrightarrow{op_\Psi}|)), \ldots, (1/\sqrt{M})\exp(j(2\pi/\lambda)\ ((\overrightarrow{op_\Psi}\cdot\overrightarrow{oa_M})/|\overrightarrow{op_\Psi}|))]^T$, and $\mathbf{e}(\Phi) = [e_1(\Phi), e_2(\Phi), \ldots, e_M\ (\Phi)]^T \in \mathbb{C}^{M\times 1}$ is a channel response vector with respect to signal direction Φ, where $\{\cdot\}^T$ and $\{\cdot\}^H$ represent the transpose and conjugate transpose of a matrix or vector, respectively. The DUT is placed in the center of the test area, $\overrightarrow{op_\Psi}$ represents the direction vector of incoming wave direction Ψ to the center origin o, and $\overrightarrow{oa_m}$ is the vector from the antenna element m of the BS to the center origin o, where $m = 1, 2, \ldots, M$. Covariance matrix $\mathbf{R} \in \mathbb{C}^{M\times M}$ of the received signals of the BS antenna is given by

$$\mathbf{R} = \oint \mathbf{e}(\Phi)P(\Phi)\mathbf{e}^H(\Phi)\mathrm{d}\Phi, \tag{2}$$

where $P(\Phi)$ is the angular spectrum density function of the angular direction Φ. The spherical angular spectrum needs to satisfy the following normalization condition [13]:

$$\oint P(\Phi)\mathrm{d}\Phi = \int_{-\pi}^{\pi}\int_{-\pi/2}^{\pi/2} P(\theta,\phi)\cos\theta\,\mathrm{d}\theta\,\mathrm{d}\phi = 1. \tag{3}$$

3.1.2. Emulated Power Angular Spectrum. The emulated angular spectrum is synthesized by a limited number of probes in the anechoic chamber, which is affected primarily by the probe positions and the power weights. Suppose that there are K available probes, the angular space set is $\{\Phi_k\}$ and the corresponding probe weight set is $\{w_k\}$, $k = 1, 2, \ldots, K$. According to the expression of the target angular spectrum, the emulated angular spectrum is [12] given by

$$\begin{aligned}\widehat{P}(\Psi, w) &= \mathbf{a}^H(\Psi)\widehat{R}\mathbf{a}(\Psi)\\ &= \mathbf{a}^H(\Psi)\sum_{k=1}^{K}\mathbf{e}(\Phi_k)w_k\mathbf{e}^H(\Phi_k)\mathbf{a}(\Psi),\end{aligned} \tag{4}$$

where w_k is the allocated power for the kth probe and K is the total number of the probes selected in the OTA experiment.

3.1.3. Objective Function. The target angular spectrum and emulated angular spectrum generated by the OTA probes are given in (1) and (4), respectively. Each vector element of the angular spectrum is a superposition of the radiant power and energy leakage from the DUT to each location on the probe wall. In order to determine the weights of probes to reconstruct the target channel, the optimization problem aiming at minimizing the deviation between the target and the emulated angular spectrum can be given by

$$\begin{aligned}\min_{\mathbf{w}}\quad & \|P(\Psi) - \widehat{P}(\Psi, \mathbf{w})\|_2^2\\ \text{s.t.}\quad & \|\mathbf{w}\|_1 = 1, \quad 0 \le w_k \le 1.\end{aligned} \tag{5}$$

It is noted that equation (5) is a quadratic programming problem with linear constraints, which can be solved by convex optimization techniques readily.

3.2. Implementation Process.

Proper probe selection can accurately reconstruct target channels and control the cost of the OTA testing setup. The multishot algorithm for the probe selection is described in [13]. The idea of the algorithm is to remove the probe with the smallest weight for each iteration and select an optimal subset of the candidate probes until the channel emulator resources (Pr_P output ports) are occupied completely. Different from switch, the advantage of the APM network is that Pr_K probes are used ($Pr_K > Pr_P$) for each cluster without increasing the channel emulator. However, Pr_P probes are a subset of Pr_K probes for the cluster using multishot algorithm, and the relationship between Pr_K and Pr_P is $Pr_P = Pr_K - \sum_{q=0}^{K-P-1} k_q$, where k_q is the number of the deleted probes for the qth iteration. In this way, the optimal probes which are required can be selected as much as possible.

Assuming that the APM network is connected to K probes which are selected and the weights $\mathbf{w} \in \mathbb{R}^{K\times 1}$ of the probes are obtained in equation (5) to synthesize the clusters of the dynamic channel in each sampling time. For simplicity and without loss of generality, the implementation process of the radiated test setup for a link is described in Figure 4. In addition, given that the delay between clusters is on the order of nanoseconds and the response time of APM is on the order of milliseconds, the MPAC testing setup with a cascaded model should reflect power-delay profiles (PDPs) accurately between the clusters. Therefore, the weight of each

cluster is controlled so that each output port of the channel emulator only outputs a series of impulse responses of a single cluster in Figure 4. Clusters with different delays are synthesized separately. During cluster synthesis, the total sampling time of the channel is assumed to be T. The impulse responses of the channel emulator are defined as $\mathbf{G} = \{\mathbf{G}(p,t)\} \in \mathbb{C}^{P\times T}$, and $\mathbf{G}(p,t)$ represents the impulse responses of the p output port at time t, $t = 1, 2, \ldots, T$ and $p = 1, 2, \ldots, P$. It should be noted that the number of the clusters L should be less than or equal to the number of the output ports of the channel emulator P (where we assume $L = P$). The restriction is proper for the mmWave channel reconstruction in [14], where the number of the identified clusters ranges from 8 to 12 in the non-line-of-sight (NLOS) scenario. Furthermore, each OTA antenna contributing to the cluster has independent fading coefficient sequences with identical statistics [8]. Therefore, the impulse responses which are output by cross-connected APM network need to ensure that probes are independently and identically distributed (i.i.d.). That is, the impulse response $\mathbf{G}$ passes the APM network and generates the i.i.d. impulse response $\mathbf{H} = \{\mathbf{H}_t(k,p)\} \in \mathbb{C}^{K\times P\times T}$ which is the expected target channel and mapped to probes through the output ports of the APM network.

Considering P clusters and achieving the exact mapping of the impulse responses of each cluster to the K output ports of the APM network at time t, there is a transition matrix $\mathbf{B}_t \in \mathbb{C}^{K\times P}$ which satisfies

$$\underset{\mathbf{B}_t, p=1,2,\ldots,P}{\text{minimize}} \left\| \begin{bmatrix} \sqrt{w_1}\cdot \mathbf{H}_t(1,p) \\ \sqrt{w_2}\cdot \mathbf{H}_t(2,p) \\ \vdots \\ \sqrt{w_K}\cdot \mathbf{H}_t(K,p) \end{bmatrix} - \begin{bmatrix} \mathbf{B}_t(1,p)\cdot \mathbf{G}(p,t) \\ \mathbf{B}_t(2,p)\cdot \mathbf{G}(p,t) \\ \vdots \\ \mathbf{B}_t(K,p)\cdot \mathbf{G}(p,t) \end{bmatrix} \right\|, \tag{6}$$

where $\mathbf{B}_t$ represents the transition matrix of the APM network at sample time t, and the weights $\{w_k\}$ are obtained in (5). The rows of the obtained transition matrix $\mathbf{B}_t$ correspond to the output ports of the APM network, and the number of columns is the output ports of the channel emulator. Each element represents the adjusted amplitude and phase of the APM network at sample time t. Given the sample time $t = 1, 2, \ldots, T$, using the i.i.d. impulse responses $\mathbf{H}$ which would be recreated accurately by the cascaded model and impulse responses $\mathbf{G}$, complex weight matrix $\mathbf{B} \in \mathbb{C}^{K\times P\times T}$ would be obtained.

Naturally, through the transition matrix $\mathbf{B}_t(p) \in \mathbb{C}^{K\times 1}$ and the impulse response $\mathbf{G}(p,t) \in \mathbb{C}$ generated by the pth port of the channel emulator, the i.i.d. impulse responses $\mathbf{H}_t(p) \in \mathbb{C}^{K\times 1}$ of K output ports of the APM network can be synthesized to achieve the effect of increasing probes at sampling time t:

$$\mathbf{H}_t(p) = \mathbf{B}_t(p)\cdot \mathbf{G}(p,t), \tag{7}$$

sampling time t and port of the channel emulator p can be traversed to obtain channel impulse responses $\mathbf{H}$.

3.3. Capacity Evaluation. Channel capacity reflects transmitted rate ability of the channel and is an important measure of the wireless communication, which can be improved effectively by using antenna array technology. Therefore, massive MIMO arrays at the BS can be utilized to improve the transmission rate of the MIMO communications. Besides the previous work focused on angular spectrum accuracy at Rx side, the impact of the Tx side antenna arrays and the propagation environments would be considered as well in this subsection. The reference channel models, i.e., GSCMs, and the channel emulation methods (PFS) are introduced later. Then, we use the MIMO rate capacity [15] as a metric to study the accuracy of the emulated channel using the APM network and the switch in the OTA testing setup, respectively.

Through the uplink established in the antenna systems, the channel capacity can be expressed by the Shannon formula:

$$C(t) = \frac{1}{N_f}\sum_{n_f=1}^{N_f} \log_2 \det\left(\mathbf{I} + \frac{\gamma}{N_t}\cdot H\left(t,n_f\right)\cdot H\left(t,n_f\right)^H\right), \tag{8}$$

where γ is the signal-to-noise ratio, N_f is the number of subcarriers, and N_t is the number of transmitter antennas. $\mathbf{H}_{\text{ref}}(t,n_f) \in \mathbb{C}^{U\times S}$ and $\mathbf{H}_{\text{ota}}(t,n_f) \in \mathbb{C}^{U\times S}$ are the reference channel matrix and emulated channel matrix in the frequency domain, respectively, which can be obtained by performing the Fourier transform of the channel impulse responses $\left\{H_{u,s}^{\text{ref}}(t,\tau)\right\}$ and $\left\{H_{u,s}^{\text{ota}}(t,\tau)\right\}$ in Appendix A. Through (7), reference channel capacity $\mathbf{C}_{\text{ref}}(t)$ and emulated channel capacity $\mathbf{C}_{\text{ota}}(t)$ are simulated to analyze the accuracy of the OTA emulated channels which are recreated by the APM network and the switch, respectively.

4. Simulation Results

In this section, simulation results are provided to verify the performance of the MPAC setup with a cascaded model. Assume that the massive MIMO DUT operates at 28 GHz. The angular spectrum is used as the performance metric, and the simulation experiments are carried out under both static and dynamic channel scenarios. Uniform line array (ULA) on the Tx side consists of 4 antennas which are ideal dipoles, and mutual coupling effect between antennas is ignored. There is an Rx antenna array which is composed of 8×8 omnidirectional antennas. In simulations, it is assumed that the distance R from the DUT center to the probe wall is far enough to meet the far-field condition. In addition, the multipath channels are simulated with 10000 time samples and a sampling interval is defined as 1 millisecond. Therefore, the update rate of the APM network in simulations is also defined as 1 millisecond to generate the expected impulse responses $\mathbf{H}$. The power angular spectrums of the target clusters obey the Laplacian distribution which is defined in [15]. Without loss of generality, 91 probes are placed fixedly on the probe wall in $[-30^\circ, 30^\circ]$ of the horizontal positions with 5° intervals and $[-15^\circ, 15^\circ]$ of the vertical positions with 5° intervals, which are used in the cascaded testing model. In addition, the multishot algorithm for the probe selection is used to select optimal 8 probes

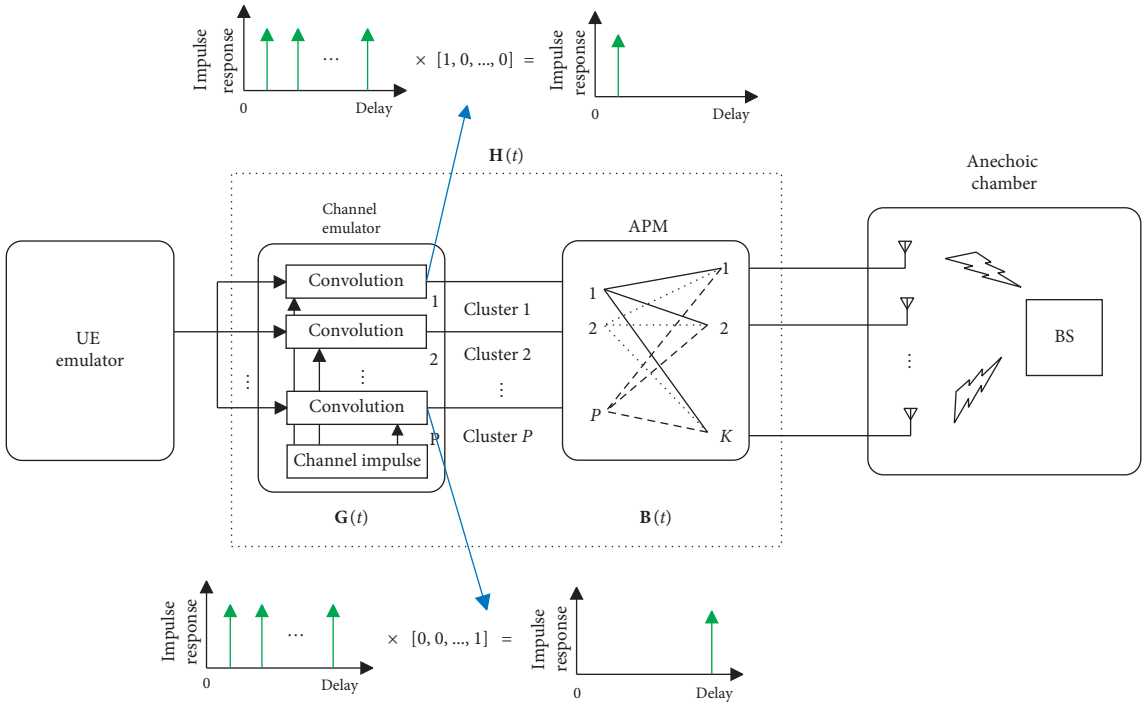

Figure 4: Block diagram of the radiated test setup.

from 91 probe antennas in the OTA testing setup with the switch. For simplicity, we will only discuss the situations for single cluster hereafter. In this study, ignoring the uncontrollable effects of the mechanical switch and the APM network, we assume that they are completely free to perform the switching at each considered moment without any distortion, and upper bounds of the performance for OTA testing setups with switch and APM network are given in the simulations, respectively.

4.1. Static Angular Spectrum. The performance of the proposed testing setup is considered for the static channel model. Angular spectrums observed by the DUT through Bartlett beamforming are compared. From equation (1) and equation (4), the target angular spectrum and the emulated angular spectrum can be calculated conveniently. Figure 5 depicts the simulation result of the target angular spectrum of a single cluster which obeys truncated Laplacian distributed 3D PAS with ASA = 10° and ESA = 3° (CDL-B model [16]), and its AoA and EoA are assumed to be 0° and 0°, respectively. The other structures of the MPAC testing system have not been changed. Figures 6(a) and 6(b) represent emulated angular spectrum emulated by the APM network and the switch, respectively. The peak of the target angular power is 15.13 dB, which has been illustrated in Figure 5. Intuitively, compared with the angular spectrum in Figure 6(b), the emulated angular spectrum using the APM network in Figure 6(a) is more similar to the target angular spectrum. According to the numerical analysis, the peak value deviation between the target and the emulated angular spectrum in Figure 6(a) is insignificant, which is 0.01 dB, indicating that the array gain in the emulated channel is

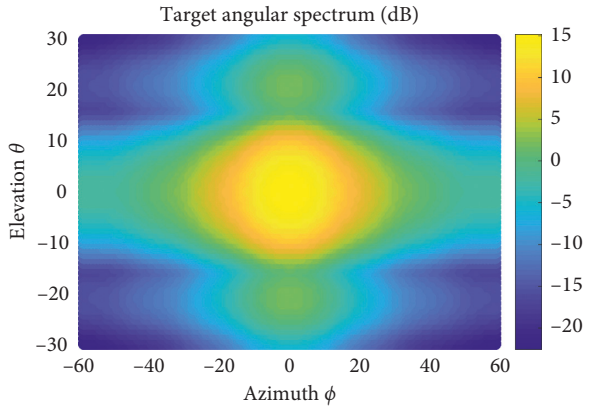

Figure 5: Target angular spectrum with AoA = 0°, EoA = 0°, ASA = 10°, and ESA = 3°.

accurate, and the error of the emulated angular spectrum in Figure 6(b) is 0.14 dB. Obviously, the angular spectrum in Figure 6(a) reconstructs the target angular spectrum in Figure 5 more accurately than that in Figure 6(b).

In Figure 7, using the APM network and the switch, respectively, the errors between the emulated angular spectrum and the target angular spectrum for the direction Ψ are defined as $10\log P(\Psi) - 10\log \widehat{P}(\Psi, w)$. In Figure 7(a), the image of the error is symmetrical. Since the mean spatial angle of the target PAS is defined as $(0°, 0°)$, and the installed probes are symmetrically distributed, the symmetry phenomenon of the Figure 7(a) can be comprehended easily. In addition, the r.m.s. error describes the average variance distance between the target angular spectrum and the emulated angular spectrum, and the r.m.s. errors are −16.65 dB and −4.18 dB in Figures 7(a) and 7(b), respectively.

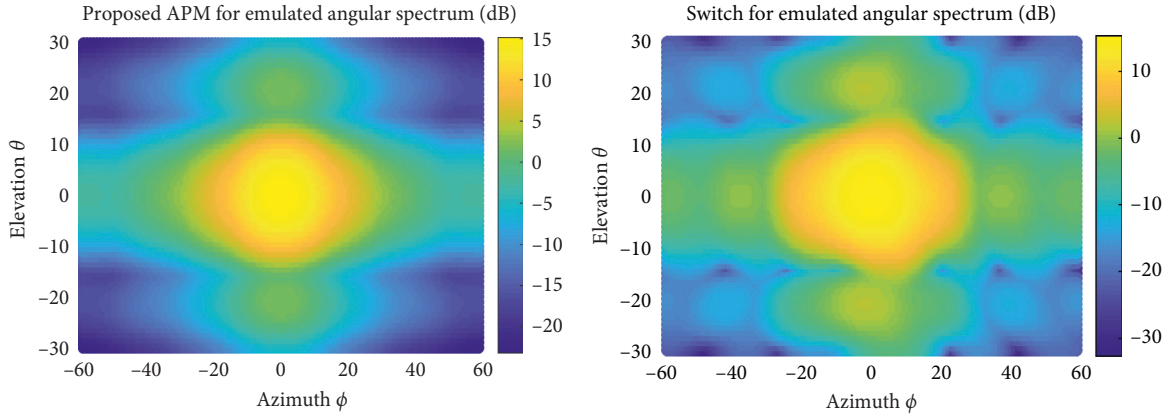

(a) (b)

Figure 6: Emulated angular spectrums with the APM network (a) and the switch (b).

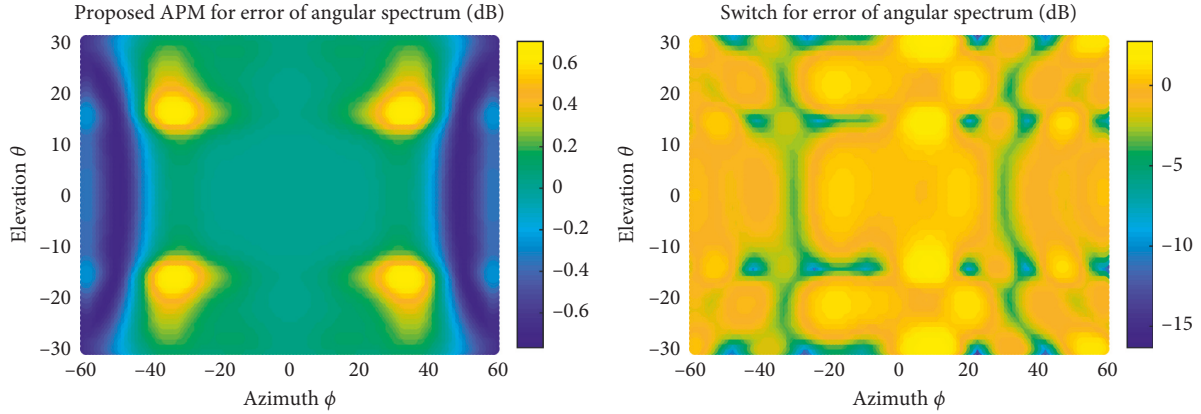

(a) (b)

Figure 7: Errors of the angular spectrum with the APM network (a) and the switch (b).

Furthermore, a large number of simulations are performed under different cluster settings to verify the performance of the MPAC testing setup using a cascaded model. Besides CDL-B link model in [16], the typical CDL-A model and CDL-C model described in [16] are simulated, and their results are given in Table 1. As summarized in Table 1, the proposed APM network can reproduce the angular spectrum with higher precision, which is advantageous for verifying the performance of the mmWave massive MIMO BS accurately.

4.2. Dynamic Angular Spectrum. Beamforming is the key technology of the mmWave BS and should be reflected in the reconstructed dynamic channel of the OTA testing. Therefore, compared the APM network with the switch, the emulated dynamic angular spectrums are discussed in the sequel. The angular spectrum can emphasize the performance of the beam, e.g., beam acquisition, tracking, refinement, and recovery. To reflect the dynamic channel intuitively, the angular spectrum is described by adding a time dimension. Without loss of generality, referencing CDL-B in [16], the ASA is 10° and ESA is defined as 3°. The azimuth target angle is increased from −10° to 10° with 0.1° intervals, and the elevation angle is decreased from 10° to −10° with 0.1° intervals gradually. Therefore, there are 201 time samples. Figure 8 describes the dynamic target angular spectrum, where each slice represents an angular spectrum at a different time samples.

It is difficult for the visual presentation to analysis 4D simulation pictures, and therefore, the target azimuth angular spectrum and the elevation with time samples are simulated in Figures 9(a) and 9(b), respectively. From the angular spectrum in Figure 9, azimuth AoA and elevation EoA change from −10° to 10° and 10° to −10°, respectively, which can describe the variety of the spatial direction Ψ. Due to the angle spread of the cluster and limited resolution of the Bartlett beamformer, there are power spreads for the variety of the dynamic channel, which have been presented at the target angular spectrum.

To achieve performance comparison between the APM network and the switch, a proper simulation scenario needs to be set up. Depending on the distribution of clusters at any sampling time, the probes are arranged evenly at intervals of 5° in the horizontal direction −30° to 30° and vertical direction −15° to 15° of the probe wall, which can be used by

Table 1: Emulation deviations for different cluster settings.

Cluster settings				Angular spectrum with APM		Angular spectrum with switch	
AoA (°)	EoA (°)	ASA (°)	ESA (°)	|peak| (dB)	r.m.s (dB)	|peak| (dB)	r.m.s (dB)
−20	10	10	3	0.0031	−5.2557	0.0438	−3.7885
−20	10	5	3	0.00017	−15.2405	0.00034	−9.1467
−20	10	2	3	0.0017	−17.1357	0.002	−14.2699
5	−5	10	3	0.0030	−14.5862	0.0585	−3.3436
5	−5	5	3	0.00039	−26.9030	0.0069	−6.1667
5	−5	2	3	0.00085	−22.3349	0.0019	−14.0239
10	−5	10	3	0.0027	−11.5519	0.1405	−3.9020
10	−5	5	3	0.00043	−26.5943	0.00071	−8.9643
10	−5	2	3	0.00082	−22.5181	0.0019	−14.0001

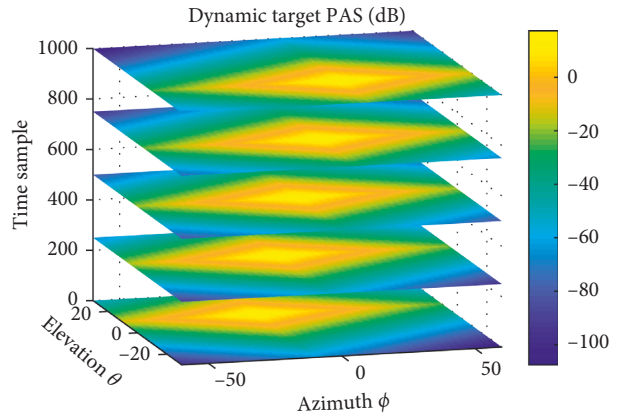

Figure 8: Dynamic target PAS of the cluster with time samples. ASA = 10°, ESA = 3°, AoA ranges from −10° to 10°, and EoA ranges from −10° to 10°.

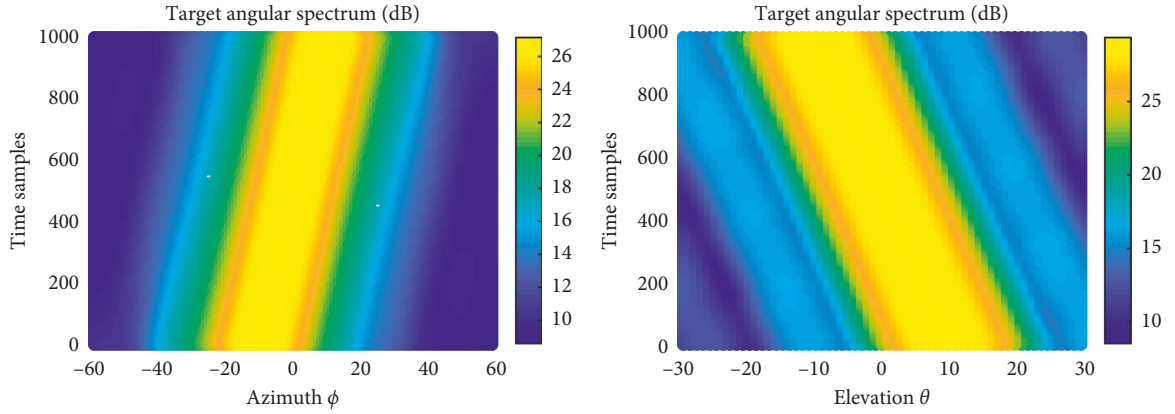

Figure 9: Power distribution of target azimuth and elevation in the dynamic channel model. AoA ranges from −10° to 10°, EoA ranges from −10° to 10°, ASA = 10°, and ESA = 3°.

the cluster fully at all sampling moments. Using the fully connected APM network system, all of the above 91 probes can be used to reconstruct the target channel. In addition, given the limited resources of the channel emulators, it is assumed that 8 probes are selected for the channel reconstruction using the multishot selection strategy. The scenario represents an existing switch configuration system.

According to equation (5), the emulated angular spectrums under two different systems are obtained. Figure 10 illustrates the emulated azimuth and elevation angular spectrum for the dynamic channel model with the APM network. The simulations use all 91 probes at each time. The vertical axis of the two subgraphs (Figures 10(a) and 10(b)) represents time samples, and the horizontal axes represent the azimuth ψ and elevation θ, respectively. It can be seen

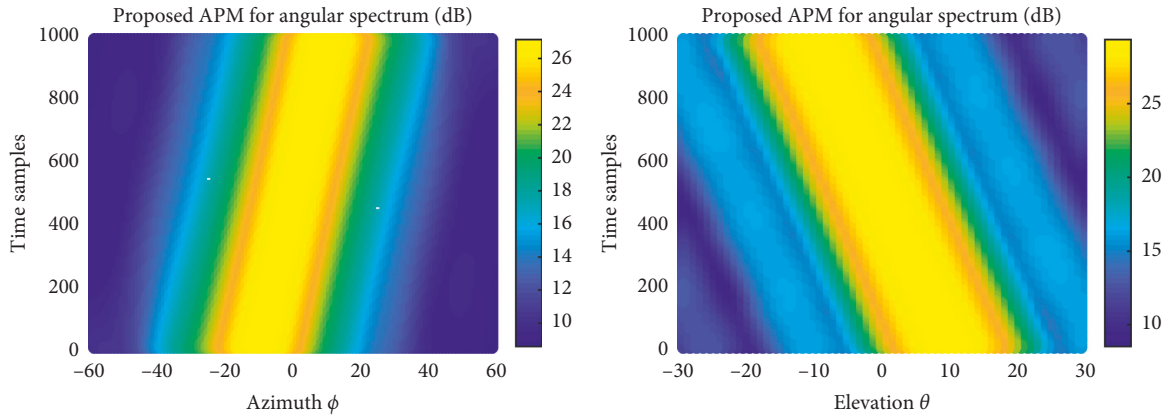

Figure 10: APM network for azimuth and elevation angular spectrum for a dynamic channel model.

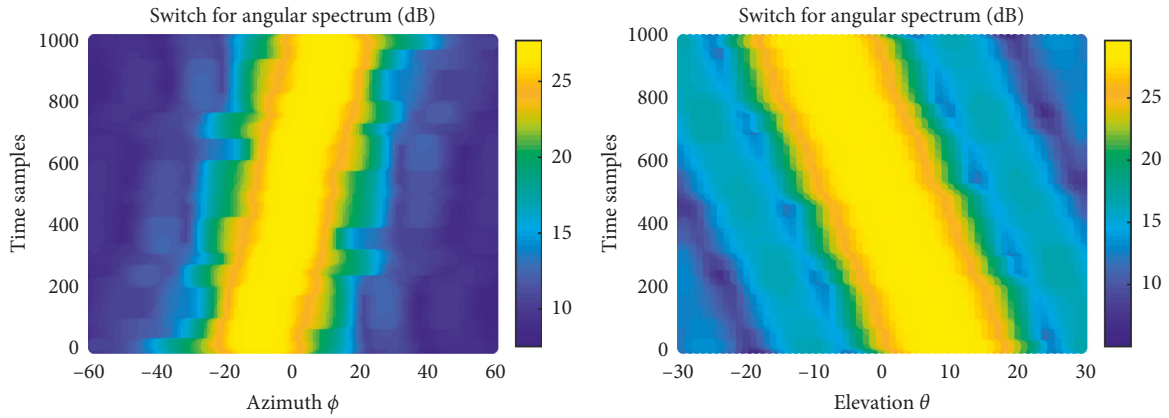

Figure 11: Switch system for azimuth and elevation angular spectrum for a dynamic channel model.

that the subgraphs in Figure 10 can match very well with the target angular spectrum. Compared with Figure 9, the angular spectrums of Figure 11 are obviously different. Although the characteristics of the beam acquisition and tracking can be realized, the beam power is significantly disturbed by other directions. The reconstructed channel has significant errors compared with the MPAC setup using a cascaded model.

Next, the angular spectrums in Figures 9–11 are compared numerically. Figure 12 describes the peak powers of the target angular spectrum and the emulated angular spectrum using the APM network and the switch at different times. As above, the peak powers are given from the azimuth and elevation at different sampling times, and the existing differences can be observed clearly. It is clear that the peak powers emulated by the APM system coincide with the target peak powers completely at different times in Figure 12. However, for the existing switch system, the deviations of the peak powers are obvious. In addition, in order to show the overall differences between the target angular spectrum and emulated angular spectrum, Figure 13 presents the r.m.s. errors obtained at different sampling times. From the obtained r.m.s. errors, the

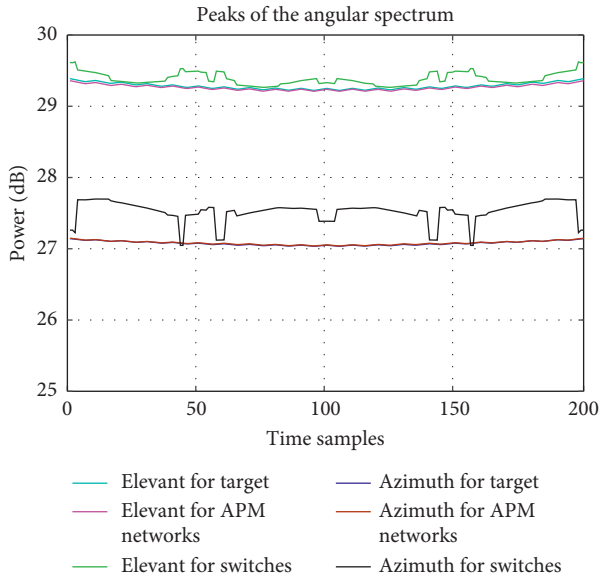

Figure 12: The peak powers of the angular spectrum at sampling time.

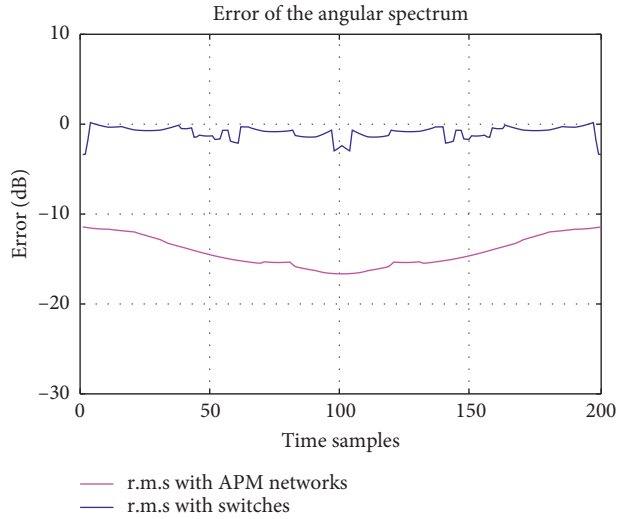

Figure 13: The r.m.s. errors of the angular spectrum at sampling times.

mean deviation of the angular spectrum simulated by the APM network is lower 10 dB than the angular spectrum emulated by the switch at each sampling time. It is verified that the reference channel can be reconstructed more accurately by increasing the number of probes without changing the size of the test area.

Another point to note is that all curves show symmetrical characteristics, which is reasonable due to the following reasons. Firstly, the DUT antennas in the test area are symmetric with respect to the center of the DUT panel in simulation. Secondly, the probes which are placed on the probe wall are distributed evenly, and the probe positions are symmetrical on the probe wall. Thirdly, at different sampling moments, the mean spatial angle of the cluster is symmetrical with respect to the center of the probe wall (AoA ranges from -10° to 10° and EoA ranges from 10° to -10°). Based on these three reasons, the symmetry presented in the simulation diagram can be explained.

4.3. Channel and the Rate Capacity. Under ideal far-field conditions, the signal-to-noise ratio is $\gamma = 20$ dB and the power of the target cluster is 1. The channel coefficients consist of the 64×4 CIR matrix from the UE antennas to the DUT elements. $\mathbf{F}_{\mathrm{OTA}}$ is ideal polarimetric antenna pattern vector $[0, 1]$ of the OTA probes, and the polarimetric antenna pattern vector $\mathbf{F}_{s,\mathrm{UE}}$ is defined as $[1, 0]^T$ for the UE. The elements of the polarization matrix are $\alpha_{l,q}^{VV} = \exp(j\Phi_{l,q}^{VV})$, $\alpha_{l,q}^{HV} = \sqrt{\kappa_{l,q}}\exp(j\Phi_{l,q}^{HV})$, $\alpha_{l,q}^{VH} = \sqrt{\kappa_{l,q}}\exp(j\Phi_{l,q}^{VH})$, and $\alpha_{l,q}^{HH} = \exp(j\Phi_{l,q}^{HH})$. $\Phi_{l,q}^{VV}$, $\Phi_{l,q}^{HV}$, $\Phi_{l,q}^{VH}$, and $\Phi_{l,q}^{HH}$ are i.i.d. random variables which are uniformly distributed over $[0, 2\pi]$. $\kappa_{l,q}$ is the XPR of the qth subpath of the lth cluster.

Figures 14 and 15 present instantaneous channels and capacities under 10000 time samples for the reference and emulated SCME CDL-B channel model. Instantaneous amplitudes of the reference channel, the estimated channel with APM network, and the estimated channel with switch are simulated in Figure 14, respectively. It can be seen from the instantaneous channels of different receiving antennas that the average power is close to 1 within the sampling time. As expected, comparing $\mathbf{H}_5(t, \tau)$ with $\mathbf{H}_6(t, \tau)$ or comparing $\mathbf{H}_{60}(t, \tau)$ with $\mathbf{H}_{61}(t, \tau)$, the channel amplitude variations of the receiving antennas at adjacent locations are approximately same. The first-order statistical feature of the reference channel and the emulated channel is approximately consistent. In Figure 15, the vertical axis of the figure represents the transmission rate per unit time of unit bandwidth. In order to compare the APM network with the switch system visually, the average channel capacity is presented. Through numerical calculation, the average channel capacity of the reference channel for single receiver antenna is about 10.02 bits/s/Hz, and the emulated capacity with APM network and switch is 9.98 bits/s/Hz and 9.92 bits/s/Hz, respectively.

Due to the fact that three instantaneous curves are messy, we plot the cumulative distribution functions (CDFs) of the capacity results for scenario CDL-B shown in Figure 16, switch and reference channel. Compared with the emulated channel generated by the switch, the CDF of the emulated channel generated by the APM network matches well with the reference channel model. Thus, based on the simulation results of both channel capacity and angular spectrum, the MPAC testing system with the APM network can reconstruct the radio channel environment better than the switch system.

The simulation results show that the cascaded model in this paper is effective. However, some practical problems may be considered in the future testing process. On the one hand, accuracy errors of the amplitude modulation and phase modulation may have impact on recreated channel, which are less than 1.4° and 0.5 dB, respectively. On the other hand, digital APM network may also have some uncertain hardware problems, i.e., insertion loss and isolation. In addition, given the sampling rate of the channel emulator and APM network, it may be difficult to create a high-speed channel environment. As a future work, we will further study the influence of the above nonideal factors on channel reconstruction.

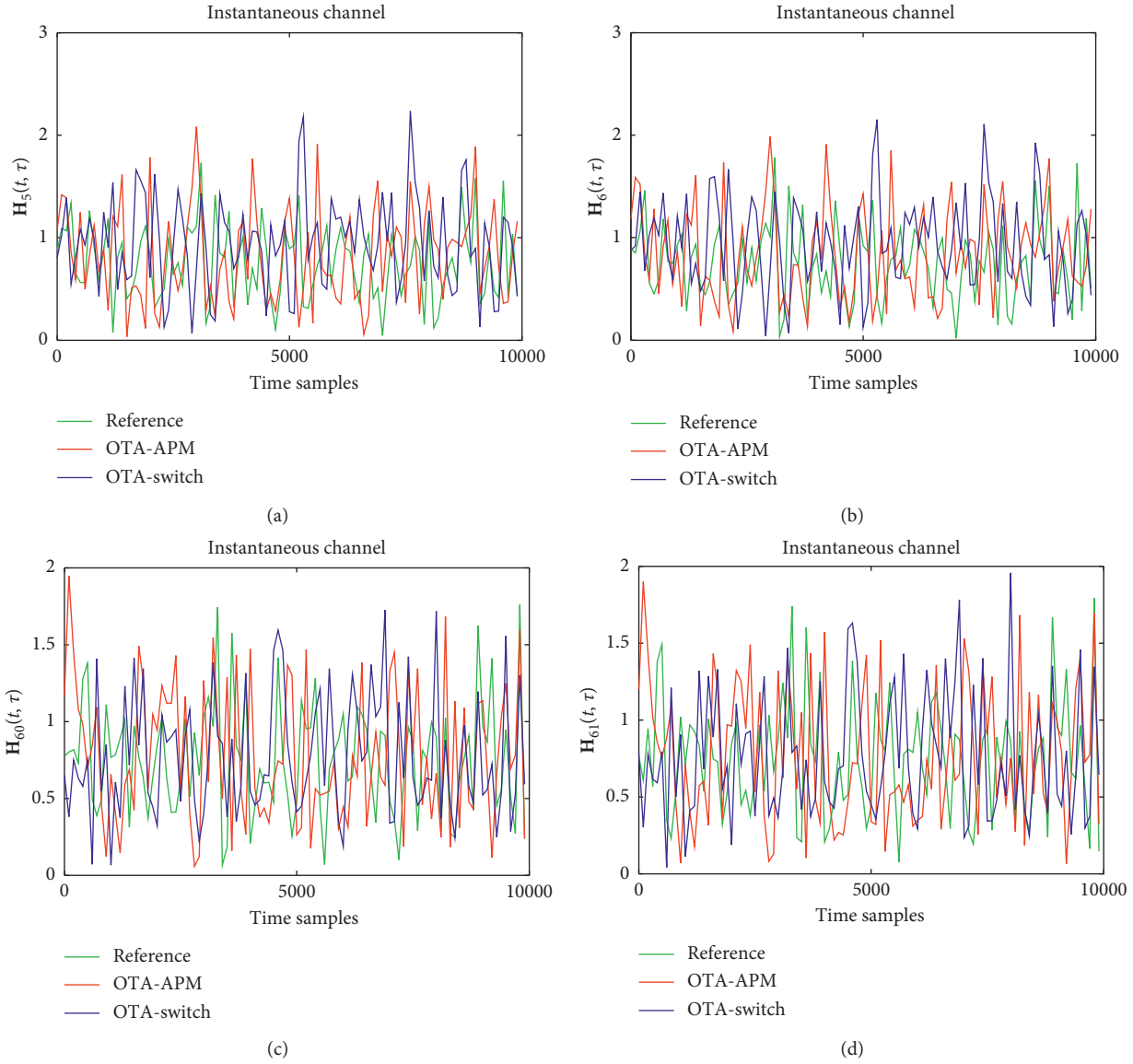

Figure 14: Instantaneous channels of the receiver antennas 5, 6, 60, and 61 for the reference and emulated SCME CDL-B channel model, $\mathbf{H}_5(t,\tau)$, $\mathbf{H}_6(t,\tau)$, $\mathbf{H}_{60}(t,\tau)$, and $\mathbf{H}_{61}(t,\tau)$.

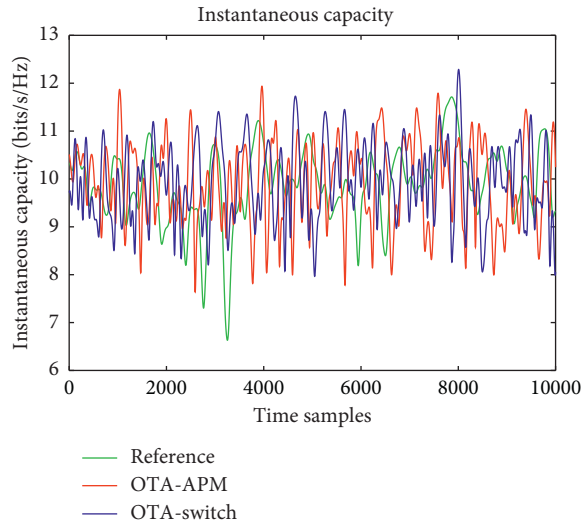

Figure 15: Instantaneous capacities for the reference and emulated SCME CDL-B channel model. The SNR σ is 20 dB.

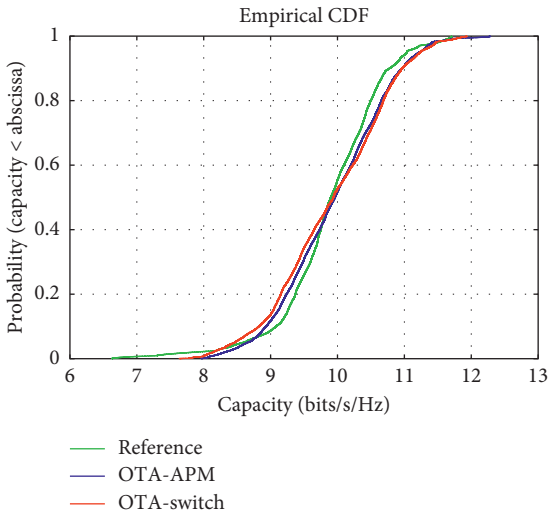

Figure 16: CDFs of the channel capacity for scenario CDL-B with average SNR $\sigma = 20$ dB.

5. Conclusion

We have proposed a MPAC testing setup for mmWave massive MIMO devices using cascaded APM network and CE. The internal structure of the APM network and the drawbacks of mechanical switch for the mmWave devices testing are introduced in detail. The paper uses spherical angular spectrum to determine probe weights instead of using the spatial correlation. Considering the resolution of the BS antenna array and the shortcomings of the spatial correlation itself, the angular spectrums are simulated to measure the reconstructed mmWave channel accurately.

Further, simulations for the single cluster based on the static and dynamic channel models have been done in this paper, confirming the superiority of the proposed APM network. In static channel model, the cluster is simulated by the angular spectrum, and the peak power and r.m.s. error are compared using the APM network and switch, respectively. For testing the mmWave massive MIMO devices, dynamic channel model and test environment have been considered carefully. Reconstructing a time-variant dynamic channel model, the weights must be updated frequently according to the channel changes. The time dimension is added to show the accuracy of the angular spectrum estimated under dynamic channel conditions. In addition, the channel capacity as a performance measure is also studied. All simulations give encouraging results for testing the performances of massive MIMO devices using MPAC setup with APM network. In addition, what needs to be made clear is that the probe configuration for multiclusters should be considered in real environment. Given that multiclusters will share the selected probes, the performance of the proposed OTA testing setup will be more prominent than for single cluster.

Appendix

A

A.1. Reference Channel Models. The ray-based channel model is a GSCM which is selected in the study at the same frequency. One simplicity of the GSCM is its ability to separate into the propagation environments, antenna at the BS and user equipment side. For the reference model, the channel impulse response (CIR) matrix $\mathbf{H}_{\text{ref}}(t,\tau) \in \mathbb{C}^{U\times S}$ can be generated in [17]. For a MIMO system that deploys U antenna elements at the BS side and S antenna elements at the UE side, the MIMO channel $\mathbf{H}_{\text{ref}}(t,\tau)$ can be represented by

$$\mathbf{H}_{\text{ref}}(t,\tau) = \begin{bmatrix} h_{1,1}(t,\tau) & \cdots & h_{1,S}(t,\tau) \\ \vdots & \ddots & \vdots \\ h_{U,1}(t,\tau) & \cdots & h_{U,S}(t,\tau) \end{bmatrix}, \tag{A.1}$$

where the time-variant radio channel transfer function $h_{u,s}(t,\tau)$ can be written as

$$h_{u,s}(t,\tau) = \sum_{l=1}^{L} h_{u,s,l}(t,\tau), \tag{A.2}$$

where L is the number of clusters and t is the time. For each receiver and transmitter element pair (u,s), the channel coefficient for lth cluster can be expressed as [17]

$$\begin{aligned} h_{u,s,l}(t,\tau) = {} & \sqrt{\frac{P_l}{Q}} \sum_{q=1}^{Q} \begin{bmatrix} F_{s,UE}^{V}(\phi_{l,q}) \\ F_{s,UE}^{H}(\phi_{l,q}) \end{bmatrix}^{T} \begin{bmatrix} \alpha_{l,q}^{VV} & \alpha_{l,q}^{VH} \\ \alpha_{l,q}^{HV} & \alpha_{l,q}^{HH} \end{bmatrix} \cdot \begin{bmatrix} F_{u,BS}^{V}(\varphi_{l,q}) \\ F_{u,BS}^{H}(\varphi_{l,q}) \end{bmatrix} \\ & \cdot \exp\left(j2\pi v_{l,q} t\right) \cdot \exp\left(j2\pi \vec{r}_{tx,l,q} \cdot \mathbf{d}_{tx,s}\right) \\ & \cdot \exp\left(j2\pi \vec{r}_{rx,l,q} \cdot \mathbf{d}_{rx,u}\right) \cdot \delta(\tau - \tau_l), \end{aligned} \tag{A.3}$$

where $\phi_{l,q}$, $\varphi_{l,q}$, and $v_{l,q}$ are the angle of departure, angle of arrival, and Doppler frequency of the qth subpath of the lth cluster, respectively. P_l and τ_l denote the power and delay of the lth cluster. $F_{s,UE}^{V}$ and $F_{s,UE}^{H}$ are the field patterns of UE antenna element s for the vertical and horizontal polarization, respectively. Similarly, $F_{u,BS}^{V}$ and $F_{u,BS}^{H}$ are the field patterns of BS antenna element u for the vertical and horizontal polarization, respectively. Coefficient $\alpha_{l,q}^{ab}$ is the complex amplitude of the qth subpath of the lth cluster for transmit polarization a and receive polarization b. $\vec{\mathbf{r}}_{rx,l,q}$ is the spherical unit vector with azimuth arrival angle $\phi_{n,m,\text{AOA}}$ and elevation arrival angle $\theta_{n,m,\text{ZOA}}$. $\vec{r}_{tx,l,q}$ is the spherical unit vector with azimuth departure angle $\phi_{n,m,\text{AOD}}$ and elevation departure angle $\theta_{n,m,\text{ZOD}}$. $\mathbf{d}_{rx,u}$ is the location vector of receiver antenna element u and $\mathbf{d}_{tx,s}$ is the location vector of transmitter antenna element s.

A.2. Emulated Channel Models. The radio channels from the UE to the DUT (BS) array are calculated for the OTA testing. For an MPAC setup equipped with K OTA probes, the channel matrix $\mathbf{H}_{\text{ota}}(t,\tau) \in \mathbb{C}^{U\times S}$ is composed of the transfer matrix $\mathbf{V} = \{v_{m,k}\} \in \mathbb{C}^{M\times K}$ from K probes to M DUT antennas and the fading components of the channel model $\mathbf{H}_{K,S}^{\text{ota}}(t,\tau) = \left\{\sum_{l=1}^{L} h_{k,s,l}^{\text{ota}}(t,\tau)\right\}$ and defined as

$$h_{k,s,l}^{\text{ota}}(t,\tau) = \sqrt{\frac{P_l}{Q}} \sum_{q=1}^{Q} \mathbf{F}_{s,\text{UE}}\left(\phi_{l,q}\right) \begin{bmatrix} \alpha_{l,q}^{VV} & \alpha_{l,q}^{VH} \\ \alpha_{l,q}^{HV} & \alpha_{l,q}^{HH} \end{bmatrix} \mathbf{F}_{\text{OTA}} \cdot \sqrt{w_{l,k}} \exp\left(j2\pi v_{l,q} t\right) \cdot \exp\left(j2\pi \overrightarrow{r}_{tx,l,q} \cdot \mathbf{d}_{tx,s}\right) \cdot \delta\left(\tau - \tau_l\right),$$

$$\mathbf{H}_{\text{ota}}(t,\tau) = \mathbf{V} \cdot \mathbf{H}_{K,S}^{\text{ota}}(t,\tau), \tag{A.4}$$

where $w_{l,k}$ are the weights of k probe for the lth cluster and $\mathbf{F}_{\text{OTA}}$ is an ideal polarimetric antenna pattern matrix of the OTA probes. In testing, the transmit power of each OTA probe is calibrated to the same level as the calibrated antenna at the center of the test area, and the pathloss caused by the free space propagation from the OTA probe to the test area is omitted.

Data Availability

The authors claim that all data generated or analysed in this article are provided by the simulations and are included in this published article. The MATLAB data used to support the findings of this study are available from the corresponding author upon request.

Conflicts of Interest

The authors declare that they have no conflicts of interest.

Acknowledgments

This work was supported in part by the National Natural Science Foundation of China (Grant no. 61971067), in part by the State Major Science and Technology Special Projects (Grant nos. 2018ZX03001028-003), and in part by the Beijing Municipal Science and Technology Project (Grant no. Z191100007519002). The work of L. Xin was supported by the BUPT Excellent PhD Students Foundation (Grant no. CX2018103).

References

[1] J. G. Andrews, T. Bai, M. N. Kulkarni, A. Alkhateeb, A. K. Gupta, and R. W. Heath, "Modeling and analyzing millimeter wave cellular systems," *IEEE Transactions on Communications*, vol. 65, no. 1, pp. 403–430, 2016.

[2] E. G. Larsson, O. Edfors, F. Tufvesson, and T. L. Marzetta, "Massive MIMO for next generation wireless systems," *IEEE Communications Magazine*, vol. 52, no. 2, pp. 186–195, 2014.

[3] W. A. T. Kotterman, C. Schirmer, M. H. Landmann, and G. Del Galdo, "New challenges in over-the-air testing," in *Proceedings of the 2017 11th European Conference on Antennas and Propagation (EUCAP)*, pp. 3676–3678, Paris, France, March 2017.

[4] P. Kyösti, L. Hentilä, W. Fan, J. Lehtomäki, and M. Latva-Aho, "On radiated performance evaluation of massive MIMO devices in multi-probe anechoic chamber OTA setups," *IEEE Transactions on Antennas and Propagation*, vol. 66, no. 10, pp. 5485–5497, 2018.

[5] P. Kyösti, W. Fan, G. F. Pedersen, and M. Latva-Aho, "On dimensions of OTA setups for massive MIMO base stations radiated testing," *IEEE Access*, vol. 4, pp. 5971–5981, 2016.

[6] W. Fan, P. Kyosti, M. Rumney, X. Chen, and G. F. Pedersen, "Over-the-air radiated testing of millimeter-wave beam-steerable devices in a cost-effective measurement setup," *IEEE Communications Magazine*, vol. 56, no. 7, pp. 64–71, 2018.

[7] R. E. Mihailovich, M. Kim, J. B. Hacker et al., "MEM relay for reconfigurable RF circuits," *IEEE Microwave and Wireless Components Letters*, vol. 11, no. 2, pp. 53–55, February 2001.

[8] P. Kyösti, T. Jams, and J.-P. Nuutinen, "Channel modelling for multiprobe over-the-air MIMO testing," *International Journal of Antennas and Propagation*, vol. 2012, Article ID 615954, 11 pages, 2012.

[9] A. Khatun, V.-M. Kolmonen, V. Hovinen et al., "Experimental verification of a plane-wave field synthesis technique for MIMO OTA antenna testing," *IEEE Transactions on Antennas and Propagation*, vol. 64, no. 7, pp. 3141–3150, 2016.

[10] W. Fan, X. C. B. Lisbona, F. Sun, J. Ø. Nielsen, M. B. Knudsen, and G. F. Pedersen, "Emulating spatial characteristics of MIMO channels for OTA testing," *IEEE Transactions on Antennas and Propagation*, vol. 61, no. 8, pp. 4306–4314, 2013.

[11] P. Stoica and R. L. Moses, *Spectral Analysis of Signals*, Prentice-Hall, Upper Saddle River, NJ, USA, 2005.

[12] Y. Li, L. Xin, and X. Zhang, "On probe weighting for massive MIMO OTA testing based on angular spectrum similarity," *IEEE Antennas and Wireless Propagation Letters*, vol. 18, no. 7, pp. 1497–1501, 2019.

[13] W. Fan, F. Sun, J. O. Nielsen et al., "Probe selection in multiprobe OTA setups," *IEEE Transactions on Antennas and Propagation*, vol. 62, no. 4, pp. 2109–2120, 2014.

[14] C. Gustafson, K. Haneda, S. Wyne, and F. Tufvesson, "On mm-Wave multipath clustering and channel modeling," *IEEE Transactions on Antennas and Propagation*, vol. 62, no. 3, pp. 1445–1455, 2014.

[15] F. Kaltenberger, D. Gesbert, R. Knopp, and M. Kountouris, "Correlation and capacity of measured multi-user MIMO channels," in *Proceedings of the2008 IEEE 19th International Symposium on Personal, Indoor and Mobile Radio Communications*, pp. 1–5, Cannes, France, September 2008.

[16] ETSI, "Study on channel model for frequencies from 0.5 to 100 GHz," 3GPP 38.901 Tech. Rep. V14.1.1, ETSI, Sophia Antipolis, France, 2017.

[17] W. Fan, P. Kyosti, S. Fan et al., "3D channel model emulation in a MIMO OTA setup," in *Proceedings of the 2013 IEEE 78th Vehicular Technology Conference (VTC Fall)*, pp. 1–5, Las Vegas, NV, USA, September 2013.

Hindawi
International Journal of Antennas and Propagation
Volume 2019, Article ID 8708762, 12 pages
https://doi.org/10.1155/2019/8708762

Research Article

A General 3D Nonstationary Vehicle-to-Vehicle Channel Model Allowing 3D Arbitrary Trajectory and 3D-Shaped Antenna Array

Qiuming Zhu,[1] **Weidong Li**,[1] **Ying Yang**,[1] **Dazhuan Xu**,[1] **Weizhi Zhong**,[2] **and Xiaomin Chen**[1]

[1]*Key Laboratory of Dynamic Cognitive System of Electromagnetic Spectrum Space, College of Electronic and Information Engineering, Nanjing University of Aeronautics and Astronautics, Nanjing 211106, China*
[2]*Key Laboratory of Dynamic Cognitive System of Electromagnetic Spectrum Space, College of Astronautics, Nanjing University of Aeronautics and Astronautics, Nanjing 211106, China*

Correspondence should be addressed to Qiuming Zhu; zhuqiuming@nuaa.edu.cn

Received 1 May 2019; Accepted 25 August 2019; Published 20 October 2019

Guest Editor: Danping He

Most of the existing channel model for multiple-input multiple-output (MIMO) vehicle-to-vehicle (V2V) communications only considered that the terminals were equipped with linear antenna arrays and moved with fixed velocities. Nevertheless, under the realistic environment, those models are not practical since the velocities and trajectories of mobile transmitter (MT) and mobile receiver (MR) could be time-variant and unpredictable due to the complex traffic conditions. This paper develops a general 3D nonstationary V2V channel model, which is based on the traditional geometry-based stochastic models (GBSMs) and the twin-cluster approach. In contrast to the traditional models, this new model is characterized by 3D scattering environments, 3D antenna arrays, and 3D arbitrary trajectories of both terminals and scatterers. The calculating methods of channel parameters are also provided. In addition, the statistical properties, i.e., spatial-temporal correlation function (STCF) and Doppler power spectrum density (DPSD), are derived in detail. Simulation results have demonstrated that the output statistical properties of the proposed model agree well with the theoretical and measured results, which verifies the effectiveness of theoretical derivations and channel model as well.

1. Introduction

Vehicle-to-vehicle (V2V) communications can improve the safety of life and property by collecting and exchanging environment information under complex traffic [1]. Meanwhile, multiple-input multiple-output (MIMO) technologies can expand the capacity and improve the communication efficiency. It is promising to apply MIMO technologies to V2V communications. To provide reasonable references for developing, analyzing, and testing V2V communication systems, a general, accurate, and easy-to-use channel model is required. Moreover, the movements, insufficient antenna space, and lack of rich scattering should be considered in channel modeling and statistical property analysis [2–7].

The wide-sense stationary (WSS) assumption was adopted in the traditional geometry-based stochastic models (GBSMs) [5, 8]. Nevertheless, the authors in [9, 10] found that the WSS was only suitable for short distances between transmitters and receivers based on the measured data. Several GBSMs for nonstationary V2V channels are proposed in the literature [11–25]. Among them, 2D nonstationary V2V GBSMs with fixed clusters [11, 12] or moving scatterers [13] were studied and the statistical properties, i.e., the temporal correlation function (TCF), spatial correlation function (SCF), and Doppler power spectrum density (DPSD), were also analyzed. The authors in [14] proposed a 2D V2V channel model with random movement scatterers. The aforementioned 2D channel models were only considered on the horizontal plane. Under

the realistic scenarios, the scatterers, e.g., vehicles, pedestrian, and infrastructures, may distribute or move in the 3D space. Meanwhile, the authors in [7] have proved that the 3D channel model is more accurate than the 2D ones for evaluating the system performance. By extending the scatterers distributed on the surface of 3D regular shapes, i.e., a hemisphere [15], two cylinders [16, 17], two spheres [18], an elliptic-cylinder [19], a rectangular tunnel [20], several 3D nonstationary V2V channel models were proposed recently. In [21], the authors proposed a 3D irregular-shaped GBSM for nonstationary V2V channels. Some 3D cluster-based nonstationary V2V channel models can also been addressed in [22–25]. However, the output phases related to the Doppler frequencies in [11–25] were inaccurate compared with the theoretical results [26, 27]. The authors in [28, 29] modified the phase item to overcome this shortcoming, but it is only suitable for 2D scattering environments. A modified 3D channel model with accurate Doppler frequency can be addressed in [30].

Note that most of the existing V2V channel models [11–26] only took the fixed velocities of the mobile transmitter (MT) and mobile receiver (MR) into account. However, under realistic traffic environments, the velocities of MT and MR could be time-variant. Although the time-variant velocities were considered in [29, 31–33], their trajectories were 2D. Meanwhile, the models in the literature [11–33] only considered 2D or even 1D antenna arrays for simplicity. With the development of antenna technologies, 3D-shaped antenna arrays begin to be used in MIMO communication systems. Very recently, a general 3D nonstationary GBSM between base station and MT with 3D arbitrary trajectories and 3D antenna arrays was proposed in [34]. This idea was adopted by [35] to model the 3D V2V channels allowing MT and MR with 3D arbitrary trajectories. However, the details of channel parameter computation and theoretical analyses of SCF, TCF, and DPSD were lacked. This paper aims at filling these gaps. The major contributions and novelties are summarized as follows:

(1) Combining the GBSM and twin-cluster approach [36], a general 3D V2V channel model was proposed. The 3D antenna array and 3D arbitrary trajectory of each terminal are allowed under the 3D scattering environment, which guarantees the proposed model is more general and has the nonstationary aspect.

(2) The upgraded computation procedure of channel parameters for the proposed model, such as the number of paths, path delays, and path powers, are developed and analyzed in detail.

(3) The theoretical closed-form expressions of statistical properties, i.e., the SCFs, TCFs, and DPSDs are investigated and verified by the simulation method and measurement data.

This paper is structured as follows. Section 2 presents a 3D general V2V channel model characterized by nonstationary aspect and generalization. The channel parameter updating algorithms are given in Section 3. In Section 4, the theoretical SCFs, TCFs, and DPSDs of the proposed model are derived in detail. Section 5 shows and compares the simulated results with the derived ones and measured data. Finally, the conclusions are drawn in Section 6.

2. 3D Nonstationary GBSM for V2V Channels

Figure 1 shows a typical 3D V2V communication system between the MT and MR, which is characterized by 3D arbitrary trajectories and 3D antenna arrays. The MT and MR are configured with S and U antennas, respectively. In the figure, the coordinate systems at the MT and MR with the centers of corresponding terminals are named as xyz and $\widetilde{x}\widetilde{y}\widetilde{z}$, respectively. Suppose that the travel directions of the MT and MR at the initial time correspond to x-axis's direction, respectively. Due to the movement and rotation of two coordinate systems, the antenna element of MT or MR is 3D and time-variant and can be expressed by $\mathbf{d}_s^{\mathrm{MT}}(t) = [d_{s,x}^{\mathrm{MT}}(t), d_{s,y}^{\mathrm{MT}}(t), d_{s,z}^{\mathrm{MT}}(t)]^{\mathrm{T}}$ or $\mathbf{d}_u^{\mathrm{MR}}(t) = [d_{u,\widetilde{x}}^{\mathrm{MR}}(t), d_{u,}\ \widetilde{y}^{\mathrm{MR}}(t), d_{u,\widetilde{z}}^{\mathrm{MR}}(t)]^{\mathrm{T}}$. Figure 1 shows that between the MT and MR, there are many propagation paths and subpaths (or rays). The 3D location of the first cluster $\mathrm{S}_n^{\mathrm{MT}}$ or the last cluster $\mathrm{S}_n^{\mathrm{MR}}$ affects the corresponding elevation angles, such as elevation angle of departure (EAoD) $\theta_{n,m}^{\mathrm{MT}}(t)$ and elevation angle of arrival (EAoA) $\theta_{n,m}^{\mathrm{MR}}(t)$, and azimuth angles, such as the azimuth angle of departure (AAoD) $\phi_{n,m}^{\mathrm{MT}}(t)$ and the azimuth angle of arrival (AAoA) $\phi_{n,m}^{\mathrm{MR}}(t)$. In addition, by adopting twin-cluster approach, the rest clusters can be viewed as a virtual link [36]. In the figure, $\mathbf{v}^i(t)$ and $\mathbf{v}^{\mathrm{S}_n^i}(t)$, $i \in \{\mathrm{MT}, \mathrm{MR}\}$, represent time-variant velocities of i and S_n^i, respectively. Table 1 shows the detailed definitions of channel parameters.

Under the V2V communication scenario of Figure 1, the V2V MIMO channel can be modeled as [30]

$$\mathbf{H}t,\tau = \begin{bmatrix} h_{1,1}t,\tau & h_{1,2}t,\tau & \cdots & h_{1,S}t,\tau \\ h_{2,1}t,\tau & h_{u,s}t,\tau & \cdots & h_{2,S}t,\tau \\ \vdots & \vdots & \ddots & \vdots \\ h_{U,1}t,\tau & h_{U,2}t,\tau & \cdots & h_{U,S}t,\tau \end{bmatrix}, \tag{1}$$

where $h_{u,s}(t,\tau)$ denotes the complex channel impulse response (CIR) between the transmitting antenna $s(s = 1, 2, \ldots, S)$ and receiving antenna $u(u = 1, 2, \ldots, U)$. In this paper, we modify the model of $h_{u,s}(t,\tau)$ in [30] and express it as

$$h_{u,s}(t,\tau) \triangleq \Pi_{\mathrm{T}_0}(t) \sum_{n=1}^{N(t)} \sqrt{P_n(t)}\widetilde{h}_{u,s,n}(t)\delta\left(\tau - \tau_n(t)\right), \tag{2}$$

where $\Pi_{\mathrm{T}_0}(t)$ is a rectangular window function:

$$\Pi_{\mathrm{T}_0}(t) \triangleq \begin{cases} 1, & 0 \le t \le \mathrm{T}_0, \\ 0, & \text{otherwise}, \end{cases} \tag{3}$$

and it is introduced to limit the length of CIR, and thus, the large-scale variations can be negligible within the time interval; $N(t)$ represents the valid path number and is related to the path delay $\tau_n(t)$, path power $P_n(t)$, and normalized coefficient $\widetilde{h}_{u,s,n}(t)$, which is expressed as

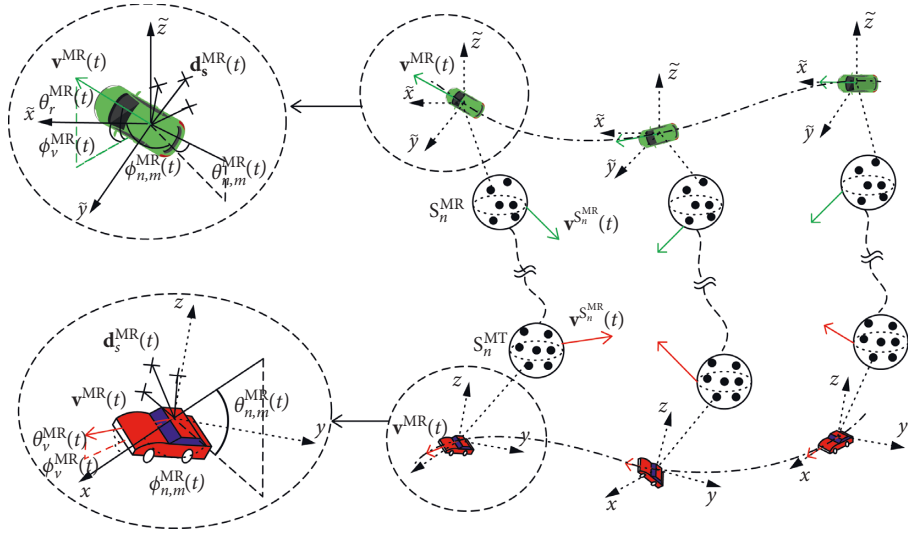

Figure 1: Typical 3D V2V communication system.

Table 1: Definitions of channel parameters.

$N(t)$	Valid path number
$P_n(t), \tau_n(t)$	The nth path power and delay
M	The number of subpaths
$\mathbf{d}_s^{\mathrm{MT}}(t), \mathbf{d}_u^{\mathrm{MR}}(t)$	Location vectors of transmitter antenna element s and receiver antenna element u, respectively
$\mathbf{L}^i(t), \mathbf{L}^{\mathrm{S}_n^i}(t)$	Location vectors of i and S_n^i, $i \in \{\mathrm{MT}, \mathrm{MR}\}$, respectively
$\mathbf{v}^i(t), \mathbf{v}^{\mathrm{S}_n^i}(t)$	Velocity vectors of i and S_n^i, $i \in \{\mathrm{MT}, \mathrm{MR}\}$, respectively
$\|\|\mathbf{v}^i(t)\|\|, \|\|\mathbf{v}^{\mathrm{S}_n^i}(t)\|\|$	Speeds of i and S_n^i, $i \in \{\mathrm{MT}, \mathrm{MR}\}$, respectively
$\phi_{\mathbf{v}}^i(t), \phi_{\mathbf{v}}^{\mathrm{S}_n^i}(t)$	Traveling azimuth angles of i and S_n^i, $i \in \{\mathrm{MT}, \mathrm{MR}\}$, respectively
$\theta_{\mathbf{v}}^i(t), \theta_{\mathbf{v}}^{\mathrm{S}_n^i}(t)$	Traveling elevation angles of i and S_n^i, $i \in \{\mathrm{MT}, \mathrm{MR}\}$, respectively
$\widetilde{\mathbf{s}}_{n,m}^i(t)$	Spherical unit vector of i along ray m of cluster n, $i \in \{\mathrm{MT}, \mathrm{MR}\}$
$\phi_{n,m}^{\mathrm{MT}}(t), \theta_{n,m}^{\mathrm{MT}}(t)$	Azimuth and elevation departure angles along ray m of cluster n, respectively
$\phi_{n,m}^{\mathrm{MR}}(t), \theta_{n,m}^{\mathrm{MR}}(t)$	Azimuth and elevation arrival angles along ray m of cluster n, respectively

$$\widetilde{h}_{u,s,n}(t) = \lim_{M \longrightarrow \infty} \sqrt{\frac{1}{M}} \sum_{m=1}^{M} e^{j\left(\Phi_{n,m}^{\mathrm{D}}(t) + \Phi_{u,s,n,m}^{\mathrm{L}}(t) + \Phi_{n,m}^{\mathrm{I}}\right)}, \tag{4}$$

where M denotes the subpath number, $\Phi_{n,m}^{\mathrm{I}}$ stands for the random initial phase distributing over $[0, 2\pi)$ uniformly, and $\Phi_{n,m}^{\mathrm{D}}(t)$ means the phase somehow affected by variant Doppler frequency. Here, we model $\Phi_{n,m}^{\mathrm{D}}(t)$ as

$$\Phi_{n,m}^{\mathrm{D}}(t) = k \int_0^t \mathbf{v}^{\mathrm{MT},\mathrm{S}_n^{\mathrm{MT}}}(t') \cdot \widetilde{\mathbf{s}}_{n,m}^{\mathrm{MT}}(t') + \mathbf{v}^{\mathrm{S}_n^{\mathrm{MR}},\mathrm{MR}}(t') \cdot \widetilde{\mathbf{s}}_{n,m}^{\mathrm{MR}}(t') dt', \tag{5}$$

where $k = 2\pi f_{\mathrm{c}}/\mathrm{c}$ denotes the wave number with f_{c} and c representing the carrier frequency and light speed, respectively. $\mathbf{v}^{i,\mathrm{S}_n^i}(t)$, $i \in \{\mathrm{MT}, \mathrm{MR}\}$, denotes the relative velocity between i and S_n^i. The departure or arrival angle unit vector of the mth subpath within the nth path $\widetilde{\mathbf{s}}_{n,m}^i(t)$ is defined as

$$\mathbf{s}_{n,m}^i(t) = \begin{bmatrix} \cos\theta_{n,m}^i(t)\cos\phi_{n,m}^i(t) \\ \cos\theta_{n,m}^i(t)\sin\phi_{n,m}^i(t) \\ \sin\theta_{n,m}^i(t) \end{bmatrix}. \tag{6}$$

In (4), $\Phi_{u,s,n,m}^{\mathrm{L}}(t)$ denotes the offset phase caused by the movements of terminals:

$$\Phi_{u,s,n,m}^{\mathrm{L}}(t) = k \cdot \left(\widetilde{\mathbf{s}}_{n,m}^{\mathrm{MT}}(t)\right)^{\mathrm{T}} \cdot \mathbf{R}_{\mathbf{v}}^{\mathrm{MT}}(t) \cdot \mathbf{d}_s^{\mathrm{MT},t_0} + k \cdot \left(\widetilde{\mathbf{s}}_{n,m}^{\mathrm{MT}}(t)\right)^{\mathrm{T}} \cdot \mathbf{R}_{\mathbf{v}}^{\mathrm{MT}}(t) \cdot \mathbf{d}_u^{\mathrm{MT},t_0}, \tag{7}$$

where $[\cdot]^{\mathrm{T}}$ means transpose operation and $\mathbf{d}_s^{\mathrm{MT},t_0}$ represents sth antenna position at initial time instant. Similarly, $\mathbf{d}_u^{\mathrm{MR},t_0}$

represents the corresponding antenna position at initial corresponding time. Note that $\mathbf{R}_{\mathbf{v}}^{i}(t)$ is a rotation matrix due to the 3D arbitrary trajectory, and it can be written as

$$\mathbf{R}_{\mathbf{v}}^{i}(t)=\begin{bmatrix}\cos\theta_{\mathbf{v}}^{i}(t)\cos\phi_{\mathbf{v}}^{i}(t) & -\sin\phi_{\mathbf{v}}^{i}(t) & -\sin\theta_{\mathbf{v}}^{i}(t)\cos\phi_{\mathbf{v}}^{i}(t)\\ \cos\theta_{\mathbf{v}}^{i}(t)\sin\phi_{\mathbf{v}}^{i}(t)\cos\phi_{\mathbf{v}}^{i}(t) & -\sin\theta_{\mathbf{v}}^{i}(t)\sin\phi_{\mathbf{v}}^{i}(t) & \\ \sin\theta_{\mathbf{v}}^{i}(t) & 0 & \cos\theta_{\mathbf{v}}^{i}(t)\end{bmatrix}. \tag{8}$$

3. Time-Variant Channel Parameters

3.1. Path Number. The valid path number has been proved to be time-variant under V2V scenarios by the measured data in [37], due to the moving clusters and two terminals. In other words, the old disappearing clusters and new appearing ones are random. We model these with a Markov process [38]. λ_G is used to denote the birth rate, and λ_R denotes the death rate. The probability of each path remaining from t to $t+\Delta t$ is calculated as [19]

$$\begin{aligned}P_{\mathrm{r}}(t;\Delta t)&=\mathrm{e}^{-\lambda_R\cdot P_c\left(\left\|\mathbf{v}^{\mathrm{S}^{\mathrm{MT}}}(t)\right\|+\left\|\mathbf{v}^{\mathrm{S}^{\mathrm{MR}}}(t)\right\|\right)\Delta t}\\&\quad\cdot\mathrm{e}^{\left(-\lambda_R\left\|\mathbf{v}^{\mathrm{MR}}(t)-\mathbf{v}^{\mathrm{MT}}(t)\right\|\Delta t\right)},\end{aligned} \tag{9}$$

where P_c means the moving percentage and $||\mathbf{v}^{S^i}(t)||$, $i\in\{\mathrm{MT},\mathrm{MR}\}$, represents clusters average speed. $N_{\mathrm{new}}(t)$ is introduced to describe newly generated path number and calculated as

$$E\{N_{\mathrm{new}}(t)\}=\frac{\lambda_G}{\lambda_R}\left(1-P_{\mathrm{r}}(t;\Delta t)\right). \tag{10}$$

Combining (9) with (10), the averaged path number can be expressed as

$$E\{N(t)\}=N(t-\Delta t)P_r(t;\Delta t)+E\{N_{\mathrm{new}}(t)\}=\frac{\lambda_G}{\lambda_R}. \tag{11}$$

3.2. Delays and Powers. For the nth valid path, the total delay at time instant t consists of the first and last bounce delays and virtual link delay, and it is a function of total distance as

$$\tau_n(t)=\frac{\left\|\mathbf{L}^{\mathrm{MT}}(t)-\mathbf{L}^{\mathrm{S}_n^{\mathrm{MT}}}(t)\right\|+\left\|\mathbf{L}^{\mathrm{MR}}(t)-\mathbf{L}^{\mathrm{S}_n^{\mathrm{MR}}}(t)\right\|}{c}+\widetilde{\tau}_n(t), \tag{12}$$

where $\mathbf{L}^{i}(t)$ and $\mathbf{L}^{\mathrm{S}_n^i}(t)$, $i\in\{\mathrm{MT},\mathrm{MR}\}$, mean the instantaneous locations of i and S_n^i and can be updated from the values of previous time instant by

$$\begin{aligned}\mathbf{L}^{i}(t)&=\mathbf{L}^{i}(t-\Delta t)+\mathbf{v}^{i}(t-\Delta t)\Delta t,\\ \mathbf{L}^{\mathrm{S}_n^i}(t)&=\mathbf{L}^{\mathrm{S}_n^i}(t-\Delta t)+\mathbf{v}^{\mathrm{S}_n^i}(t-\Delta t)\Delta t,\end{aligned} \tag{13}$$

where $\widetilde{\tau}_n(t)$ denotes the equivalent delay of virtual link and it can be updated by the first-order filtering method in [26] as follows:

$$\widetilde{\tau}_n(t)=\widetilde{\tau}_n(t-\Delta t)\mathrm{e}^{-\left(\Delta t/\tau_{\mathrm{dec}}\right)}+\left(1-\mathrm{e}^{-\left(\Delta t/\tau_{\mathrm{dec}}\right)}\right)X, \tag{14}$$

where $X\sim U[\|\mathbf{L}^{\mathrm{MT}}(t)-\mathbf{L}^{\mathrm{MR}}(t)\|/c,\tau_{\max}]$, in which $\tau_{\max}$ denotes the maximum delay, and τ_{dec} denotes the decorrelation speed of time-variant delays. Based on the measurement-based method, we can get the averaged power as

$$P_n'(t)=\mathrm{e}^{-\tau_n(t)\left(1-r_{\mathrm{DS}}/r_{\mathrm{DS}}\sigma_{\mathrm{DS}}\right)}\times 10^{-\xi_n/10}, \tag{15}$$

where ξ_n, r_{DS}, and σ_{DS} mean the shadowing degree, delay factor, and delay spread, respectively, which are all related with the environments. Finally, all the normalized power can be denoted as

$$P_n(t)=\frac{P_n'(t)}{\sum_{n=1}^{N(t)}P_n'(t)}. \tag{16}$$

3.3. Time-Variant Angles. Measurements in [39] revealed that the azimuth and elevation angles at two terminals are not independent and cannot be depicted by two independent distributions such as Gaussian or Laplacian. In this paper, we take the 3D von Mises–Fisher (VMF) distribution to describe these two joint angles [40]. The probability density function (PDF) of VMF distribution can be expressed as [39]

$$\begin{aligned}p(\phi,\theta)&=\frac{\kappa\cos\theta\mathrm{e}^{\kappa(\cos\theta\cos\overline{\theta}\cos(\phi-\overline{\phi})+\sin\theta\sin\overline{\theta})}}{4\pi\sinh(\kappa)},\\&\quad-\pi\le\phi\le\pi,-\frac{\pi}{2}\le\theta\le\frac{\pi}{2},\end{aligned} \tag{17}$$

where $\overline{\phi}$ and $\overline{\theta}$ represent the mean values of azimuth and elevation angles, respectively, and κ is the shape factor and can be extracted from the measurement data.

As long as κ is determined, the time-variant angle of departure (AoD) and angle of arrival (AoA) can be obtained by $\overline{\phi}(t)$ and $\overline{\theta}(t)$, respectively, which can be expressed as follows:

$$\overline{\theta}_n^i(t)=\arcsin\left(\frac{\mathbf{L}_z^{\mathrm{S}_n^i}(t)-\mathbf{L}_z^i(t)}{\left\|\mathbf{L}^{\mathrm{S}_n^i}(t)-\mathbf{L}^i t)\right\|}\right),$$

$$\overline{\phi}_n^i(t)=\begin{cases}\arccos\left(\dfrac{\mathbf{L}_x^{\mathrm{S}_n^i}(t)-\mathbf{L}_x^i(t)}{\left(\left\|\mathbf{L}^{\mathrm{S}_n^i}(t)-\mathbf{L}^i(t)\right\|\right)\cos\left(\overline{\theta}_n^i(t)\right)}\right), & \mathbf{L}_y^{\mathrm{S}_n^i}(t)-\mathbf{L}_y^i(t)\ge 0\\ -\arccos\left(\dfrac{\mathbf{L}_x^{\mathrm{S}_n^i}(t)-\mathbf{L}_x^i(t)}{\left(\left\|\mathbf{L}^{\mathrm{S}_n^i}(t)-\mathbf{L}^i(t)\right\|\right)\cos\left(\overline{\theta}_n^i(t)\right)}\right), & \mathbf{L}_y^{\mathrm{S}_n^i}(t)-\mathbf{L}_y^i(t)<0,\end{cases} \tag{18}$$

where $i\in\{\mathrm{MT},\mathrm{MR}\}$. Note that κ almost unchanged during the short simulation time period. Figure 2 gives an example of VMF distributed angles of AoA (or AoD) on the unit sphere with different parameters. It also reveals that with the

increase in shape factor κ, the shape of distribution becomes more concentrated.

4. Time-Variant Statistical Properties

The normalized spatial-temporal correlation function (STCF) between two different subchannels can be defined by [16, 19, 25]

$$\widetilde{R}^{u_2,s_2,n}_{u_1,s_1,n}(t;\Delta t,\Delta\mathbf{d}) = \frac{E\left[\widetilde{h}_{u_1,s_1,n}(t)\widetilde{h}^{*}_{u_2,s_2,n}(t+\Delta t)\right]}{\sqrt{E\left[\left|\widetilde{h}_{u_1,s_1,n}(t)\right|^2\right]E\left[\left|\widetilde{h}_{u_2,s_2,n}(t+\Delta t)\right|^2\right]}}, \tag{19}$$

where $E[\cdot]$ represents the expectation function, $(\,)^*$ is complex conjugate, and Δt means time lag. Moreover, $\Delta\mathbf{d} = \{\Delta\mathbf{d}^{\mathrm{MT}}, \Delta\mathbf{d}^{\mathrm{MR}}\}$ denotes the space lag and consists of $\Delta\mathbf{d}^{\mathrm{MT}}$ and $\Delta\mathbf{d}^{\mathrm{MR}}$, which are the corresponding space lags at two terminals, respectively. By substituting our proposed channel model (4) into (19), the expression of STCF can be obtained as

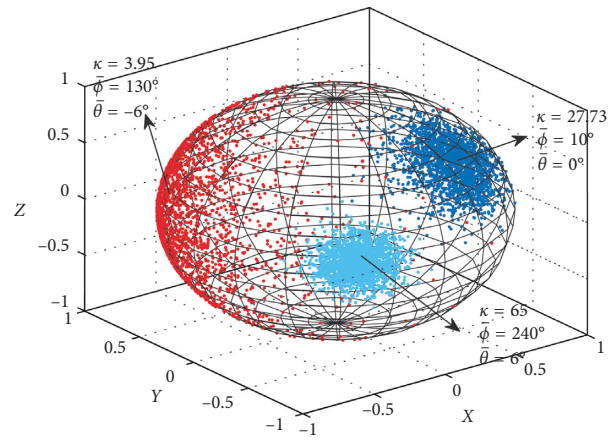

Figure 2: The VMF distributed angles on the unit sphere.

$$\begin{aligned}\widetilde{R}^{u_2,s_2,n}_{u_1,s_1,n}(t;\Delta t,\Delta\mathbf{d}) &= \lim_{M\to\infty}\sqrt{\frac{1}{M}}\sum_{m=1}^{M} e^{j\left(\Phi^{\mathrm{D}}_{u_2,s_2,n,m}(t+\Delta t)+\Phi^{\mathrm{L}}_{u_2,s_2,n,m}(t+\Delta t)+\Phi^{\mathrm{I}}_{n,m}\right)}e^{-j\left(\Phi^{\mathrm{D}}_{u_1,s_1,n,m}(t)+\Phi^{\mathrm{L}}_{u_1,s_1,n,m}(t)+\Phi^{\mathrm{I}}_{n,m}\right)}\\ &= \int\int\int\int_{\{\theta_n^{\mathrm{MT}},\phi_n^{\mathrm{MT}},\theta_n^{\mathrm{MR}},\phi_n^{\mathrm{MR}}\}}\sqrt{p\left(\phi_n^{\mathrm{MT}}(t+\Delta t),\theta_n^{\mathrm{MT}}(t+\Delta t)\right)}\sqrt{p\left(\phi_n^{\mathrm{MR}}(t+\Delta t),\theta_n^{\mathrm{MR}}(t+\Delta t)\right)}\\ &\quad\cdot\sqrt{p\left(\phi_n^{\mathrm{MR}}(t),\theta_n^{\mathrm{MR}}(t)\right)}\cdot\sqrt{p\left(\phi_n^{\mathrm{MT}}(t),\theta_n^{\mathrm{MT}}(t)\right)}e^{j\left(\Phi^{\mathrm{D}}_{u_2,s_2,n}(t+\Delta t)-\Phi^{\mathrm{D}}_{u_1,s_1,n}(t)+\Phi^{\mathrm{L}}_{u_2,s_2,n}(t+\Delta t)-\Phi^{\mathrm{L}}_{u_1,s_1,n}(t)\right)}d\theta_n^{\mathrm{MT}}d\phi_n^{\mathrm{MT}}d\theta_n^{\mathrm{MR}}d\phi_n^{\mathrm{MR}}.\end{aligned} \tag{20}$$

4.1. Time-Variant SCFs. The SCFs is reduced from STCF when the time lag Δt equals to zero. Then, it can be expressed as

$$\widetilde{R}^{u_2,s_2,n}_{u_1,s_1,n}(t;\Delta\mathbf{d}) = \int\int\int\int_{\{\theta_n^{\mathrm{MT}},\phi_n^{\mathrm{MT}},\theta_n^{\mathrm{MR}},\phi_n^{\mathrm{MR}}\}} p\left(\phi_n^{\mathrm{MT}}(t),\theta_n^{\mathrm{MT}}(t)\right)p\left(\phi_n^{\mathrm{MR}}(t),\theta_n^{\mathrm{MR}}(t)\right)\cdot e^{j\left(\Phi^{\mathrm{L}}_{u_2,s_2,n}(t)-\Phi^{\mathrm{L}}_{u_1,s_1,n}(t)\right)}d\theta_n^{\mathrm{MT}}d\phi_n^{\mathrm{MT}}d\theta_n^{\mathrm{MR}}d\phi_n^{\mathrm{MR}}. \tag{21}$$

Since the clusters $\mathrm{S}_n^{\mathrm{MT}}$ and $\mathrm{S}_n^{\mathrm{MR}}$ are independent, we can rewrite (21) as

$$\widetilde{R}^{u_2,s_2,n}_{u_1,s_1,n}(t;\Delta\mathbf{d}) = \widetilde{R}_n^{\mathrm{MT}}\left(t;\Delta\mathbf{d}^{\mathrm{MT}}\right)\cdot\widetilde{R}_n^{\mathrm{MR}}\left(t;\Delta\mathbf{d}^{\mathrm{MR}}\right), \tag{22}$$

where $\widetilde{R}_n^i(t;\Delta\mathbf{d}^i)$, $i\in\{\mathrm{MT},\mathrm{MR}\}$, denotes the normalized SCF at the MT or MR. By substituting (7) into (21), the following equation can be obtained:

$$\begin{aligned}\widetilde{R}_n^i\left(t;\Delta\mathbf{d}^i\right) &= \int_{-\pi}^{\pi}\int_{-\pi}^{\pi} e^{\mathrm{j}k\left(\widetilde{s}_n^i(t)\right)^{\mathrm{T}}\cdot\mathbf{R}_{\mathrm{V}}^i(t)\cdot\Delta\mathbf{d}^{i,t_0}}\\ &\quad\cdot p_{\phi_{n,m}^i(t),\theta_{n,m}^i(t)}\left(\phi_n^i(t),\theta_n^i(t)\right)d\phi_n^i d\theta_n^i.\end{aligned} \tag{23}$$

It is shown in (23) that not only the angle of horizontal plane $\phi_n^i(t)$ but also the one of vertical plane $\theta_n^i(t)$ affects the result of (23). Thus, traditional 2D models cannot obtain accurate correlation functions in 3D scattering environments. By setting $\theta_n^i(t) = \overline{\theta}_n^i(t) + \zeta$ and $\phi_n^i(t) = \overline{\phi}_n^i(t) + \upsilon$ and substituting them into (23), it yields

$$\widetilde{R}_n^i\left(t;\Delta\mathbf{d}^i\right) = \int\int_{\{\zeta,\upsilon\}}\frac{\kappa\cos\left(\overline{\theta}_n^i(t)+\zeta\right)A^iB^i}{4\pi\sinh(\kappa)}d\zeta d\upsilon, \tag{24}$$

where

$$A^i = e^{\kappa\left(\cos\left(\overline{\theta}_n^i(t)+\zeta\right)\cos\overline{\theta}_n^i(t)\cos(\upsilon)+\sin\left(\overline{\theta}_n^i(t)+\zeta\right)\sin\overline{\theta}_n^i(t)\right)}, \tag{25}$$

$$B^i = e^{\mathrm{j}k\widetilde{s}\left(\overline{\phi}_n^i(t)+\upsilon,\overline{\theta}_n^i(t)+\zeta\right)\mathbf{R}_{\mathrm{V}}^i(t)\Delta\mathbf{d}^{i,t_0}}. \tag{26}$$

The measurement data demonstrate that the angle spread is usually narrow under V2V communication scenarios. With this assumption, we have $\cos(\zeta) \approx \cos(\upsilon) \approx 1$, $\sin(\zeta) \approx \zeta$, $\sin(\upsilon) \approx \upsilon$, $\kappa\cos(\upsilon) \approx \kappa(1 - \upsilon^2/2)$, and $\kappa\cos(\zeta) \approx \kappa(1 - \zeta^2/2)$. Consequently, we can rewrite (25) and (26) as

$$A^i \approx \mathrm{e}^{\kappa\left(1-\zeta^2/2-2\cos^2\left(\overline{\theta}_n^i(t)\right)(\upsilon/2)^2\right)}, \tag{27}$$

$$B^i \approx \mathrm{e}^{\mathrm{jk}\left(\widetilde{s}\left(\overline{\phi}_n^i(t),\overline{\theta}_n^i(t)\right)+\mathbf{C}^i(t)\zeta+\mathbf{E}^i(t)\upsilon\right)\mathbf{R}_{\mathrm{V}}^i(t)\Delta\mathbf{d}^{i,t_0}}, \tag{28}$$

where

$$\mathbf{C}^i(t) = \left[-\sin\overline{\theta}_n^i(t)\cos\overline{\phi}_n^i(t), -\sin\overline{\theta}_n^i(t)\sin\overline{\phi}_n^i(t), \cos\overline{\theta}_n^i(t)\right], \tag{29}$$

$$\mathbf{D}^i(t) = \left[-\sin\overline{\phi}_n^i(t), \cos\overline{\phi}_n^i(t), 0\right]. \tag{30}$$

By substituting (27)–(30) into (24) and using Euler formula, we can obtain the following equation:

$$\begin{aligned}\widetilde{R}_n^i\left(t;\Delta\mathbf{d}^i\right) \approx{}& \frac{\mathrm{e}^{\mathrm{jk}\widetilde{s}\left(\overline{\phi}_n^i(t),\overline{\theta}_n^i(t)\right)\mathbf{R}_{\mathrm{V}}^i(t)\Delta\mathbf{d}^{i,t_0}+\kappa}\cos\left(\overline{\theta}_n^i(t)\right)}{\left(\kappa^{1-m/2}\right)(2\pi)^{m/2}\mathrm{I}_{m/2-1}(\kappa)}\\ &\cdot\int_{-\Delta_\phi^i}^{\Delta_\phi^i}\mathrm{e}^{-E^i(t)\upsilon^2}\cos\left(\mathrm{k}\mathbf{D}^i(t)\mathbf{R}_{\mathrm{V}}^i(t)\Delta\mathbf{d}^{i,t_0}\upsilon\right)d\upsilon\\ &\cdot\int_{-\Delta_\theta^i}^{\Delta_\theta^i}\mathrm{e}^{-\kappa\zeta^2/2}\cos\left(\mathrm{k}\mathbf{C}^i(t)\mathbf{R}_{\mathrm{V}}^i(t)\Delta\mathbf{d}^{i,t_0}\zeta\right)d\zeta,\end{aligned} \tag{31}$$

where $E^i(t) = \kappa\cos^2(\overline{\theta}_n^i(t))/2$ and Δ_ϕ^i and Δ_θ^i are the angle spreads of AAoA and EAoA. With the help of integration formula,

$$\int_{-c}^{c}\mathrm{e}^{-ax^2}\cos(bx)\mathrm{d}x = \frac{j\sqrt{\pi}\mathrm{e}^{-b^2/4a}\left(\mathrm{erfi}(b-2jac)/2\sqrt{a}\right)-\mathrm{erfi}(b+2jac/2\sqrt{a})}{2\sqrt{a}}. \tag{32}$$

where $\mathrm{erfi}(\cdot)$ is the imaginary error function.

The approximate closed-form result of SCF is as follows:

$$\begin{aligned}\widetilde{R}_n^i\left(t;\Delta\mathbf{d}^i\right) \approx{}& \frac{-\mathrm{Im}\left(\mathrm{erfi}\left(F^i(t)\right)\right)\mathrm{Im}\left(\mathrm{erfi}\left(G^i(t)\right)\right)}{8\sinh(\kappa)}\\ &\cdot\mathrm{e}^{\mathrm{jk}\widetilde{s}\left(\overline{\phi}_n^i(t),\overline{\theta}_n^i(t)\right)\mathbf{R}_{\mathrm{V}}^i(t)\Delta\mathbf{d}^{i,t_0}}\\ &\cdot\mathrm{e}^{-\left(\mathrm{k}\mathbf{R}_{\mathrm{V}}^i(t)\Delta\mathbf{d}^{i,t_0}\right)^2\left(\left(\mathbf{D}^i(t)/\sqrt{2\kappa}\right)^2+\left(\mathbf{C}^i(t)/\sqrt{2\kappa}\right)^2\right)+\kappa},\end{aligned} \tag{33}$$

$$F^i(t) = \frac{\mathrm{k}\mathbf{D}^i(t)\mathbf{R}_{\mathrm{V}}^i(t)\Delta\mathbf{d}^{i,t_0} - j\kappa\cos^2\left(\overline{\theta}_n^i(t)\right)\Delta_\phi^i}{\sqrt{2\kappa\cos^2\left(\overline{\theta}_n^i(t)\right)}}, \tag{34}$$

$$G^i(t) = \frac{\mathrm{k}\mathbf{C}^i(t)\mathbf{R}_{\mathrm{V}}^i(t)\Delta\mathbf{d}^{i,t_0} - j\kappa\Delta_\theta^i}{\sqrt{2\kappa}}, \tag{35}$$

$$\begin{aligned}\widetilde{R}_{u_1,s_1,n}^{u_1,s_1,n}(t;\Delta t) = {}& \int\int\int\int_{\left\{\theta_n^{\mathrm{MT}},\phi_n^{\mathrm{MT}},\theta_n^{\mathrm{MR}},\phi_n^{\mathrm{MR}}\right\}}\sqrt{p\left(\phi_n^{\mathrm{MT}}(t+\Delta t),\theta_n^{\mathrm{MT}}(t+\Delta t)\right)}\sqrt{p\left(\phi_n^{\mathrm{MR}}(t+\Delta t),\theta_n^{\mathrm{MR}}(t+\Delta t)\right)}\sqrt{p\left(\phi_n^{\mathrm{MR}}(t),\theta_n^{\mathrm{MR}}(t)\right)}\\ &\cdot\sqrt{p\left(\phi_n^{\mathrm{MT}}(t),\theta_n^{\mathrm{MT}}(t)\right)}\mathrm{e}^{j\left(\Phi^{\mathrm{D}}_{u_1,s_1,n}(t)-\Phi^{\mathrm{D}}_{u_1,s_1,n}(t+\Delta t)+\Phi^{\mathrm{L}}_{u_1,s_1,n}(t)-\Phi^{\mathrm{L}}_{u_1,s_1,n}(t+\Delta t)\right)}d\theta_n^{\mathrm{MT}}d\phi_n^{\mathrm{MT}}d\theta_n^{\mathrm{MR}}d\phi_n^{\mathrm{MR}},\end{aligned} \tag{36}$$

$$\widetilde{R}_n^i(t;\Delta t) = \iint_{\left\{\phi_n^i,\theta_n^i\right\}}\sqrt{p\left(\phi_n^i(t),\theta_n^i(t)\right)}\sqrt{p\left(\phi_n^i(t+\Delta t),\theta_n^i(t+\Delta t)\right)}\mathrm{e}^{-\mathrm{jk}\int_t^{t+\Delta t}\mathbf{v}^{i,S_n^i}(t')\cdot\mathbf{s}_{n,m}^i(t')dt'}d\phi_n^i d\theta_n^i, \tag{37}$$

$$\widetilde{R}_n^i(t;\Delta t)=\frac{\kappa}{4\pi\sinh(\kappa)}\int_{-\Delta_\theta}^{\Delta_\theta}\int_{-\Delta_\phi}^{\Delta_\phi}\sqrt{\cos\left(\overline{\theta}_n^i(t)+\zeta\right)}e^{\kappa\left(\cos\left(\overline{\theta}_n^i(t)+\zeta\right)\cos\left(\overline{\theta}_n^i(t)\right)\cos(\upsilon)+\sin\left(\overline{\theta}_n^i(t)+\zeta\right)\sin\overline{\theta}_n^i(t)\right)}$$
$$\cdot\sqrt{\cos\left(\overline{\theta}_n^i(t+\Delta t)+\zeta\right)}e^{\kappa\left(\cos\left(\overline{\theta}_n^i(t+\Delta t)+\zeta\right)\cos\overline{\theta}_n^i(t+\Delta t)\cos(\upsilon)+\sin\left(\overline{\theta}_n^i(t+\Delta t)+\zeta\right)\sin\overline{\theta}_n^i(t+\Delta t)\right)}$$
$$\cdot e^{-\mathrm{jk}\int_t^{t+\Delta t}\left\|\mathbf{v}^{i,S_n^i}(t)\right\|\left[\cos\left(\phi_{\mathbf{v}}^{i,S_n^i}(t)-\left(\overline{\phi}_n^i(t)+\upsilon\right)\right)\cos\left(\overline{\theta}_n^i(t)+\zeta\right)\cos\theta_{\mathbf{v}}^{i,S_n^i}(t)+\sin\left(\overline{\theta}_n^i(t)+\zeta\right)\sin\theta_{\mathbf{v}}^{i,S_n^i}(t)\right]dt}d\upsilon d\zeta, \tag{38}$$

$$\widetilde{R}_n^i(t;\Delta t)=\frac{\kappa}{4\pi\ \sinh(\kappa)}\int_{-\Delta_\theta}^{\Delta_\theta}\int_{-\Delta_\phi}^{\Delta_\phi}\sqrt{\cos\left(\overline{\theta}_n^i(t)+\zeta\right)}e^{\kappa\left(\cos\left(\overline{\theta}_n^i(t)+\zeta\right)\cos\left(\overline{\theta}_n^i(t)\right)\cos(\upsilon)+\sin\left(\overline{\theta}_n^i(t)+\zeta\right)\sin\overline{\theta}_n^i(t)\right)}$$
$$\cdot\sqrt{\cos\left(\overline{\theta}_n^i(t+\Delta t)+\zeta\right)}e^{\kappa\left(\cos\left(\overline{\theta}_n^i(t+\Delta t)+\zeta\right)\cos\overline{\theta}_n^i(t+\Delta t)\cos(\upsilon)+\sin\left(\overline{\theta}_n^i(t+\Delta t)+\zeta\right)\sin\overline{\theta}_n^i(t+\Delta t)\right)}$$
$$\cdot e^{-\mathrm{jk}\left\|\mathbf{v}^{i,S_n^i}(t)\right\|\left[\cos\left(A^i(t;\Delta t;\upsilon,\zeta)\right)D^i(t;\Delta t)+\cos\left(B^i(t;\Delta t;\upsilon,\zeta)\right)E^i(t;\Delta t)+\sin\left(C^i(t;\Delta t;\zeta)\right)F^i(t;\Delta t)\right]}d\upsilon d\zeta. \tag{39}$$

Finally, by substituting (33)–(35) into (22), the final result of SCF in our proposed model can be obtained. Due to time-variant communication environments, SCF is also time-dependent.

4.2. Time-Variant TCFs. The TCF is reduced from STCF when $\Delta\mathbf{d}$ is set to be zero. Then, TCF can be derived as (36). It also equals to the product of TCFs at the MT and MR $\widetilde{R}_n^i(t;\Delta t)$, $i\in\{\mathrm{MT},\mathrm{MR}\}$, when the clusters S_n^{MT} and S_n^{MR} are independent. For simplicity, we assumed that the antenna array is placed at the origin of the coordinate system. By substituting (5) and (7) into (36), it can be obtained as (37).

By setting $\theta_n^i(t)=\overline{\theta}_n^i(t)+\zeta$ and $\phi_n^i(t)=\overline{\phi}_n^i(t)+\upsilon$ and substituting them into (37), it yields (38), where $\phi_{\mathbf{v}}^{i,S_n^i}(t)$ and $\theta_{\mathbf{v}}^{i,S_n^i}(t)$ mean the azimuth and elevation angles of the relative velocity between i and cluster S_n^i, respectively. It is reasonable to assume that the elevation AoDs and azimuth AoDs change linearly during the short time interval as $\overline{\phi}_n^i(t)=k_1t+b_1$, $\overline{\theta}_n^i(t)=k_2t+b_2$, where $k_1=(\overline{\phi}_n^i(t+\Delta t_{\max})-\overline{\phi}_n^i(t))/\Delta t_{\max}$, $k_2=(\overline{\theta}_n^i(t+\Delta t_{\max})-\overline{\theta}_n^i(t))/\Delta t_{\max}$, $b_1=\overline{\phi}_n^i(t)-k_1t$, and $b_2=\overline{\theta}_n^i(t)-k_2t$. By integrating the Doppler frequency, we can rewrite (38) as (39), where

$$A^i(t;\Delta t;\upsilon,\zeta)=\left(\frac{t+\Delta t}{2}\right)(-k_1+k_2)+\phi_{\mathbf{v}}^{i,S_n^i}(t)-b_1+b_2-\upsilon+\zeta,$$

$$B^i(t;\Delta t;\upsilon,\zeta)=\left(\frac{t+\Delta t}{2}\right)(-k_1-k_2)+\phi_{\mathbf{v}}^{i,S_n^i}(t)-b_1-b_2-\upsilon-\zeta,$$

$$C^i(t;\Delta t;\zeta)=k_2\left(\frac{t+\Delta t}{2}\right)+b_2+\zeta,$$

$$D^i(t;\Delta t)=\cos\theta_{\mathbf{v}}^{i,S_n^i}(t)\sin\left(\frac{(\Delta t(-k_1+k_2)/2)}{(-k_1+k_2)}\right),$$

$$E^i(t;\Delta t)=\cos\theta_{\mathbf{v}}^{i,S_n^i}(t)\sin\left(\frac{(\Delta t(k_1+k_2)/2)}{(k_1+k_2)}\right), \tag{40}$$

$$F^i(t;\Delta t)=2\sin\theta_{\mathbf{v}}^{i,S_n^i}(t)\sin\left(\frac{(k_2\Delta t/2)}{k_2}\right),$$

$$\widetilde{R}_n^i(t;\Delta t)\approx\frac{\kappa e^{\kappa}}{4\pi\sinh(\kappa)}\sqrt{\cos\left(\overline{\theta}_n^i(t)\right)\cos\left(\overline{\theta}_n^i(t+\Delta t)\right)}e^{-\mathrm{jk}G^i(t;\Delta t)}$$
$$\cdot\int_{-\Delta_\theta}^{\Delta_\theta}e^{-\kappa\zeta^2/2}\cos\left(kI^i(t;\Delta t)\zeta\right)d\zeta\cdot\int_{-\Delta_\phi}^{\Delta_\phi}e^{-J^i(t;\Delta t)\upsilon^2}\cos\left(kH^i(t;\Delta t)\upsilon\right)d\upsilon. \tag{41}$$

Measurement data have revealed that small angle spreads exist under some scenarios. In other words, κ is usually big or ζ and υ are small. Holding this condition, we have $\cos(\upsilon-\zeta)\approx 1$, $\cos(\upsilon+\zeta)\approx 1$, $\sin(\upsilon-\zeta)\approx \upsilon-\zeta$, $\sin(\upsilon+\zeta)\approx \upsilon+\zeta$, $\cos(\zeta)\approx 1$, $\cos(\upsilon)\approx 1$, $\sin(\zeta)\approx \zeta$, and $\sin(\upsilon)\approx \upsilon$. Thus, we can approximate (39) as (41), where

$$\begin{aligned}
G^i(t;\Delta t) &= \left\|\mathbf{v}^{i,S_n^i}(t)\right\|\cdot D^i(t;\Delta t)\cos\left(A^i(t;\Delta t)\right)+\left\|\mathbf{v}^{i,S_n^i}(t)\right\|\cdot E^i(t;\Delta t)\cos\left(B^i(t;\Delta t)\right)+\left\|\mathbf{v}^{i,S_n^i}(t)\right\|\cdot F^i(t;\Delta t)\sin\left(C^i(t;\Delta t)\right),\\
H^i(t;\Delta t) &= \left\|\mathbf{v}^{i,S_n^i}(t)\right\|\cdot D^i(t;\Delta t)\sin\left(A^i(t;\Delta t)\right)+\left\|\mathbf{v}^{i,S_n^i}(t)\right\|\cdot E^i(t;\Delta t)\sin\left(B^i(t;\Delta t)\right),\\
I^i(t;\Delta t) &= -\left\|\mathbf{v}^{i,S_n^i}(t)\right\|\cdot D^i(t;\Delta t)\sin\left(A^i(t;\Delta t)\right)+\left\|\mathbf{v}^{i,S_n^i}(t)\right\|\cdot E^i(t;\Delta t)\sin\left(B^i(t;\Delta t)\right)+\left\|\mathbf{v}^{i,S_n^i}(t)\right\|\cdot F^i(t;\Delta t)\cos\left(C^i(t;\Delta t)\right),\\
J^i(t;\Delta t) &= \frac{\kappa\left(\cos^2\left(\overline{\theta}_n^i(t)\right)+\cos^2\left(\overline{\theta}_n^i(t+\Delta t)\right)\right)}{4},
\end{aligned} \tag{42}$$

$$\begin{aligned}
\widetilde{R}_n^i(t;\Delta t) = &-\frac{\kappa}{8\sinh(\kappa)}\sqrt{\cos\left(\overline{\theta}_n^i(t)\right)\cos\left(\overline{\theta}_n^i(t+\Delta t)\right)}\,e^{\kappa-\left(k^2I^{i^2}(t,\Delta t)/2\kappa\right)-\left(k^2H^{i^2}(t,\Delta t)/4J^i(t,\Delta t)\right)-\mathrm{j}kG^i(t,\Delta t)}\\
&\cdot\frac{\mathrm{Im}\left(\mathrm{erfi}\left(kH^i(t,\Delta t)-2jJ^i(t,\Delta t)\Delta_\phi/2\sqrt{J^i(t,\Delta t)}\right)\right)}{\sqrt{J^i(t,\Delta t)}}\,\frac{\mathrm{Im}\left(\mathrm{erfi}\left(\left(kI^i(t,\Delta t)-j\kappa\Delta_\theta/\sqrt{2\kappa}\right)\right)\right)}{\sqrt{2\kappa}}.
\end{aligned} \tag{43}$$

where $A^i(t;\Delta t)$, $B^i(t;\Delta t)$, and $C^i(t;\Delta t)$ are the value of $A^i(t;\Delta t;\upsilon,\zeta)$, $B^i(t;\Delta t;\upsilon,\zeta)$, and $C^i(t;\Delta t;\zeta)$ when $\upsilon=\zeta=0$, respectively. Using the integration formula in (32), the closed-form expression of (41) can be expressed as (43). On this basis, we can obtain the final TCF expression of the proposed model.

4.3. Time-Variant DPSDs. The DPSD is the Fourier transform of TCF $\widetilde{R}_{u,s,n}(t;\Delta t)$. For the nonstationary aspect of our proposed model, the DPSD can be calculated with short-time Fourier transform as

$$S_n(f;t)=\int_{-\infty}^{\infty}\widetilde{R}_{u,s,n}(t;\Delta t)\,e^{-j2\pi f\Delta t}\nu(t-\Delta t)d\Delta t, \tag{44}$$

where window function $\nu(t-\Delta t)$ lasting time is shorter than the stationary interval (about several milliseconds [10]).

5. Simulation Results and Validation

Firstly, in order to evaluate the accuracy of our derived SCF and TCF, we calculate the maximum difference between the approximated and numerical integral results over $\overline{\phi}_n^i\in[-180^\circ,180^\circ]$ and $\overline{\theta}_n^i\in[-10^\circ,10^\circ]$. Figure 3 shows the results of maximum absolute error with different κ, normalized space lags, and time lags. As we can see that the maximum absolute error of SCF is less than 0.025 when κ is more than 50 and d/λ is less than 3, and it increases as κ decreases or d/λ increases. Meanwhile, the absolute error of TCF is less than 0.02 when κ is more than 50 and the time lag is less than 0.05 s, and it increases as κ decreases or the time lag increases. Overall, the maximum error is acceptable, and thus, the derived expressions can be used to calculate the SCF and TCF efficiently.

Secondly, in order to verify the generality of the proposed channel model. Three V2V communication scenarios with different trajectories are selected and given in Figure 4. In the figure, the MT travels straightly with the fixed velocity, and the MR travels in three different velocities with the same departure and arrival points. Path I has fixed speed and travel direction, and Path II allows speed variation with 2D direction movement. Furthermore, Path III has 3D variations in both vertical and horizontal directions. For demonstration purpose, the distribution of clusters is uniform, and we adopt VMF distribution to depict AoAs and AoDs and set κ as 3.95 [39]. With the referred data in [41], we assume that the speeds of cluster are Gaussian-distributed with 1 km/h mean value and 0.1 variance. Furthermore, the carrier frequency $f_c=2.4$ GHz, $\phi_{\mathbf{v}_n}^{\mathrm{S^{MT}}}$, $\phi_{\mathbf{v}_n}^{\mathrm{S^{MR}}}$, $\theta_{\mathbf{v}_n}^{\mathrm{S^{MT}}}$ and $\theta_{\mathbf{v}_n}^{\mathrm{S^{MR}}}$ are all uniformly distributed. The former pair distributes over 0 and 2π, but the later one only distributes over $-\pi/36$ and $\pi/36$.

It should be mentioned that the V2V channel models in [11–26, 28, 30] only considered fixed velocities of two terminals like Path I, while the models in [31–33] allowed for 2D curve trajectories like Path II. The absolute values of the theoretical SCFs of different models including the model considering Path I in [30] and the one focusing on Path II in [32] are simulated and compared in Figure 5. The good agreement of SCFs between our proposed and other models indicates the generalization and compatibility of our proposed model. In particular, the models in [30, 32] can be viewed as two special applications in straight or curved trajectories.

Thirdly, in order to verify the correctness of statistical properties of our proposed model under 3D trajectories like Path III, the theoretical, approximated, and simulated values of SCFs and TCFs are shown in Figure 6. The x-axis of Figure 6(a) represents normalized space between antennas,

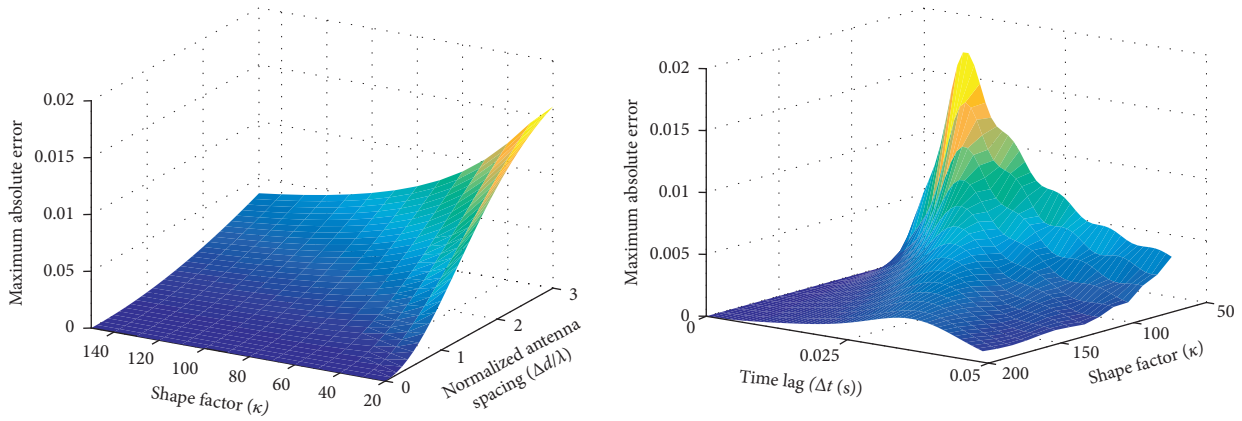

Figure 3: Maximum absolute errors between the theoretical and approximate (a) SCFs and (b) TCFs.

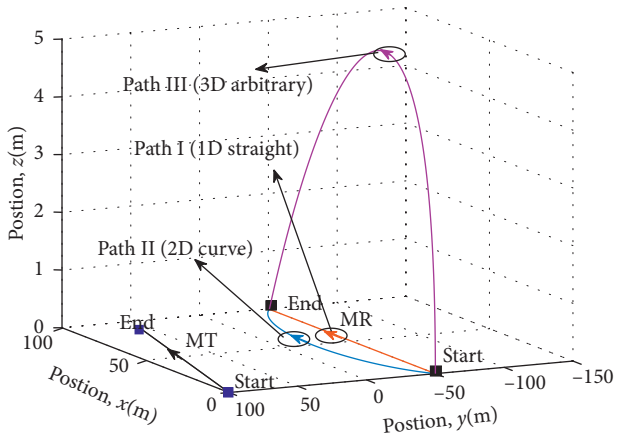

Figure 4: Three typical trajectories of the MR.

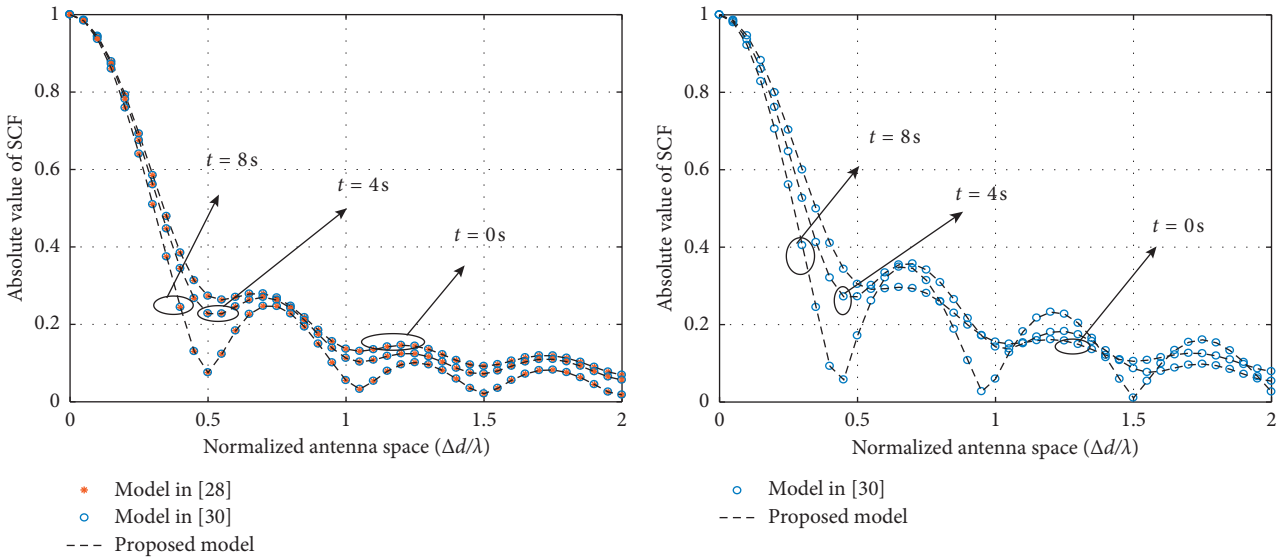

Figure 5: Comparison of absolute SCFs for (a) Path I and (b) Path II.

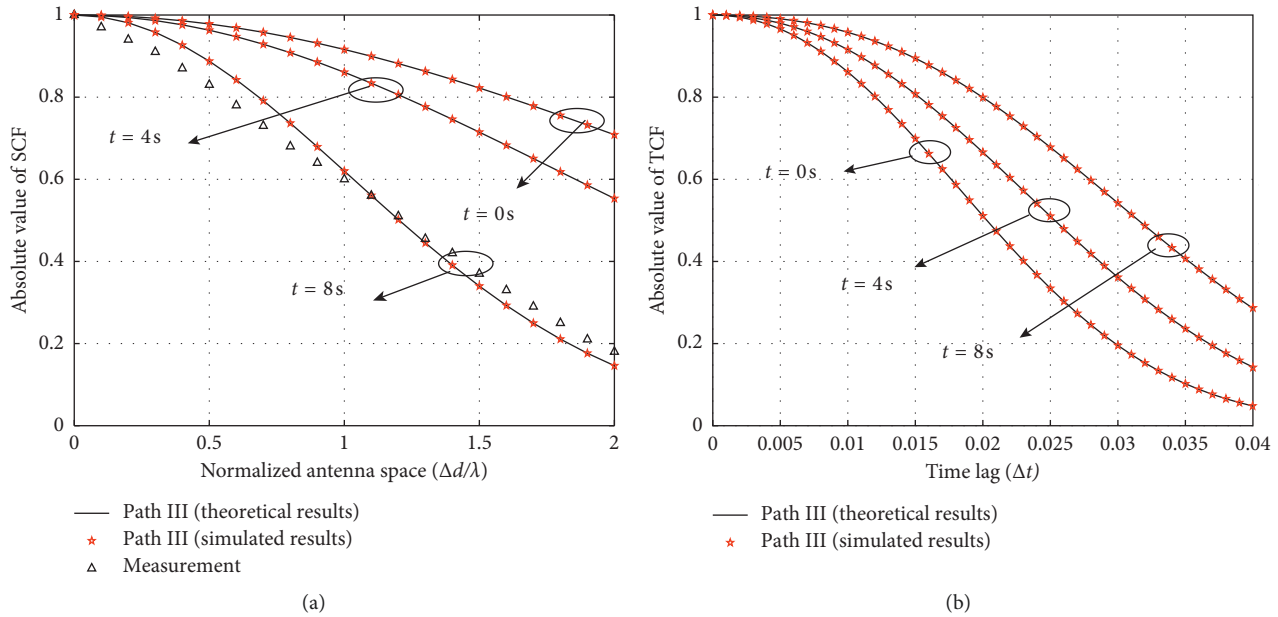

Figure 6: Comparison of absolute theoretical and simulated (a) SCFs and (b) TCFs at different time instants.

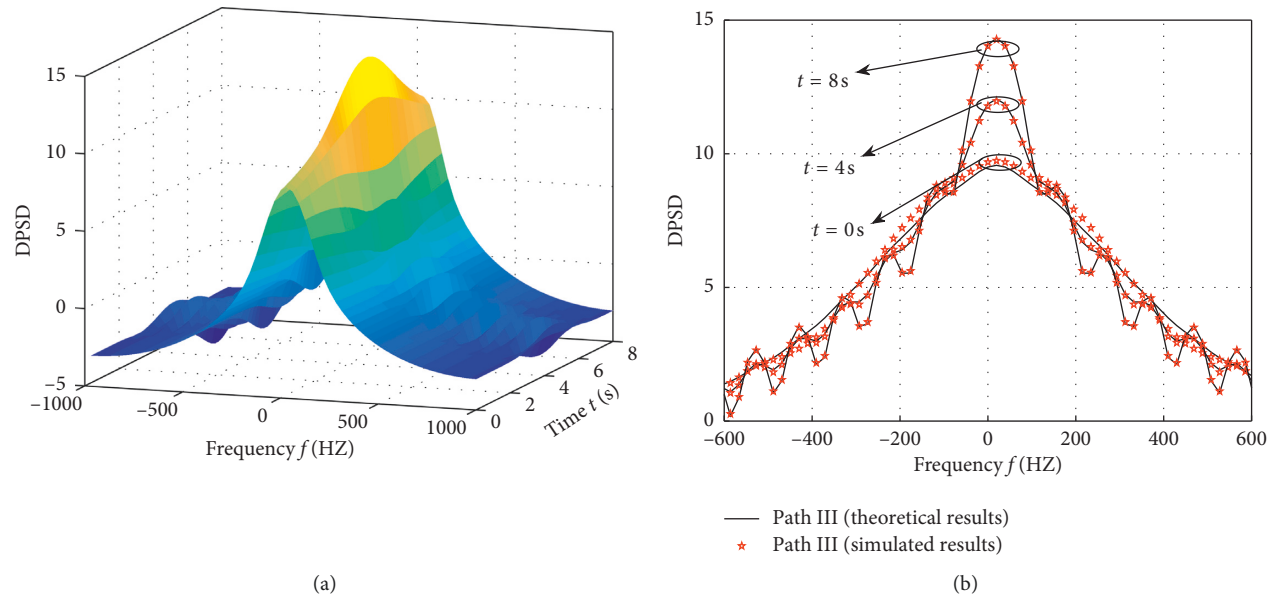

Figure 7: (a) Theoretical 3D DPSD and (b) theoretical and simulated DPSDs at different time instants for Path III.

which is similar at two terminals in the communication system. By substituting $u_1 = s_1 = 1$, $u_2 = s_2 = 2$, and $n = 1$ into (21) and (33), we can get the theoretical and approximated values of SCFs. In addition, the measured results in [42] are also shown in Figure 6(a). The good agreement of SCFs shows the correctness of both the theoretical model and derivations. Similarly, by substituting $u = s = 1$ and $n = 1$ into (36) and (43), we obtain and show the theoretical and approximated values of TCFs in Figure 6(b). The good agreements between theoretical, simulated, and approximated results reveal that our simulation and derivation are correct.

Finally, substituting TCFs into (44), we can get the theoretical and simulated values of DPSDs for Path III, which are also shown in Figure 7. It clearly shows that moving clusters and two terminals have an influence on the drifting of DPSDs. Moreover, good agreements between the simulated and theoretical results indicate that our proposed model is correct.

6. Conclusion

This paper has proposed a general channel model characterized by 3D scattering environments, 3D movements, and

3D-shaped antenna arrays of two terminals for V2V communication system. The upgraded algorithms for time-evolving parameters such as the number of paths, path delays, path powers, and angles have been developed and analyzed in detail. Meanwhile, the approximated expressions of statistical properties including SCF, TCF, and DPSD have been derived and verified by simulations. Simulated and analyzed results show that different moving trajectories significantly affect the V2V channel characteristic. Meanwhile, the generalization and compatibility of our proposed model also demonstrate that some previous models with 2D or even 1D movements have special applications. The new model can be used to develop, analyze, and test realistic V2V communication systems in the future.

Data Availability

The data used to support the findings of this study are available from the corresponding author upon request.

Conflicts of Interest

The authors declare that they have no conflicts of interest.

Acknowledgments

This work was supported by the National Key Scientific Instrument and Equipment Development Project (Grant no. 61827801), Aeronautical Science Foundation of China (Grant no. 2017ZC52021), and Open Foundation for Graduate Innovation of NUAA (Grant no. KFJJ 20180408).

References

[1] C.-X. Wang, X. Cheng, and D. I. Laurenson, "Vehicle-to-vehicle channel modeling and measurements: recent advances and future challenges," *IEEE Communications Magazine*, vol. 47, no. 11, pp. 96–103, 2009.

[2] K. Guan, B. Ai, M. Liso Nicolas et al., "On the influence of scattering from traffic signs in vehicle-to-x communications," *IEEE Transactions on Vehicular Technology*, vol. 65, no. 8, pp. 5835–5849, 2016.

[3] X. Cheng, C.-X. Wang, B. Ai, and H. Aggoune, "Envelope level crossing rate and average fade duration of nonisotropic vehicle-to-vehicle ricean fading channels," *IEEE Transactions on Intelligent Transportation Systems*, vol. 15, no. 1, pp. 62–72, 2014.

[4] Q. Zhu, C. Xue, X. Chen, and Y. Yang, "A new MIMO channel model incorporating antenna effects," *Progress In Electromagnetics Research M*, vol. 50, pp. 129–140, 2016.

[5] A. G. Zajic and G. L. Stubber, "Space-time correlated mobile-to-mobile channels: modelling and simulation," *IEEE Transactions on Vehicular Technology*, vol. 57, no. 2, pp. 715–726, 2008.

[6] W. Fan, X. Carreno Bautista de Lisbona, F. Sun, J. O. Nielsen, M. B. Knudsen, and G. F. Pedersen, "Emulating spatial characteristics of MIMO channels for OTA testing," *IEEE Transactions on Antennas and Propagation*, vol. 61, no. 8, pp. 4306–4314, 2013.

[7] J. Zhang, Y. Zhang, Y. Yu, R. Xu, Q. Zheng, and P. Zhang, "3-D MIMO: how much does it meet our expectations observed from channel measurements?," *IEEE Journal on Selected Areas in Communications*, vol. 35, no. 8, pp. 1887–1903, 2017.

[8] J. Karedal, F. Tufvesson, N. Czink et al., "A geometry-based stochastic MIMO model for vehicle-to-vehicle communications," *IEEE Transactions on Wireless Communications*, vol. 8, no. 7, pp. 3646–3657, 2009.

[9] A. Paier, T. Zemen, L. Bernado et al., "Non-WSSUS vehicular channel characterization in high-way and urban scenarios at 5.2 GHz using the local scattering function," in *Proceedings of the 2008 International ITG Workshop on Smart Antennas*, pp. 9–15, Darmstadt, Germany, February 2008.

[10] R. He, O. Renaudin, V.-M. Kolmonen et al., "Characterization of quasi-stationarity regions for vehicle-to-vehicle radio channels," *IEEE Transactions on Antennas and Propagation*, vol. 63, no. 5, pp. 2237–2251, 2015.

[11] Y. Ma, L. Yang, and X. Zheng, "A geometry-based non-stationary MIMO channel model for vehicular communications," *China Communications*, vol. 15, no. 7, pp. 30–38, 2018.

[12] C. A. Gutirrez, J. T. Gutirrez-Mena, J. M. Luna-Rivera, D. U. Campos-Delgado, R. Velzquez, and M. Patzold, "Geometry-based statistical modeling of non-WSSUS mobile-to-mobile Rayleigh fading channels," *IEEE Transactions on Vehicular Technology*, vol. 67, no. 1, pp. 362–377, 2018.

[13] A. Chelli and M. Patzold, "A non-stationary MIMO vehicle-to-vehicle channel model derived from the geometrical street model," in *Proceedings of the Vehicular Technology Conference*, pp. 1–6, San Francisco, CA, USA, September 2011.

[14] A. Borhani and M. Patzold, "Correlation and spectral properties of vehicle-to-vehicle channels in the presence of moving scatterers," *IEEE Transactions on Vehicular Technology*, vol. 62, no. 9, pp. 4228–4239, 2013.

[15] H. Jiang, Z. Zhang, L. Wu, and J. Dang, "Novel 3-D irregular-shaped geometry-based channel modeling for semi-ellipsoid vehicle-to-vehicle scattering environments," *IEEE Wireless Communications Letters*, vol. 7, no. 5, pp. 836–839, 2018.

[16] A. G. Zajic, "Impact of moving scatterers on vehicle-to-vehicle narrow-band channel characteristics," *IEEE Transactions on Vehicular Technology*, vol. 63, no. 7, pp. 3094–3106, 2014.

[17] X. Zhao, X. Liang, S. Li, and B. Ai, "Two-cylinder and multi-ring GBSSM for realizing and modeling of vehicle-to-vehicle wideband MIMO channels," *IEEE Transactions on Intelligent Transportation Systems*, vol. 17, no. 10, pp. 2787–2799, 2016.

[18] Y. Bi, J. Zhang, M. Zeng, M. Liu, and X. Xu, "A novel 3D nonstationary channel model based on the von Mises-Fisher scattering distribution," *Mobile Information Systems*, vol. 2016, Article ID 2161460, pp. 1–9, 2016.

[19] Y. Yuan, C.-X. Wang, Y. He, M. M. Alwakeel, and E.-H. M. Aggoune, "3D wideband non-stationary geometry-based stochastic models for non-isotropic MIMO vehicle-to-vehicle channels," *IEEE Transactions on Wireless Communications*, vol. 14, no. 12, pp. 6883–6895, 2015.

[20] N. Avazov, S. M. R. Islam, D. Park, and K. S. Kwak, "Statistical characterization of a 3-D propagation model for V2V channels in rectangular tunnels," *IEEE Antennas and Wireless Propagation Letters*, vol. 16, pp. 2392–2395, 2017.

[21] H. Jiang, Z. Zhang, J. Dang, and L. Wu, "A novel 3-D massive MIMO channel model for vehicle-to-vehicle communication environments," *IEEE Transactions on Communications*, vol. 66, no. 1, pp. 79–90, 2018.

[22] N. Avazov, S. M. R. Islam, D. Park, and K. S. Kwak, "Cluster-based non-stationary channel modeling for vehicle-to-vehicle communications," *IEEE Antennas and Wireless Propagation Letters*, vol. 16, pp. 1419–1422, 2016.

[23] D. Du, X. Zeng, X. Jian, L. Miao, and H. Wang, "Three-dimensional vehicle-to-vehicle channel modeling with multiple moving scatterers," *Mobile Information Systems*, vol. 2017, Article ID 7231417, pp. 1–14, 2017.

[24] X. Liang, W. Cao, and X. Zhao, "Doppler power spectra for 3D vehicle-to-vehicle channels with moving scatterers," *IEEE Access*, vol. 6, pp. 42822–42828, 2018.

[25] X. Chen, Y. Fang, Y. Sun, Y. Pan, and W. Xiang, "Statistical characterization of novel 3D cluster-based MIMO vehicle-to-vehicle models for urban street scattering environments," *International Journal of Antennas and Propagation*, vol. 2018, Article ID 6742346, pp. 1–11, 2018.

[26] Q. Zhu, H. Li, Y. Fu et al., "A novel 3D non-stationary wireless MIMO channel simulator and hardware emulator," *IEEE Transactions on Communications*, vol. 66, no. 9, pp. 3865–3878, 2018.

[27] K. Jiang, X. Chen, Q. Zhu, L. Chen, D. Xu, and B. Chen, "A novel simulation model for nonstationary rice fading channels," *Wireless Communications and Mobile Computing*, vol. 2018, Article ID 8086073, pp. 1–9, 2018.

[28] M. Patzold, C. A. Gutierrez, and N. Youssef, "On the consistency of non-stationary multipath fading channels with respect to the average doppler shift and the doppler spread," in *Proceedings of the IEEE Wireless Communications and Networking Conference (WCNC)*, pp. 1–6, San Francisco, CA, USA, 2017.

[29] Q. Zhu, W. Li, C.-X. Wang et al., "Temporal correlations for a non-stationary vehicle-to-vehicle channel model allowing velocity variations," *IEEE Communications Letters*, vol. 23, no. 7, pp. 1280–1284, 2019.

[30] Q. Zhu, Y. Yang, X. Chen et al., "A novel 3D non-stationary vehicle-to-vehicle channel model and its spatial-temporal correlation properties," *IEEE Access*, vol. 6, pp. 43633–43643, 2018.

[31] W. Dahech, M. Patzold, and N. Youssef, "A non-stationary mobile-to-mobile multipath fading channel model taking account of velocity variations of the mobile stations," in *Proceedings of the IEEE International Symposium on Antennas and Propagation*, pp. 1–4, Lisbon, Portugal, April 2015.

[32] W. Dahech, M. Patzold, C. A. Gutierrez, and N. Youssef, "A non-stationary mobile-to-mobile channel model allowing for velocity and trajectory variations of the mobile stations," *IEEE Transactions on Wireless Communications*, vol. 16, no. 3, pp. 1987–2000, 2017.

[33] C. A. Gutierrez, M. Patzold, W. Dahech, and N. Youssef, "A non-WSSUS mobile-to-mobile channel model assuming velocity variations of the mobile stations," in *Proceedings of the Wireless Communications and Networking Conference (WCNC)*, pp. 1–6, San Francisco, CA, USA, March 2017.

[34] Q. Zhu, Y. Yang, C. X. Wang et al., "Spatial correlations of a 3D non-stationary MIMO channel model with 3D antenna arrays and 3D arbitrary trajectories," *IEEE Wireless Communications Letters*, vol. 8, no. 2, pp. 512–515, 2019.

[35] Y. Yang, Q. Zhu, W. Li et al., "A general 3D non-stationary twin-cluster model for vehicle-to-vehicle MIMO channels," in *Proceedings of the Wireless Communications and Signal Processing*, pp. 1–6, Hangzhou, China, Octobor 2018.

[36] H. Hofstertter, A. F. Molisch, and N. Czink, "A twin-cluster MIMO channel model," in *Proceedings of the Antennas and Propagation (EuCAP)*, pp. 1–8, Nice, France, November 2006.

[37] I. Sen and D. W. Matolak, "Vehicle-vehicle channel models for the 5-GHz band," *IEEE Transactions on Intelligent Transportation Systems*, vol. 9, no. 2, pp. 235–245, 2008.

[38] T. Zwick, C. Fischer, D. Didascalou, and W. Wiesbeck, "A stochastic spatial channel model based on wave-propagation modeling," *IEEE Journal on Selected Areas in Communications*, vol. 18, no. 1, pp. 6–15, 2000.

[39] K. Mammasis and R. W. Stewart, "The Fisher-Bingham spatial correlation model for multielement antenna systems," *IEEE Transactions on Vehicular Technology*, vol. 58, no. 5, pp. 2130–2136, 2009.

[40] M. Konstantinos, S. W. Robert, and J. S. Thompson, "Spatial fading correlation model using mixtures of Von Mises Fisher distributions," *IEEE Transactions on Wireless Communications*, vol. 8, no. 4, pp. 2046–2055, 2009.

[41] A. Fayziyev, M. Patzold, E. Masson, Y. Cocheril, and M. Berbineau, "A measurement-based channel model for vehicular communications in tunnels," in *Proceedings of the Wireless Communications and Networking Conference (WCNC)*, pp. 116–121, Istanbul, Turkey, April 2014.

[42] S. Payami and F. Tufvesson, "Channel measurements and analysis for very large array systems at 2.6 GHz," in *Proceedings of the Antennas and Propagation (EUCAP)*, pp. 433–437, Prague, Czech Republic, March 2012.

Hindawi
International Journal of Antennas and Propagation
Volume 2019, Article ID 2071895, 8 pages
https://doi.org/10.1155/2019/2071895

Research Article

Compact Wideband Circularly Polarized Antenna with Symmetric Parasitic Rectangular Patches for Ka-Band Applications

Rongling Jian, Yueyun Chen, and Taohua Chen

University of Science & Technology Beijing, Xueyuan Road 30, Haidian District, Beijing, China

Correspondence should be addressed to Yueyun Chen; chenyy@ustb.edu.cn

Received 28 April 2019; Revised 21 August 2019; Accepted 21 September 2019; Published 13 October 2019

Guest Editor: Sami Myllymäki

In this paper, a novel wideband circularly polarized (CP) millimeter wave (mmWave) microstrip antenna is presented. The proposed antenna consists of a central patch and a microstrip line radiator. The CP radiation is achieved by loading a rectangular slot on the ground plane. To improve the 3-dB axial ratio bandwidth (ARBW), two symmetric parasitic rectangular patches paralleled to a central patch and a slit positioned to the right of the central patch are loaded. To verify this design, the proposed antenna is fabricated with a small antenna of $2.88 \times 3.32 \times 0.508$ mm^3. The measured impedance bandwidth (IMBW) for $|S_{11}| < -10$ dB of the proposed antenna is 35.97% (22.8 to 33.8 GHz). Meanwhile, the simulation result shows that the 3-dB ARBW is 15.19% (28.77 to 33.5 GHz) within impedance bandwidth, and the peak gain is from 5.08 to 5.22 dBic within 3-dB ARBW. The proposed antenna is suitable for CP applications in the Ka-band.

1. Introduction

With the rapid development of the 5th generation (5G) wireless communication, circularly polarized (CP) antennas have received increasing attention because they can overcome multipath interferences, polarization mismatch, and Faraday rotation effects [1–5]. However, the study of bandwidth enhancement of the CP antenna in the Ka-band is an open issue.

In recent years, many technologies were proposed to enhance CP antenna bandwidth such as loading parasitic strips or protruding stub [6–9], loading slots or slits [10–13], and cavity model-based methodology [14, 15]. Patch antennas with parasitic strips and ring patches are presented for wideband circular polarization [6, 7]. Through protruding a horizontal stub from the ground plane, the 3-dB axial ratio bandwidth (ARBW) is enhanced [8]. A hybrid *Z*-shaped cylindrical resonator antenna for multiband applications is proposed in [9]. Meanwhile, by loading a lightning-shaped slot for achieving good CP radiation, an annular-slot dual-broadband CP antenna is achieved [10]. The 3-dB ARBW is enhanced by cutting a rectangular slit [11] and moving the feeding ports to the upper portion of the U-shaped slot [12]. To achieve CP radiation and antenna size reduction, an arrow-head-shaped slot is embedded in a square patch [13]. In addition, the CP antenna is designed by cavity model-based methodology. An omnidirectional dual-band dual-CP antenna with wide beam radiation patterns using TM_{01} and TM_{02} modes is investigated in [14]. A new CP antenna design method based cavity model-based methodology is proposed in [15].

To achieve a broadband CP antenna in mmWave, the aperture antenna [16–18], waveguide antenna [19], and patch antenna [20] are proposed. However, these antennas have more complex geometry, larger size, or higher loss at the feed network due to the resistors. In [16], a differentially fed CP planar aperture antenna is proposed for broadband mmWave applications, and the 3-dB ARBW is set to 16.7% (56 to 66.2 GHz) within its impedance bandwidth. The differentially driven planar aperture CP antenna is proposed to improve gain and expand the 3-dB ARBW to 17.9% (56.5 to 67.5 GHz) [17]. The CP antenna is proposed through addition of a hybrid microstrip and elliptical dielectric ring resonator, and the 3-dB ARBW is set to 10% (56 to 62 GHz) [18]. Due to many advantages, such as simple feeding, easy manufacture, precise control

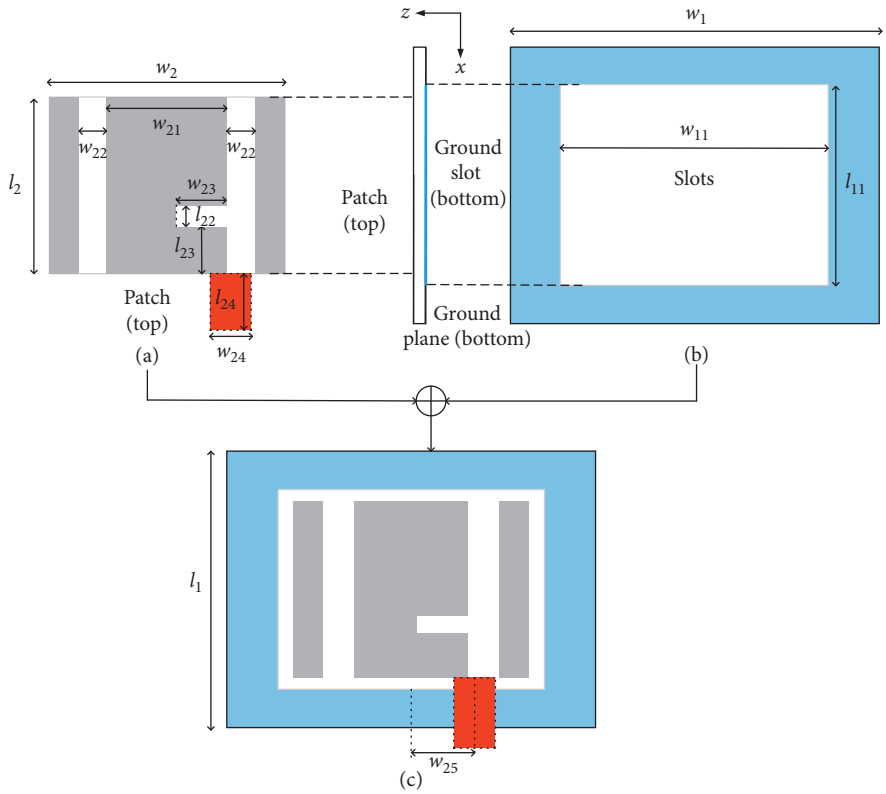

Figure 1: The geometries of the proposed CP antenna.

Table 1: The parameters of the proposed antenna structure.

Parameters	Value (mm)
l_1	5.76
w_1	6.64
l_{11}	3
w_{11}	3.32
l_2	2.88
w_2	3.32
l_{22}	0.26
l_{24}	1.44
w_{21}	1.84
w_{22}	0.6
w_{23}	0.75
w_{24}	0.6
w_{25}	0.8
l_{23}	0.88

of aperture distribution, and low loss, the slotted waveguide antenna has found wide applications in wireless communications. A CP waveguide antenna is presented for Ka-band applications [19]. The L-shaped patch and a tapered elliptical cavity CP antenna are proposed, and the 3-dB ARBW is set to 11.9% (56.9 to 64 GHz) [20].

The purpose of this paper is to develop a CP antenna with bandwidth enhancement, which can be used in a Ka-band wireless communication system. With careful design of the rectangular slot on the ground plane, equal amplitude and 90° phase difference between two orthogonal polarizations can be achieved, leading to a circular polarization at the design frequency. To enhance bandwidth of proposed antenna, two symmetric parasitic rectangular patches are loaded, which are parallel to the central patch, and a slit is loaded to the right of the central patch.

The remainder of this paper is organized as follows. Antenna design and analysis, including the proposed antenna structure, steps of the proposed antenna, and parameter studies, is described in Section 2. The antenna design results are presented in Section 3. Conclusion is drawn in Section 4.

2. Antenna Design and Analysis

2.1. Antenna Structure. The configuration of the proposed antenna is shown in Figure 1. This antenna is printed on a rectangular Rogers RT/Duroid 5880 substrate, where height (h) is 0.508 mm, dielectric constant (ε_r) is 2.2 and dielectric loss tangent is 0.0009. It consists of a microstrip line feeding port, ground plane with a rectangular slot, two parasitic rectangular patches, and a slit loaded in the central patch. The size of total patches is $l_2 \times w_2 = 2.88 \times 3.32\ \text{mm}^2$ [21]. The CP wave is generated by two orthogonal electric field vectors with equal amplitude and 90° phase difference, which is mainly implemented by loading a rectangular slot on the ground plane. The 3-dB ARBW is enhanced by loading two symmetric parasitic rectangular patches paralleled to the central patch and a slit positioned to the right of the central patch. The parameters of the proposed antenna are shown in Table 1.

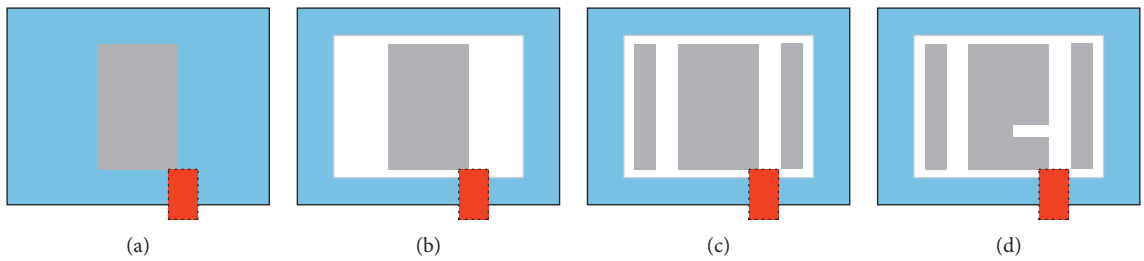

Figure 2: Steps to realize the proposed antenna. (a) ANT.1. (b) ANT 2. (c) ANT.3. (d) ANT.4.

2.2. Steps of the Proposed Antenna. The four antenna evolutions of the broadband Ka-band CP antenna are depicted in Figure 2 to explain the design process of bandwidth enhancement. In this paper, all the simulations are performed by Ansoft High Frequency Structure Simulator (version 13.0) based on the finite element method.

ANT.1 includes a basic rectangular patch and feed structure, which has received much attention in array applications [22]. As shown in Figure 3, ANT.1 has the disadvantage of narrow bandwidth, and it is linearly polarized (LP). In ANT.2, the CP radiation is achieved by loading a rectangular slot on the ground plane. Meanwhile, the impedance bandwidth (IBW) of ANT.2 is enhanced because input impedance is changed after loading the rectangular slot. However, the 3-dB AR bandwidth is poor. Wide ARBW is achieved by loading two symmetric parasitic rectangular patches paralleled to the central patch in ANT.3, and it is shown from Figure 4 that the 3-dB ARBW is from 2.2 to 3.1 GHz. The ARBW is further enhanced by loading a small slit positioned to the right of the central patch in ANT.4. Figure 5 shows the simulated peak gain for ANT.1, ANT.2, and ANT.3 within the ARBW.

2.3. Parameter Studies. In order to clearly understand the design rules of the proposed antenna, a set of parameters, including the change in the width of rectangular slots on the patch (w_{22}), the length of the slit (w_{23}), and the feeding position (w_{25}), will be discussed in this section. Meanwhile, the width of the central rectangular slot is decided by w_{22}. Note that when one parameter is studied, the other parameters are fixed as listed in Table 1.

By adjusting the width of rectangular slots on the patch (w_{22}), the width of the central patch is also changed. As shown in Figure 6, the IMBW is expanded from 32.61% (23.48 GHz to 31.46 GHz) to 35.42% (24.11 GHz to 34.49 GHz) with the increase of w_{22} from 0.4 to 0.6 mm. However, the IMBW is reduced with the increase of w_{22} from 0.6 to 0.7 mm. As shown in Figure 7, the 3-dB ARBW is enhanced with the increase of w_{22} from 0.4 to 0.6 mm. However, ANT.4 becomes LP when w_{22} is from 0.6 to 0.7 mm. In this paper, we choose $w_{22} = 0.6$ mm for the proposed CP antenna design.

Figure 8 shows the simulated results of ANT.4 with the length of w_{23} from 0.45 to 0.9 mm. It can be seen from Figure 8 that the IMBW is increased as w_{23} increases from 0 to 0.75 mm. However, the IMBW is reduced with the increase of

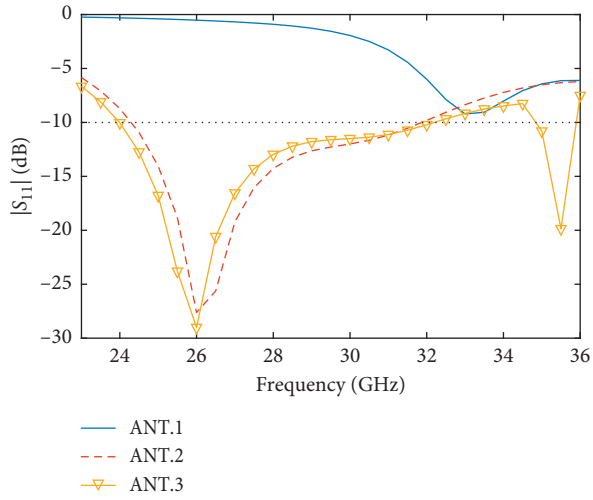

Figure 3: Simulated S_{11} for ANT.1, ANT.2, and ANT.3.

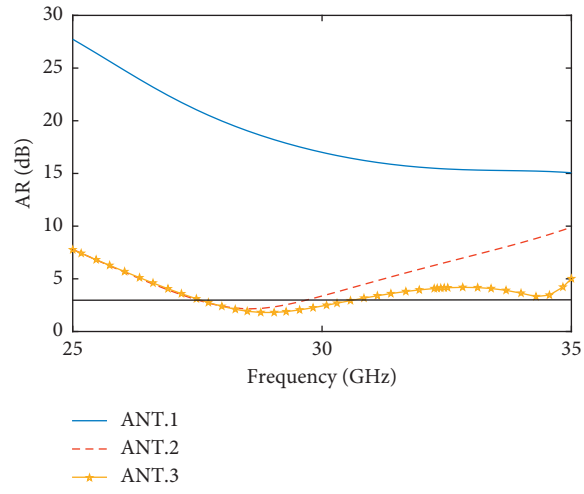

Figure 4: Simulated AR for ANT.1, ANT.2, and ANT.3.

w_{23} from 0.75 to 0.9 mm. Meanwhile, it can be seen from Figure 9 that the 3-dB ARBW is also increased as w_{23} increases from 0.45 to 0.75 mm. However, the IMBW is reduced with the increase of w_{23} from 0.75 to 0.9 mm. With the analysis above, we choose $w_{23} = 0.75$ mm for the proposed CP antenna design.

Through analysis, the effects of feeding position on impedance matching and feeding position (w_{25}) can be decided. When the feeding position is studied, the other

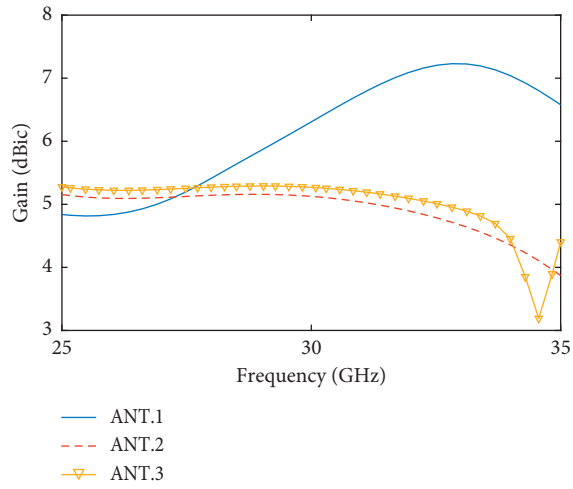

Figure 5: Simulated peak gain for ANT.1, ANT.2, and ANT.3.

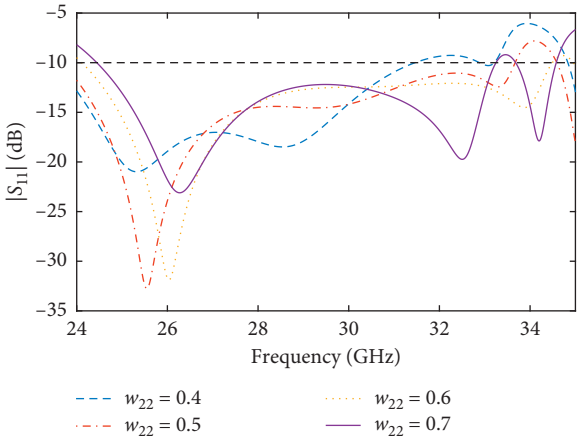

Figure 6: Effects of various w_{22} on S_{11}.

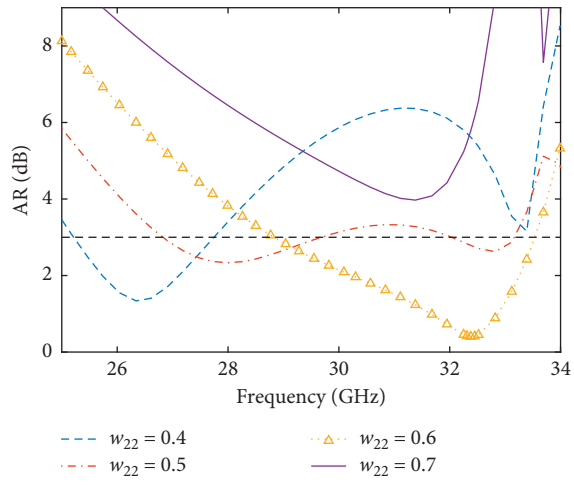

Figure 7: Effects of various w_{22} on AR.

parameters are fixed as listed in Table 1. It is discovered from Figures 10 and 11 that it can achieve better impedance matching when w_{25} is 0.8 mm.

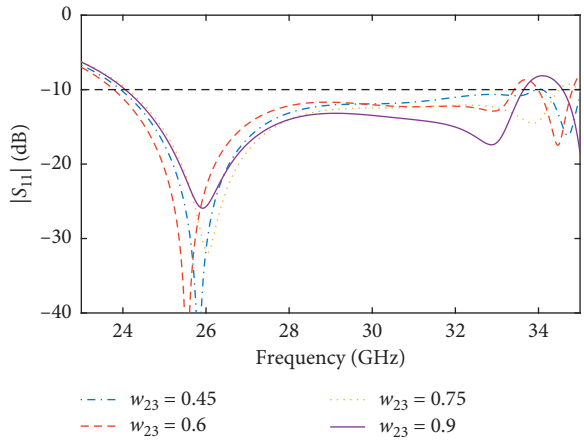

Figure 8: Effects of various w_{23} on S_{11}.

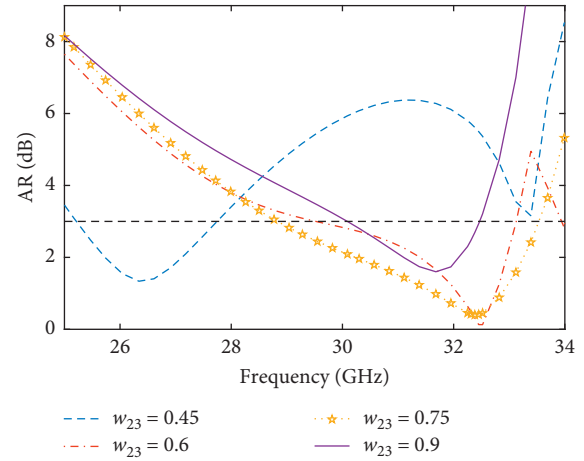

Figure 9: Effects of various w_{23} on AR.

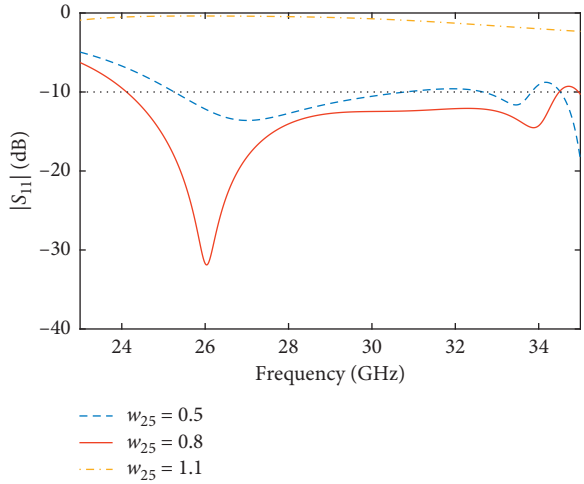

Figure 10: Effects of various w_{25} on S_{11}.

3. Design Results

The final optimized antenna parameters are shown in Table 1. Based on the optimized parameters, the antenna is

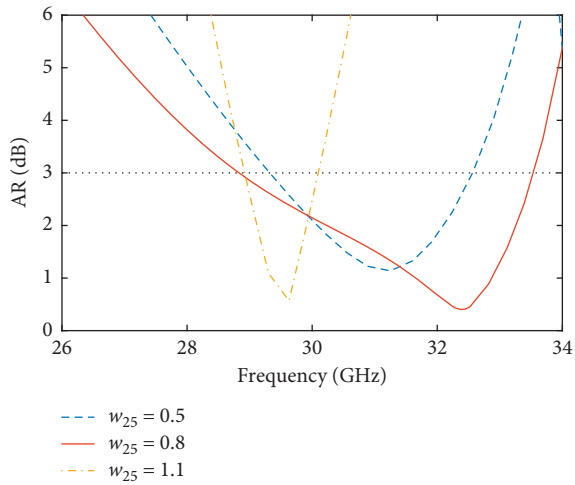

Figure 11: Effects of various w_{25} on AR.

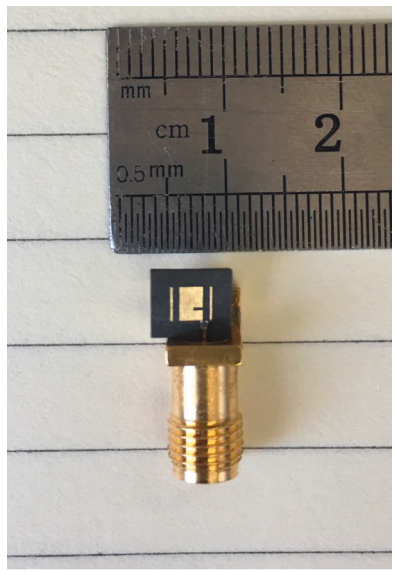

Figure 12: Photographs of the fabricated CP antenna showing the patch view.

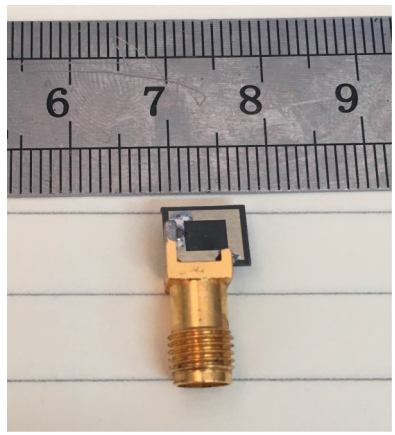

Figure 13: Photographs of the fabricated CP antenna showing the ground view.

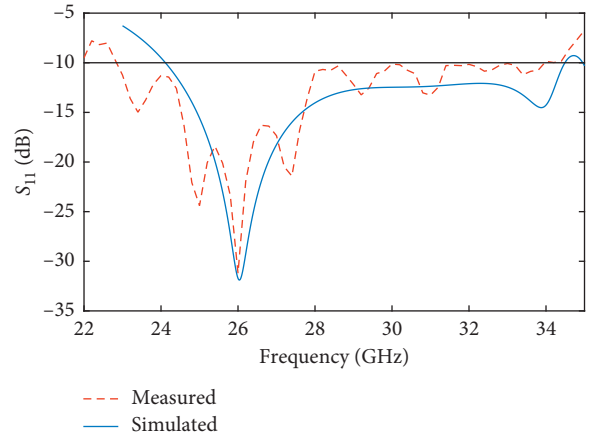

Figure 14: Simulated and measured S_{11}.

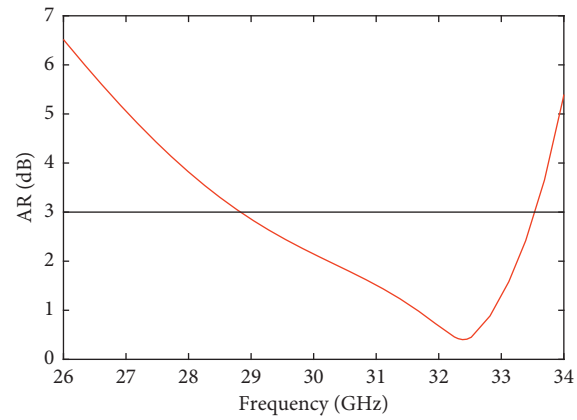

Figure 15: Simulated AR of the proposed antenna.

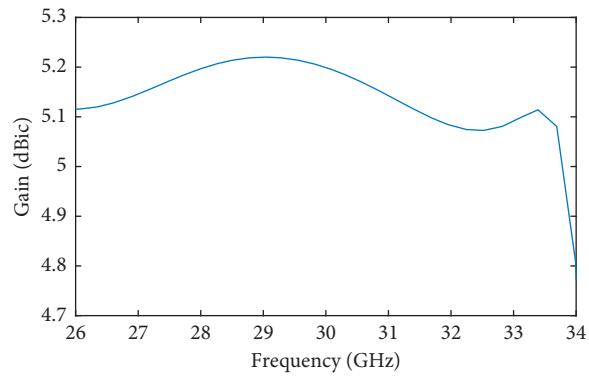

Figure 16: Simulated peak gain of the proposed antenna.

fabricated, and S_{11} is measured to validate the design and simulated results. This antenna is tested by a vector network analyzer (AgilentN5227A). Photographs of the fabricated CP antenna showing the patch and ground views are shown in Figures 12 and 13, respectively.

Simulated and measured S_{11} are shown in Figure 14. The simulated impedance bandwidth for $|S_{11}| < -10$ dB is 35.43% (24.11 to 34.49 GHz). The measured IMBW for $|S_{11}| < -10$ dB is 35.97% (22.8 to 33.8 GHz), which agree with the simulated result.

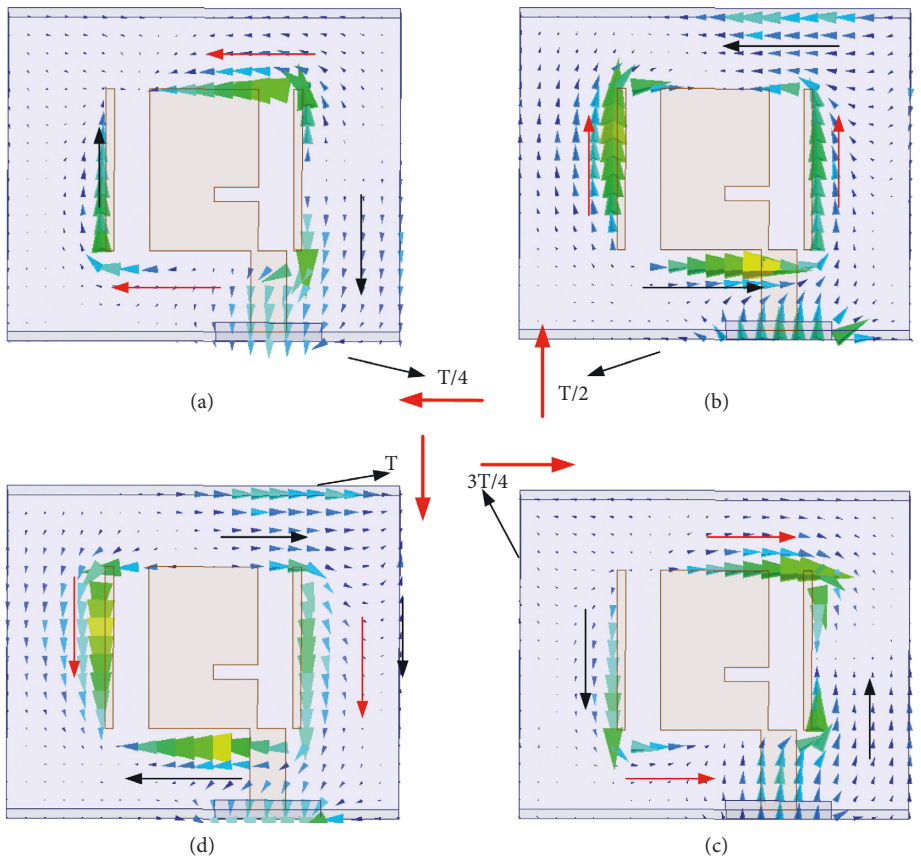

Figure 17: Simulated surface current distributions at 32.4 GHz.

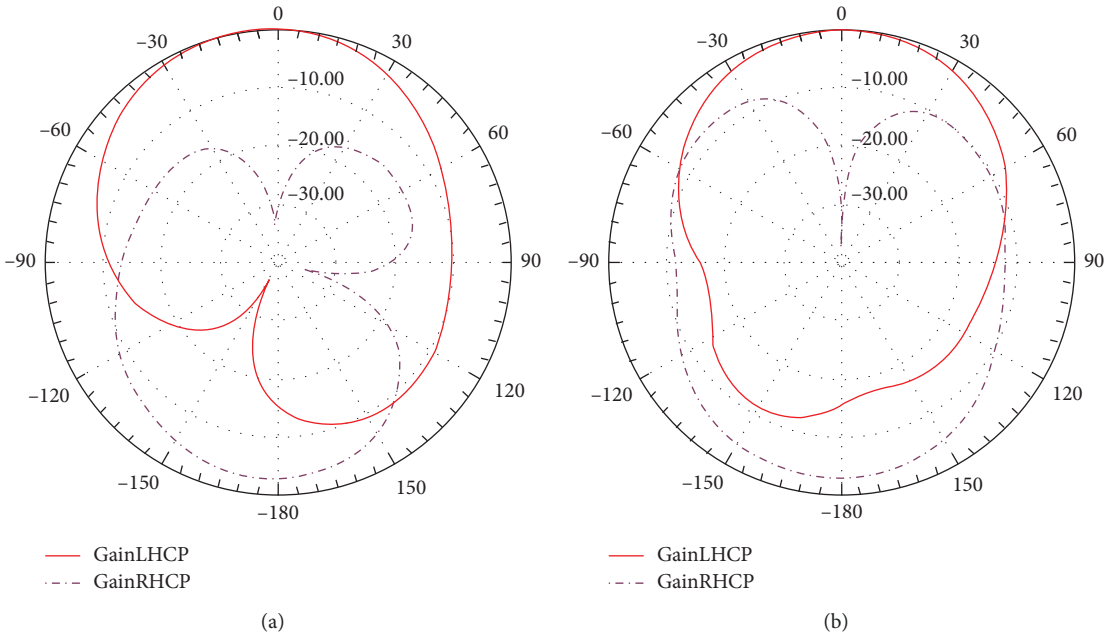

Figure 18: Simulated normalized radiation patterns at 32.4 GHz.

As shown in Figure 15, the simulated 3-dB ARBW is enhanced to 15.19% (28.77 GHz to 33.5 GHz). In Figure 16, a peak gain between 5.08 dBic and 5.22 dBic is achieved at the boresight direction within 3-dB ARBW.

As shown in Figure 17, the simulated time-varying surface current distributions of ANT4 at 32.4 GHz are illustrated to verify the generation of CP radiation. Two orthogonal resonant modes with a 90° phase difference and equal amplitude can

Table 2: Comparison of CP Antennas at mmWave.

ANT type	Size (λ_0^3)	IMBW (%)	3-dB ARBW (%)
Aperture [16]	$1.58 \times 1.58 \times 0.16$	18	16.3
Aperture [17]	$2 \times 1.82 \times 0.16$	>17.9	16.3
Aperture and patch [18]	$1.14 \times 1.32 \times 0.105$	12	10
Waveguide [19]	$3.57 \times 2.07 \times 0.90$	1.3	1.1
Patch [20]	$1.12 \times 0.86 \times (>0.12)$	10.9	>11.57
Proposed ANT	$0.27 \times 0.31 \times 0.047$	35.97	15.19

achieve CP radiation. It can be observed that the proposed antenna is LHCP towards the $+z$-direction.

The normalized radiation patterns of the proposed antenna at 32.4 GHz in xz plane and yz plane are shown in Figure 18.

A comparison between the proposed antenna and previous works [16–20] at mmWave frequency band is illustrated in Table 2, including the antenna type, size, impedance bandwidth (IMBW), and 3-dB ARBW. It shows the proposed antenna has a simper structure, more compact size, wider impedance bandwidth, and wider 3-dB ARBW. Additionally, because the profiles in [16, 17] are about three times those of the proposed antenna, the 3-dB ARBW of the proposed antenna is slightly smaller than that in [16, 17].

4. Conclusion

A novel design of Ka-band broadband CP antenna with compact structure has been presented, which is excited by a microstrip line radiator. The CP is achieved by loading a rectangular slot on the ground plane. Meanwhile, the antenna with broad IMBW and ARBW is satisfactorily realized by loading two symmetric parasitic rectangular patches paralleled to the central patch and a slit positioned to the right of the central patch. The results show that the measured impedance bandwidth of the proposed antenna for $|S_{11}| < -10$ dB is 35.97% (22.8 to 33.8 GHz). Meanwhile, the simulated 3-dB ARBW is enhanced to 15.19% (28.77 GHz to 33.5 GHz). Meanwhile, there are about 34 dB difference between the simulated LHCP and RHCP components at 32.4 GHz. It is useful for 5G wireless applications in Ka-band.

Data Availability

The data in the HFSS used to support the findings of this study were supplied by Rongling Jian, Yueyun Chen, and Taohua Chen under license and so cannot be made freely available. Requests for access to these data should be made to Rongling Jian, jrl_ustb@126.com.

Conflicts of Interest

The authors declare that they have no conflicts of interest.

Acknowledgments

This work was supported by National Science and Technology Major Project no. 2017ZX03001021-005.

References

[1] Nasimuddin, Z. N. Chen, and X. Qing, "A compact circularly polarized cross-shaped slotted microstrip antenna," *IEEE Transactions on Antennas and Propagation*, vol. 60, no. 3, pp. 1584–1588, 2012.

[2] ETSI, *Base Station (BS) Radio Transmission and Reception (Release 15) 3GPP TS 38.104 V15.0*, ETSI, Sophia Antipolis, France, 2018.

[3] W. Roh, J.-Y. Seol, J. Park et al., "Millimeter-wave beamforming as an enabling technology for 5G cellular communications: theoretical feasibility and prototype results," *IEEE Communications Magazine*, vol. 52, no. 2, pp. 106–113, 2014.

[4] M. Akbari, H. Abo Ghalyon, M. Farahani, A.-R. Sebak, and T. A. Denidni, "Spatially decoupling of CP antennas based on FSS for 30-GHz MIMO systems," *IEEE Access*, vol. 5, pp. 6527–6537, 2017.

[5] J. S. Silva, E. B. Lima, J. R. Costa, C. A. Fernandes, and J. R. Mosig, "Tx-Rx lens-based satellite-on-the-move ka-band Antenna," *IEEE Antennas and Wireless Propagation Letters*, vol. 14, pp. 1408–1411, 2015.

[6] J. Wu, Y. Yin, Z. Wang, and R. Lian, "Broadband circularly polarized patch antenna with parasitic strips," *IEEE Antennas and Wireless Propagation Letters*, vol. 14, pp. 559–562, 2015.

[7] S. Fu, Q. Kong, S. Fang, and Z. Wang, "Broadband circularly polarized microstrip antenna with coplanar parasitic ring slot patch for L-band satellite system application," *IEEE Antennas and Wireless Propagation Letters*, vol. 13, pp. 943–946, 2014.

[8] M. S. Ellis, Z. Zhao, J. Wu, X. Ding, Z. Nie, and Q.-H. Liu, "A novel simple and compact microstrip-fed circularly polarized wide slot antenna with wide axial ratio bandwidth for C-band Applications," *IEEE Transactions on Antennas and Propagation*, vol. 64, no. 4, pp. 1552–1555, 2016.

[9] A. Sharma and R. K. Gangwar, "Circularly polarised hybrid Z-shaped cylindrical dielectric resonator antenna for multiband applications," *IET Microwaves, Antennas & Propagation*, vol. 10, no. 12, pp. 1259–1267, 2016.

[10] L. Ge, C.-Y.-G. Sim, H.-L. Su, J. Y. Lu, and C. Ku, "Single-layer dual-broadband circularly polarised annular-slot antenna for WLAN applications," *IET Microwaves, Antennas & Propagation*, vol. 12, no. 1, pp. 99–107, 2017.

[11] R. Xu, J.-Y. Li, Y. X. Qi, G.-W. Yang, and J.-J. Yang, "A design of triple-wideband triple-sense circularly polarized square slot antenna," *IEEE Antennas and Wireless Propagation Letters*, vol. 16, pp. 1763–1766, 2017.

[12] R. Xu, J.-Y. Li, J.-J. Yang, K. Wei, and Y.-X. Qi, "A design of U-shaped slot antenna with broadband dual circularly polarized radiation," *IEEE Transactions on Antennas and Propagation*, vol. 65, no. 6, pp. 3217–3220, 2017.

[13] A. K. Gautam, A. Kunwar, and B. K. Kanaujia, "Circularly polarized arrowhead-shape slotted microstrip antenna," *IEEE Antennas and Wireless Propagation Letters*, vol. 13, pp. 471–474, 2014.

[14] D. Yu, S. X. Gong, Y. T. Wan et al., "Omnidirectional dual-band dual circularly polarized microstrip antenna using TM01 and TM02 modes," *IEEE Antennas and Wireless Propagation Letters*, vol. 13, pp. 1104–1107, 2014.

[15] D. F. Mona, E. S. Sakomura, and D. C. Nascimento, "Circularly polarised rectangular microstrip antenna design with arbitrary input impedance," *IET Microwaves, Antennas & Propagation*, vol. 12, no. 9, pp. 1532–1540, 2018.

[16] J. B. Diaaaldin, S. Liao, and Q. Xue, "High gain and low cost differentially fed circularly polarized planar aperture antenna for broadband millimeter-wave applications," *IEEE Transactions on Antennas and Propagation*, vol. 64, no. 1, pp. 33–42, 2016.

[17] J. B. Diaaaldin, S. Liao, and Q. Xue, "Circularly polarized planar aperture antenna for millimeter-wave applications," *IEEE Transactions on Antennas and Propagation*, vol. 63, no. 12, pp. 5316–5324, 2015.

[18] A. Perron, T. A. Denidni, and A. R. Sebak, "Circularly polarized microstrip/elliptical dielectric ring resonator antenna for millimeter-wave applications," *IEEE Antennas and Wireless Propagation Letters*, vol. 9, pp. 783–786, 2010.

[19] X. Wu, F. Yang, F. Xu, and J. Zhou, "Circularly polarized waveguide antenna with dual pairs of radiation slots at ka-band," *IEEE Antennas and Wireless Propagation Letters*, vol. 16, pp. 2947–2950, 2017.

[20] X. Bai, S.-W. Qu, S. Yang, J. Hu, and Z.-P. Nie, "Millimeter-wave circularly polarized tapered-elliptical cavity antenna with wide axial-ratio beamwidth," *IEEE Transactions on Antennas and Propagation*, vol. 64, no. 2, pp. 811–814, 2016.

[21] R. Garg, P. Bhartia, I. Bahl et al., *Microstrip Antenna Design Handbook*, Artech House, Norwood, MA, USA, 2001.

[22] F. Yang, X. X. Zhang, X. Ye, and Y. Rahmat-Samii, "Wide-band E-shaped patch antennas for wireless communications," *IEEE Transactions on Antennas and Propagation*, vol. 49, no. 7, pp. 1094–1100, 2001.

Hindawi
International Journal of Antennas and Propagation
Volume 2019, Article ID 3981678, 10 pages
https://doi.org/10.1155/2019/3981678

Research Article

Outdoor-to-Indoor Channel Measurement and Coverage Analysis for 5G Typical Spectrums

Zhimeng Zhong, Jianyao Zhao, and Chao Li

Shanghai Huawei Technologies Ltd., Shanghai 201206, China

Correspondence should be addressed to Zhimeng Zhong; zhongzhimeng@huawei.com

Received 7 March 2019; Revised 28 May 2019; Accepted 30 July 2019; Published 16 September 2019

Guest Editor: Danping He

The fifth-generation (5G) mobile communications system will adopt the millimeter wave (mmWave) band for outdoor-to-indoor (O2I) coverage to achieve ultrahigh data rate. However, it is a challenging task because of the large path loss and almost total blocking by building walls. In this work, we performed extensive measurements on the O2I propagation at 3.5, 4.9, and 28 GHz simultaneously by using a multiband channel sounder. We captured the path loss distribution and angular power arrival profiles. We also measured the penetration loss at 28 GHz through different kinds of glass windows. The widely adopted ordinary glass windows introduce the penetration loss of 3 to 12 dB that is acceptable and makes mmWave O2I coverage feasible. But the low-emissivity (low-E) windows that will be more popular in the future introduce 10 dB higher loss. The measurement results in this work can help analyse and anticipate the O2I coverage by mmWave, which is important for the design and deployment of the 5G network.

1. Introduction

In the fifth-generation (5G) mobile communication system, the outdoor-to-indoor (O2I) coverage in urban areas is an important scenario for the network deployment. The base stations on building rooftops or towers provide O2I coverage for nearby buildings. Meanwhile, the millimeter wave (mmWave) band is a key feature in the 5G system that is expected to provide very large bandwidth to support extremely high data rates for the eMBB (enhanced mobile broadband) applications. The performance of coverage depends critically on the propagation characteristics of the radio channels, such as the large-scale fading and angular power spectra in the mmWave band. Therefore, the radio channel models in different frequency bands, especially the sub-6G (frequency band below 6 GHz) and mmWave bands, are critical for the design and deployment of the 5G base stations. This work can reveal the signal coverage of both the low- and high-frequency bands and also accurately compare the channel characteristics among the different frequency bands. Therefore, this work can be used to guide the deployment of the 5G network using different frequency band resources.

Whether the 5G mmWave band can satisfy the O2I communication link requirement and provide reliable coverage remains an open question. To address this issue, the field channel measurements on the signal strength path loss are critical for the analysis and evaluate the feasibility of O2I coverage in mmWave band. Furthermore, the measurement results can also provide useful guidance for the design and deployment of the 5G networks.

In this article, we firstly survey the current efforts in both industrial and academic communities on the channel characterization in candidate 5G spectra. The channel models are the enabling tools for the evaluation and deployment of 5G networks in realistic environments.

Then, in order to study the feasible approach for coverage in the future 5G networks, we present our measurement campaign and analysis on the large-scale fading of O2I downlink channels in both sub-6 GHz and mmWave bands (3.5, 4.9, and 28 GHz). The propagation from an outdoor rooftop base station (BS) to positions in a room and several corridors with various depths into a building were measured using a multiband channel sounder. The path losses at the three frequency points are compared and evaluated for the

O2I coverage. In addition, the horn antenna for 28 GHz channel sounding was rotated at multiple positions and heights in a room to capture the angle of arrival of propagation paths. Thus, we can analyse and enhance coverage based on the spatial (angular) propagation characteristics of mmWave in the O2I channels.

The glass window penetration propagation loss is critical for designing and optimizing O2I coverage, which depends on the composition, thickness, and layers of windows and varies greatly over frequency. We measured the penetration loss at 28 GHz through dozens of windows. The coverage in urban buildings is analysed according to our measurement results and the practical exterior windows in North America and Europe.

Finally, the O2I coverage using mmWave is discussed based on our channel measurement results and window market analysis. It is found that 28 GHz signals can provide coverage in outer-ring rooms by propagation through exterior windows. However, mmWave signals cannot provide coverage for inner rooms and corridors due to severe blocking by concrete walls. In this case, the sub-6 GHz band such as 3.5 GHz can provide good coverage.

2. Related Work

2.1. Current O2I Channel Measurement. The authors measured the propagation property in 3.5 and 6 GHz frequencies according to the channel impulse response (CIR) of O2I links [1–3]. In [1], the authors performed the O2I channel measurements with 56×32 antenna elements at 3.5 GHz with 100 MHz bandwidth at different locations and routes. It was found that the three-dimensional (3D) multiple-input-multiple-output (MIMO) channel which fully utilized the elevation domain could improve capacity and also enhance the contributing eigenvalue number in the O2I scenario. The authors in [2] presented the cluster-parameter-based analysis of an O2I MIMO measurement campaign which was carried out at 3.5 GHz in an office. The authors observed that the multipath components (MPCs) within one cluster in MIMO channels could be divided into several clusters and each had MPCs with smaller power weighted multipath component distance. In order to catch the propagation characteristics of channels in O2I scenarios, the authors in [3] presented the results of the 3D MIMO measurement in urban microcellular (UMi) O2I scenario at 6 GHz with the bandwidth of 100 MHz.

Similarly, the authors in [4, 5] also presented a low-cost channel sounder and post-processing algorithms suitable for investigating the 3D MIMO channels to obtain the elevation and azimuth characteristics from 2.52 to 2.54 GHz. The channel measurement provided the elevation and azimuth angular spreads under different heights in urban macrocellular (UMa) and UMi environments.

For the higher frequency bands of O2I scenarios, studies are found to cover many frequency bands, such as 10, 28, and 60 GHz [6–8]. Reference [6] studied the indoor coverage at different frequencies (10, 30, and 60 GHz) in a single building with an outdoor-deployed base station (BS). The work illustrated the general trends of how coverage varied across the frequency range. But the O2I coverage at 60 GHz may be quite difficult for some building types and the throughput was seriously affected, depending on the wall materials, interior layout, and building size. In [7], the authors presented results for path loss, penetration loss for two different type of housing, including single-family unit and multistory brick building.

2.2. Millimeter-Wave Channel Measurement and Modelling. The industry has much interests in the higher frequency band and proposed a series of 3GPP technical reports, which contain the channel models for frequencies from 0.5 up to 100 GHz [9–12]. Meanwhile, the additional considerations on building penetration loss modelling for the 5G system is also investigated in [13].

While in academic community, many researchers have also explored the property of the high-frequency channels. In [14], the authors presented the radio propagation measurements and analysis for the mmWave transmission for in-building and urban cellular communications in the 28 GHz band. Based on the measurements, the spatiotemporal channel characteristics, such as multipath delay, angular statistics, and path loss were analysed and modelled. In [15], the authors considered the path loss modelling in UMi environments. The authors established a spatially consistent stochastic street-by-street path loss model which could correctly describe the path LOS as a function of the street orientation as well as the large variance observed for all the path loss model parameters. The authors in [16] investigated the intracluster channel characteristics of NLOS 28 GHz channels in street canyon scenarios. The channel characteristics include cluster numbers, number of subpaths within each cluster, intracluster delay spreads, and intracluster angular spreads.

The 38 GHz mmWave frequency band is also a strong candidate for the future deployment of the 5G system. In [17], the authors presented a detailed measurement-based analysis of urban outdoor and O2I propagation characteristics at 38 GHz. The measurement results confirmed that, at this particular frequency, propagation in urban scenarios was mainly driven by LOS and reflection.

The above works have performed extensive channel measurements in both the lower-frequency bands and the mmWave band in different scenarios. However, the O2I coverage by using the mmWave band has been less explored. In this paper, we measured the path loss as well as the spatial power arrival profiles by using a triple-frequency channel sounder. This multiband channel sounding scheme enables us to compare and accurately analyse the propagation characteristics in different bands. We have also investigated the glazing markets in several countries and measured the penetration loss through a dozen of different types of windows. The results are critical for the design and deployment of the 5G system to achieve O2I coverage.

3. Multiband O2I Measurement and Comparison

3.1. Multiband Channel Sounder. The transmitter (TX) is comprises three radio frequency (RF) chains at 3.5, 4.9, and

28 GHz, as show in Figure 1(a). Every RF chain consists of a signal generator, power amplifier, and transmitting antenna. Based on the narrow-band sounding scheme, each chain generates and transmits a single tone at the target frequency. The two white cylindrical antennas on the right are for 4.9 and 3.5 GHz with the gain of 0.5 and 4 dBi, respectively. They are omnidirectional in the azimuth plane and have a half-power beam width (HPBW) of 40° in the elevation plane. The horn antenna on the left works at 28 GHz with a gain of 8.5 dBi. It has 110° and 40° HPBW in the azimuth and elevation plane, respectively. The parameters of TX antennas are summarized in Table 1.

The receiver (RX) is equipped with two types of antennas to capture the sounding signal, as shown in Figure 1(b). Firstly, a wideband antenna can receive signals at 3.5, 4.9, and 28 GHz with the gain of 4, 0.5, and 2.5 dBi, respectively. It is omnidirectional in the azimuth plane and has a HPBW of 40° in the elevation dimension. Secondly, we use a horn antenna to capture the probing signals at 28 GHz that has a 25 dBi gain and 10° HPBW in both the azimuth and elevation planes. It is mounted on a numerical-control turntable to rotate around and capture the impinging signal from different directions. Also to better express it, the parameters of RX antennas are summarized in Table 1. In the field measurements on propagation path loss, the three RF chains in the TX transmit signals simultaneously and the multiband sounding signal received on the wideband antenna is input into a portable spectrum analyzer (SA). The SA has been programmed to record the received power at the three marked frequency points for 50 times continuously with the interval of 300 millisecond (ms). Then, it calculates the average power at each frequency and transfers the data to a computer for storage.

As shown in Figure 1, the signal-transmitting/ signal-receiving systems at the three frequencies are placed together at the same positions in order to compare the propagation characteristics accurately, as for the horn antenna on the RX side, by adjusting the horizontal and vertical angel of the horn antenna, firstly to find the direction with largest receive power. Then, the vertical tilt angle is fixed, and the horn antenna is rotated in the horizontal plane by a circle for capturing power in different directions.

3.2. Multiband O2I Propagation Measurement Scenario. The measurement campaign was conducted in a typical urban microcell O2I scenario in Shanghai, China. The TX was installed on the top of five-story building to emulate a BS. The height of the antennas was about 26 meters. The RX, emulating a UE, was moved on the 5th and 7th floors in a modern apartment building on the opposite side of the TX, as shown in Figure 2. The heights of the two stories were 17 and 23 meters. The line-of-sight (LOS) direction from the TX to the room for measurement was about 10° to the east, and the distance from the TX to the window at the 7th floor was only 20 meters. On either floor, the RX was moved at 8 positions in a room and 40 positions in four corridors, as annotated in the floorplan in Figure 3. To analyse the propagation characteristics, the measurement routes were divided into four regions. The first region was the room where the RX was placed at 8 positions (P1 to P8) along a line with a spacing of 1 meter between adjacent positions. The second region was a horizontal corridor next to the outer-ring rooms including the measurement positions from P11 to P23. The third region included two vertical corridors which had the measurement positions from P24 to P29 and from P34 to P40 excluding P35 and P36. Finally, the fourth region was a horizontal corridor in the inner part of the building, which included P29 to P36. The spacing between adjacent positions in the corridors was 2 meters.

3.3. Measurement Results of Multiband O2I Coverage. The contour diagrams in Figure 3 demonstrate the distributions of the pass loss magnitudes at the three frequencies of 3.5, 4.9, and 28 GHz. For Area 1 (an outer room), the signals can propagate through the window and achieve good coverage at all the three frequencies. According to the link budget design, the maximal tolerable path loss for the BS-to-UE links is PL_{th} = 140 dB. The maximal tolerable path loss of 140 dB is widely used in the industry [18, 19]. Actually, it will be slightly different for different frequencies and different companies. Generally, this tolerable path loss is used for brief evaluation of link budget during the design of wireless communication system or architecture. We can see that the path loss in the room is much smaller than PL_{th} at 3.5 and 4.9 GHz. For 28 GHz, the path loss satisfies the requirement in almost all the room but is just close to PL_{th} near the door. Therefore, the BS can cover the room entirely at all the three frequencies. How the 28 GHz signals propagate in space and cover the room will be discussed in detail later.

In Area 2 (the long corridor in the middle), the path loss at all the three frequencies is obviously larger than that in Area 1 and increases with the horizontal depth along the corridor. It is noticed that the path loss is the smallest at position RX 11. This is because there is a high-rise building to the west, as shown in Figure 2. Thus, some signals are reflected into the corridor through the window near RX 11, resulting in the decreasing trend of the path loss from the west to the east. In addition, near the door of each room, the path loss decreases slightly. This is because the signals from the BS arrive at these positions through a window and a door. Hence, the path loss near the doors is smaller than that at other positions where the signals need to pass through two walls.

The average path loss in Area 2 at 4.9 and 28 GHz is larger by 12 and 30 dB, respectively, than that at 3.5 GHz. As shown in Figure 3, the path loss at the two sub-6 GHz frequencies is well below PL_{th}, ensuring good coverage in Area 2. But the 28 GHz band cannot meet the path loss requirement except the small part near the west window. As mentioned above, this is due to the paths reflected by a building outside the window.

Area 3 is the two vertical corridors, where the path loss is larger than that in Area 2, as shown in Figure 3. The average path loss at 4.9 and 28 GHz is larger by 12 and 40 dB, respectively, than that at 3.5 GHz. In Figures 3(a) and 3(b), we can see that the path loss in the corridor on the right hand side (to the east) is obviously smaller than that in the left corridor

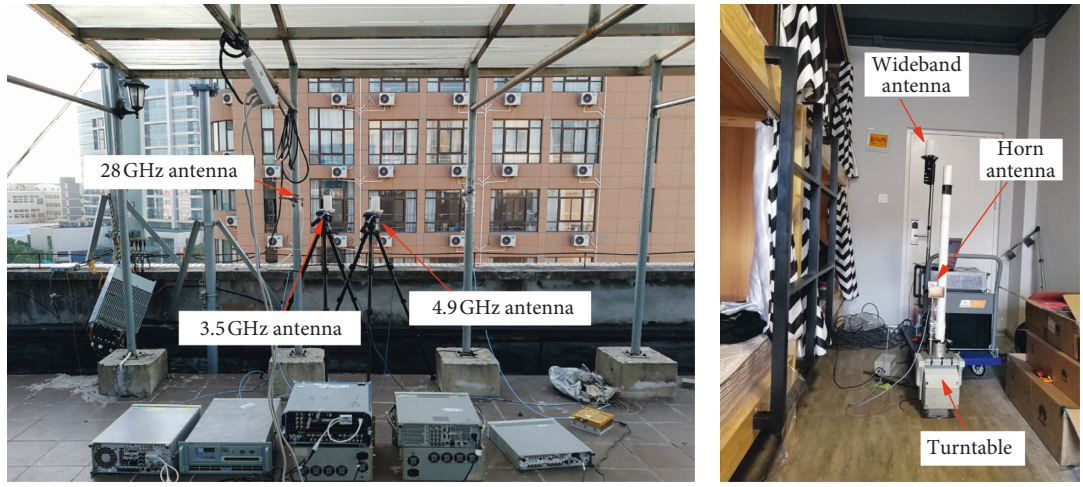

(a) (b)

Figure 1: Multiband channel sounder at 3.5, 4.9, and 28 GHz. (a) Transmitter with three RF chains and antennas. (b) Receiver with two antennas.

Table 1: The configuration of antennas.

Class	Subclass	HPBW in horizontal plane (°)	HPBW in elevation plane (°)	Antenna gain (dBi)
TX antenna	3.5 GHz TX antenna	360	40	4
	4.9 GHz TX antenna	360	40	0.5
	28 GHz TX antenna	110	40	8.5
RX antenna	3.5 GHz RX antenna	360	40	4
	4.9 GHz RX antenna	360	40	0.5
	28 GHz RX antenna type 1	360	40	2.5
	28 GHz RX antenna type 2	10	10	25

Figure 2: Multiband O2I channel measurement scenario.

(to the west). This is because, as mentioned earlier, the BS is to the east with respect to Area 1, and thus is closer to the right corridor. The signals at the sub-6 GHz frequencies can penetrate the walls and arrive at the two corridors. Since the propagation distance to the right corridor is shorter, the path loss is smaller. However, there is no obvious difference for the two corridors at 28 GHz in Figure 3(c), as the mmWave signals cannot penetrate the walls. It is found that 3.5 and 4.9 GHz can achieve full coverage over Area 3, but 28 GHz cannot satisfy the path loss requirement any more.

Area 4 is the horizontal corridor at the bottom. The distribution of the path loss in Area 4 is similar with that in Area 2. The path loss is relatively small near the window to the west end and increases along the corridor to the east. The average path loss at 4.9 and 28 GHz is larger by 12 and 35 dB, respectively, than that at 3.5 GHz. Since the path loss is still below PL_{th}, 3.5 and 4.9 GHz can achieve full coverage for Area 4. But 28 GHz can only cover the area near the window.

By comparison, it can be found that the difference between the pass loss at 3.5 and 4.9 GHz does not change, which is always 12 dB. This indicates that the penetration loss through the windows or walls is quite similar for sub-6 GHz bands. However, the path loss difference between 3.5 and 28 GHz varies in the areas. The difference becomes larger when the RX is moved to the inner part of the building. This indicates that the penetration loss of mmWave signals through walls is much larger.

In summary, we can see that the 28 GHz band can provide coverage for indoor areas near exterior windows, such as outer rooms and ends of corridors. The propagation through windows results in the received power and hence determines the O2I coverage. Meanwhile the received power decays quickly with the depth of the indoor position due to large path loss. Consequently, mmWave cannot cover inner space of buildings without direct propagation through exterior windows. On the contrary, the sub-6 GHz bands can provide reliable coverage for the whole building in the UMi

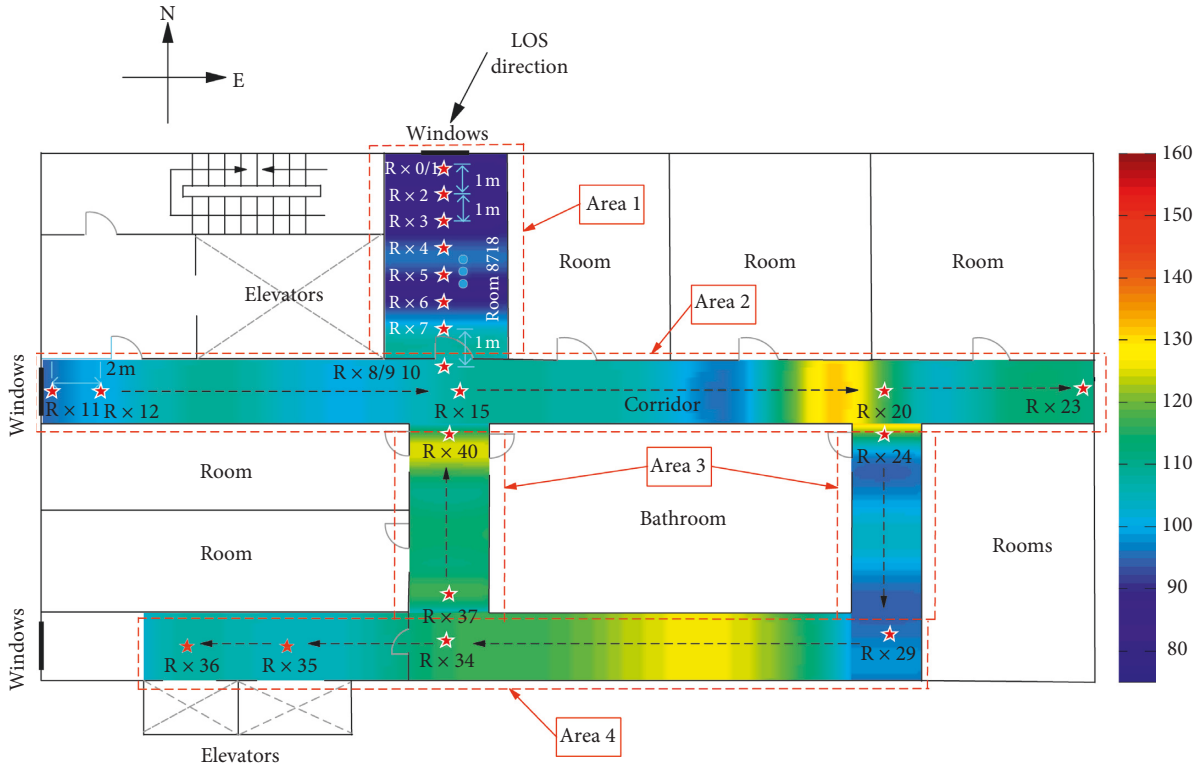

(a)

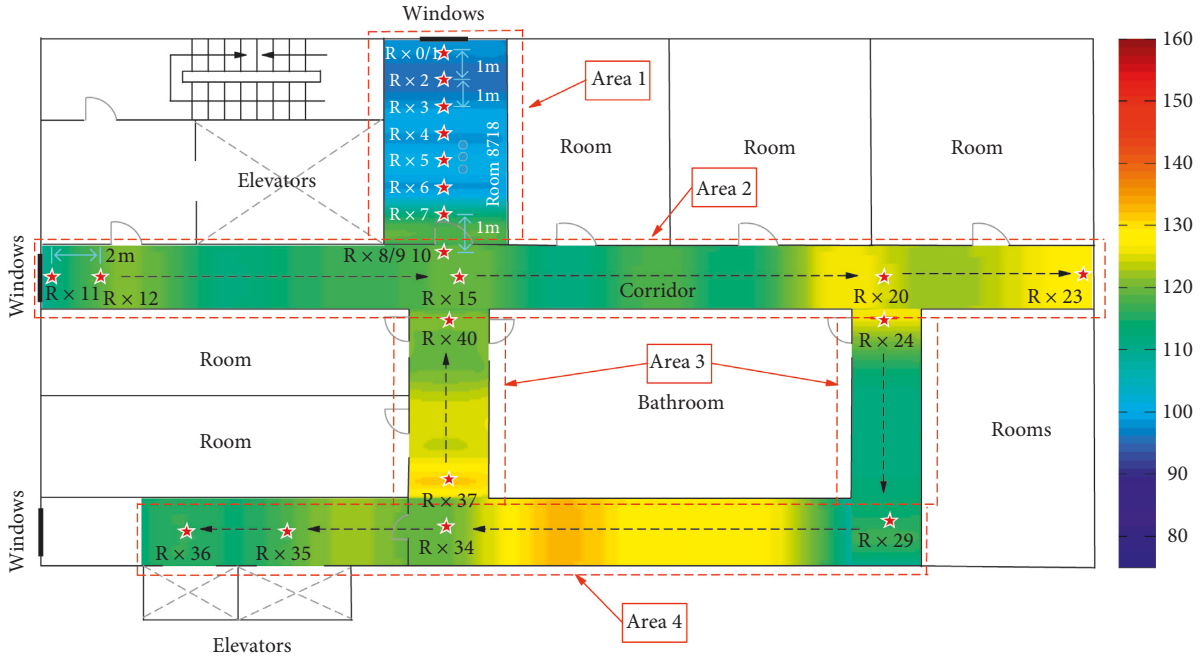

(b)

Figure 3: Continued.

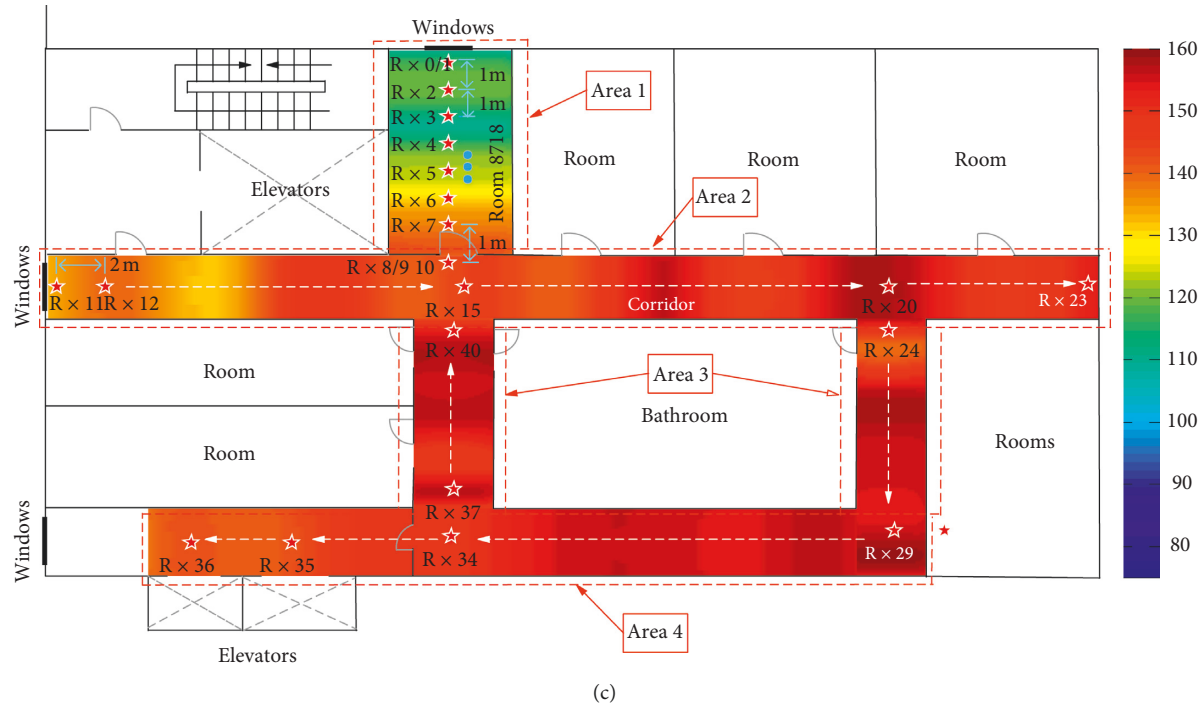

(c)

Figure 3: Measurement results for multiband O2I coverage. (a) Path loss on the 7th floor at 3.5 GHz. (b) Path loss on the 7th floor at 4.9 GHz. (c) Path loss on the 7th floor at 28 GHz.

O2I scenario, thanks to the good propagation characteristics of wall penetration and much smaller path loss.

3.4. Spatial Propagation Measurement for O2I Coverage at 28 GHz. As discussed in the previous subsection, the indoor coverage is achieved by the signal propagation through exterior windows. In this subsection, we study how the mmWave signals propagate in a room and are reflected inside to achieve indoor coverage. For this purpose, we performed the spatial propagation measurements on the 28 GHz signals using the steering antenna method. As mentioned in Section 3.1, a 28 GHz horn antenna was mounted on a turntable. The RX was placed 1, 2.5, and 5.5 meters away from the window along a straight line in the rooms on the 5th and 7th floors, as illustrated in Figure 3. At each position, the receiving antenna was raised to the heights of 0.5, 1.5, and 2.5 m. It was rotated around with the step of the HPBW of 10°, to capture the received power at the directions [20]. As illustrative examples, the angular power profiles at the three measurement positions are plotted in Figure 4.

As can be seen in Figure 4(a), there are three significant clusters. The first one is at the angle of arrival (AoA) of 10°, which is the direction of the LOS path. Hence, this is the direct propagation cluster through the glass window. The second cluster is at the AoA of about 330°. It is the reflection from the wall on the left, which is coincident with the geometric relationship. Its power is slightly smaller than that of the LOS cluster due to the reflection loss. The third cluster is at the AoA of about 190°, which should be the reflection on the back wall of the room. Its power is smaller than the other two clusters because of longer propagation distance and reflection loss.

As shown in Figure 4(b), when the RX was moved to the second position (with more depth into the room), the power of the LOS cluster decays more than the reflection cluster by the left wall. This is because the LOS path is partially blocked but the wall reflection is not affected much and the power is still quite significant. Finally, at the third position, the power of the LOS cluster further reduces and the wall reflection cluster still has large power, as shown in Figure 4(c). Meanwhile, because the RX is now very close to the back wall of the room, the reflection by the metal door becomes quite significant. Also, we can see many scattered clusters in the power arrival profile from different directions, which should be generated by the reflections on the walls. In addition, it is found that, at the same RX position, the angular power arrival profiles at different heights are identical and do not change with height.

The results show that 28 GHz band can provide full coverage over the rooms that are close to an outdoor BS. The LOS cluster contributes most power when the RX is close to the window, but it decays quickly when the RX moves away from the window. The one-bound reflection on a wall always generates a significant cluster, no matter the position of the RX, which plays an important role in indoor coverage, even more than the LOS cluster. The mmWave signals through the window also experience intensive reflections inside the room and make a significant contribution in the received power, especially when the RX is located deep inside the room.

3.5. Path Loss Results of O2I Propagation at Different Frequencies. In order to predict the indoor coverage in the sub-6 GHz and mmWave bands, we evaluate the fitting curve of path loss in the O2I channels based on our

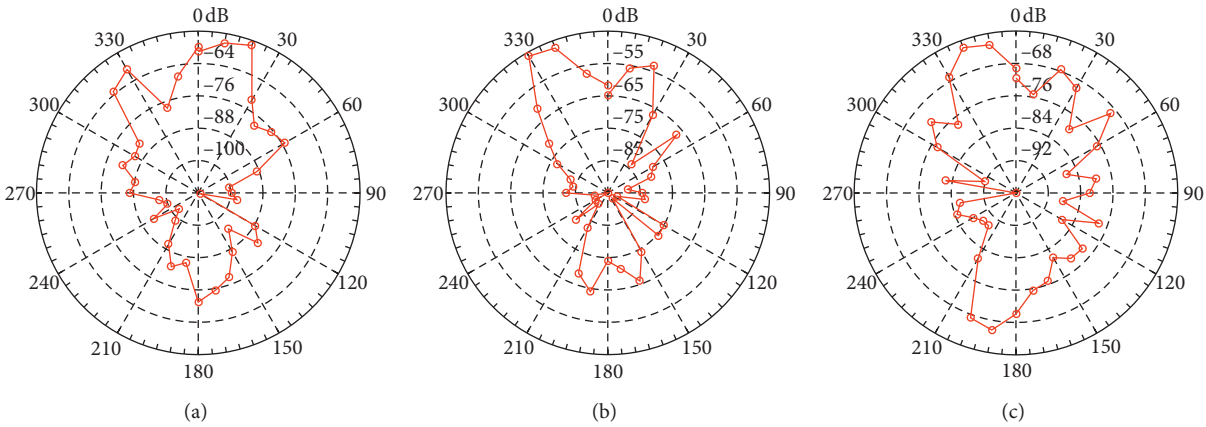

Figure 4: Measurement results of the angular power arrival profiles in the O2I channels at 28 GHz ("D" is the distance between the RX and the window. "H" is the height of the RX horn antenna.). (a) $D = 1$ m, $H = 1.5$ m; (b) $D = 2.5$ m, $H = 2$ m; (c) $D = 5.5$ m, $H = 0.5$ m.

measurement results. The path loss measurement results in Area 1, at the positions from RX 1 to RX 7 on the 7th and 5th floors, in Figure 3 are plotted in Figures 5(a) and 5(b), respectively, for easy analysis. The linear-function fitting model is also plotted. At first, the path loss increases basically linearly with the increase of the depth in the room. On the 7th floor, as shown in Figure 5(a), the path loss exponents (slopes of the linear functions) are all about 1.5 dB/meter for the three frequencies. But the exponent becomes about 6 dB/meter for 28 GHz at the 5th floor.

This indicates that, when there is a clear LOS path, the path loss increments are identical for both sub-6 GHz and mmWave bands. The difference is mainly caused by the frequency gap. However, without a clear LOS path between the BS and UE (but there is a LOS path from the BS to the building window), the path loss for mmWave increases significantly. This may be because the signals cannot penetrate the wall and the received power is collected mainly by reflections. Thus, the path loss increases quickly when the RX moves deeply into the building.

Furthermore, the building penetration loss is another interesting parameter that required to be discussed. Here, we use results of RX 1 to RX 7 in Area 1 for such analysis since other Rx locations involve the deep indoor propagation scheme. For RX in Area 1, we obtain the building penetration loss by removing free space path loss from the whole receiver's path loss. It is shown that the averaging building penetration loss is 10.7 dB, 16.5 dB, and 22.5 dB for 3.5, 4.9, and 28 GHz, respectively. As RX moves deeper into the room, the building penetration loss generally becomes larger. Since the window is not wide enough for all RX in Area 1 to have direct propagation path through glass window, the building penetration is due to hybrid of window and concrete walls.

4. Glass Window Penetration Loss Measurement

As revealed by the measurement results in Section 3, the coverage in the room at 28 GHz depends mainly on the propagation through the exterior glass window. The signal power through the exterior walls is ignorable. Therefore, the propagation loss through glass windows is critical for mmWave to realize O2I coverage. The loss is determined by the ingredients, thickness, and layers of glasses. Various types of glass windows are used in the global market. We have investigated the glazing type distributions in several countries, and the windows can be divided into three main categories: ordinary, low-E (low-emissivity), and IRR (infrared-reflective) glasses, based on the radiation energy differences and energy-saving requirements. Ordinary glass has good light transmission and can transfer almost all the indoor radiation and solar energy. Ordinary glass is mainly used in old-style residential and commercial areas with different thicknesses, colors, and layers. The light transmittance of low-E glass is slightly lower than that of ordinary glass, and the infrared light poorly penetrates. Low-E glass can make room cold in summer and warm in winter with a good energy-saving effect. Low-E glass is mainly used in new residential and commercial areas, with a typical double and metal film and inert gas in the middle. IRR glass has poor transmittance for both visible and infrared light but a good energy-saving effect. IRR glass is mainly used for exterior walls of modern business office buildings.

Each category further includes a number of subtypes. To study the feasibility of mmWave O2I coverage for the 5G network, we selected nine typical kinds of glass windows to measure their penetration loss at 28 GHz. We utilized a vector network analyzer (VNA) with two horn antennas. The transmitting and receiving antennas were placed face to face on the two sides of a window. The penetration loss was obtained by comparing the received power measured with and without the window.

The measurement results and glazing distribution of the glass windows are listed in Table 2. It is found that the penetration loss varies greatly over the glass types. According to the measurement results in Section 3, the additional penetration loss by the window of 6 dB may reduce the indoor coverage depth only by 1 meter. The low-E glass windows in Shanghai and Vancouver both introduce about 15 dB loss, equivalently reducing the indoor coverage

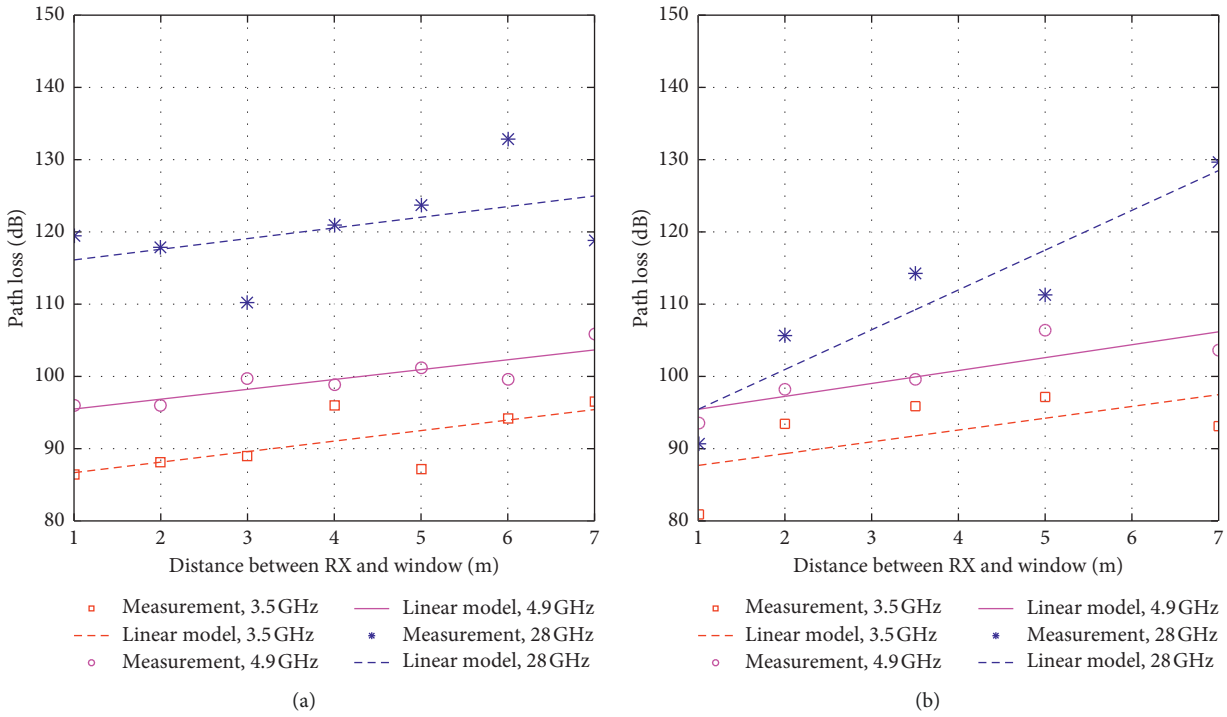

Figure 5: Measurement results of the path loss at different positions in the room at multiple frequencies. (a) The room on the 7th floor. (b) The room on the 5th floor.

Table 2: Penetration loss of various types of glass windows.

Class	Subclass	Penetration loss	Application scenario	Information [13]
Ordinary glass	Ordinary glass (<15 mm)	3–8 dB	Old houses/shops (full coverage over rooms through exterior windows)	Europe: ~86% Austrian: <20% Canada: ~60% United States: 80% China: 45%–85%
	Coated glass (6 mm)	11.83 dB		
Low-E glass	Shanghai, China (18 mm)	15 dB	New/renovated homes/shops (coverage over areas close to exterior windows)	Europe: ~12% Austrian: >80% Canada: ~30% United States: 10% China: 10%~50%
	Vancouver, Canada	16 dB		
IRR glass	IRR ordinary window	31.4 dB [13]	New CBD office building (O2I coverage is difficult)	Europe: ~2% Canada: ~10% United States: 10% China: 5%
	Modern IRR glass	33 dB [13]		
	Tinted glass (38 mm)	40.1 dB [21]		

depth by 2 to 3 m. Therefore, the indoor coverage is still feasible for outer rooms. However, the IRR glass generates much larger loss from 31.4 to 40.1 dB, and thus, the indoor coverage may be difficult. The ordinary glass is, obviously, most beneficial to O2I coverage by mmWave. As listed in Table 2, the ordinary glass is mostly widely used in the considered countries and occupies more than half of the markets [13]. Meanwhile, the IRR glass windows are adopted in less than 10% buildings.

As we can see, it is feasible to provide indoor coverage using mmWave in most areas at present, thanks to the low penetration loss and wide adoption of ordinary glass windows. However, low-E glass windows will be more and more adopted globally for better energy efficiency. For example, as shown in [13], the new or renovated residential buildings in Vancouver and Toronto all use low-E windows. The market occupancy of low-E window in China will increase by 15% to 20% per year and is anticipated to achieve 20% in 2020. Therefore, with the popularity of low-E windows, the O2I coverage by mmWave will become more challenging in the future.

In addition, it is also noticed that the uncoated glass generates loss of only 3 to 8 dB, depending on its thickness (at most 15 mm), glazing (single- or double-layered), and color. But the coated ordinary glass generates almost 12 dB loss even when it is only 6 mm thick. Hence, coating can

significantly increase the penetration loss for ordinary glass windows.

5. Conclusions

The measurement results in this paper reveal the path loss distribution and coverage conditions at 3.5, 4.9, and 28 GHz in a typical UMi O2I scenario. It can be seen that the signals at 28 GHz propagate into the room and corridors mainly through the windows and doors. The path loss is smaller than the threshold of 140 dB and thus the outer rooms can be covered. But the path loss is too high to cover the inner part of the building (>140 dB). The average path loss at 4.9 and 28 GHz is larger by 12 and 35 dB, respectively, than that at 3.5 GHz. The sub-6G signals can penetrate the concrete wall much better and ensure good coverage for the whole building. The difference between the path loss at 3.5 and 4.9 GHz is consistently 12 dB. Based on the comparison, we can conclude that the mmWave band can meet the coverage requirement for outer rooms with exterior windows. The direct LOS cluster can provide required received power for the areas close to windows, but the reflection of mmWave signals by walls is more significant and ensures the coverage over the whole room. The penetration losses through uncoated glass windows of the ordinary, low-E, and IRR windows are 6, 15, and 35 dB. The hybrid approach using both sub-6G and mmWave bands is promising to provide seamless coverage. To design the multiband access network and allocate the spectrum resource based on the propagation characteristics is an interesting and important research topic for 5G.

Data Availability

The channel measurement data used to support the findings of this study are restricted in order to protect the commercial confidentiality. Data are available for researchers who meet the criteria for access to confidential data.

Conflicts of Interest

The authors declare that there are no conflicts of interest regarding the publication of this paper.

References

[1] J. Zhang, Y. Zhang, Y. Yu, R. Xu, Q. Zheng, and P. Zhang, "3D MIMO: how much does it meet our expectations observed from channel measurements," *IEEE Journal on Selected Areas in Communications*, vol. 35, no. 8, pp. 1887–1903, 2017.

[2] D. Du, J. Zhang, C. Pan, and C. Zhang, "Cluster characteristics of wideband 3D MIMO channels in outdoor-to-indoor scenario at 3.5 GHz," in *Proceedings of the 2014 IEEE 79th Vehicular Technology Conference (VTC Spring)*, pp. 1–6, IEEE, Seoul, South Korea, May 2014.

[3] Q. Zheng, J. Zhang, H. Yu, Y. Zhang, and L. Tian, "Propagation statistic characteristic of 3D MIMO channel in outdoor-to-indoor scenario with different antenna heights," in *Proceedings of the 2016 19th International Symposium On Wireless Personal Multimedia Communications (WPMC)*, pp. 411–416, IEEE, Shenzhen, China, November 2016.

[4] V. Kristem, S. Sangodoyin, C. U. Bas et al., "3D MIMO outdoor-to-indoor propagation channel measurement," *IEEE Transactions on Wireless Communications*, vol. 16, no. 7, pp. 4600–4613, 2017.

[5] R. Zhang, S. Wang, X. Lu, W. Duan, and L. Cai, "Two-dimensional DoA estimation for multipath propagation characterization using the array response of PN-sequences," *IEEE Transactions on Wireless Communications*, vol. 15, no. 1, pp. 341–356, 2016.

[6] E. Semaan, F. Harrysson, A. Furuskar, and H. Asplund, "Outdoor-to-indoor coverage in high frequency bands," in *Proceedings of the 2014 IEEE Globecom Workshops (GC Wkshps)*, pp. 393–398, IEEE, Austin, TX, USA, December 2014.

[7] C. U. Bas, R. Wang, T. Choi et al., "Outdoor to indoor penetration loss at 28 GHz for fixed wireless access," in *Proceedings of the 2018 IEEE International Conference on Communications (ICC)*, vol. 99, pp. 1–6, IEEE, Kansas City, MO, USA, May 2018.

[8] L. Ahumada, E. Carreno, A. Angles, and D. Schkolnik, "Studying the dynamics of outdoor-indoor wireless links at 60 GHz," in *Proceedings of the 2018 IEEE-APS Topical Conference on Antennas and Propagation in Wireless Communications (APWC)*, pp. 834–837, IEEE, Cartagena des Indias, Colombia, September 2018.

[9] ETSI, "Study on channel model for frequencies from 0.5 to 100 GHz (release 14) (3GPP technical specification group radio access networks)," Tech. Rep. TR 38.901 V14.0.0, ETSI, Sophia Antipolis, France, 2017.

[10] ITU, *Prediction of Building Entry Loss, Recommendation ITU-R P.2109-0*, ITU, Geneva, Switzerland, 2017.

[11] ITU, "Compilation of measurement data relating to building entry loss," Report ITU-R P.2346-2, ITU, Geneva, Switzerland, 2017.

[12] mmMAGIC, "Measurement results and final mmMAGIC channel models," H2020-ICT-671650-mmMAGIC/D2.2 v2.0, 2017, https://5g-ppp.eu/mmmagic/.

[13] Additional considerations on building penetration loss modeling for 5G system performance evaluation," Straight Path Communications, Tech. Rep. R1-163408, 2016.

[14] J. Ko, Y.-J. Cho, S. Hur et al., "Millimeter-wave channel measurements and analysis for statistical spatial channel model in in-building and urban environments at 28 GHz," *IEEE Transactions on Wireless Communications*, vol. 16, no. 9, pp. 5853–5868, 2017.

[15] A. Karttunen, A. F. Molisch, S. Hur, J. Park, and C. J. Zhang, "Spatially consistent street-by-street path loss model for 28 GHz channels in micro cell urban environments," *IEEE Transactions on Wireless Communications*, vol. 16, no. 11, pp. 7538–7550, 2017.

[16] S. Wu, S. Hur, K. Whang, and M. Nekovee, "Intra-cluster characteristics of 28 GHz wireless channel in urban micro street canyon," in *Proceedings of the 2016 IEEE Global Communications Conference (GLOBECOM)*, pp. 1–6, IEEE, Washington, DC, USA, December 2016.

[17] I. Rodriguez, H. C. Nguyen, T. B. Sorensen et al., "Analysis of 38 GHz mmwave propagation characteristics of urban scenarios," in *Proceedings of European Wireless 2015; 21th European Wireless Conference*, pp. 1–8, VDE, Budapest, Hungary, May 2015.

[18] J. S. Seybold, *Introduction to RF Propagation*, John Wiley & Sons, Hoboken, NJ, USA, 2005.

[19] J.-H. Park, K.-W. Cheun, W.-I. Roh, and J.-W. Cho, "Method and apparatus for transmitting or receiving rach signal in beamforming system," US20140348051A1, 2014.

[20] R. Zhang, Y. Zhou, X. Lu, C. Cao, and Q. Guo, "Antenna deembedding for mmWave propagation modeling and field measurement validation at 73 GHz field measurement validation at 73 GHz," *IEEE Transactions on Microwave Theory and Techniques*, vol. 65, no. 10, pp. 3648–3659, 2017.

[21] H. Zhao, R. Mayzus, S. Sun et al., "28 GHz millimeter wave cellular communication measurements for reflection and penetration loss in and around buildings in New York city," in *Proceedings of the 2013 IEEE International Conference on Communications (ICC)*, pp. 5163–5167, IEEE, Budapest, Hungary, May 2013.

Hindawi
International Journal of Antennas and Propagation
Volume 2019, Article ID 6529343, 12 pages
https://doi.org/10.1155/2019/6529343

Research Article

Continuously Frequency-Tunable Horn Filtennas Based on Dual-Post Resonators

Andreia A. C. Alves,[1,2] **Luis G. da Silva**,[1] **Evandro C. Vilas Boas**,[1] **Danilo H. Spadoti**,[2] **and S. Arismar Cerqueira Jr.**[1]

[1]*Wireless and Optical Convergent Access Laboratory (WOCA), National Institute of Telecommunication (Inatel), Santa Rita do Sapucaí 3754000, Brazil*
[2]*Department of Institute of Systems Engineering and Information Technology, Federal University of Itajubá (Unifei), Itajubá 37500 903, Brazil*

Correspondence should be addressed to S. Arismar Cerqueira Jr.; arismar@inatel.br

Received 3 May 2019; Revised 4 July 2019; Accepted 23 July 2019; Published 15 September 2019

Guest Editor: Marko Sonkki

This work reports the concept and development of two mechanically frequency-tunable horn filtennas for microwave and millimeter-waves. Our design approach relies on the integration of a horn antenna with a mechanically tunable filter based on dual-post resonators. The proposed filtennas have been manufactured and experimentally characterized, by means of reflection coefficient, radiation pattern, and gain. Measurements demonstrate that both filtennas have a tuning ratio of approximately 1.37 with continuous adjustment. The first prototype operates from 2.56 to 3.50 GHz, whereas in the second one the bandwidth is from 17.4 to 24.0 GHz. In addition, the higher-frequency filtenna has been implemented in a 5.0-meter-reach indoor environment, using a 16-QAM signal at 24 GHz. The best configuration in terms of performance resulted in a root mean square error vector magnitude (EVM_{RMS}) and antenna radiation efficiency of 3.69% and 97.0%, respectively.

1. Introduction

The usage spectrum has been increased significantly in the last decades and trends to accelerate even more in the next years due to the fifth-generation cellular networks (5G). This new generation aims at a 100-fold increase in traffic capacity [1, 2]. The motivation to increase the 5G network bandwidth will probably be the most promising approach to increase the overall capacity. In this direction, the wireless research community needs to exploit efficient and more effective spectrum management techniques [3–7]. Among various approaches, the dynamic spectrum access techniques, including cognitive radio (CR), have been distinguished. Although the use of millimeter-waves (mm-waves) represents a hot topic, low-frequency bands have indeed been considered for 5G systems [5]. Therefore, the basic structure will be a hybrid network, in which the low- and high-frequency communications coexist [6, 7].

In this direction, the demand for new antennas with a capability to work in the newly proposed architectures has increased, and reconfigurable antennas represent a potential candidate to fulfill the 5G requirements [8–11]. Furthermore, the CR applications require using two different antennas: a broadband antenna for spectrum sensing and a tunable narrowband antenna after selecting the operating channel [12]. Apart from the need of continuously operating through different channels, it becomes necessary to reject those that are not in use. In this way, the filter requirements of the front-end circuits can be greatly reduced.

As an attempt to reduce the hardware complexity, researchers have proposed to move some of the filtering parts to the antenna in order to discharge the filter bank constraints inside the front end. Examples of frequency-reconfigurable antennas with integrated filtering capabilities can be found in [13–16]. A single-port reconfigurable antenna for CR applications was presented in [13]. The

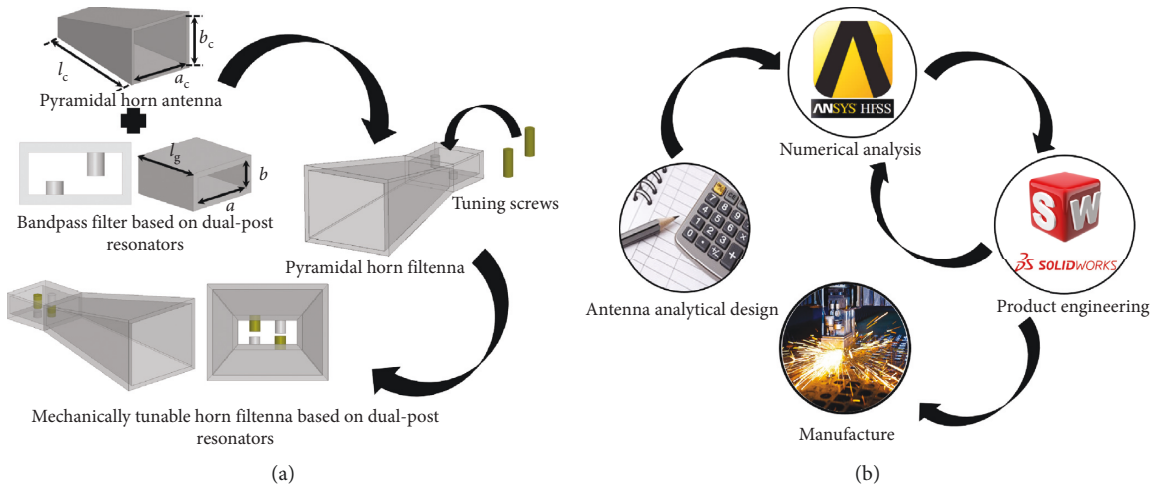

Figure 1: Horn filtennas design (a) and development methodology (b).

proposed antenna was based on an ultra-wideband (UWB) design and has a reconfigurable bandpass filter integrated into its feed line. Electronic switches were incorporated on the filter to activate/deactivate it and control its bandpass frequency. In [14], a defected microstrip structure (DMS) based on a reconfigurable bandpass filter was integrated with a dual-sided tapered slot antenna. By manipulating the slots in the DMS, the filter could be used for frequency tuning. The authors in [15] presented, for the first time, the filtenna concept. Filtenna or "filtering antenna" is the antenna-filter combination with filtering ability, while preserving the radiation performance. This was achieved by changing the filter total capacitance via an integrated varactor within its structure. We have recently proposed the concept and reported the development of an optically controlled reconfigurable filtenna [16], which was based on the integration of a broadband printed antenna with a bandpass reconfigurable filter and photoconductive switches.

Finally, from the waveguide point of view, there are some publications on filter devices and horn antennas integration, due to its high gain and high efficiency [17–23]. Luo et al. proposed a filtenna structure, in which a horn antenna was covered by a frequency-selective surface (FSS) based on substrate integrated waveguide (SIW) cavities for suppression of out-band interference [17]. In [18], Bilotti et al. reported a self-filtering and low-noise horn antenna for satellite applications. The filtering element was based on metallic omega particles [19]. On the other hand, Barbuto et al. designed a combined bandpass filter and polarization transformer for horn antennas [20]. The solution was based on the design of a linear-to-circular polarization transformer, which consisted of a complementary electrically small resonator etched on a metallic screen. Ma et al. [21] presented a dual circularly polarized horn antenna, by employing a chiral metamaterial composed of two-layered periodic metallic arc structure. The designed antenna provides left-handed circular polarization from 12.4 to 12.5 GHz and right-handed circular polarization from 14.2 to 14.4 GHz. Barbuto et al. have used electrically small magnetic resonators to design filtering horn antennas with band-stop characteristics [22]. By properly placing a split-ring resonator (SRR) inside a standard horn antenna, the radiating and matching properties of the overall structure are affected by the SRR strong resonance only around its resonant frequency, leading to a band notch filter. Recently, Wang et al. reported a wideband pattern-reconfigurable horn antenna [23]. The antenna consisted of incorporating a power divider, eight reconfigurable band-stop filters, and eight TEM horn antenna elements.

Particularly, we have very recently reported preliminary results of a mechanically tunable horn filtenna [24]. That work is regarding the development of two high-performance reconfigurable and tunable horn filtennas. The first proposed filtenna has been idealized for sub-3.0 GHz bands, which had been recommended by the U.S. Federal Communications Commission for 5G transmission in urban environments [25]. On the other hand, the second prototype is devoted to mm-wave 5G systems, which are typically referred to as enhanced mobile broadband applications. The manuscript is structured in five sections. Section 2 is regarding the mechanically tunable horn filtenna design and development methodology. The numerical and experimental results of the two proposed filtennas are presented in Section 3. Section 4 reports an implementation and an experimental performance analysis of the mm-wave horn filtenna. Conclusions and final comments are addressed in Section 5.

2. Horn Filtenna Design and Development Methodology

The horn filtennas design and development methodology are presented in Figure 1. Initially, the horn antenna and RF bandpass filter, corresponding to each filtenna, have been analytically calculated as individual structures, with the purpose of satisfying the project requirements. After, they were integrated into a single structure for creating the frequency-reconfigurable filtenna, as illustrated in Figure 1(b). As described in Figure 1(a), the development methodology can be summarized into four phases: the horn antenna and filter analytical design; numerical analysis;

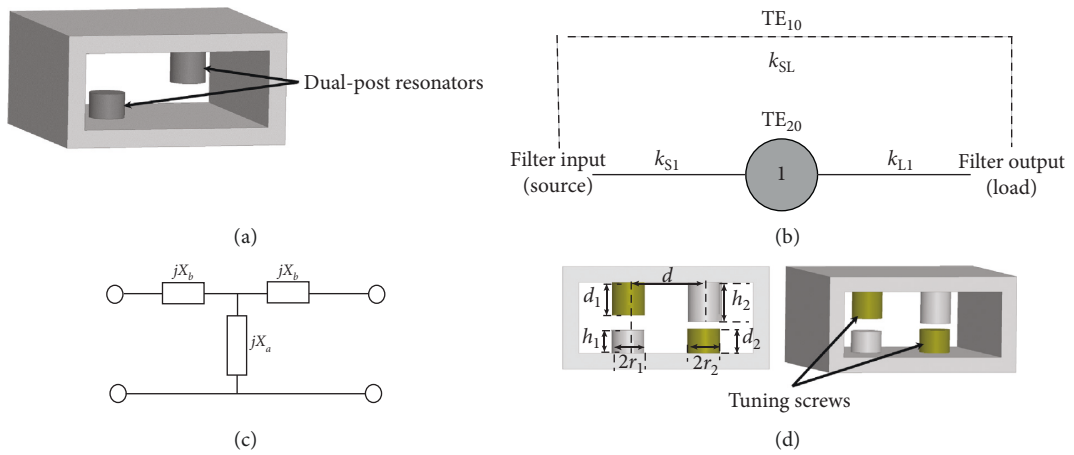

Figure 2: Dual-post resonator filter. (a) The dual-post resonators. (b) The DPR filter singlet schematic. (c) The DPR equivalent circuit. (d) The dual-post resonators and tuning screws variables.

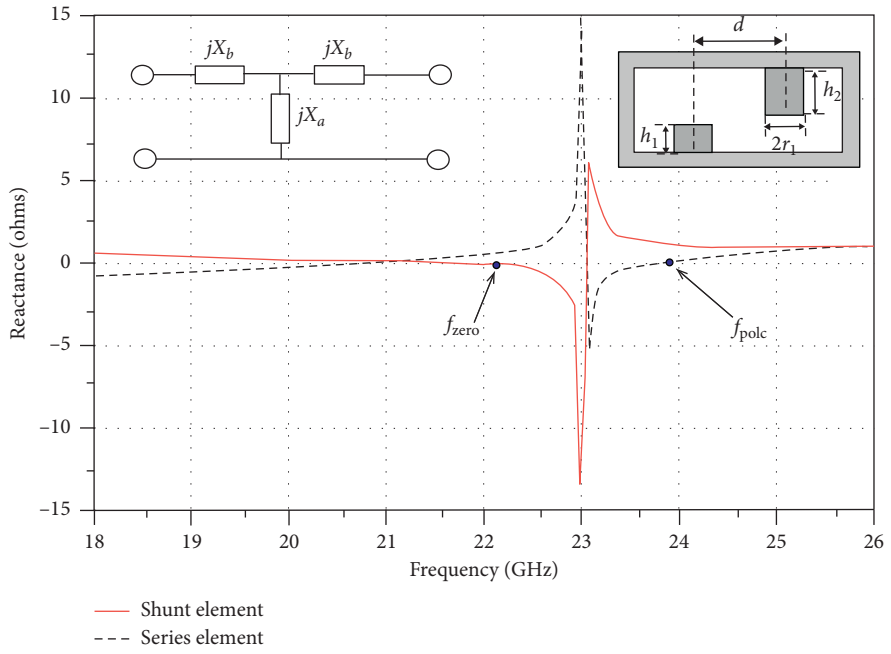

Figure 3: The dual-post resonator reactance for $r_1 = 1$ mm, $d = 4.67$ mm, $h_1 = 1.4$ mm, and $h_2 = 2.4$ mm.

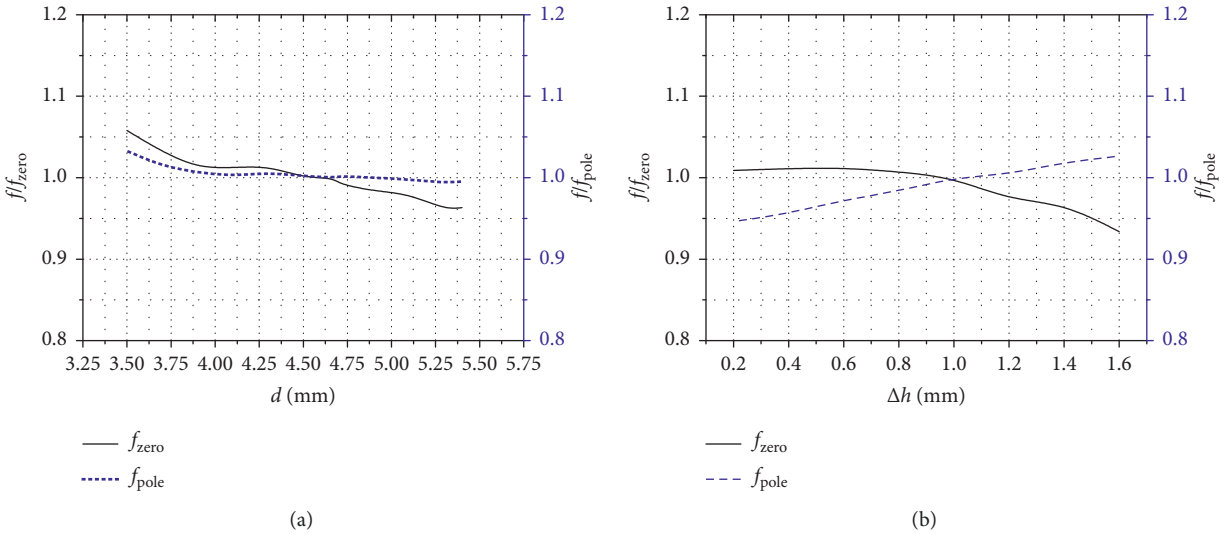

Figure 4: Continued.

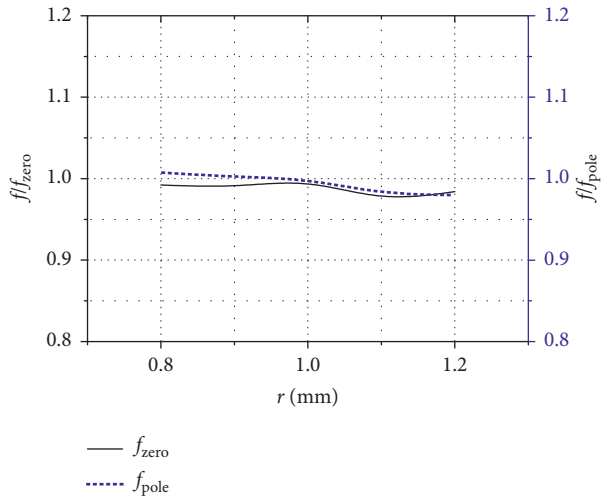

(c)

Figure 4: Dual-post resonator design curves example. Transmission zero and pole frequencies as a function of (a) the resonator distance for $r_1 = 1$ mm, $h_1 = 1.4$ mm, and $h_2 = 2.4$ mm; (b) resonator height difference for $r_1 = 1$ mm and $d = 4.67$ mm; and (c) resonator radii for $d = 4.67$ mm, $h_1 = 1.4$ mm, and $h_2 = 2.4$ mm.

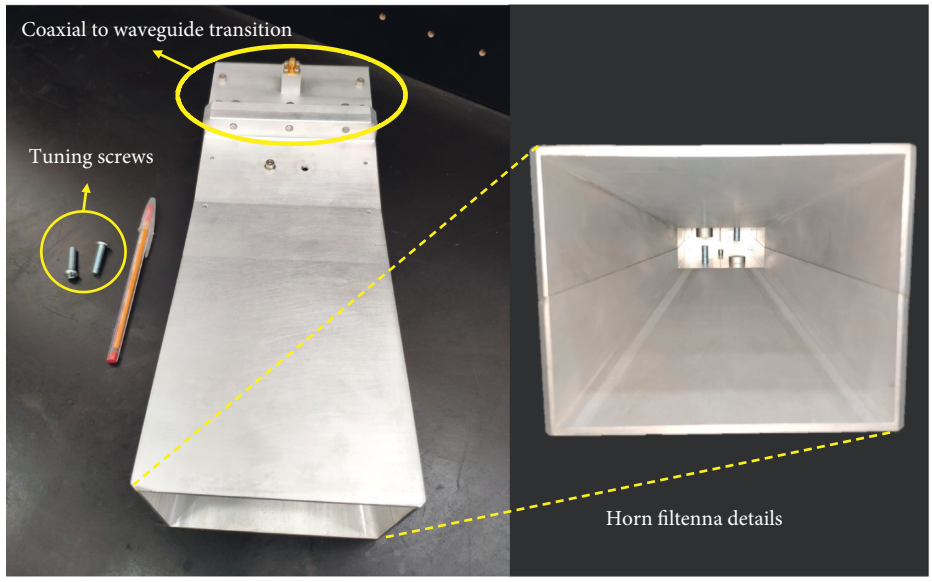

Figure 5: Microwave horn filtenna prototype.

product engineering; and manufacture. Numerical sweeps of the filtenna design variables have been performed in ANSYS HFSS®, using the finite element method (FEM), for making its bandwidth reconfigurable without disturbing its radiation pattern. Posteriorly, the antenna model has been modified in product engineering using SolidWorks®, giving rise to a mechanical model suitable for prototyping using the milling aluminum process. For electromagnetic validation purposes of the mechanical model, it has exported from SolidWorks®, imported in HFSS®, and resimulated. Finally, the manufacturing has been realized using the final CAD model, exported from HFSS®.

The filtenna radiator is a pyramidal horn antenna with the same half-power beamwidth (HPBW) in the electrical (E) and magnetic (H) field planes. Figure 1(a) displays its design variables: a and b are the waveguide cross-sectional dimension; l_g is the waveguide section length; a_c and b_c are the horn aperture dimensions; and l_c is the horn longitudinal length.

The bandpass filter has been placed into the waveguide section between the horn and feeder, without increasing the overall size. The available waveguide section length l_g is less than one guided wavelength at the desired central frequency. Filter topologies such as inductively coupled rectangular waveguide filters, E-plane metal insert filters, and evanescent mode waveguide filters have standard structures consisting of several cavities with overall longitudinal length equal or greater than a guided wavelength, which makes them infeasible to this application [26]. On the other side, multimode and dual-post resonator (DPR) filters provide

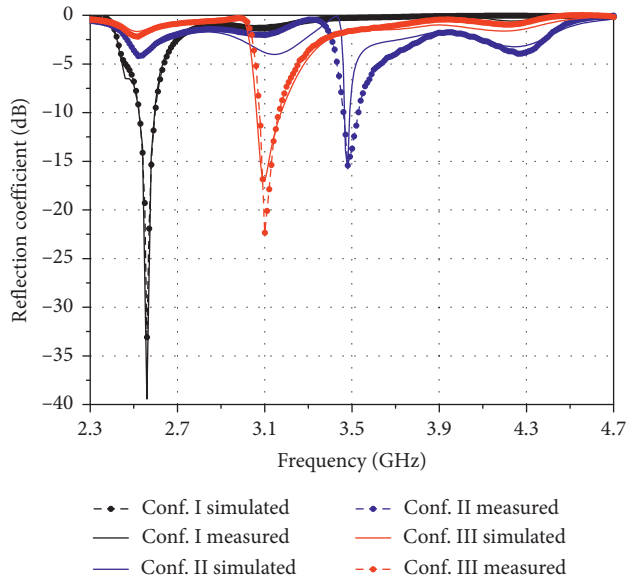

FIGURE 6: Microwave horn filtenna reflection coefficient. Conf. I ($d_1 = 17.70$ mm and $d_2 = 19.96$ mm) centered at 2.56 GHz; Conf. II ($d_1 = 19.0$ mm and $d_2 = 12.3$ mm) centered at 3.1 GHz; and Conf. III ($d_1 = 13.0$ mm and $d_2 = 13.5$ mm) centered at 3.5 GHz.

compact structures [27–29]. Multimode filters enable multiple resonance frequencies. Its design modifies the waveguide cross-sectional dimensions in order to allow supporting the dominant mode in the vertical and horizontal polarizations for decreasing its longitudinal length [28]. A DPR filter does not change the waveguide main dimensions and is highly selective, easily tunable, and works as inductive obstacles, which are commonly used in conventional waveguide filters. In addition, it is a singlet structure, i.e., with a reflection and a transmission zero at a real frequency [29]. For all these reasons, the DPR approach has been applied to the horn filtenna design.

The DPR filter is a single pole structure composed of two partial-height antipodal metal posts with different lengths and symmetrically located along the waveguide transverse section, as depicted in Figure 2(a). The antipodal position provides a higher difference between the resonant and nonresonant modes than the parallel position, as well as a higher quality factor (Q) [30]. In addition, the different post lengths excite the filter resonant mode without extra coupling sections, reducing the filter overall dimension and complexity [29]. The nonresonant mode defines a resonant frequency away from the filter passband, which might be propagation or an evanescent mode that bypasses the resonant mode [28]. This additional path between the filter input and output ports is used to create a transmission zero in the vicinity of the passband and increase its selectivity. Figure 2(b) presents the filter singlet schematic, in which the TE_{20} is the DPR filter resonant mode, whereas the nonresonant mode is the TE_{10} fundamental mode. TE_{20} generates the filter pole and is coupled to the filter input and output by the coupling coefficients k_{S1} and k_{L1}, respectively. The DPR equivalent circuit is based on inductive obstacles for waveguides [31, 32], as presented in Figure 2(c). The shunt and series elements reactance change from capacitive to inductive, as a function of the DPR height and frequency. Lastly, TE_{10} gives rise to a transmission zero located below the resonant mode pole, representing a direct coupling between input and output ports, by a coupling coefficient k_{SL}. The DPR might also be treated as inverter admittance in the filter passband [29]. This approach is commonly used in microwave filters design, with the purpose of allowing a common resonator type for the entire structure [33]. Figure 2(d) shows the dual-post resonator and tuning screws variables, in which h_1 and h_2 are the filter resonator lengths; d is the separation between the post resonators; d_1 and d_2 are the tuning screw lengths; and r_1 and r_2 are the resonator and screw radii, respectively. The metal screws have been inserted into the filter cavity to mechanically tuning the horn filtenna frequency response. The screws have different lengths in order to produce similar loading capacitance, since dual-post resonators have different heights.

The simulated DPR reactance for a WR-42 rectangular waveguide is presented in Figure 3 for $r_1 = 1$ mm, $d = 4.67$ mm, $h_1 = 1.4$ mm, and $h_2 = 2.4$ mm. The shunt and series elements reactance had been defined as shown in Figure 2(c) and calculated by S-parameters [34]. According to Figure 3, when the shunt element reactance reaches zero, the filter transmission zero frequency (f_{zero}) is obtained. Complementarily, when the series element reactance reaches zero, the filter pole frequency (f_{pole}) is determined. As a filter design methodology [24, 29, 34], we have varied the DPR filter design parameters r_1, d, and $\Delta h = h_2 - h_1$ for illustrating their impact on the transmission zero and pole frequencies. The DPR design curves are reported in Figure 4, including the normalized transmission zero and pole frequencies. First, the DPR transmission zero frequency is inversely proportional to resonators separation distance d, as reported in Figure 4(a). The pole frequency is practically insensitive to the resonator separation distance; only for small values of d, the pole frequency slightly increases. Figure 4(b) presents the DPR frequency response as a function of the resonator

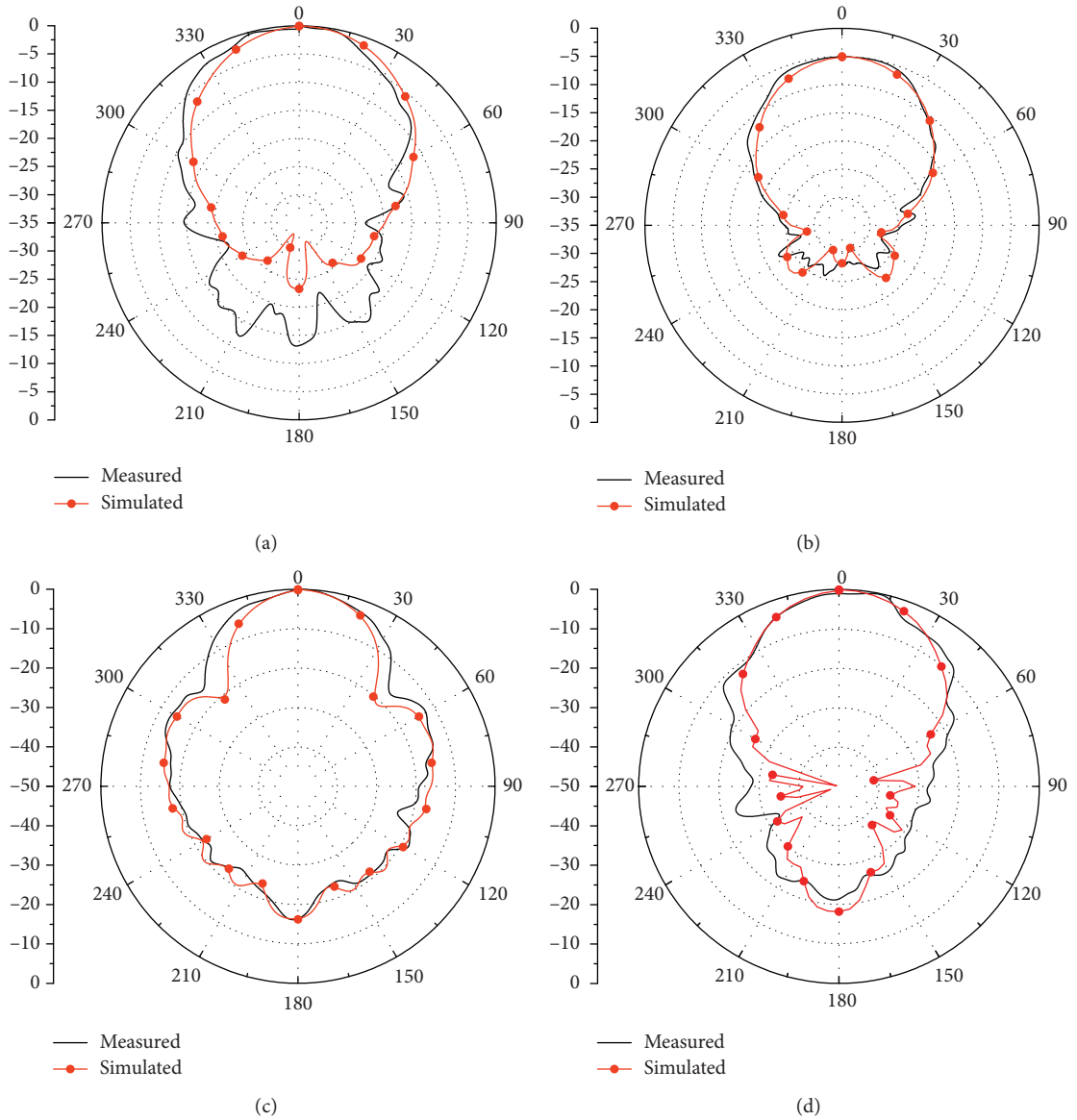

Figure 7: Microwave horn filtenna radiation pattern. (a) *E*-plane at 2.56 GHz. (b) *H*-plane at 2.56 GHz. (c) *E*-plane at 3.50 GHz. (d) *H*-plane at 3.50 GHz.

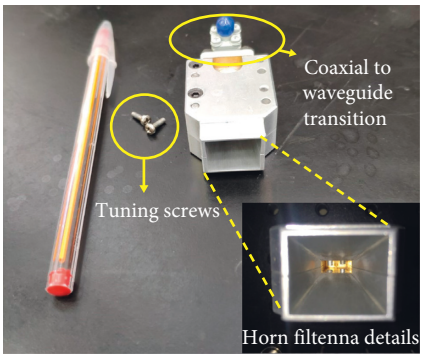

Figure 8: Millimeter-wave horn filtenna prototype.

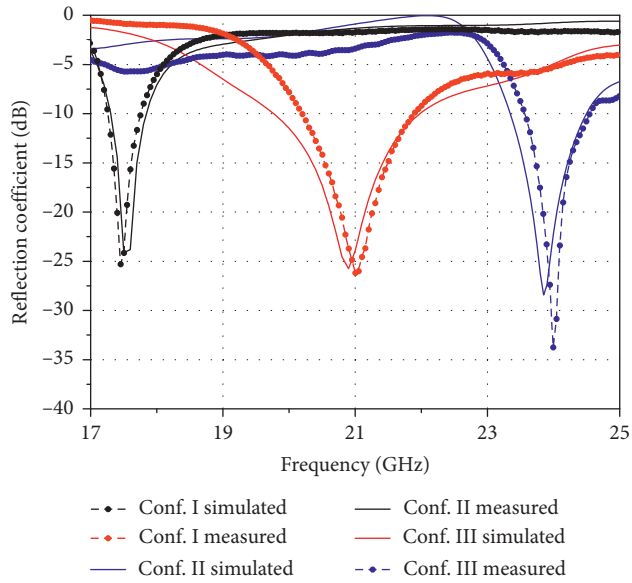

Figure 9: Millimeter-wave horn filtenna reflection coefficient. Conf. I ($d_1 = 2.55$ mm and $d_2 = 0$ mm) centered at 17.4 GHz; Conf. II ($d_1 = 0.85$ mm and $d_2 = 1.8$ mm) centered at 21 GHz; Conf. III ($d_1 = 0.5$ mm and $d_2 = 1$ mm) centered at 24 GHz.

height difference. This parameter is directly proportional to the pole frequency and controls the DPR filter passband. The transmission zero frequency is stable for small values of Δh and starts to decrease after the 1 mm threshold. Finally, the results for resonators radii variation are presented in Figure 4(c). The transmission zero and pole frequencies have small dependence on the resonator radii, for this reason cannot be used as a tuning parameter. In short, d is used to control the transmission zero frequency, whereas the pole frequency is controlled by Δh. The resonator radii might be defined according to the manufacturing process constraints. As a conclusion, DPR filters can be efficiently designed by applying the presented circuital model and design curves, since no closed formulas have been obtained for its structure yet.

3. Horn Filtennas Results

This section reports the numerical and experimental results of the two proposed filtennas, namely, microwave horn filtenna and millimeter-wave horn filtenna.

3.1. Microwave Horn Filtenna. For the microwave horn filtenna, a noncommercial waveguide ($a = 66$ mm and $b = 30$ mm) has been designed in order to cover the frequency range from 2.56 to 3.50 GHz with single mode operation (TE_{10}). The horn filtenna final dimensions were $a_c = 127.65$ mm, $b_c = 98.3$ mm, and $l_c = 212.73$ mm. The waveguide section between the feeder and radiator with length equal to $l_g = 80$ mm has been used to design the DPR filter. The resonators were positioned in the waveguide center, separated by a distance $d = 27$ mm and with a radius equal to 7.0 mm. By considering the desired range from 2.56 to 3.50 GHz, the resonators lengths $h_1 = 5.1$ mm and $h_2 = 9.1$ mm were obtained by numerical sweep in ANSYS HFSS. A few interactions between HFSS and SolidWorks have been done to obtain a suitable and feasible filtenna mechanical model. Figure 5 reports the resultant prototype made in aluminum.

A waveguide to coaxial transition has also been developed to facilitate its connection to RF components and pieces of equipment. The filtenna characterization starts from reflections (S_{11}) measurements, using the Keysight PNA Network Analyzer N5224A for different screw depths. The filtenna operating frequency could be continuously tuned from 2.56 to 3.50 GHz by appropriately tightening the tuning screws. Figure 6 presents the reflection coefficient response for the initial, central, and final frequencies for both simulations and measurements. The filtenna operating modes have been defined as Conf. I ($d_1 = 17.70$ mm and $d_2 = 19.96$ mm); Conf. II ($d_1 = 19.0$ mm and $d_2 = 12.3$ mm); and Conf. III ($d_1 = 13.0$ mm and $d_2 = 13.5$ mm). The filtenna bandwidth can be managed by manipulating d_1 and d_2, since the loading capacitance is proportional to the screws' depths. An excellent agreement is observed between the measured and simulated results for the three operating modes. The measured filtenna central frequency and fractional bandwidth (FBW) were 2.56 GHz and 2.7% for Conf. I; 3.10 GHz and 2.8% for Conf. II; and 3.50 GHz and 2% for Conf. III. The microwave horn filtenna tuning ratio was approximately 1.36, which is higher than most of the tunable filtenna reported in the literature [13–15] that are typically based on microstrip antennas. Additionally, the main advantage of our approach is the remarkable possibilities of continuously tuning the bandwidth due to use of dual-post resonator structure.

The filtenna radiation pattern and gain measurements were performed using a standard log-periodic antenna as a reference antenna, positioned 7 m away. Both antennas were mounted on masts at 1.8 m. Radiation pattern measurements has been carried out at 2.56

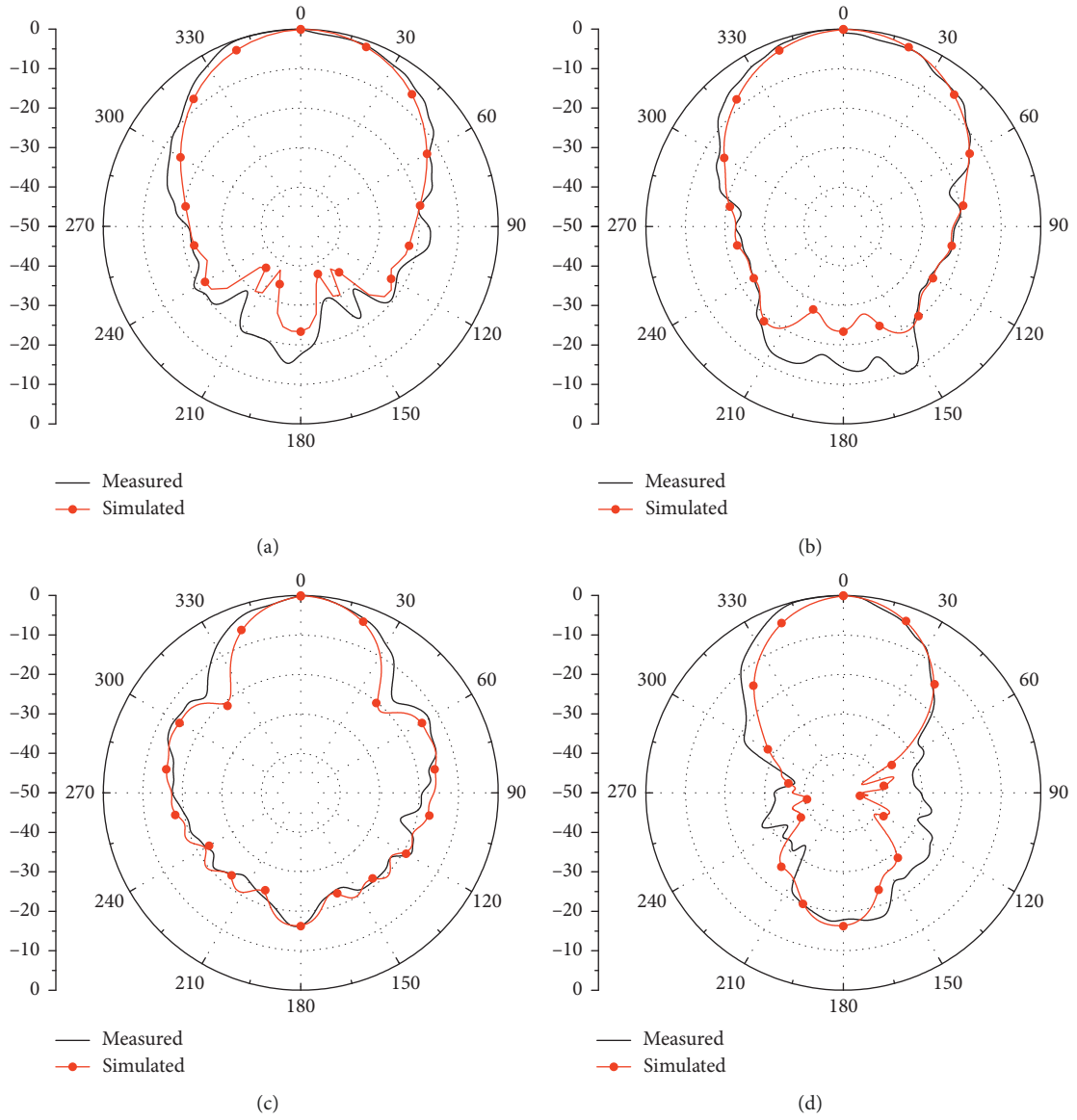

Figure 10: Millimeter-wave horn antenna radiation pattern. (a) E-plane at 17.5 GHz. (b) H-plane at 17.5 GHz. (c) E-plane at 24 GHz. (d) H-plane at 24 GHz.

and 3.50 GHz for E-plane and H-plane, as summarized in Figure 7. A discrepancy at 2.56 GHz in the front-back region for E-plane is observed in Figure 7(a). Regarding the main lobe, the measured and simulated results have consistently been shown for all frequencies and planes. The measured peak gain was 8 dBi at 2.56 GHz and 10 dBi at 3.50 GHz.

3.2. Millimeter-Wave Horn Filtenna. A standard waveguide WR-42 (10.67 mm × 4.3 mm) has been used for the mm-wave horn filtenna and its final dimensions were $a_c = 19.88$ mm, $b_c = 15.46$ mm, and $l_c = 33.13$ mm. Following the same design procedure adopted for the microwave horn filtenna, the waveguide section between the feeder and radiator ($l_g = 12$ mm) has been used for allocating the DPR filter. The 2 mm diameter resonators were positioned in the waveguide center with a separation distance of 4.67 mm. The resonator heights are $h_1 = 1.4$ mm and $h_2 = 2.4$ mm from 17.4 to 24.0 GHz. Figure 8 presents the mm-wave filtenna prototype, manufactured by milling process in aluminum.

The filtenna reflection coefficient has been measured using a Keysight PNA Network Analyzer N5224A and a commercial waveguide to coaxial transition. The measured results are presented in Figure 9 for the initial, central, and final frequency, from 17.4 to 24.0 GHz. Once again, the filtenna bandwidth could be continuously tuned over a wide frequency range. The measured and simulated results presented in Figure 9 corroborate with the proposed horn filtenna design procedure. The filtenna measured operating modes according to screws positions are Conf. I ($d_1 = 2.55$ mm and $d_2 = 0$ mm) centered at 17.4 GHz with 2.8% FBW; Conf. II ($d_1 = 0.85$ mm and

(a) (b)

Figure 11: Implementation of the mm-wave tunable horn filtenna at 24.7 GHz. (a) Transmission side and (b) reception side.

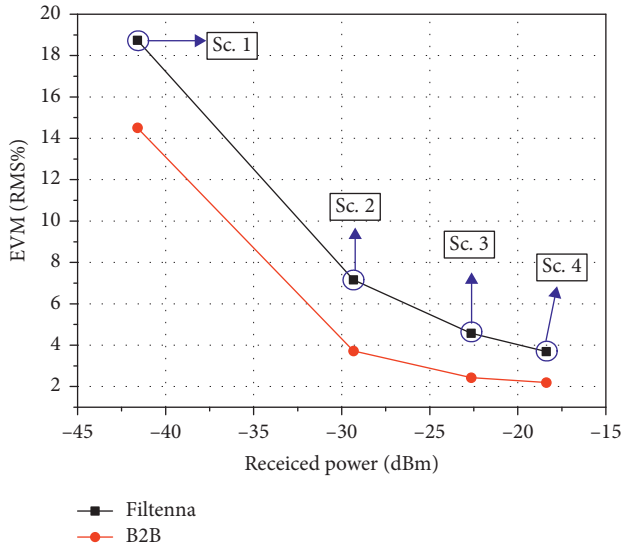

Figure 12: EVM as a function of the received power for four different scenarios.

$d_2 = 1.8$ mm) centered at 21 GHz with 7.9% FBW; and Conf. III ($d_1 = 0.5$ mm and $d_2 = 1$ mm) centered at 24 GHz with 4.11% FBW. The millimeter-wave horn filtenna tuning ratio is approximately 1.37 with FBW from 2.8 to 7.9%.

Radiation pattern measurements have been carried out at 17.5 and 24 GHz for the *E*-plane and *H*-plane, as summarized in Figure 10. A good qualitative agreement is observed for all cases, mainly for the half-power beamwidth. The main difference is related to the back lobe for the *H*-plane at 17.5 GHz. Its measured peak gain was 8.5 dBi and 12.3 dBi at 17.5 and 24.0 GHz, respectively.

4. Implementation of the Millimeter-Wave Tunable Horn Filtenna

Our main objective was demonstrating its applicability in radio cognitive, in which operating bandwidth can be dynamically allocated as a function of the opportunistic scenario of primary/secondary users. Figure 11 displays photographs of the indoor environments used for the implementation. At the transmission side, a vector signal generator (VSG) provides a 16-QAM of 800 Mb/s signal at 24.7 GHz. The RF power transmission was 1 dBm, and an electrical amplifier (EA) with 23 dB gain was applied in order to increase the effectively radiated power by the filtenna. The transmission antenna was a 20 dBi gain horn antenna. The free-space loss, calculated by the Friis equation, was approximately 55.8 dB at 24.7 GHz for 5 meters. The received side was composed by the mm-wave filtenna followed by a low-noise amplifier and a vector signal analyzer (VSA).

Figure 12 reports the experimental results of the root mean square error vector magnitude (EVM_{RMS}) as a function of the received power. In accordance with 3GPP (http://www.3GPP.org), EVM_{RMS} for 16-QAM modulation should not exceed 12.5% [35]. For comparison purposes, the red curve depicts a back-to-back (B2B) condition by directly connecting VSG to VSA. In other words, there was no wireless transmission for the B2B scenario. The black curve with squares represents the wireless transmission for four different scenarios (Sc.) based on the screw depth position. Sc. 1 was the worst case, for which the filtenna does not provide a suitable impedance matching at the chosen frequency with these screw depths configuration; thus, the constellation has been shown poor, giving rise to EVM_{RMS} of 18.47%. As soon as the screw depths were modified, the system performance has been significantly improved,

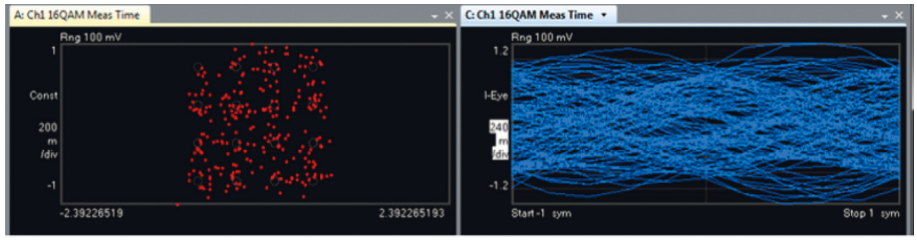

(a)

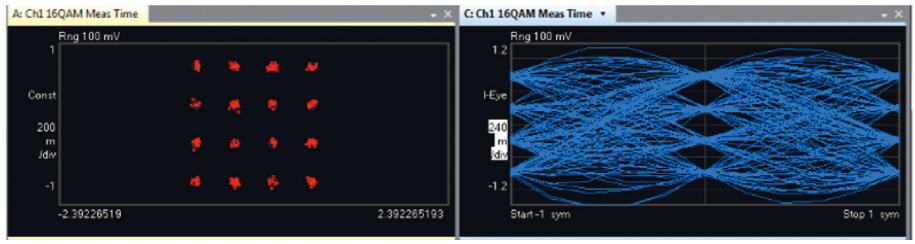

(b)

Figure 13: Experimental performance investigation at 24.7 GHz with 800 Mbit/s throughput. (a) Scenario 1 and (b) Scenario 4.

Table 1: Experimental characterization of the proposed filtenna for four configurations.

Scenario	Screw depth (mm)	S_{11} (dB)	Radiation efficiency (%)	Received power (dBm)	EVM (RMS%)	SNR (dB)
Sc. 1	$d_1 = 1.2$ $d_2 = 1.8$	−1	18.25	−41.64	18.47	11.54
Sc. 2	$d_1 = 0.8$ $d_2 = 1.4$	−7	73.86	−29.32	7.155	24.17
Sc. 3	$d_1 = 0.6$ $d_2 = 1.2$	−15	87.16	−22.64	4.58	20.31
Sc. 4	$d_1 = 0.5$ $d_2 = 1$	−20	97.8	−18.46	3.69	11.54

resulting EVM_{RMS} and power received of 3.69% and −18.46 dBm, respectively. Additionally, Figure 13(a) and Figure 13(b) depict the experimental performance results at 800 Mbit/s RF signal in terms of the constellation and eye diagram for Sc. 1 and Sc. 4, respectively.

As explained and demonstrated in the previous section, the filtenna bandwidth can be efficiently managed by optimizing the screws depths of the DPR filter. Its reflection coefficient at 24.7 GHz varies from −1 to −20 dB, deepening on the screw depths. Accordingly, the filtenna radiation efficiency alters from 18 to 97%. Table 1 summarizes the experimental results scenarios. These experimental results demonstrate the applicability of the proposed tunable horn filtenna for radio cognitive in the mm-wave.

5. Conclusions

This paper reported the development of two high-performance continuously frequency-tunable horn filtennas for microwave and mm-waves. Both filtennas are based on the integration of a broadband horn antenna with a dual-post resonator filter for enabling mechanical reconfiguration of their bandwidth. Numerical simulations and experimental results have been shown in excellent agreement, and a tuning ratio of 1.36 and 1.37 for the lower-frequency (from 2.56 to 3.5 GHz) and higher-frequency (from 17.4 to 24 GHz) filtennas has been reported, respectively. Additionally, the mm-wave horn filtenna has been implemented in a high-throughput indoor wireless system at 800 Mbps with line of sight. The experimental analysis as a function of diverse performance metrics (constellation, eye diagram, EVM, and SNR) has successfully demonstrated the applicability of the proposed filtenna in cognitive radio applications, for instance, mm-wave 5G systems. It has been obtained a measured EVM_{RMS} as low as 3.69%, which is far below the 3GPP requirement of 12.5% for 16-QAM. Future works regard the implementation of either microwave and mm-wave filtenna in a real 5G network based on the use of the Brazilian 5G transceiver, which has been previously developed by our research group [36].

Data Availability

No data were used to support this study.

Conflicts of Interest

The authors declare that are no conflicts of interest regarding the publication of this paper.

Acknowledgments

This work was partially supported by RNP, with resources from MCTIC, Grant no. 01250.075413/2018-04, under the Radiocommunication Reference Center (Centro de Referência em Radiocomunicações—CRR) project of the National Institute of Telecommunications (Instituto Nacional de Telecomunicações—Inatel),

Brazil. The authors also thank the financial support from CNPq, CAPES, FINEP, and FAPEMIG.

References

[1] G. Liu and D. Jiang, "5G: vision and requirements for mobile communication system towards year 2020," *Chinese Journal of Engineering*, vol. 2016, Article ID 5974586, 8 pages, 2016.

[2] G. Kalfas, C. Vagionas, A. Antonopoulos et al., "Next generation fiber-wireless fronthaul for 5G mm wave networks," *IEEE Communications Magazine*, vol. 57, no. 3, pp. 138–144, 2019.

[3] P. Masek, E. Mokrov, K. Zeman et al., "A practical perspective on 5G-ready highly dynamic spectrum management with LSA," *Wireless Communications and Mobile Computing*, vol. 2018, Article ID 2103868, 10 pages, 2018.

[4] A. Roy, S. Sengupta, K.-K. Wong, V. Raychoudhury, K. Govindan, and S. Singh, "5G wireless with cognitive radio and massive IoT"," *IETE Technical Review*, vol. 34, no. 1, pp. 1–3, 2017.

[5] K. Xiao, W. Li, M. Kadoch, and C. Li, "On the secrecy capacity of 5G mm wave small cell networks," *IEEE Wireless Communications*, vol. 25, no. 4, pp. 47–51, 2018.

[6] M. S. Omar, M. A. Anjum, S. A. Hassan, H. Pervaiz, and Q. Niv, "Performance analysis of hybrid 5G cellular networks exploiting mm wave capabilities in suburban areas," in *Proceedings of the 2016 IEEE International Conference on Communications (ICC)*, pp. 1–6, Kuala Lumpur, Malaysia, May 2016.

[7] G. Ghatak, A. De Domenico, and M. Coupechoux, "Coverage analysis and load balancing in HetNets with millimeter wave multi-RAT small cells," *IEEE Transactions on Wireless Communications*, vol. 17, no. 5, pp. 3154–3169, 2018.

[8] J. T. Bernhard, "Reconfigurable antennas," in *Encyclopedia of RF and Microwave Engineering*, K. Chang, Ed., Wiley, New York, NY, USA, 2005.

[9] I. F. da Costa, D. H. Spadoti, A. C. Sodré Jr. et al., "Optically controlled reconfigurable antenna for 5G future broadband cellular communication networks," *Journal of Microwaves, Optoelectronics and Electromagnetic Applications*, vol. 16, no. 1, pp. 208–217, 2017.

[10] A. Boukarkar, X. Q. Lin, Y. Jiang, Y. J. Chen, L. Y. Nie, and P. Mei, "Compact mechanically frequency and pattern reconfigurable patch antenna," *IET Microwaves, Antennas & Propagation*, vol. 12, no. 11, pp. 1864–1869, 2018.

[11] L. Safatly, M. Bkassiny, M. Al-Husseini, and A. El-Hajj, "Cognitive radio transceivers: RF, spectrum sensing, and learning algorithms review," *International Journal of Antennas and Propagation*, vol. 2014, Article ID 548473, 21 pages, 2014.

[12] J. Kelly, E. Ebrahimi, P. S. Hall, P. Gardner, and F. Ghanem, "Combined wideband and narrowband antennas for cognitive radio applications," in *Proceedings of the IET seminar on Cognitive Radio and Software Defined Radios: Technologies and Techniques*, London, UK, September 2008.

[13] M. Zamudio, Y. Tawk, J. Costantine, J. Kim, and C. G. Christodoulou, "Integrated cognitive radio antenna using reconfigurable band pass filters," in *Proceedings of the 5th European Conference on Antennas and Propagation (EUCAP)*, pp. 2108–2112, Rome, Italy, April 2011.

[14] M. Al-Husseini, A. Ramadan, M. E. Zamudio, C. G. Christodoulou, A. El-Hajj, and K. Y. Kabalan, "A UWB antenna combined with a reconfigurable bandpass filter for cognitive radio applications," in *Proceedings of the 2011 IEEE-APS Topical Conference on Antennas and Propagation in Wireless Communications*, pp. 902–904, Torino, Italy, September 2011.

[15] Y. Tawk, J. Costantine, and C. G. Christodoulou, "A varactor-based reconfigurable filtenna," *IEEE Antennas and Wireless Propagation Letters*, vol. 11, pp. 716–719, 2012.

[16] L. G. Silva, A. A. C. Alves, and A. C. Sodré Jr., "Optically controlled reconfigurable filtenna," *International Journal of Antennas and Propagation*, vol. 2016, Article ID 7161070, 9 pages, 2016.

[17] G. Q. Luo, W. Hong, H. J. Tang et al., "Filtenna consisting of horn antenna and substrate integrated waveguide cavity FSS," *IEEE Transactions on Antennas and Propagation*, vol. 55, no. 1, pp. 92–98, 2007.

[18] F. Bilotti, L. Di Palma, D. Ramaccia, and A. Toscano, "Self-filtering low-noise horn antenna for satellite applications," *IEEE Antennas and Wireless Propagation Letters*, vol. 11, pp. 354–357, 2012.

[19] D. Ramaccia, L. Di Palma, D. Ates, E. Ozbay, A. Toscano, and F. Bilotti, "Analytical model of connected Bi-omega: robust particle for the selective power transmission through sub-wavelength apertures," *IEEE Transactions on Antennas and Propagation*, vol. 62, no. 4, pp. 2093–2101, 2014.

[20] M. Barbuto, F. Trotta, F. Bilotti, and A. Toscano, "A combined bandpass filter and polarization transformer for horn antennas," *IEEE Antennas and Wireless Propagation Letters*, vol. 12, pp. 1065–1068, 2013.

[21] X. Ma, C. Huang, W. Pan, B. Zhao, J. Cui, and X. Luo, "A dual circularly polarized horn antenna in Ku-band based on chiral metamaterial," *IEEE Transactions on Antennas and Propagation*, vol. 62, no. 4, pp. 2307–2311, 2014.

[22] M. Barbuto, F. Trotta, F. Bilotti, and A. Toscano, "Varying the operation bandwidth of metamaterial-inspired filtering modules for horn antennas," *Progress in Electromagnetics Research C*, vol. 58, pp. 61–68, 2015.

[23] Z. Wang, P. S. Hall, J. R. Kelly, and P. Gardner, "Wideband frequency-domain and space-domain pattern reconfigurable circular antenna array," *IEEE Transactions on Antennas and Propagation*, vol. 65, no. 10, pp. 5179–5189, 2017.

[24] A. A. C. Alves, L. G. da Silva, E. C. V. Boas, D. H. Spadoti, and A. C. Sodré Jr., "Mechanically tunable horn filtenna for mm-waves," in *Proceedings of EUCAP 2019 European Conference on Antennas and Propagation*, Krakow, Poland, March–April 2019.

[25] WRC-15 documents and proposals, 2015, https://www.itu.int/en/ITU-R/conferences/wrc/2015/Pages/docsandprops.aspx.

[26] V. Boria and B. Gimeno, "Waveguide filters for satellites," *IEEE Microwave Magazine*, vol. 8, no. 5, pp. 60–70, 2007.

[27] S. Amari and U. Rosenberg, "Characteristics of cross (bypass) coupling through higher/lower order modes and their applications in elliptic filter design," *IEEE Transactions on Microwave Theory and Techniques*, vol. 53, no. 10, pp. 3135–3141, 2005.

[28] S. Bastioli, "Nonresonating mode waveguide filters," *IEEE Microwave Magazine*, vol. 12, no. 6, pp. 77–86, 2011.

[29] C. Tomassoni and R. Sorrentino, "A new class of pseudoelliptic waveguide filters using dual-post resonators," *IEEE Transactions on Microwave Theory and Techniques*, vol. 61, no. 6, pp. 2332–2339, 2013.

[30] C. Tomassoni and R. Sorrentino, "A new class of pseudo-elliptic waveguide filters using resonant posts," in *Proceedings of the IEEE/MTT-S International Microwave Symposium Digest*, pp. 1–3, Montreal, Canada, June 2012.

[31] P. Guan, A. T. Adams, Y. Leviatan, and J. Perini, Multiple-post inductive obstacles in rectangular waveguide," *IEEE*

Transactions on Microwave Theory and Techniques, vol. 32, no. 4, pp. 365–373, 1984.

[32] N. Marcuvitz, "Waveguide handbook," in *IET Electromagnetic Waves Series*, vol. 21, pp. 257–273, McGraw-Hill, New York, NY, USA, 1986.

[33] G. L. Matthaei, L. Young, and E. M. T. Jones, *Microwave Filters, Impedance-Matching Networks and Coupling Structures*, McGraw-Hill, New York, NY, USA, 1964.

[34] U. Rosenberg and S. Amari, "A novel band-reject element for pseudoelliptic bandstop filters," *IEEE Transactions on Microwave Theory and Techniques*, vol. 55, no. 4, pp. 742–746, 2007.

[35] 3rd Generation Partnership Project; Technical Specification Group Radio Access Network; NR; User Equipment (UE) Radio Transmission and Reception; Part 1: Range 1 Standalone (release 15), 3GPP TS 38.101-1 V15.5.0, 2019.

[36] R. M. Borges, T. R. R. Marins, M. S. B. Cunha et al., "Integration of a GFDM-based 5G transceiver in a GPON using radio over fiber technology," *Journal of Lightwave Technology*, vol. 36, no. 19, pp. 4468–4477, 2018.

Hindawi
International Journal of Antennas and Propagation
Volume 2019, Article ID 5425703, 13 pages
https://doi.org/10.1155/2019/5425703

Research Article

Vehicular Channel in Urban Environments at 23 GHz for Flexible Access Common Spectrum Application

Longhe Wang,[1,2] **Bo Ai**,[1,2] **Jingya Yang**,[1,2] **Hao Qiu**,[1,2] **Wanqiao Wang**,[1,2] **and Ke Guan**[1,2]

[1]*State Key Laboratory of Rail Traffic Control and Safety, Beijing Jiaotong University, Beijing 100044, China*
[2]*Beijing Engineering Research Center of High-Speed Railway Broadband Mobile Communications, Beijing 100044, China*

Correspondence should be addressed to Bo Ai; boai@bjtu.edu.cn

Received 3 May 2019; Accepted 30 July 2019; Published 12 September 2019

Guest Editor: Marko Sonkki

With the development of the vehicular network, new radio technologies have been in the spotlight for maximizing the utilization of the limited radio spectrum resource while accommodating the increasing amount of services and applications in the wireless mobile networks. New spectrum policies based on dynamic spectrum access technology such as flexible access common spectrum (FACS) have been adopted by the Korea Communications Commission (KCC). 23 GHz bands have been allocated to FACS bands by the KCC, which is expected extensively for vehicular communications. The comprehensive knowledge on the radio channel is essential to effectively support the design, simulation, and development of such radio technologies. In this paper, the characteristics of 23 GHz vehicle-to-infrastructure (V2I) channels are simulated and extracted for the urban environment in Seoul. The path loss, shadow factor, Ricean *K*-factor, root-mean-square (RMS) delay spread, and angular spreads are characterized from the calibrated ray-tracing simulation results, and it can help researchers have a better understanding of the propagation channel for designing vehicular radio technologies and a communication system in a similar environment.

1. Introduction

Recently, flexible access common spectrum (FACS) has been considered to have an important role in accommodating the fast-growing spectrum demands in vehicular communications, which will ramp up the development of mobile and wireless vehicular communication technologies to advance safety and convenience on the roads [1, 2]. Among them, vehicle-to-infrastructure (V2I) robust connectivity is the key enabler for enhancing traffic safety, reliability, and efficiency [3, 4]. The channel characteristic is a critical role in the design and performance evaluation of V2I connectivity networks. For example, the realistic large-scale fading channel parameters are indispensable for efficient network deployment and optimization; the fidelity small-scale fading channel parameters are crucial in physical layer design, such as optimal modulation, coding, diversity, and protocol scheme development [5].

Most of the previous works on vehicular propagation channels are focused on the 5 GHz band, e.g., [6–16], which use the lower frequency band to increase the V2I and vehicle-to-vehicle (V2V) link ranges. In [6], based on the narrowband channel measurement at 5.2 GHz, the propagation loss (PL) parameters of the vehicular channel are studied under a highway and under urban, suburban, and village environments. In [7], a large number of vehicular narrowband channel measurements are carried out at 5.9 GHz. A dual-slope PL model is proposed for the suburban environment. Meanwhile, it is found that, in such an environment, the small-scale fading of the channel obeys the Nakagami distribution, and the effect of speed and relative distance of the transmitting and receiving vehicles on the Doppler spectrum and quasistationary time is discussed. Based on the wideband multi-input multioutput (MIMO) channel measurement at the 5.3 GHz band, the authors in [8, 9] discuss the nonstationary delay spread (DS) and small-

scale fading characteristics (following Ricean distribution) in vehicular channels. In [10], under a highway environment, the PL, delay distribution, and Doppler characteristics of the V2I channel are studied according to the MIMO channel measurement. Similarly, the dispersion of multipath components (MPCs) in delay and Doppler domains is analyzed for V2I channels under urban and rural environments, and the geometry of scatterers is also being constructed to illustrate the MPC distribution [11, 12]. Moreover, in [13], the authors present a three-dimensional (3D) distribution estimation of MPCs and discuss the power ratio of different propagation mechanisms associated with the actual propagation environment. The work in [14–16] describes the MPC dispersion in delay and angle domains for the non-line-of-sight (NLOS) environments and explores MPC distribution and its propagation mechanisms in different propagation environments. All of those important vehicular channel characteristics show that the vehicular channel exhibits severe fading and statistical nonstationarity. The propagation mechanisms and spatial distributions of MPCs are mainly determined by the vehicular propagation environment.

For the 20–60 GHz band, the studies in [17, 18] show that the large spectrum in a higher frequency band provides a possibility of high data rate, but the channel is much different from that in the 5 GHz band, and directional antennas are adopted by transceivers in such vehicular communication systems to overcome the heavy loss at those high frequencies [19, 20]. But the obvious limitation by using directional antennas for the higher frequency applications is the difficulty of providing an "always connected" V2I or V2V link. In [21], the two-ray channel model with random reflected paths is used to represent 60 GHz vehicular channel, and the system performance has been theoretically evaluated by varying modulation formats, coding complexity, and propagation characteristics for vehicular communications. The similar works in [22, 23] analyze the characteristics of MPC propagation and verify the availability of the vehicular communication system at 60 GHz. Based on channel measurement with rotating directional antennas, the DS, path loss exponent (PLE), and angular spread of arrival (ASA) are compared between line-of-sight (LOS) and NLOS conditions at 60 GHz under outdoor environments in [24, 25]. The channel impulse response and scattering functions, as well as the DS, are obtained from 38 GHz to 60 GHz channel measurements in [26]. Such measurements show that the MPC in the channel typically contains LOS, road reflection paths, and reflection paths from the guard rails. However, the two distinguishing features of vehicular channels at higher frequency bands, e.g., directionality and blockage, are not fully explored in the work, which are the significant challenge remaining in the design of such vehicular networks.

An overview of the previous work is to study the typical behavior of vehicle lanes, identifying missing features in currently available channel models to design and evaluate vehicle radio links in a safe and efficient environment.

In this paper, intensive simulations at the 23 GHz band with 1 GHz bandwidth in a realistic V2I urban environment are performed by a calibrated ray-tracing (RT) simulator to complement these missing characteristics, e.g., directionality and blockage. Besides, different road widths, traffic flows, vehicle types, antenna heights, and traffic signs are considered in the RT simulation to fully explore the V2I channel behaviors under different conditions. The time-varying power delay profile (PDP), path loss (PL), shadow factor, DS, Ricean K-factor, and angular spreads (ASs)—azimuth angular spread of arrival (ASA), azimuth angular spread of departure (ASD), elevation angular spread of arrival (ESA), and elevation angular spread of departure (ESD)—are analyzed and extracted from the simulation results. In addition, the propagation mechanism in different environments is analyzed that can illustrate the impact of the actual environment on the channel characteristics. Furthermore, the extracted parameters can be input to the channel generator, like QuaDRiGa or METIS, to generate similar channels, which can be used to evaluate or verify the performance of the system- or link-level design.

The rest of this paper is organized as follows: In Section 2, the realistic vehicular environments are reconstructed and introduced. In Section 3, extensive RT simulations are performed in all cases. Then, based on the RT results, the vehicular channels are comprehensively characterized in Section 4. Finally, the conclusions are drawn in Section 5.

2. Realistic Vehicular Moving Network Environments

In order to obtain realistic behavior of vehicular channels in the moving network (MN), the influence of vehicles must be considered in the propagation model [27, 28]. In this paper, to map the MN architecture defined by 3GPP TR 37.885 to the real propagation environments, the 3D models of a set of comprehensive vehicular environments are reconstructed.

2.1. Overview of Environments

2.1.1. Urban Environments. The 3D details of the considered environment are built by OpenStreetMap (OSM). OSM is a collaborative project to create a free editable map of the world, and in addition to street-level map information, it can provide 3D building information. In order to make it easier to access the OSM data, a plugin for SketchUp (3D modeling software) is developed in this work. The plugin can import both street and building information from OSM data. It is the open source software that can be obtained from http://www.raytracer.cloud/software. As shown in Figure 1, the typical urban area in Seoul is selected. This urban environment is universal and can represent most of the vehicular propagation environment in the urban area. In addition to OSM, KakaoMap, the Korean map software, is also used to reconstruct the real environment more completely, which has a 360-degree street view, and some landmark buildings such as cafes and restaurants will be specially marked. Combined with OpenStreetMap and KakaoMap, the urban environments in Seoul can be reconstructed by the SketchUp software, which is shown in Figure 2. Considering the

Figure 1: Seoul map from OpenStreetMap.

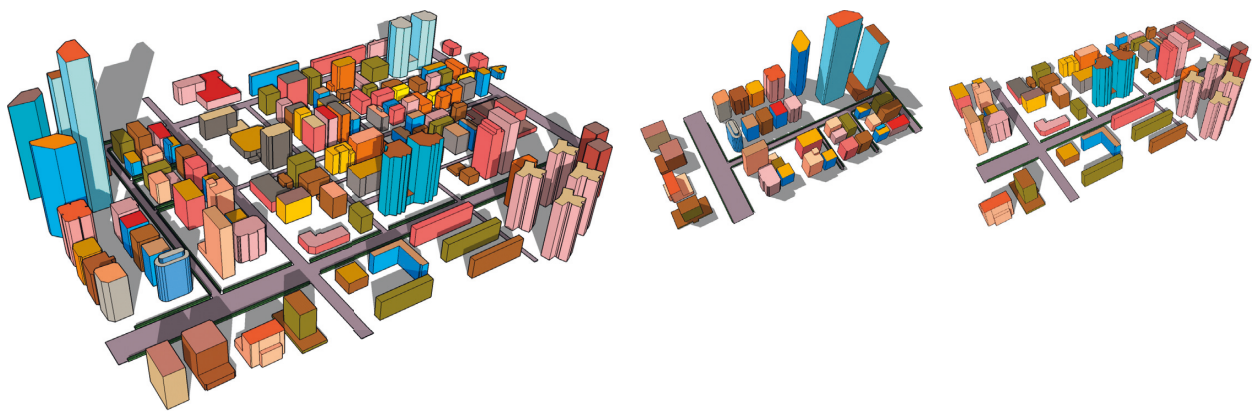

(a) (b) (c)

Figure 2: (a) 3D model of Seoul urban environment. (b) 3D model of Area 1. (c) 3D model of Area 2.

impact of different neighborhood environments on the vehicular channel, two typical urban streets in the city are selected as the simulation environments. As shown in Figure 1, the selected streets were marked with red lines on the maps. Figures 2(b) and 2(c) show the 3D environment models of these two areas. The difference between the two areas is the width of the road, characterized by the number of lanes.

2.1.2. Small-Scale Structures. In addition to the large buildings, the common small-scale structures such as roadside trees, traffic lights, traffic signs, and bus stations are considered in the environment model. These small-scale structures are on the same order of magnitude as the wavelength, and the most relevant propagation mechanism of them in vehicular environments is scattering [29]. Figure 3 shows the 3D models of small-scale structures in urban environments.

2.2. Vehicle Types and Mobility Modeling

2.2.1. Vehicle Types. In this work, three different vehicle types are selected by considering the recommendation by 3GPP TR 37.885 [30], which are defined as follows:

(i) Type 1 (passenger vehicle with a lower antenna position): length 5 m, width 2.0 m, height 1.6 m, and antenna height 0.75 m, as shown in Figure 4(a)

(ii) Type 2 (passenger vehicle with a higher antenna position): length 5 m, width 2.0 m, height 1.6 m, and antenna height 1.6 m, as shown in Figure 4(a)

(iii) Type 3 (truck/bus): length 13 m, width 2.6 m, height 3 m, and antenna height 3 m, as shown in Figure 4(b)

To more comprehensively reflect the impact of vehicle types on signal propagation, another type of vehicle is also considered:

(iv) Type 4 (delivery van): length 13.5 m, width 2.6 m, height 3.5 m, and antenna height 3.5 m, as shown in Figure 4(c)

2.2.2. Mobility Modeling. As per the recommendation by 3GPP TR 37.885, the vehicles are dropped for the urban environments according to the following process:

(i) The distance between the rear bumper of a vehicle and the front bumper of the following vehicle in the same lane follows an exponential distribution

(ii) All the vehicles in the same lane have the same speed

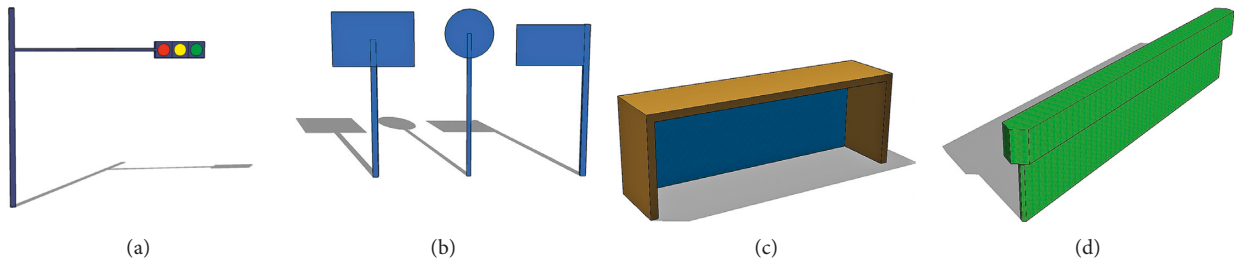

Figure 3: 3D models of small-scale structures. (a) Traffic light model. (b) Traffic sign model. (c) Bus station model. (d) Tree model.

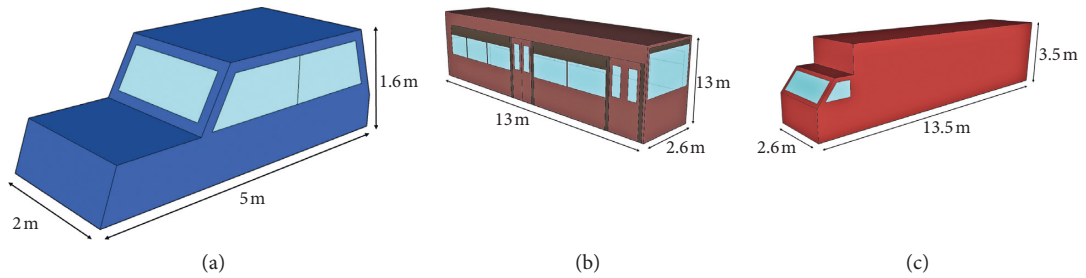

Figure 4: 3D models of different vehicle types. (a) Passenger car model. (b) Bus model. (c) Delivery van model.

(iii) Vehicle-type distribution is not dependent on the lane

In general, the width of the line is 3.5 m. In Area 1 (shown in Figure 2(b)), the road is with four lanes. Considering the traffic congestion in the actual environments, the speed and the direction of vehicles in each lane are shown in Figure 5. The width of the road in Area 2, as shown in Figure 2(c), is more extensive than that in Area 1, and the eight-lane road is designed in Area 2. The vehicle speed on such a road is shown in Figure 6. According to the recommendations of 3GPP TR 37.885, the distribution of vehicle types in the urban environment is determined:

(i) 60% Type 1 vehicles and Type 2 vehicles (passenger car)

(ii) 20% Type 3 vehicles (bus)

(iii) 20% Type 4 vehicles (delivery van)

The vehicles in each lane are randomly generated according to vehicle distribution. Vehicles do not change their direction at the intersection.

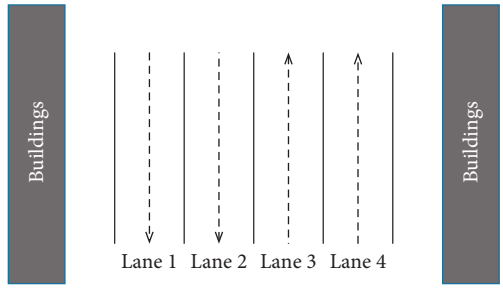

Lane	1	2	3	4
Speed (km/h)	15	25	15	25

Figure 5: Vehicle speed in the 4-lane road (Area 1).

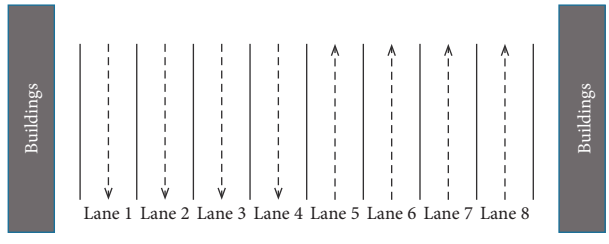

Lane	1	2	3	4	5	6	7	8
Speed (km/h)	15	25	50	60	15	25	50	60

Figure 6: Vehicle speed in the 8-lane road (Area 2).

2.3. Antenna Model. The antennas of the base station (BS) and the user equipment (UE) of the MN system defined are with the same antenna pattern [30], as shown in Figure 7. The locations and heights of the transmitter (Tx) at the BS and receiver (Rx) at the UE are given in Table 1. The settings follow the recommendations of 3GPP TR 37.885.

3. RT Simulations in Realistic Vehicular Scenarios

In this section, in order to characterize the 23 GHz vehicular channels, RT simulations with different antenna height setups are developed in different realistic environment cases. First, the calibration and verification of the RT simulator are discussed, and then the RT configuration and different propagation mechanisms caused by the surrounding environment in various environment cases are presented.

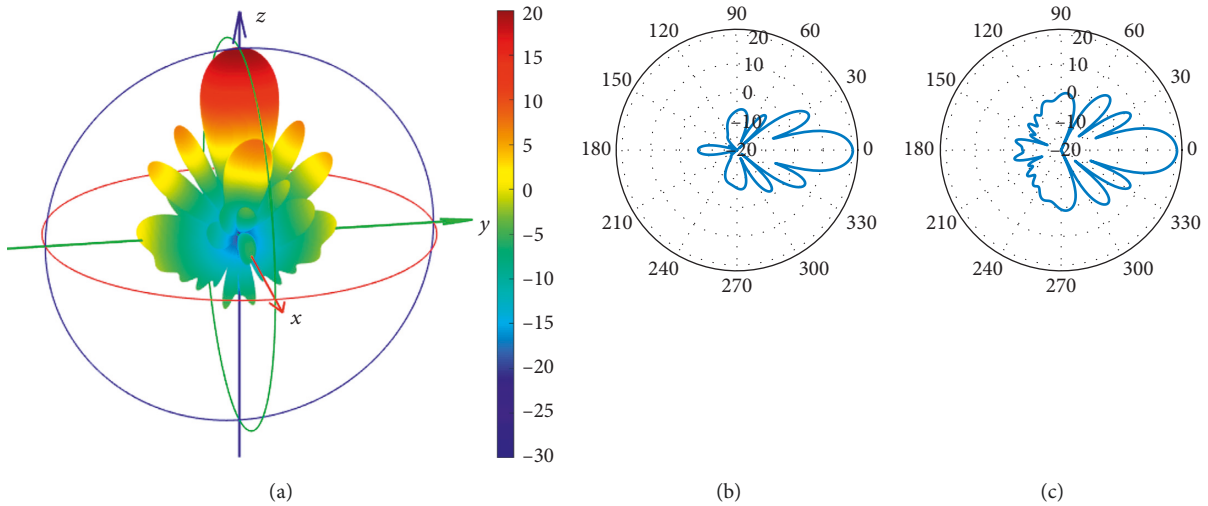

Figure 7: (a) 3D antenna pattern of the transceiver. (b) *E* plane. (c) *H* plane.

Table 1: Locations and heights of the Tx and Rx.

Parameters	Urban
BS antenna height	Top of the building: 25 m On the traffic light: 5 m
UE antenna height	Top of the bus: 3.2 m

3.1. RT Simulation Verification. According to realistic urban 3D maps and design specifications for urban infrastructure, the vehicular environment features, and typical small-scale structures is presented in the above section. Based on which, a large number of statistical consistent environment models can be generated to simulate urban vehicular channels. Before this, RT needs to be calibrated via propagation measurement, and then the intensive close-to-real channel simulations can be conducted with standard-defined configurations.

The validations of the RT simulator against various measurements have been presented in various propagation environments and different frequency bands. For example, RT is calibrated and verified in the tunnel environment at 25 GHz [31], in the urban environment at 28 GHz [28], in the indoor environment at 26 GHz [32], in the viaduct environment at 93 GHz [33], and so on. After the calibration, the corresponding material parameters are obtained. The calibrated materials basically cover all the material composition of the considered propagation environments in this paper, e.g., concrete, brick, granite, marble, glass, and metal. Note that applying appropriate material parameters in RT is a precondition to obtain practical channel results. In general, the material parameters are frequency dependent. The material parameters are calibrated in similar propagation environments at the adjacent frequency band, i.e., 25 GHz and 28 GHz [28, 31]. In Rec. ITU-R P.1238-7 [34] and Rec. ITU-R P.2040 [35], such material parameters for urban and indoor environments can be obtained for 1 GHz–100 GHz, indicate an insignificant difference, and are almost independent of the frequency in the range from 20 GHz to 30 GHz.

3.2. RT Simulation Configuration. Considering the vehicular MN in the urban environment, not only the bus equipped with the Rx can move but also other vehicles such as cars, delivery vans, and other buses can move around as the moving scatterers. Aiming at supporting these features, the workflow is shown in Figure 8. Dynamic mobility patterns of moving objects and the Tx/Rx should be defined prior to simulation. After all the models and configurations are uploaded to the RT simulator, the geometry and visibility relationship of the objects are updated for each snapshot.

The carrier frequency of V2I simulation is 22.6 GHz with a bandwidth of 1 GHz. Both Tx and Rx beam patterns are the same as the Tx antenna beam pattern of the MHN-E system shown in Figure 7. The deployment of the Tx and Rx is shown in Figure 9; the Tx is placed at the top of the building with a height of 25 m or installed on the pillar of the traffic light with a height of 5 m. The Rx is placed on the top of the bus. The travel distance of the bus where the Rx is located is 500 m. The RT simulation includes two simulation granularity settings:

(i) The low-resolution simulation: with the sampling interval 1.38–1.67 m, it is used to get the channel profile and determine the propagation zones where the high-resolution simulations will take place. Different propagation zones indicate different propagation mechanism combinations.

(ii) The high-resolution simulation: for every propagation zone in every case, one CIR will be simulated per OFDM symbol duration (which is much shorter than half of the wavelength), in order to feed into the link-level simulator.

The simulation setups are based on the RT frequency-domain method for the ultra-wideband channel, and the material parameters are extracted from measurements or literature. The involved material parameters are summarized in Table 2, where ε_r' is the real part of the relative permittivity, $\tan\delta$ is the loss tangent, and S and α are the scattering

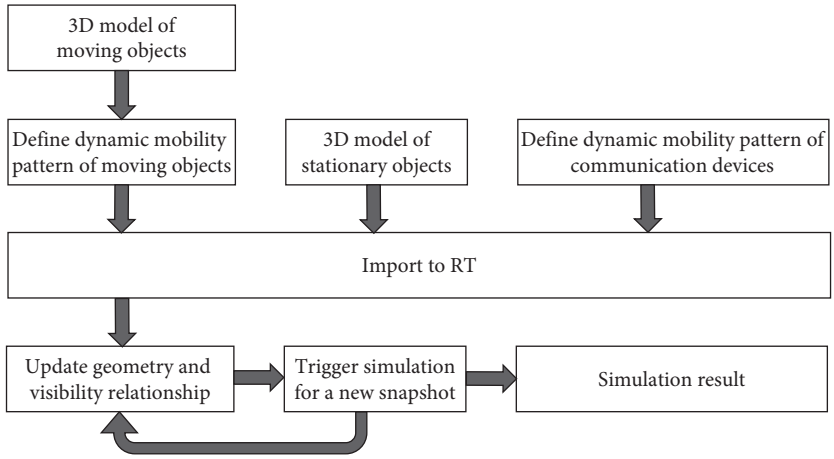

Figure 8: Workflow of simulating moving environments.

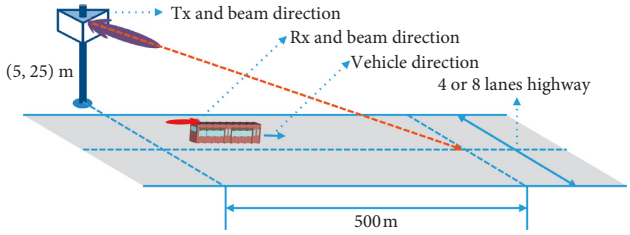

Figure 9: Deployment of the Tx and Rx.

Table 2: Electromagnetic parameters of different materials.

Material	ε_r'	tan δ	S	α
Brick	1.9155	0.0568	0.0019	49.5724
Marble	3.0045	0.2828	0.0022	15.3747
Toughened glass	1.0538	23.9211	0.0025	5.5106
Metal	1	10^7	0.0026	17.7691
Concrete	5.4745	0.0021	0.0011	109
Wood	6.6	0.9394	0.0086	13.1404

coefficient and scattering exponent of the directive scattering model [36]. Particularly, the parameters of wood are calibrated in [37, 38], and the parameters of concrete are calibrated in [39]. Therefore, with the provided calibrated material parameters, various V2I Tx/Rx deployments can be simulated by an RT simulator.

Propagation mechanisms in the simulations are LOS, scattering (multiple scattering theory for vegetation and single-lobe directive model for others), diffraction (uniform theory of diffraction (UTD)), reflection (up to 2 orders), and transmission. The detailed configuration of the RT simulated channels in urban environments is summarized in Table 3. The propagation mechanisms for different objects in the simulation environment are summarized in Table 4.

3.3. Propagation Mechanism Analysis. In this work, 3 different traffic flows are considered:

(i) Full traffic flow: 100% randomly generated vehicles on the road

(ii) Half traffic flow: 50% randomly generated vehicles on the road

(iii) Low traffic flow: 10% randomly generated vehicles on the road

The considered simulation cases are summarized in Table 5 for clarity, and the exemplified simulation results are shown in Figure 10. Figures 10(a) and 10(b) show the MPC distribution of the typical snapshots for Case 9 and Case 10, respectively; moreover, the time-varying PDPs are also given to distinguish the MPC distribution in the delay domain intuitively. According to different MPC distribution and propagation mechanisms, the "zone" concept is proposed. Different zones for different cases are used for channel characterization in the next section. For Case 9, three zones can be detected, and two zones are marked for Case 10. According to the RT simulation results for each case, there are 12 typical divided zones in Table 6, in which the details of propagation mechanisms for different zones are listed. For example, in Zone 2, the Rx is out of the Tx main lobe, the LOS path and reflected and scattered paths (from urban furniture and other vehicles) exist, and no ground reflection exists, as shown in Figure 10(c); in Zone 9, the Rx is in the Tx main lobe, LOS and ground reflected paths exist, and no reflection or scattering from urban furniture or other vehicles is seen, as shown in Figure 10(d); in Zone 11, the Rx is in the Tx main lobe and the LOS path is blocked by a vehicle, as shown in Figure 10(e). Note that the rays whose power is more than 80 dB lower than that of the strongest ray are cut off to get the dominant propagation mechanisms.

Extensive high-resolution simulations are conducted in each propagation zone for different cases. All simulated channel data can be imported to the V2I link-level simulator to guide the construction of the vehicular infrastructure for better road services.

4. Key Channel Parameters for Link-Level Simulation

In order to support the link-level simulation, for every propagation zone, the spatial sampling interval is set to 80λ for high-resolution simulation. The delay resolution is

Table 3: Environment configuration.

Frequency	22.1–23.1 GHz	
Bandwidth	1 GHz	
Antenna	Directional antenna	
Tx	Power	0 dBm
	Height	5 m, 25 m
Rx	Height	3.2 m
	Travel distance for the urban environment	500 m
V2I path	D1: Rx on lane 2 (4-lane urban street; Figure 5), $v = 25$ km/h	
	D2: Rx on lane 4 (8-lane urban street; Figure 6), $v = 60$ km/h	
Vehicle type	Passenger car	60%
	Bus	20%
	Delivery van	20%
Propagation	Direct	✓
	Reflection	Up to 2 orders
	Diffraction	UTD
	Scattering	Directive scattering model
	Transmission	✓
Material	Building	Brick, marble, toughened glass
	Urban furniture, vehicle	Metal
	Tree	Wood
	Ground, highway fence	Concrete

Table 4: Propagation mechanism.

Object	LOS	Reflection (up to 2 orders)	Scattering	Transmission	Diffraction
Trees	✓		✓	✓	
Buildings	✓	✓			✓
Traffic signs	✓	✓			✓
Signal lights	✓	✓			✓
Bus stations	✓	✓			✓
Ground	✓	✓	✓		
Vehicles	✓	✓	✓		✓

Table 5: Analysis cases.

Index	Environment	Lane	Tx height (m)	Traffic flow	Terminology
1	Seoul	4	25	Full	Seoul-4Lanes-Tx25-TFFull
2	Seoul	4	25	Half	Seoul-4Lanes-Tx25-TFHalf
3	Seoul	4	25	Low	Seoul-4Lanes-Tx25-TFLow
4	Seoul	4	5	Full	Seoul-4Lanes-Tx5-TFFull
5	Seoul	4	5	Half	Seoul-4Lanes-Tx5-TFHalf
6	Seoul	4	5	Low	Seoul-4Lanes-Tx5-TFLow
7	Seoul	8	25	Full	Seoul-8Lanes-Tx25-TFFull
8	Seoul	8	25	Half	Seoul-8Lanes-Tx25-TFHalf
9	Seoul	8	25	Low	Seoul-8Lanes-Tx25-TFLow
10	Seoul	8	5	Full	Seoul-8Lanes-Tx5-TFFull
11	Seoul	8	5	Half	Seoul-8Lanes-Tx5-TFHalf
12	Seoul	8	5	Low	Seoul-8Lanes-Tx5-TFLow

8.14 ns, and the time sampling rate is 8.92 μs. Based on extensive RT simulation results, the comprehensive features of 23 lanes in urban environments are analyzed and extracted. The channel characteristics include PL, root-mean-square (RMS) DS, Ricean K-factor (KF), ASA, ASD, ESA, ESD, and blockage loss (BL). All these channel parameters are fitted by the normal distribution with the mean value and standard deviation. All the extracted parameters are summarized in Tables 7–9, where μDS, μKF, μASA, μASD, μESA, and μESD are the mean values of DS, KF, ASA, ASD, ESA, and ESD, respectively. σDS, σKF σASA, σASD, σESA, and σESD are the standard deviations of DS, KF, ASA, ASD, ESA, and ESD, respectively.

4.1. Path Loss. The PL in dB is modeled by the A-B model, which is expressed as

$$\mathrm{PL}(d\mathrm{B}) = A \cdot \log_{10}\left(\frac{d}{d_0}\right) + B + X_\sigma, \quad (1)$$

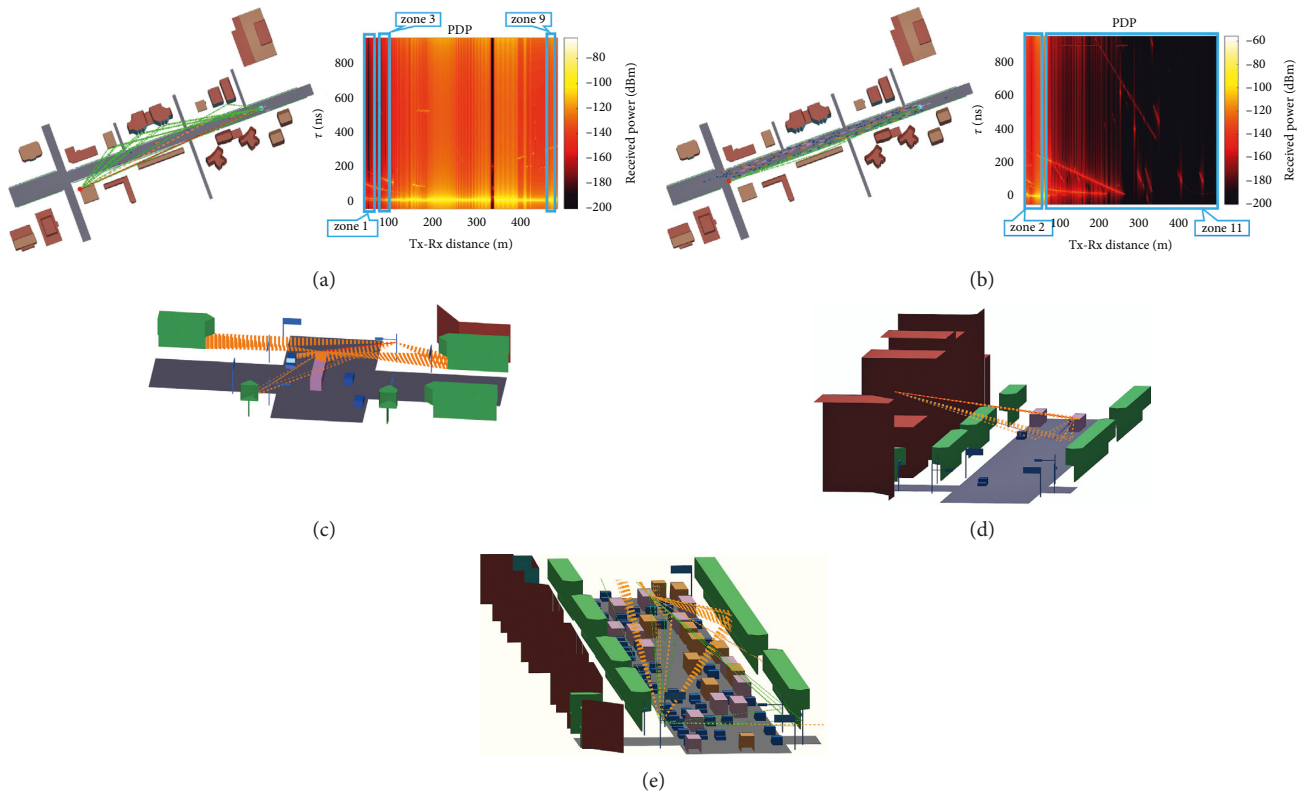

Figure 10: Exemplified RT simulation results in different cases and zones. (a) Case 9: Seoul-8Lanes-Tx25-TFLow. (b) Case 10: Seoul-8Lanes-Tx5-TFFull. (c) One typical snapshot of Zone 2. (d) One typical snapshot of Zone 9. (e) One typical snapshot of Zone 11.

Table 6: Zones of simulation results.

Zone	Antenna alignment	LOS condition			Propagation mechanism	
		LOS	NLOS			
			Blocked by vehicle	Blocked by urban furniture	Ground reflection	Reflection/scattering from urban furniture and other vehicles
1	×	✓	×	×	×	×
2	×	✓	×	×	×	✓
3	×	✓	×	×	✓	×
4	×	✓	×	×	✓	✓
5	×	×	✓	×	—	—
6	×	×	×	✓	—	—
7	✓	✓	×	×	×	×
8	✓	✓	×	×	×	✓
9	✓	✓	×	×	✓	×
10	✓	✓	×	×	✓	✓
11	✓	×	✓	×	—	—
12	✓	×	×	✓	—	—

✓: within main lobe; ×: outside main lobe.

where d is the distance between the Tx and the Rx in m; d_0 is the reference distance, equal to 1 m; A is the PL exponent; B is the offset; and X_σ is the shadow factor (SF), which can be modeled as a Gaussian variable with zero mean and a standard deviation σ_{SF}.

The fitting results of all 23 zones for different analysis cases are listed in Table 7, where $A < 0$ is under the conditions that the Tx and Rx antenna beams are misaligned at the beginning and that the moving Rx gradually approached the main lobe of the Tx. The similar result is presented in the previous work [31]. It can be found that the absolute value of A in Zone 1 to Zone 4 (outside the main lobe of the Tx and LOS condition) and Zone 11 and Zone 12 (within the main lobe of the Tx and NLOS condition) is larger than that in Zone 7 to Zone 10 (within the main lobe of the Tx and LOS condition). This indicates that the main lobe and the

Table 7: Extracted parameters for the PL.

Environment	Zone	PL (dB)		
		A	B	σ_{SF}
Seoul-4Lanes-Tx25-TFFull	8	10.71	37.32	1.14
	10	−415.00	1104.00	3.69
Seoul-4Lanes-Tx25-TFLow	1	−96.78	271.93	0.29
	9	24.39	3.47	4.36
	12	−106.41	418.49	4.53
Seoul-4Lanes-Tx5-TFFull	8	29.81	−11.58	0.84
Seoul-4Lanes-Tx5-TFHalf	2	141.50	−31.47	3.17
	10	5.37	47.69	5.37
Seoul-4Lanes-Tx5-TFLow	1	34.54	56.56	5.44
	3	−77.27	152.50	2.60
Seoul-8Lanes-Tx25-TFFull	2	135.07	−122.46	4.21
	8	7.40	46.50	0.84
	12	1674	−4100	10.46
Seoul-8Lanes-Tx25-TFHalf	1	−243.70	497.19	3.96
	4	30.19	44.80	1.51
	7	−46.56	170.31	0.59
Seoul-8Lanes-Tx25-TFLow	3	−374.55	760.65	7.22
	9	62.08	−97.05	5.33
Seoul-8Lanes-Tx5-TFFull	2	−58.31	158.92	5.28
	11	90.38	−71.97	15.06
Seoul-8Lanes-Tx5-TFHalf	8	14.89	25.98	2.71
Seoul-8Lanes-Tx5-TFLow	4	−61.72	164.97	6.10
	10	12.85	30.87	5.89

Table 8: Extracted parameters for the DS and K-factor.

Environment	Zone	DS (ns)		KF (dB)	
		μ_{DS}	σ_{DS}	μ_{KF}	σ_{KF}
Seoul-4Lanes-Tx25-TFFull	8	1.39	0.23	52.26	15.46
	10	2.30	1.06	27.38	27.50
Seoul-4Lanes-Tx25-TFLow	1	1.29	0.01	47.23	6.04
	9	4.77	2.04	23.60	20.81
	12	81.32	83.08	0.47	6.82
Seoul-4Lanes-Tx5-TFFull	8	1.77	0.21	44.22	4.07
Seoul-4Lanes-Tx5-TFHalf	2	19.42	4.73	−1.37	1.67
	10	5.44	0.87	42.04	3.96
Seoul-4Lanes-Tx5-TFLow	1	17.28	7.08	2.81	3.48
	3	14.54	9.48	7.94	9.14
Seoul-8Lanes-Tx25-TFFull	2	23.95	8.42	9.79	5.30
	8	1.89	1.35	44.23	10.64
	12	75.4	42.14	−4.55	12.89
Seoul-8Lanes-Tx25-TFHalf	1	28.17	12.52	10.74	5.74
	4	16.36	4.41	7.58	3.22
	7	2.60	1.04	41.54	4.29
Seoul-8Lanes-Tx25-TFLow	3	32.1	4.65	2.07	2.84
	9	4.00	0.37	38.21	2.22
Seoul-8Lanes-Tx5-TFFull	2	8.17	11.72	25.16	17.74
	11	46.54	66.15	0.74	15.21
Seoul-8Lanes-Tx5-TFHalf	8	2.84	3.36	56.32	15.16
Seoul-8Lanes-Tx5-TFLow	4	13.19	17.37	11.77	7.67
	10	9.07	3.46	53.24	15.13

barriers, i.e., other vehicles and traffic signs, have a great influence on path loss. With the increase of traffic flow, the probability of occurrence of Zone 5 and Zone 11 (LOS path is blocked by other vehicles) rises.

4.2. RMS DS and Ricean K-Factor. The Ricean K-factor is defined as the ratio of the power of the strongest MPC to the power of the sum of the remaining MPCs in the received signal [40]. Traditionally, the Ricean K-factor is calculated from the narrowband channel sounding results by using a moment-based method [41]. However, the ultra-wideband (UWB) channel sounding results in this measurement have high resolution in the time domain. Thus, the Ricean K-factor can be calculated according to its definition as follows:

$$\mathrm{KF} = 10 \cdot \log_{10}\left(\frac{P_{\text{strongest}}}{\sum P_{\text{remaining}}}\right), \tag{2}$$

where KF denotes the Ricean K-factor and $P_{\text{strongest}}$ and $P_{\text{remaining}}$ denote the power of the strongest MPC and the power of the remaining MPCs, respectively. RMS DS is used to quantify the dispersion effect of the wide channel. It is defined as the square root of the second central moment of the PDP [42]:

$$\sigma_\tau = \sqrt{\frac{\sum_{n=1}^{N} \tau_n^2 \cdot P_n}{\sum_{n=1}^{N} P_n} - \left(\frac{\sum_{n=1}^{N} \tau_n \cdot P_n}{\sum_{n=1}^{N} P_n}\right)^2}, \tag{3}$$

where σ_τ denotes the RMS delay spread and P_n and τ_n denote the power and the excess delay of the n-th multipath. The fitting parameters for KF and σ_τ are listed in Table 8.

As it can be seen from Table 8, the zones with the LOS path are outside the main lobes of transceivers (as shown in Figure 11), the Ricean K-factor is smaller than that of the zones with the LOS path in such main lobes, yet the delay spread is larger than that in the zones with the LOS path in the main lobes. The reason is that the MPCs in the main lobes would have higher gain than the LOS path which gives rise to increasing $P_{\text{remaining}}$ with a long delay. Another finding is that, in the case of the same environment, i.e., the same Tx height and the same zone, the mean value of Ricean K-factor in full traffic flow is smaller than that under the half and low traffic flow conditions; meanwhile, the mean value of DS is larger. As shown in Figure 12, there are more MPCs caused by more vehicles in the case of full traffic flow, resulting in an increase in power to diffuse MPCs. As shown in Figure 13, the Ricean K-factor in some cases of the NLOS channel with reflection is larger than that in other cases of the NLOS channel without reflection. The channel with the strongly reflected path is close to the cases of the LOS channel. It has been found that such strong reflected paths are mainly from a metal vehicle or the ground, and power of them is almost as strong as the LOS path.

4.3. Angular Spread. According to the 3GPP definition, the conventional AS calculation for the composite signal is given by

Table 9: Extracted parameters for the AS.

Environment	Zone	ASA (°)		ESA (°)		ASD (°)		ESD (°)	
		μ_{ASA}	σ_{ASA}	μ_{ESA}	σ_{ESA}	μ_{ASD}	σ_{ASD}	μ_{ESD}	σ_{ESD}
Seoul-4Lanes-Tx25-TFFull	8	0.14	0.21	0.42	1.33	0.19	0.03	0.05	0.17
	10	0.03	0.00	2.28	2.13	0.19	0.10	0.29	0.10
Seoul-4Lanes-Tx25-TFLow	1	0.07	0.01	0.02	0.00	0.30	0.03	0.00	0.00
	9	0.37	0.83	3.27	1.10	0.26	0.29	0.42	0.14
	12	143.83	29.62	2.04	0.58	7.48	9.69	0.57	0.04
Seoul-4Lanes-Tx5-TFFull	8	1.55	0.57	0.11	0.18	0.00	0.00	0.01	0.02
Seoul-4Lanes-Tx5-TFHalf	2	52.11	27.11	18.06	1.59	72.27	13.14	8.26	1.69
	10	1.37	0.10	1.24	0.14	0.00	0.00	0.80	0.09
Seoul-4Lanes-Tx5-TFLow	1	43.55	26.66	18.28	1.70	72.67	12.85	8.37	1.78
	3	47.28	41.54	12.06	6.69	40.63	32.22	8.39	5.44
Seoul-8Lanes-Tx25-TFFull	2	46.97	11.44	24.65	3.66	1.23	0.40	2.13	0.59
	8	6.54	31.00	0.22	1.00	0.09	0.23	0.04	0.06
	12	52.62	25.63	2.53	1.34	3.68	1.50	0.42	0.15
Seoul-8Lanes-Tx25-TFHalf	1	39.26	9.23	24.85	3.68	1.17	0.50	2.07	0.65
	4	79.11	28.25	10.02	2.53	3.93	1.10	0.55	0.24
	7	0.27	0.29	0.01	0.00	0.16	0.10	0.05	0.00
Seoul-8Lanes-Tx25-TFLow	3	98.51	18.6	21.54	1.06	7.25	0.73	3.62	0.65
	9	0.01	0.00	2.90	0.06	0.01	0.00	0.37	0.01
Seoul-8Lanes-Tx5-TFFull	2	22.72	35.31	2.73	4.84	8.62	10.32	1.78	1.89
	11	28.98	31.14	1.01	0.75	2.45	3.07	0.77	1.36
Seoul-8Lanes-Tx5-TFHalf	8	14.16	46.64	0.07	0.25	0.10	0.25	0.05	0.11
Seoul-8Lanes-Tx5-TFLow	4	21.78	35.13	4.71	4.34	10.82	11.74	4.22	3.55
	10	0.01	0.01	0.90	0.15	0.01	0.00	0.58	0.10

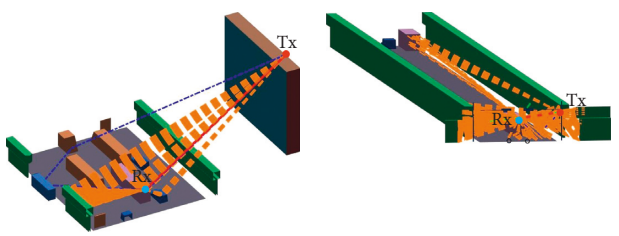

(a) (b)

Figure 11: Rays in the main lobes of the transceiver. (a) Reflected rays aligned with the main lobe. (b) Scattered rays aligned with the main lobe.

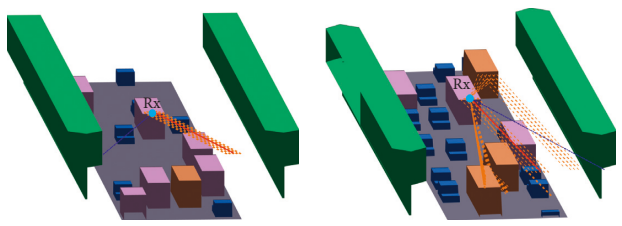

(a) (b)

Figure 12: MPC distribution in the same environment with different traffic flows. (a) Zone 8 in Case 2 (Seoul-4Lanes-Tx25-TFHalf). (b) Zone 8 in Case 1 (Seoul-4Lanes-Tx25-TFFull).

$$\sigma_{AS} = \sqrt{\frac{\sum_{n=1}^{N}\left(\theta_{n,\mu}\right)^2 \cdot P_n}{\sum_{n=1}^{N} P_n}}, \tag{4}$$

where σ_{AS} denotes the AS, P_n denotes the power of the n-th ray, and $\theta_{n,\mu}$ is defined by

$$\theta_{n,\mu} = \mathrm{mod}\left(\theta_n - \mu_\theta + \pi, 2\pi\right) - \pi, \tag{5}$$

where θ_n is the ASA/ASD/ESA/ESD of the n-th ray and μ_θ is

$$\mu_\theta = \frac{\sum_{n=1}^{N}\theta_n \cdot P_n}{\sum_{n=1}^{N} P_n}. \tag{6}$$

Generally speaking, ASD and ASA are larger than ESD and ESA, implying that most of the MPCs come from the horizontal direction. This reflects the fact that more objects (scatterers) are located on the two sides of the Rx vehicle in the urban environment than above/under the Rx vehicle (as shown in Figure 14). Figure 15 shows the variation of the AS with Tx-Rx distance for the urban environment. It can be seen that, in the case of the LOS channel, the mean value of angular spread within the main lobe is generally smaller than that outside the main lobe. This indicates that when the Rx is within the main lobe, the distance between the Rx and the Tx is larger, and the object that produces reflection and scattering is closer to the Tx than the Rx. Moreover, the main lobe filters low-energy rays, resulting in the reduced AS.

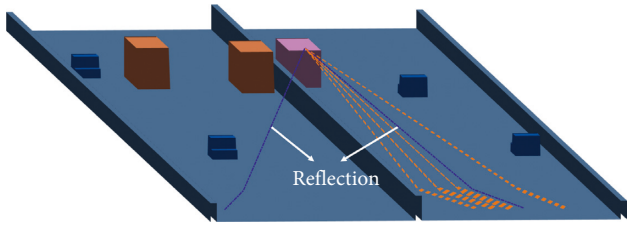

Figure 13: NLOS channel with the strong reflected path.

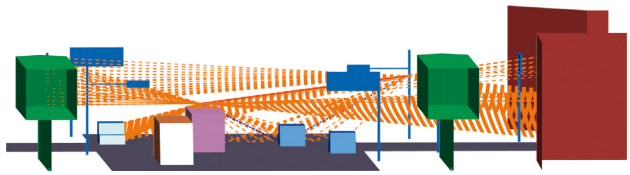

Figure 14: MPC spatial distribution in the vehicular channel in urban environments.

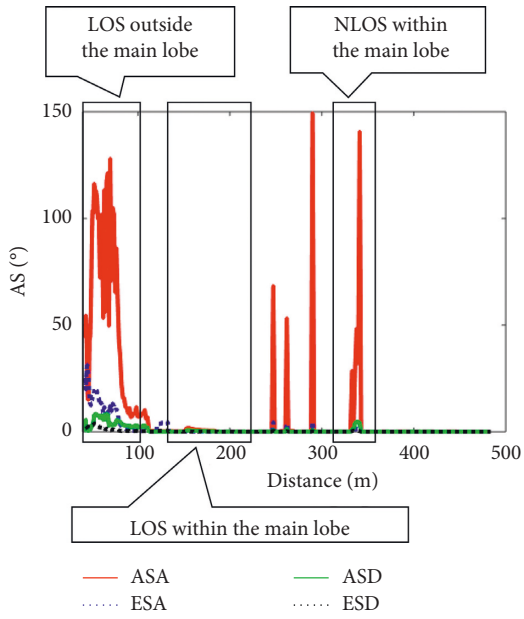

Figure 15: AS of urban environments in both azimuth and elevation domains.

Another finding is that when the Rx vehicle is within the main lobe, the AS for NLOS channels is much larger than that for LOS channels.

4.4. Blockage Loss. There are buildings, small-scale structures, and moving vehicles in the analyzed urban environments. When the vehicle on which the Rx is located is moving on the road, the directed ray may be blocked by these objects. As shown in Figure 16, the maximum blockage loss and the corresponding blockage time for each segment are calculated and fitted by the normal distribution with the mean value μBL, σBL_t, and standard deviation μBL, σBL_t, respectively. The parameters are summarized in Table 10.

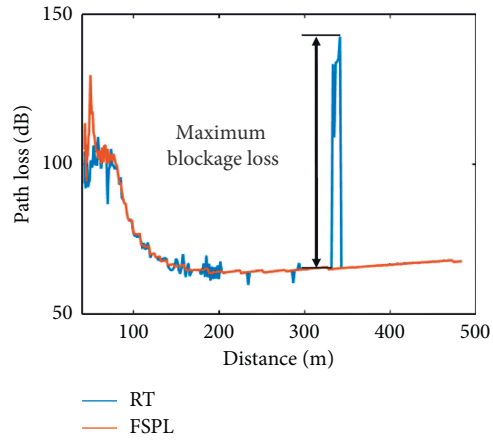

Figure 16: An example of blockage loss, RT, raytracing; FSPL, free space path loss.

Table 10: Extracted parameters for the blockage loss.

μBL (dB)	σBL (dB)	μBL_t (s)	σBL_t (s)
59.75	35.94	2.76	5.67

5. Conclusion

In this paper, the 23 GHz V2I channels are characterized by measurement-validated RT simulations for different antenna heights in various propagation environments. The PL, shadow fading, Ricean K-factor, DS, AS, and blockage loss of the channels are characterized for each zone in different cases. In the considered 3D Seoul urban environments, all the main buildings and small-scale structures, such as traffic lights, traffic signs, bus stations, and trees, are included with their typical geometries and materials in reality. The fundamental channel parameters analyzed are summarized in tables, which can be imported to standard channel models for generating realistic channels for similar environments. The study of this paper and the provided suggestions will be useful to guide the design and deployment of vehicular communication systems with FACS technologies.

Data Availability

The environment models and simulation data of this study are available from the corresponding author upon request.

Conflicts of Interest

The authors declare that they have no conflicts of interest.

Acknowledgments

This work was supported by the National Key Research and Development program under Grant 2016YFE0200900, NSFC under Grants 61771036, U1834210, and 61725101, Newton Fund under Grant 6181101396, Beijing Natural Science Foundation under Grant L161009, Beijing Natural Haidian Joint Fund under Grant L172020, major projects of Beijing Municipal Science and Technology Commission under Grant Z181100003218010, Fundamental Research

Funds for the Central Universities under Grants 2017RC031, 2018RC030, and 2019JBM074, State Key Lab of Rail Traffic Control and Safety under Grants RCS2018ZZ007 and RCS2019ZZ005, and Teaching Reform Project under Grant 134496522.

References

[1] A. Molisch, F. Tufvesson, J. Karedal, and C. Mecklenbrauker, "A survey on vehicle-to-vehicle propagation channels," *IEEE Wireless Communications*, vol. 16, no. 6, pp. 12–22, 2009.

[2] T. Hwang, S. Kang, and H. Hong, "Technical analysis for flexible access common spectrum (FACS)," in *Proceedings of the 2006 International Symposium on Communications and Information Technologies*, pp. 1000–1003, Bangkok, Thailand, October 2006.

[3] T. Sukuvaara and P. Nurmi, "Wireless traffic service platform for combined vehicle-to-vehicle and vehicle-to-infrastructure communications," *IEEE Wireless Communications*, vol. 16, no. 6, pp. 54–61, 2009.

[4] X. Chen, S. Guo, and Q. Wu, "Link-level analysis of a multiservice indoor distributed antenna system [wireless corner]," *IEEE Antennas and Propagation Magazine*, vol. 59, no. 3, pp. 154–162, 2017.

[5] K. Guan, D. He, B. Ai et al., "5-GHz obstructed vehicle-to-vehicle channel characterization for internet of intelligent vehicles," *IEEE Internet of Things Journal*, vol. 6, no. 1, pp. 100–110, 2019.

[6] J. Kurner, N. Czink, A. Paier, F. Tufvesson, and A. F. Molisch, "Path loss modeling for vehicle-to-vehicle communications," *IEEE Transactions on Vehicular Technology*, vol. 60, no. 1, pp. 323–328, 2011.

[7] L. Cheng, B. Henty, D. Stancil, F. Bai, and P. Mudalige, "Mobile vehicle-to-vehicle narrow-band channel measurement and characterization of the 5.9 GHz dedicated short range communication (DSRC) frequency band," *IEEE Journal on Selected Areas in Communications*, vol. 25, no. 8, pp. 1501–1516, 2007.

[8] O. Renaudin, V. Kolmonen, P. Vainikainen, and C. Oestges, "Wideband MIMO car-to-car radio channel measurements at 5.3 GHz," in *Proceedings of the 2008 IEEE 68th Vehicular Technology Conference*, pp. 1–5, Calgary, Canada, September 2008.

[9] X. Chen, S. Zhang, and Q. Li, "A review of mutual coupling in MIMO systems," *IEEE Access*, vol. 6, pp. 24706–24719, 2018.

[10] A. Paier, J. Karedal, N. Czink et al., "Car-to-car radio channel measurements at 5 GHz: pathloss, power-delay profile, and delay-doppler spectrum," in *Proceedings of the 2007 4th International Symposium on Wireless Communication Systems*, pp. 224–228, Trondheim, Norway, October 2007.

[11] A. Paier, J. Karedal, N. Czink et al., "First results from car-to-car and car-to-infrastructure radio channel measurements at 5.2 GHz," in *Proceedings of the 2007 IEEE 18th International Symposium on Personal, Indoor and Mobile Radio Communications*, pp. 1–5, Athens, Greece, September 2007.

[12] X. Cheng, Q. Yao, M. Wen, C. Wang, L. Song, and B. Jiao, "Wideband channel modeling and intercarrier interference cancellation for vehicle-to-vehicle communication systems," *IEEE Journal on Selected Areas in Communications*, vol. 31, no. 9, pp. 434–448, 2013.

[13] R. He, O. Renaudin, V.-M. Kolmonen et al., "A dynamic wideband directional channel model for vehicle-to-vehicle communications," *IEEE Transactions on Industrial Electronics*, vol. 62, no. 12, pp. 7870–7882, 2015.

[14] T. Abbas, L. Bernado, A. Thiel, C. Mecklenbrauker, and F. Tufvesson, "Radio channel properties for vehicular communication: merging lanes versus urban intersections," *IEEE Vehicular Technology Magazine*, vol. 8, no. 4, pp. 27–34, 2013.

[15] R. He, A. F. Molisch, F. Tufvesson, Z. Zhong, B. Ai, and T. Zhang, "Vehicle-to-vehicle propagation models with large vehicle obstructions," *IEEE Transactions on Intelligent Transportation Systems*, vol. 15, no. 5, pp. 2237–2248, 2014.

[16] R. He, O. Renaudin, V.-M. Kolmonen et al., "Vehicle-to-vehicle radio channel characterization in crossroad scenarios," *IEEE Transactions on Vehicular Technology*, vol. 65, no. 8, pp. 5850–5861, 2016.

[17] T. S. Rappaport, G. R. MacCartney, M. K. Samimi, and S. Sun, "Wideband millimeter-wave propagation measurements and channel models for future wireless communication system design," *IEEE Transactions on Communications*, vol. 63, no. 9, pp. 3029–3056, 2015.

[18] W. Fan, F. Zhang, and G. F. Pedersen, "Validation of test environment in simple sectored MPAC setups for over-the-air testing of 5G communication systems," *IEEE Antennas and Propagation Magazine*, vol. 16, no. 3, 2019.

[19] I. Sen and D. W. Matolak, "Vehicle-vehicle channel models for the 5-GHz band," *IEEE Transactions on Intelligent Transportation Systems*, vol. 9, no. 2, pp. 235–245, 2008.

[20] C. Wang, X. Cheng, and D. I. Laurenson, "Vehicle-to-vehicle channel modeling and measurements: recent advances and future challenges," *IEEE Communications Magazine*, vol. 47, no. 11, pp. 96–103, 2009.

[21] O. Andrisano, M. Chiani, M. Frullone, C. Moss, and V. Tralli, "Propagation effects and countermeasures analysis in vehicle-to-vehicle communication at millimeter waves," in *Proceedings of the Vehicular Technology Society 42nd VTS Conference—Frontiers of Technology*, vol. 1, pp. 312–316, Denver, CO, USA, May 1992.

[22] A. Kato, K. Sato, M. Fujise, and S. Kawakami, "Propagation characteristics of 60-GHz millimeter waves for ITS inter-vehicle communications," *IEICE Transactions on Communications*, vol. 84, no. 9, pp. 2530–2539, 2001.

[23] T. Wada, M. Maeda, M. Okada, K. Tsukamoto, and S. Komaki, "Theoretical analysis of propagation characteristics in millimeter-wave intervehicle communication system," *Electronics and Communications in Japan (Part II: Electronics)*, vol. 83, no. 11, pp. 33–43, 2000.

[24] E. Ben-Dor, T. S. Rappaport, Y. Qiao, and S. J. Lauffenburger, "Millimeter-wave 60 GHz outdoor and vehicle AOA propagation measurements using a broadband channel sounder," in *Proceedings of the IEEE Global Telecommunications Conference—GLOBECOM 2011*, pp. 1–6, Houston, TX, USA, December 2011.

[25] J. Zhang, Y. Zhang, Y. Yu, R. Xu, Q. Zheng, and P. Zhang, "3-D MIMO: how much does it meet our expectations observed from channel measurements?," *IEEE Journal on Selected Areas in Communications*, vol. 35, no. 8, pp. 1887–1903, 2017.

[26] M. G. Sánchez, M. P. Táboas, and E. L. Cid, "Millimeter wave radio channel characterization for 5G vehicle-to-vehicle communications," *Measurement*, vol. 95, pp. 223–229, 2017.

[27] K. Guan, D. He, B. Ai et al., "Realistic channel characterization for 5G millimeter-wave railway communications," in *Proceedings of the 2018 IEEE Globecom Workshops (GC Wkshps)*, pp. 1–6, Abu Dhabi, UAE, December 2018.

[28] D. He, B. Ai, K. Guan, L. Wang, Z. Zhong, and T. Kurner, "The design and applications of high-performance ray-tracing simulation platform for 5G and beyond wireless

communications: a tutorial," *IEEE Communications Surveys & Tutorials*, vol. 21, no. 1, pp. 10–27, 2019.

[29] K. Guan, B. Ai, B. Peng et al., "Towards realistic high-speed train channels at 5G millimeter-wave band—part I: paradigm, significance analysis, and scenario reconstruction," *IEEE Transactions on Vehicular Technology*, vol. 67, no. 10, pp. 9112–9128, 2018.

[30] "Study on evaluation methodology of new vehicle-to-everything (V2X) use cases for LTE and NR (Release 15), 3rd Generation Partnership Project (3GPP) TR 37.885-15.0.0," June 2018.

[31] D. He, B. Ai, K. Guan et al., "Channel measurement, simulation, and analysis for high-speed railway communications in 5G millimeter-wave band," *IEEE Transactions on Intelligent Transportation Systems*, vol. 19, no. 10, pp. 3144–3158, 2018.

[32] B. Ai, K. Guan, R. He et al., "On indoor millimeter wave massive MIMO channels: measurement and simulation," *IEEE Journal on Selected Areas in Communications*, vol. 35, no. 7, pp. 1678–1690, 2017.

[33] J. Yang, B. Ai, K. Guan et al., "A geometry-based stochastic channel model for the millimeter-wave band in a 3GPP high-speed train scenario," *IEEE Transactions on Vehicular Technology*, vol. 67, no. 5, pp. 3853–3865, 2018.

[34] ITU-R, *P.1238-7: Propagation Data and Prediction Methods for the Planning of Indoor Radiocommunication Systems and Radio Local Area Networks in the Frequency Range 900 MHz to 100 GHz*, ITU Recommendations, Geneva, Switzerland, 2012.

[35] ITU-R, *P.2040: Effects of Building Materials and Structures on Radiowave Propagation above about 100 MHz*, ITU Recommendations, Geneva, Switzerland, 2013.

[36] V. Degli-Esposti, F. Fuschini, E. M. Vitucci, and G. Falciasecca, "Measurement and modelling of scattering from buildings," *IEEE Transactions on Antennas and Propagation*, vol. 55, no. 1, pp. 143–153, 2007.

[37] F. Wang and K. Sarabandi, "An enhanced millimeter-wave foliage propagation model," *IEEE Transactions on Antennas and Propagation*, vol. 53, no. 7, pp. 2138–2145, 2005.

[38] H. M. Rahim, C. Y. Leow, and T. A. Rahman, "Millimeter wave propagation through foliage: comparison of models," in *Proceedings of the 2015 IEEE 12th Malaysia International Conference on Communications (MICC)*, pp. 236–240, Kuching, Malaysia, November 2015.

[39] K. Guan, B. Ai, B. Peng et al., "Towards realistic high-speed train channels at 5G millimeter-wave band: part II: case study for paradigm implementation," *IEEE Transactions on Vehicular Technology*, vol. 67, no. 10, pp. 9129–9144, 2018.

[40] L. Bernado, T. Zemen, F. Tufvesson, A. F. Molisch, and C. F. Mecklenbrauker, "Time- and frequency-varying K-factor of non-stationary vehicular channels for safety-relevant scenarios," *IEEE Transactions on Intelligent Transportation Systems*, vol. 16, no. 2, pp. 1007–1017, 2015.

[41] T. Zhou, C. Tao, S. Salous, L. Liu, and Z. Tan, "Channel characterization in high-speed railway station environments at 1.89 GHz," *Radio Science*, vol. 50, no. 11, pp. 1176–1186, 2015.

[42] T. Rappaport, *Wireless Communications: Principles and Practice*, Prentice-Hall, Upper Saddle River, NJ, USA, 2002.

Hindawi
International Journal of Antennas and Propagation
Volume 2019, Article ID 3137583, 10 pages
https://doi.org/10.1155/2019/3137583

Research Article

Channel Characteristics of High-Speed Railway Station Based on Ray-Tracing Simulation at 5G mmWave Band

Lei Xiong,[1] **Haiyang Miao**,[1] **Bo Ai**,[1] **Tutun Juhana**,[2] **and Adit Kurniawan**[2]

[1]*The State Key Laboratory of Rail Traffic Control and Safety, Beijing Jiaotong University, 100044 Beijing, China*
[2]*School of Electrical Engineering and Informatics, Institut Teknologi Bandung, Jl. Ganesa No. 10, Bandung, Indonesia*

Correspondence should be addressed to Lei Xiong; lxiong@bjtu.edu.cn

Received 3 May 2019; Accepted 15 July 2019; Published 2 September 2019

Guest Editor: Marko Sonkki

In order to satisfy the increasing demand for the higher transmission capacity of "smart station", millimeter wave (mmWave) technology is expected to play a significant role in the high data rate communication system. Based on the ray-tracing simulation technology, this paper would study wireless channel characteristics of the three-dimensional (3D) model of high-speed railway station at the mmWave band. Key parameters such as path loss exponent, shadow fading factor, delay spread, Rician *K*-factor, angular spread, power angle spectrum, and spatial correlation are extracted and investigated. These channel characteristics are of value for the selection of antenna arrays and even the design of future 5G communication networks in the railway environment.

1. Introduction

Nowadays, with the convenience and flexibility of high-speed railway (HSR), more and more people prefer to take rail traffic for travel or for work. In order to meet these goals in regard to safety, convenience, and efficiency, the investigations about the fifth-generation (5G) wireless communication system have become a trend [1–4] in different railway scenes. At present, the first 5G smart railway station has been established at Shanghai Hongqiao Railway Station, which is expected to have the ability to guarantee the 5G network depth coverage in this year. Smart railway station would show the wisdom of railway technology to the public from the perspective of operation and service, including indoor navigation, face identification, and 5G-guided robot. In other words, smart station has been the vital application environment in intelligent transportation systems (ITSs) [5, 6] and the analysis of the wireless channel model in the railway system for the 5G communication system is essential.

To meet the demand for seamless high data rate wireless connectivity for railway services, the efficient transmission technologies like massive multiple-input multiple-output (MIMO) is proposed [7] to improve system capacity and data rate. The large-scale fading characteristics of different railway scenarios have been summarized for the first time in [8]. Based on [8], it is noted that railway station [9, 10] is significantly different from common public network scenarios or other high-speed railway scenarios (such as viaducts, cuttings, tunnels, etc.) [11]. In [11], the authors also explored channel characteristics in different HSR scenarios by the 3D ray tracing (RT) [12–14] which could compensate for the shortcoming of traditional models and accurately analyze the special channel characteristics in 5G systems. Previous simulations focused on the single-input single-output (SISO) system and MIMO channel for indoor and outdoor communication [15–17], but they missed the research of multipath parameters such as spatial correlation in the railway system. As a result, there is still an urgent demand for a complete investigation by considering large-scale parameters, small-scale parameters, and spatial parameters [18, 19] for station scenario in MIMO systems.

This paper mainly focuses on the medium HSR station, which is the most common station scenario with two platforms and four lines. First of all, channel parameters such as path loss exponent, shadow fading factor, multipath delay, and angular spread can be obtained based on RT. The experiment will be carried out at the HSR station where base

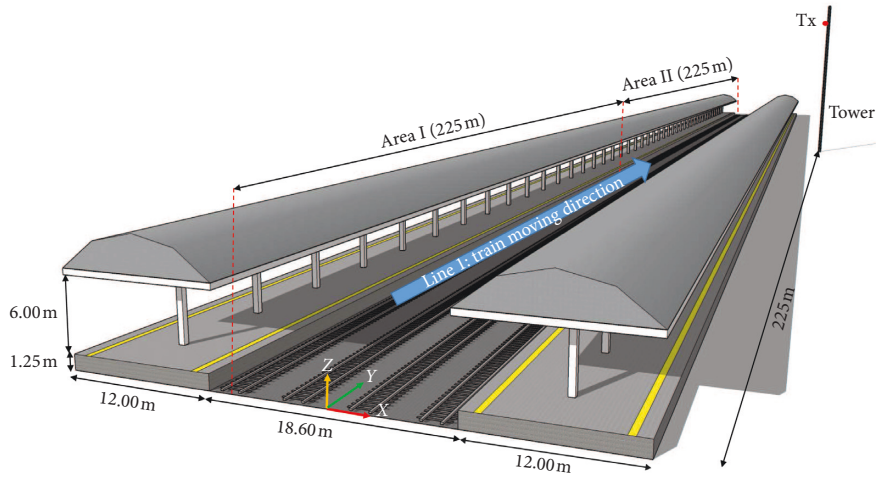

Figure 1: High-speed railway station scenario. Line 1 is divided into two parts: Area I (the area of Rx approaching the Tx) and Area II (the area of Rx leaving the Tx).

station antennas are arranged on the tower. On the contrary, the strengths of the massive MIMO system to compensate for the high path loss of the mmWave band have made high carrier frequencies become an integral component of the upcoming 5G networks. Because of the available larger transmission bandwidths, the 5G network is able to supply high data rates and enhance the quality of experience. Although propagation signals at higher frequencies have the higher path loss and are more susceptible to rapid signal degradations caused by moving or fixed obstacles [20], higher frequencies can allow the deployment of smaller antennas which enables the function of multiantenna technology to be integrated into the antenna array. In this paper, not only have the channel characteristics that can guide 3D channel modeling in 5G environment been discussed but optimized deployment recommendations have also been provided for antenna configuration based on the spatial correlation in massive MIMO systems at 37.0–42.5 GHz mmWave band.

The rest of the paper is organized as follows. The defined high-speed railway station scenario and simulation parameters are presented in Section 2. The wireless channel model for the station scenario is provided in Section 3. According to simulation results, we point out the main channel characteristics to discuss the antenna deployment in Section 4. Conclusions are drawn in Section 5.

2. Ray-Tracing Simulation

2.1. Scenario Modeling. As shown in Figure 1, the 3D scenario model with a 450 m (length) high-speed railway station is established by SketchUp in the three-dimensional Cartesian coordinate system. There are 6 types of objects and 6 materials (Table 1) in the scenario model. The LOS paths, scattering, and up to 2nd-order reflections are considered, and the initialized dielectric parameters are listed in Table 2.

Then, referring to the CRH380A, the high-speed train model is built in Figure 2. With simulation and measurement results, the effect of adjacent train compartments almost can be ignored for the received signal, which indicates the front of the train could be considered individually in the simulation environment.

Table 1: Scenario composition.

Object	Material
Platform	Granite, brick, plaster
Canopy	Plaster, metal
Ground	Tiles-rough
Rail	Metal
Crosstie	Concrete
Single-tube tower	Metal

Table 2: Material parameters.

Material	Relative permittivity	Loss tangent
Granite	4.91	0.14
Brick	4.20	0.39
Plaster	2.50	2×10^{-3}
Metal	1.00	10^{7}
Tiles-rough	3.77	3×10^{-3}
Concrete	5.60	0.05

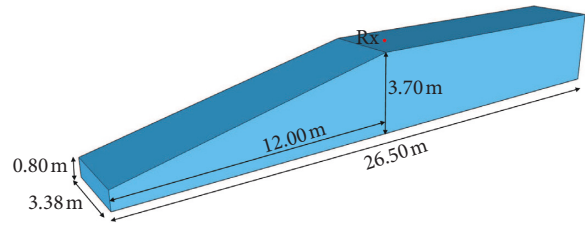

Figure 2: High-speed train model (CRH380A).

2.2. Ray-Tracing Simulation Parameters. In Figure 1, the height of the single-tube tower next to the high-speed railway station is 40 m [21]. The distance from the center line of the tower to the edge of station platform is 10 m, and the

distance to the X-axis is 225 m. The omnidirectional vertical polarization antenna is employed in this work. As the transmitter (Tx) antenna, the base station antenna is deployed on a platform of tower [21] whose height is 38.5 m and vertical distance to the center line of the tower is 0.8 m. Hence, the coordinates can be set to (30.5, 225, 38.5).

In the top view of Figure 1, simulating on Line 1, the process of passing the train through the station on Line 1 is divided into Area I where the train is approaching the tower and Area II where the train is leaving the tower. The top antenna is the receiver (Rx) which is located at the middle line on the top of train, and the vertical distance to the rear section of the train is 13 m. The Rx antenna moves along the positive direction of Y-axis, and the height is 4.16 m which is the sum of the distance to the top of train (0.15 m), the height of the train (3.70 m), and the height from the bottom of the train to the ground (0.31 m). The Y-axis coordinate of Rx antenna is 0 : 2:450 on Line 1. The key configurations of ray-tracing simulation are listed in Table 3.

Table 3: Simulation parameters.

Parameter	Value
Frequency (GHz)	37.0–42.5
Bandwidth (GHz)	5.5
Resolution (MHz)	5.5
Reflection order	2
Scattering mode	Directive mode
Antenna (Tx, Rx)	Omnidirectional vertical polarization
Tx antenna gain (dBi)	10
Rx antenna gain (dBi)	3
Tx height (m)	38.5
Rx height (m)	4.16
Tx transmit power (dBm)	43
Tx coordinate	(30.5, 225, 38.5)
Rx coordinate	(−7.5, y, 4.16)

3. Wireless Channel Model

In signal processing and wireless communication, the channel transfer function $H(f)$ at frequency f is expressed as the coherent sum of different multipath components $H_n(f)$ coupling with the polarimetric Tx and Rx antenna radiation patterns $(G_{\mathrm{Tx}}, G_{\mathrm{Rx}})$ [22].

$$H(f) = \sum_{n=1}^{N} G'_{\mathrm{Tx}} H_n(f) G_{\mathrm{Rx}},$$
$$H_n(f) = a_n(f) e^{j\Psi_n(f)} \delta\left(\phi_{\mathrm{AoD}} - \phi_{\mathrm{AoD},n}\right)\delta\left(\theta_{\mathrm{AoD}} - \theta_{\mathrm{AoD},n}\right) \cdot \delta\left(\phi_{\mathrm{AoA}} - \phi_{\mathrm{AoA},n}\right)\delta\left(\theta_{\mathrm{AoA}} - \theta_{\mathrm{AoA},n}\right), \quad (1)$$

where N denotes the number of multipath, a_n and Ψ_n are the signal amplitude and phase, respectively, ϕ_{AoD}, ϕ_{AoA}, θ_{AoD}, and θ_{AoA} are the azimuth angle of departure/arrival and elevation angle of departure/arrival, respectively [23], all of which are for the n-th multipath component.

In addition, in the wireless channel model, the line-of-sight (LOS) paths and the non-line-of-sight (NLOS) paths are usually separated because the LOS paths are obvious, whereas the NLOS paths are based on the simulation transmission modes of the RT platform including reflection, scattering, and diffraction.

4. Wireless Channel Characteristics

In this section, the simulation results of high-speed railway station on Line 1 are presented and analyzed. Furthermore, suggestions on optimized antenna array deployment are also provided.

4.1. Path Loss and Shadow Fading. Path loss refers to the loss caused by the diffusion of electromagnetic wave energy when the wave propagates. From the macroscopic point of view, it is reflected in the function of the received signal power changing with distance.

By analyzing the channel data obtained by the RT simulation platform, with the change of Y-axis coordinate of the Rx antenna, the path loss is shown in Figure 3.

In Figure 3, the path loss is almost symmetrical with respect to the Y-axis coordinate of Tx, whose maximum is 132.2 dB when the Y-axis coordinate is 22 m. In [24], assuming that the receiving sensitivity of the Rx antenna is −125.23 dBm and combining the parameters of Table 3, the maximum allowable of path loss is about 148.73 dB considering penetration loss.

In this paper, the fitting results of path loss, by the model in (2) that combines the path loss and shadow fading [25], are shown in Figure 4:

$$\mathrm{PL}(d) = A + 10n\log_{10}(d) + X_\sigma, \quad (2)$$

where A is the interception, d is the distance between the Tx antenna and the Rx antenna (unit: m), and n is the path loss exponent. X_σ indicates the zero mean Gaussian random variable with a standard deviation σ which is the shadow fading factor reflecting the large-scale fading that is caused by obstacle occlusion on the wireless channel.

From Section 2, Line 1 is divided into Area I and Area II. The fitted parameter values are shown in Table 4.

According to Figure 4 and Table 4, on Line 1, as a result of a few obstacles (such as canopy) in the scenario, the fitting path loss exponent ($n = 2.26$) is slightly larger than that in the free space path loss (FSPL) model ($n = 2$). In Area I, n is 2.69 because of more obstacles. It should be noted that n is 1.83 in Area II on account of the superposition of the LOS path, more reflection, and scattering which can be found in [11] regarding rich multipath propagation at mmWave channels. In addition, all shadow fading factors σ in the scenario are close to 6 dB which is the value of the LOS environment for rural macro (RMa) scenario in 3GPP [26].

4.2. RMS Delay Spread. Figure 5 shows the mean root mean square (RMS) delay spreads and cumulative distribution functions (CDFs) of RMS delay spreads.

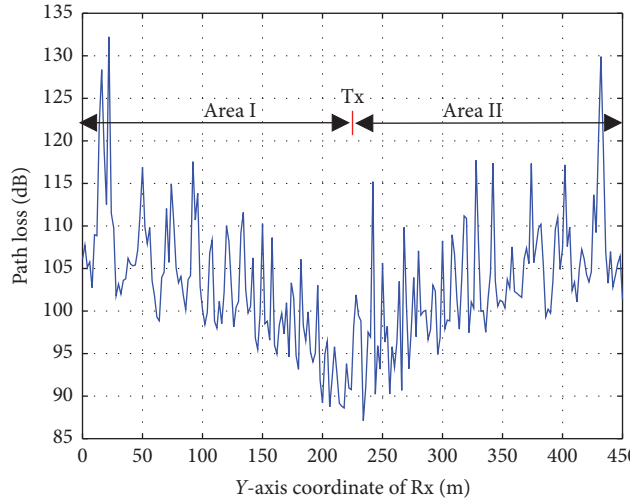

Figure 3: Path loss.

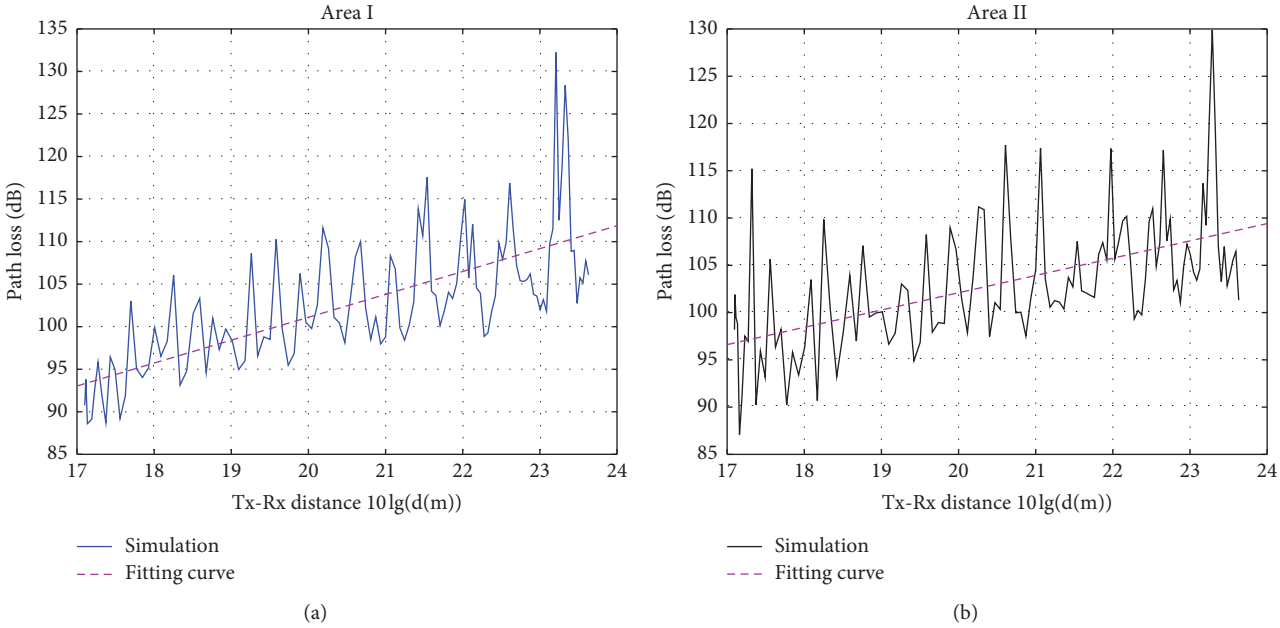

Figure 4: Simulation and fitting results. (a) Area I. (b) Area II.

Table 4: Parameter fitted value.

Parameter	A	n	σ (dB)
Area I	47.31	2.69	5.52
Area II	65.52	1.83	5.69
Line 1	56.42	2.26	5.66
FSPL	64.27	2.00	—

In Figure 5(a), the RMS delay spread curve is almost symmetric. The RMS delay spreads near Tx antenna are larger than the two ends of the station. The mean RMS delay spread 0.28 ns on Line 1 is less than the measurement result of delay spread 0.8 ns in rural [4] because the semiclosed station space limits the range of multipaths [11]. Simultaneously, due to the high-speed railway station is a semilimited type, the rays are occluded and reflected by various buildings and the train body during the propagation process. LOS paths provide the primary energy, and the RMS delay spreads are relatively small. In Figure 5(b), all values of RMS delay spread on Line 1 are less than 1.2 ns, which mean most of the powerful multipath components are concentrated around LOS path in the time delay domain. The mean values of RMS delay spread are shown in Table 5, and values of two areas are almost the same which

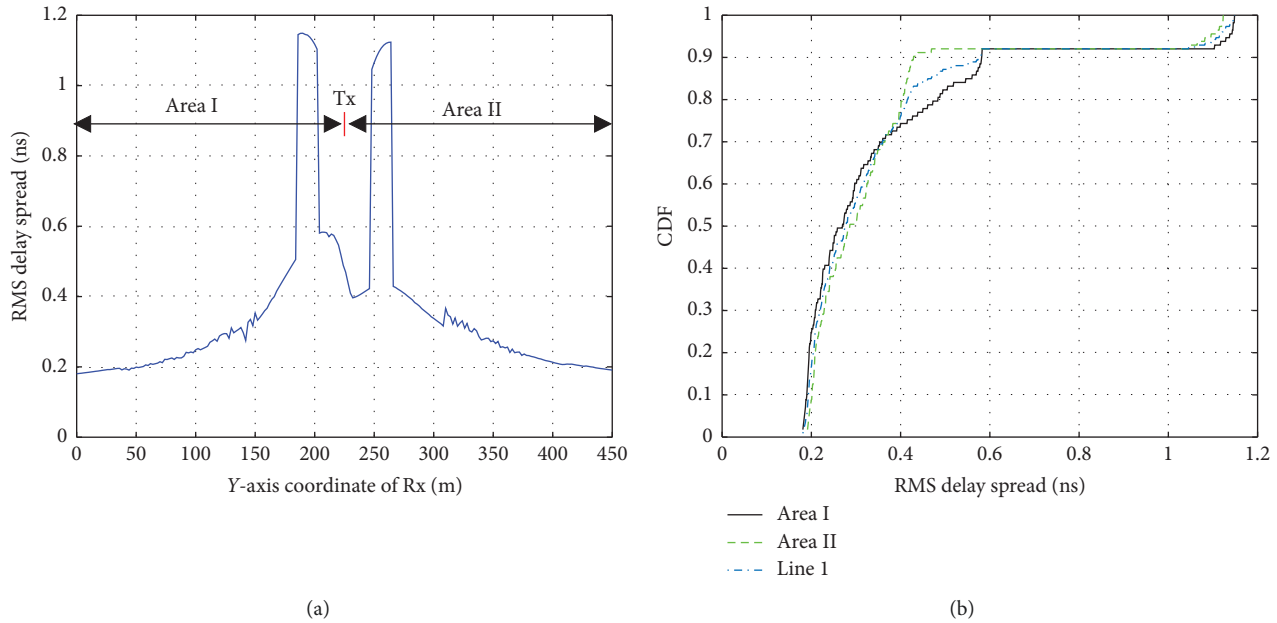

Figure 5: (a) RMS delay spread. (b) CDF of RMS delay spread.

Table 5: Mean value of parameters.

Parameter	Area I	Area II	Line 1
RMS delay spread (ns)	0.27	0.29	0.28
K (dB)	28.97	27.47	28.72

suggest Line 1 has the similar channel characteristics in the time delay domain.

4.3. Rician K-Factor. From the analysis of previous chapters, there are LOS paths and a large number of NLOS paths on Line 1. So it is indispensable to analyze the relationship between LOS path and NLOS path with the Rician K-factor [27].

With the Y-axis coordinate position of Rx antenna changing, the Rician K-factor is shown in Figure 6(a). Additionally, Figures 6(b)–6(d) demonstrate CDFs and fitting results of Rician K-factor. The mean values of the Rician K-factor are summarized in Table 5.

As shown in Figure 6(a), with the Rx antenna close to Tx antenna (Area I), the overall process of Rician K-factor is a decreasing trend. Rician K-factors near Tx antenna are the smallest, whose fluctuation is relatively serious. Conversely, in Area I and Area II, the Rician K-factors become larger with the distance between Tx antenna and Rx antenna increasing, which denotes the fading is getting weaker.

In Table 5, the mean of Rician K-factor on Line 1 is 28.72 dB that is far greater than 0 dB, which means LOS path contributed the main energy. The similar observation at mmWave band could be found in rural scenario [4] regarding the mean value 25.7 dB. As shown in Figures 6(b)–6(d), it should also be noted from the fitting results that Rician K-factors obey the Gaussian distribution owing to the wideband channel characteristic of the 5G communication system. Furthermore, when the bandwidth is wider, the multipath resolution capability that leads to a decrease in the power of the NLOS component of the main path gets stronger, so Rician K-factors become greater in the 5G wideband channel system.

4.4. Spatial Parameters

4.4.1. RMS Angular Spread. On Line 1, the RMS angular spreads of angle of arrival (AoA) and angle of departure (AoD) are shown in Figure 7(a). ASA, ESA, ASD, and ESD are angular spreads of the azimuth angle of arrival, the elevation angle of arrival, the azimuth angle of departure, and the elevation angle of departure, respectively. The CDFs of angular spreads are illustrated in Figure 7(b).

In Figure 7, the ESA is relatively larger, and most (≥80%) values are greater than 10.7°, while the 80% of ASA are less than 7.8°, which explains there are more scatterers from the elevation domain at the Rx and the train body plays a major role. Then, the ESD is relatively smaller, and most (≥80%) values are less than 1.7° whereas the ASD is relatively larger and 80% are greater than 5.5°, which explains there are less scatterers at the elevation domain at the Tx. Besides, the measurement scenario in [28] is similar to the station scenario in the paper, and the results in [28] agree with the

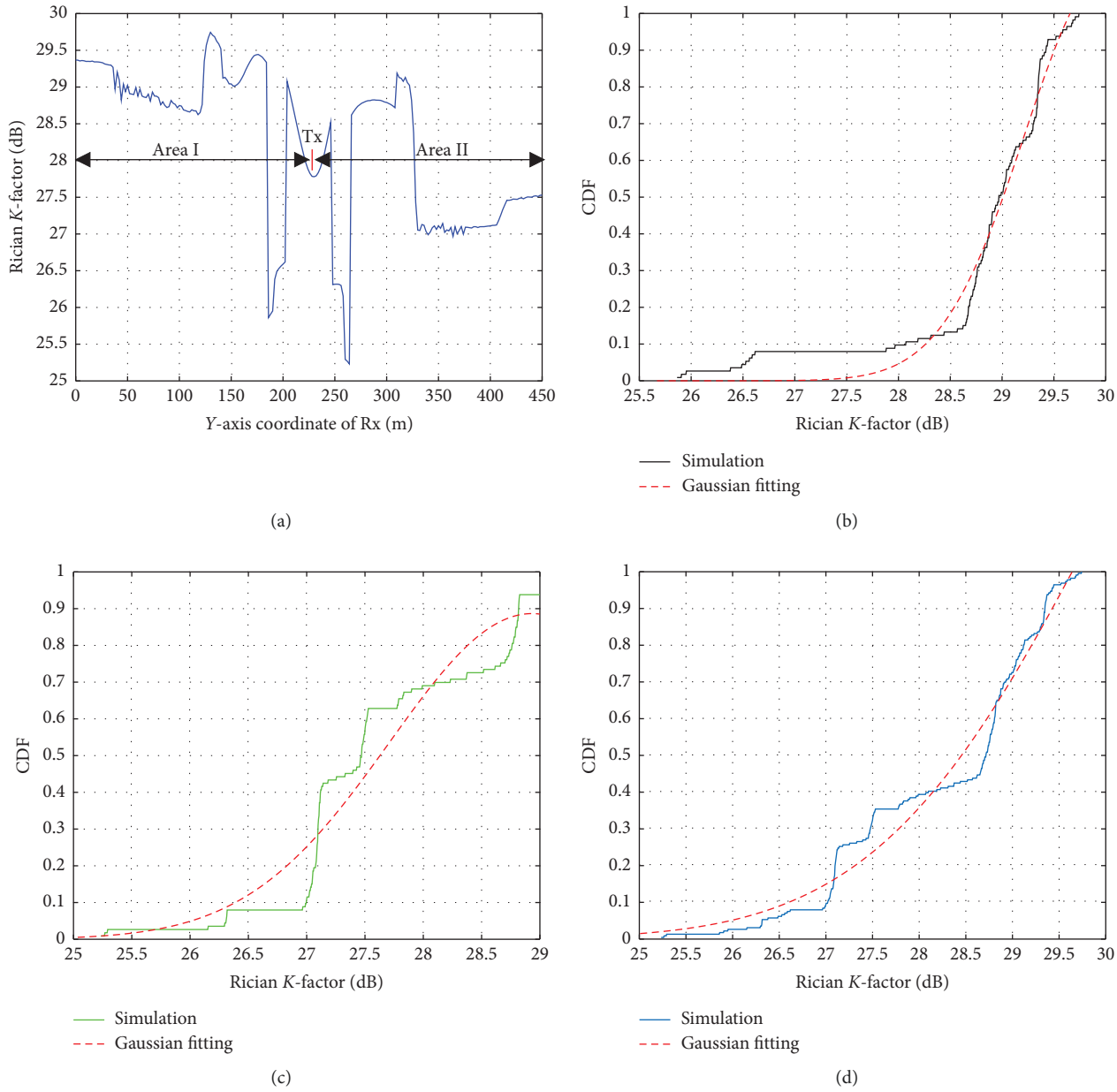

Figure 6: (a) Rician K-factor. (b) Area I. (c) Area II. (d) Line 1.

simulation results in the paper. Since there is a similar environment that more reflectors and scatterers in both scenarios, the scenarios have the same characteristic that the maximum of angular spread does not exceed 70°.

4.4.2. Power Angle Spectrum. In Figure 7(a), the angular spreads at two ends of the station are relatively small. That is why we need to focus on the power angle spectrum (PAS) [29] at two ends of the station. In this section, Figure 8 shows the PAS of AoA and AoD when the Y-axis coordinates of the Rx antenna are 6 m and 444 m, respectively.

In Figure 8(a), at the Y-axis coordinate 6 m, the main beam at Rx could be horizontal because values of normalized power are relatively the largest as the elevation angle of AoA is about 90°. Fortunately, elevation angle directions of the main beam are also distributed around 90° at the Y-axis coordinate 444 m. Furthermore, the relatively large ESA and horizontal beam at Rx show that the linear Rx antenna array should be perpendicular to the top of the train in order to achieve the low correlation among beams.

In Figure 8(b), at the 6 m, while the azimuth angle of AoD is about −20°, the normalized powers are the largest, which implies that the azimuth angle direction of the main beam at Tx could be about −20°. Conversely, at the 444 m, the azimuth angle directions of main beam are mainly distributed around 20°, but the elevation angles always approach 100°. Then, the ASDs of Tx antenna are greater than ESDs in Figure 7(a), which means the antenna array

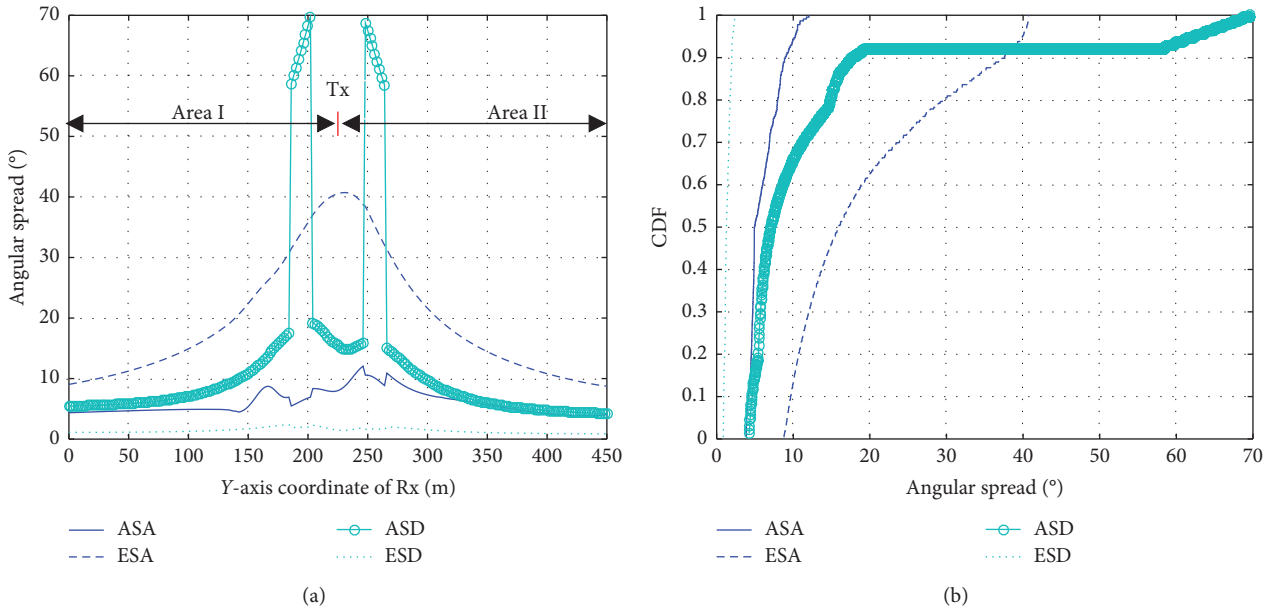

Figure 7: (a) RMS angular spread. (b) CDF of RMS angular spread on Line 1.

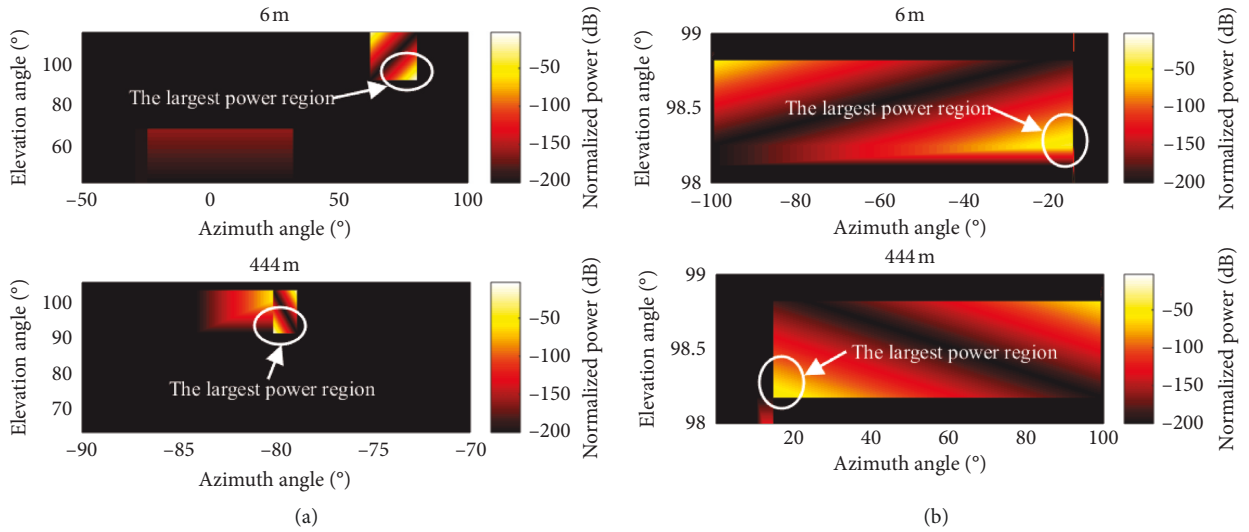

Figure 8: (a) PAS of AoA. (b) PAS of AoD.

could be horizontal and perpendicular to rails on the tower platform. Considering the direction of the main beam in Figure 8(b), the antenna array should be rotated counterclockwise or clockwise horizontally to be perpendicular to the direction of main beam for the low correlation.

4.5. Spatial Correlation. As we all know, the diversity gain and multiplexing gain of the MIMO system [30, 31] are directly related to the spatial characteristics of the channel. The above is the investigation of some spatial characteristic parameters at 5G mmWave band. In addition, as the important aspect of MIMO channels [32], the spatial correlation among beams must be discussed to achieve the suitable antenna spacing.

In this section, in order to improve the performance of the location where there is worser signal coverage, the angular spreads at that position are selected for correlation calculation to ensure the user experience of the overall scenario.

According to Figure 7(b), more than 90% of ASA and 90% of ESA are beyond 4.15° and 9.71°, respectively, and over 90% of ASD and 90% of ESD are larger than 4.64° and 0.92°, respectively, which result in the necessity of investigation about the spatial correlation among antenna elements in the case of relatively worser angular spread. The correlation coefficient between Rx antenna elements with ASA (4.15°) and ESA (9.71°) is shown in Figure 9(a), and the correlation coefficient of Tx antenna elements is drawn in Figure 9(b) as the ASD is 4.64° and ESD is 0.92°.

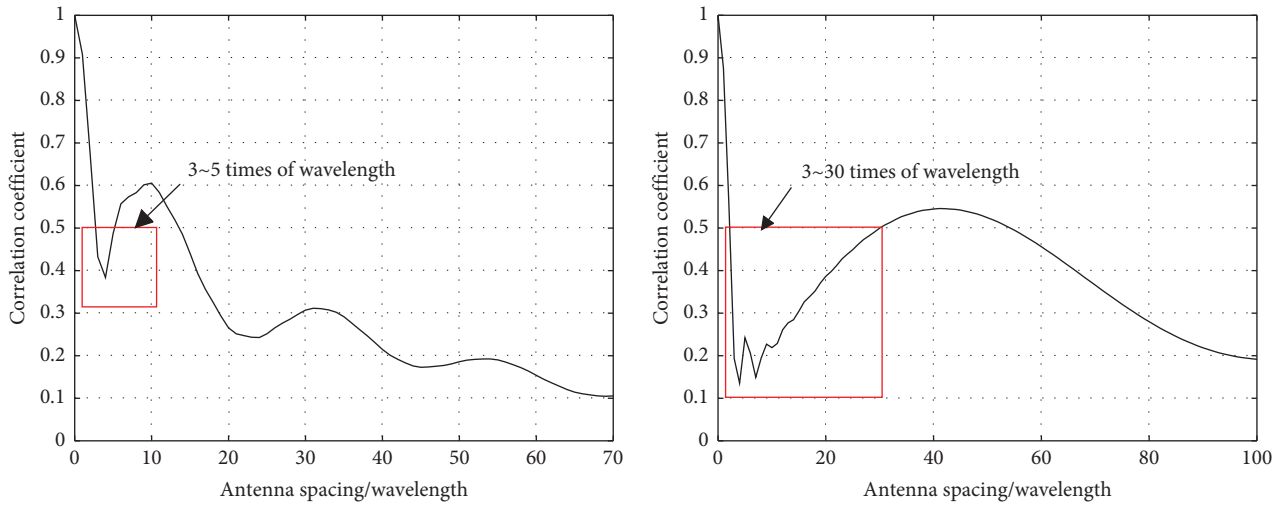

Figure 9: Correlation coefficient. (a) Rx antenna elements: ASA = 4.15°; ESA = 9.71°. (b) Tx antenna elements: ASD = 4.64°; ESD = 0.92°.

The wavelength at 40 GHz is approximately 7.5 mm. From Figure 9(a), the relative distance of Rx antenna array elements is at least 68 times to ensure that correlation coefficient between adjacent antenna elements is less than 0.1, but the antenna element spacing is around 51 cm that is too large to meet the engineering requirements. If the correlation coefficient can be relaxed to 0.5, it indicates the antenna element spacing only will be about 2.25~3.75 cm that might meet the requirement for application at the Rx.

In Figure 9(b), when the correlation coefficient of adjacent Tx antenna elements is less than 0.5, antenna spacing can be set to about 3~30 times of wavelength which means around 2.25~22.50 cm.

5. Conclusion

In this paper, channel characteristics of 5G mmWave band have been investigated at the high-speed railway station. Based on the measurement and simulation results, key channel parameters, such as path loss, delay spread, Rician K-factor, angular spread, PAS, and spatial correlation, are all analyzed. Some important results and suggestions are summarized as follows:

(1) When Tx antennas are installed on the tower, the maximum path loss on Line 1 is about 132.2 dB, which is so large that multiantenna technology is expected to ensure signal coverage strength and increase system capacity.

(2) The high-speed railway station is a semilimited space where the values of RMS delay spreads are almost less than 1.2 ns on Line 1, which is reasonable and acceptable in 5G systems.

(3) In the scenario, the Rician K-factors obey the Gaussian distribution which is owing to the large bandwidth in 5G systems.

(4) When the Tx and Rx both adopt uniform linear antenna arrays, the antenna spacing could be 2.25~22.50 cm at Tx, whereas the Rx antenna spacing might be set to 2.25~3.75 cm.

(5) The Rx antenna array should be vertical to the top of the train, while the horizontal Tx antenna array should be rotated counterclockwise or clockwise horizontally to obtain low correlation due to the propagation direction of the main beam.

(6) By analyzing the train's moving speed and the angle between the train's moving direction and incident wave direction, it can be found that the angle is approaching 90° as the Rx reaches the Tx, which makes Doppler shift decline. Due to simulation on Line 1 where the train needs to stop at the platform and the speed is relatively low, this paper does not focus on the Doppler effect and more related research could be conducted in future work.

Data Availability

The data used to support the findings of this study are available from the corresponding author upon request.

Conflicts of Interest

The authors declare that there are no conflicts of interest regarding the publication of this paper.

Acknowledgments

This work was supported by the National Key Research and Development Program under Grant 2016YFE0200900, NSFC under Grants 61725101 and U1834210, Beijing Natural Haidian Joint Fund under Grant L172020, Major Projects of Beijing Municipal Science and Technology Commission under Grant Z181100003218010, and the Royal Society Newton Advanced Fellowship (Grant no.: NA191006).

References

[1] T. S. Rappaport, Y. Xing, G. R. MacCartney, A. F. Molisch, E. Mellios, and J. Zhang, "Overview of millimeter wave communications for fifth-generation (5G) wireless networks—with a focus on propagation models," *IEEE Transactions on Antennas and Propagation*, vol. 65, no. 12, pp. 6213–6230, 2017.

[2] J. Zhang, Z. Zheng, Y. Zhang, J. Xi, X. Zhao, and G. Gui, "3D MIMO for 5G NR: several observations from 32 to massive 256 antennas based on channel measurement," *IEEE Communications Magazine*, vol. 56, no. 3, pp. 62–70, 2018.

[3] C. T. Neil, M. Shafi, P. J. Smith, P. A. Dmochowski, and J. Zhang, "Impact of microwave and mmWave channel models on 5G systems performance," *IEEE Transactions on Antennas and Propagation*, vol. 65, no. 12, pp. 6505–6520, 2017.

[4] D. He, B. Ai, K. Guan et al., "Channel measurement, simulation, and analysis for high-speed railway communications in 5G millimeter-wave band," *IEEE Transactions on Intelligent Transportation Systems*, vol. 19, no. 10, pp. 3144–3158, 2018.

[5] X. Cheng, L. Yang, and X. Shen, "D2D for intelligent transportation systems: a feasibility study," *IEEE Transactions on Intelligent Transportation Systems*, vol. 16, no. 4, pp. 1784–1793, 2015.

[6] B. Ai, X. Cheng, T. Kürner et al., "Challenges toward wireless communications for high-speed railway," *IEEE Transactions on Intelligent Transportation Systems*, vol. 15, no. 5, pp. 2143–2158, 2014.

[7] S. Priebe and T. Kürner, "Stochastic modeling of THz indoor radio channels," *IEEE Transactions on Wireless Communications*, vol. 12, no. 9, pp. 4445–4455, 2013.

[8] K. Guan, Z. Zhong, B. Ai, C. Briso-Rodriguez, and L. Zhang, "Large scale fading characteristics in rail traffic scenarios," in *Proceedings of the IEEE International Symposium on Antennas and Propagation & USNC/URSI National Radio Science Meeting*, pp. 83-84, Vancouver, Canada, July 2015.

[9] K. Guan, Z. Zhong, B. Ai, and T. Kürner, "Empirical models for extra propagation loss of train stations on high-speed railway," *IEEE Transactions on Antennas and Propagation*, vol. 62, no. 3, pp. 1395–1408, 2014.

[10] K. Guan, Z. Zhong, B. Ai, and T. Kürner, "Propagation measurements and analysis for train stations of high-speed railway at 930 MHz," *IEEE Transactions on Vehicular Technology*, vol. 63, no. 8, pp. 3499–3516, 2014.

[11] K. Guan, X. Lin, D. He et al., "Scenario modules and ray-tracing simulations of millimeter wave and terahertz channels for smart rail mobility," in *Proceedings of the 2017 11th European Conference on Antennas and Propagation (EUCAP)*, pp. 113–117, Paris, France, March 2017.

[12] L. Wang, K. Guan, B. Ai et al., "An accelerated algorithm for ray tracing simulation based on high-performance computation," in *Proceedings of the 2016 11th International Symposium on Antennas, Propagation and EM Theory (ISAPE)*, pp. 512–515, Guilin, China, October 2016.

[13] S. Priebe, S. Rey, and T. Kürner, "From broadband ray tracing propagation modeling to physical layer simulations of THz indoor communication systems," in *Proceedings of the IEEE Radio and Wireless Symposium*, pp. 142–144, Austin, TX, USA, January 2013.

[14] Y. Yoon, M. Jung, and J. Kim, "Intelligent ray tracing for the propagaiton prediction," in *Proceedings of the IEEE Antennas and Propagation Society International Symposium*, pp. 1-2, Chicago, IL, USA, July 2012.

[15] S. Sun, T. Rappaport, R. Heath, A. Nix, and S. Rangan, "MIMO for millimeter-wave wireless communications: beamforming, spatial multiplexing, or both?," *IEEE Communications Magazine*, vol. 52, no. 12, pp. 110–121, 2014.

[16] X. Cheng, Q. Yao, C.-X. Wang et al., "An improved parameter computation method for a MIMO V2V Rayleigh fading channel simulator under non-isotropic scattering environments," *IEEE Communications Letters*, vol. 17, no. 2, pp. 265–268, 2013.

[17] J. Zhang, Y. Zhang, Y. Yu, R. Xu, Q. Zheng, and P. Zhang, "3-D MIMO: how much does it meet our expectations observed from channel measurements?," *IEEE Journal on Selected Areas in Communications*, vol. 35, no. 8, pp. 1887–1903, 2017.

[18] L. Zhang, C. Briso, J. R. O. Fernandez et al., "Delay spread and electromagnetic reverberation in subway tunnels and stations," *IEEE Antennas and Wireless Propagation Letters*, vol. 15, no. 4, pp. 585–588, 2016.

[19] J. Zhang, C. Pan, F. Pei, G. Liu, and X. Cheng, "Three-dimensional fading channel models: a survey of elevation angle research," *IEEE Communications Magazine*, vol. 52, no. 6, pp. 218–226, 2014.

[20] G. R. MacCartney, T. S. Rappaport, and S. Rangan, "Rapid fading due to human blockage in pedestrian crowds at 5G millimeter-wave frequencies," in *Proceedings of the IEEE Global Communications Conference*, pp. 1–7, Singapore, December 2017.

[21] B. Yuan and H. Zhang, "Research on standard tower section in communication monopole," *Hans Journal of Civil Engineering*, vol. 7, no. 1, pp. 62–73, 2018.

[22] K. Guan, D. Zhong, B. Ai et al., "Deterministic propagation modeling for the realistic high-speed railway environment," in *Proceedings of the 2013 IEEE 77th Vehicular Technology Conference (VTC Spring)*, IEEE, Dresden, Germany, June 2013.

[23] D. He, B. Ai, K. Guan, L. Wang, Z. Zhong, and T. Kurner, "The design and applications of high-performance ray-tracing simulation platform for 5G and beyond wireless communications: a tutorial," *IEEE Communications Surveys & Tutorials*, vol. 21, no. 1, pp. 10–27, 2019.

[24] Y. Chen, F. Yang, and Y. Yu, "Research on 5G coverage capability," *Communications Technology*, vol. 51, no. 12, pp. 2866–2873, 2018.

[25] D. He, J. Yang, K. Guan et al., "Ray-tracing simulation and analysis of propagation for 3GPP high speed scenarios," in *Proceedings of the 2017 11th European Conference on Antennas and Propagation (EUCAP)*, pp. 2890–2894, Piscataway, NJ, USA, March 2017.

[26] "Study on channel model for frequency spectrum above 6 GHz (Release 15)," 3rd Generation Partnership Project (3GPP) TR 38.900-15.0.0, June 2018.

[27] Z. Wang, P. Wang, and H. Xiong, "Estimation and measurement of K parameter for rice fading channel," *Journal of Data Acquisition & Processing*, vol. 24, no. 1, pp. 109–113, 2009.

[28] S. Hur, J. H. Park, T. Kim et al., "Wideband spatial channel model in an urban cellular environments at 28 GHz," in *Proceedings of the European Conference on Antennas & Propagation*, Lisbon, Portugal, April 2015.

[29] W. Meng, D. Wei, and S. Gong, "Power angle spectrum of satellite communication downlink in rainfall environment," in *Proceedings of the IEEE International Symposium on Microwave*, pp. 373–377, Chengdu, China, October 2013.

[30] N. Khalid and O. B. Akan, "Experimental throughput analysis of low-THz MIMO communication channel in 5G wireless

networks," *IEEE Wireless Communications Letters*, vol. 5, no. 6, pp. 616–619, 2016.

[31] A. A. Kalachikov and N. S. Shelkunov, "Performance evaluation of the detection algorithms for MIMO spatial multiplexing based on analytical wireless MIMO channel models," in *2018 XIV International Scientific-Technical Conference on Actual Problems of Electronics Instrument Engineering (APEIE)*, pp. 180–183, Novosibirsk, Russia, October 2018.

[32] U. Karabulut, A. Awada, I. Viering, M. Simsek, and G. P. Fettweis, "Spatial and temporal channel characteristics of 5G 3D channel model with beamforming for user mobility investigations," *IEEE Communications Magazine*, vol. 56, no. 12, pp. 38–45, 2018.

Hindawi
International Journal of Antennas and Propagation
Volume 2019, Article ID 4656141, 7 pages
https://doi.org/10.1155/2019/4656141

Research Article

A Wideband Differential-Fed Microstrip Patch Antenna Based on Radiation of Three Resonant Modes

Taohua Chen, Yueyun Chen, and Rongling Jian

University of Science & Technology Beijing, College Road 30, Haidian District, Beijing, China

Correspondence should be addressed to Yueyun Chen; chenyy@ustb.edu.cn

Received 1 May 2019; Accepted 18 June 2019; Published 28 August 2019

Academic Editor: Eva Antonino-Daviu

A wideband differential-fed microstrip patch antenna based on radiation of three resonant modes of TM_{12}, TM_{30}, and slot is proposed in this paper. Firstly, two symmetrical rectangular slots are cut on the radiating patch where the zero-current position of the TM_{30} mode excites another resonant slot mode. In addition, the slot's length is enlarged to decrease the frequency of the slot mode with little effect on that of the TM_{30} mode. To further expand the impedance bandwidth, the width of patch is reduced to increase the frequency of the TM_{12} mode, while having little influence on that of the TM_{30} and slot modes. Moreover, a pair of small rectangular strips is adopted on the top of the feeding probes to achieve a good impedance matching. Finally, based on the arrangements above, a broadband microstrip patch antenna with three in-band minima is realized. The results show that the impedance bandwidth ($|S_{dd11}| < -10$ dB) of the proposed antenna is extended to 35.8% at the profile of 0.067 free-space wavelength. Meanwhile, the proposed antenna maintains a stable radiation pattern in the operating band.

1. Introduction

Microstrip patch antennas (MPAs) have been extensively investigated and developed over the past decades because of their advantages of low profile, small cost, ease of manufacture, and so on [1]. However, conventional MPAs always suffer from a narrow impedance bandwidth of about 3% because of the high-quality factor Q [2]. In order to expand the impedance bandwidth, a few approaches have been proposed in past decades.

The simplest method to expand the bandwidth is to enhance the antenna thickness and decrease the substrate permittivity, which can reduce the quality factor Q [3]. However, thick substrates enlarge the surface wave leakage leading to poor radiation efficiency, and decreasing the permittivity is limited because the lowest substrate dielectric constant is 1. In addition, the feeding scheme was reconfigured in [4] to extend the impedance bandwidth to 115% at the profile of 0.25 λ_0 (λ_0 is the free-space wavelength); the reason for bandwidth enhancement is that another nonradiative resonant mode is introduced around the fundamental mode. However, it is difficult to implement the feeding scheme in a thin substrate. Moreover, the authors in [5] used a Wang-shaped radiating patch to extend the bandwidth of 49.3% with the profile of 0.2 λ_0. In [6], an inverted U-shaped slot was adopted on the radiating patch to extend the impedance bandwidth to 17.8% with the thickness of 0.09 λ_0. In [7], a simple E-shaped patch was proposed for bandwidth enhancement, and the impedance bandwidth was expanded to 30.3% at the 0.1 λ_0 profile. Nevertheless, all the antennas mentioned above always need a high profile, which will destroy the low-profile property of microstrip antenna.

Furthermore, in recent years, coupling two odd modes of MPAs together becomes a new attractive method because of keeping the advantage of low profile of MPAs. In [8], the TM_{10} and TM_{30} modes were combined to extend the bandwidth to 18% at the height of 0.08 λ_0. In [9], the authors proposed to combine TM_{10} and TM_{12} modes together, and the impedance bandwidth was enlarged to 10% with the profile of 0.039 λ_0. Additionally, The TM_{12} and TM_{30} modes were also adopted to achieve bandwidth enhancement in [10], and a bandwidth of 14.8% was realized at the profile of 0.048 λ_0. However, since only two odd modes are combined,

the impedance bandwidth of these antennas is only twice as wide as that of traditional microstrip antennas, which may hinder the application of these MPAs in broadband communication systems.

In this paper, a novel wideband differential-fed MPA based on radiation of three resonant modes of TM_{12}, TM_{30}, and slot is proposed. Firstly, two symmetrical rectangular slots are cut at the position of zero-current of the TM_{30} mode of the radiating patch to excite another resonant slot mode with little effect on the TM_{30} mode. Besides, through increasing the slot's length, the TM_{30} and slot modes can be adjusted in proximity to each other. To further expand the impedance bandwidth, the patch width is reduced to increase the frequency of the TM_{12} mode. With these arrangements, the TM_{12}, TM_{30}, and slot modes can be combined to form a wideband. Moreover, a pair of small rectangular strips is used on the top of the feeding probes to achieve a good impedance matching. The results show that the proposed antenna has realized an impedance bandwidth ($|S_{dd11}| < -10$ dB) of 35.8% at the profile of 0.067 λ_0. Additionally, the proposed antenna maintains a stable radiation pattern over the operating band.

2. Geometry and Design Process

The geometry of the proposed differential-fed wideband MPA is shown in Figure 1. It consists of a radiating patch with the size of $L \times W$ and a ground plane with the size of $L_S \times W_S$. And a dielectric substrate RO5880 with permittivity of $\varepsilon_r = 2.2$ and thickness of $H_1 = 0.508$ mm is selected in this paper for antenna design. The radiating patch is printed on the top surface of the substrate RO5880, while the ground plane is placed below the substrate with an air gap of $H = 3$ mm. Meanwhile, two symmetrical rectangular slots ($L_1 \times W_1$) with the spacing of D_1 are cut on the radiating patch, which can excite another resonant slot mode. In addition, differential-fed with spacing of D_2 is used and a pair of small rectangular strips ($L_2 \times W_2$) is adopted on the top of the feeding probes. All parameters for the proposed antenna in Figure 1 are tabulated in Table 1. In this paper, HFSS 13.0 is used for simulation calculation.

Firstly, as can be seen from Figure 2(a), a square MPA with differential-fed scheme is used for antenna design to suppress the undesired even-order modes which are null in the boresight [11]. Secondly, in Figure 2(b), two symmetrical rectangular slots are cut on the radiating patch to excite another slot mode near the TM_{30} mode to expand the bandwidth. Thirdly, to further enlarge the bandwidth, in Figure 2(c), the patch width is reduced to increase the frequency of the TM_{12} mode to proximity to that of the slot and TM_{30} modes. Finally, in Figure 2(d), the slot's width and position are modified slightly and a pair of small rectangular strips is adopted on the top of the feeding probes to achieve a good impedance matching.

3. Parametric Studies and Design Flow

3.1. Exciting Another Resonant Slot Mode. The current distribution of the TM_{30} mode of the patch is plotted in Figure 3. It can be seen from Figure 3 that there are two zero-current lines on the patch. Therefore, as shown in Figure 2(b), when slots are cut on the patch near these positions, it will have little effect on the TM_{30} mode while can excite the resonant slot mode. Through modifying the slot's length properly, TM_{30} and slot modes can be combined to expand the bandwidth. To better understand the effect of slot length, the frequency of the TM_{30} mode (f_{30}) and slot mode (f_{slot}) under different slot length L_1 is plotted in Figure 4. Note that, in this subsection, the W_1 is 1 mm and D_1 is 21 mm.

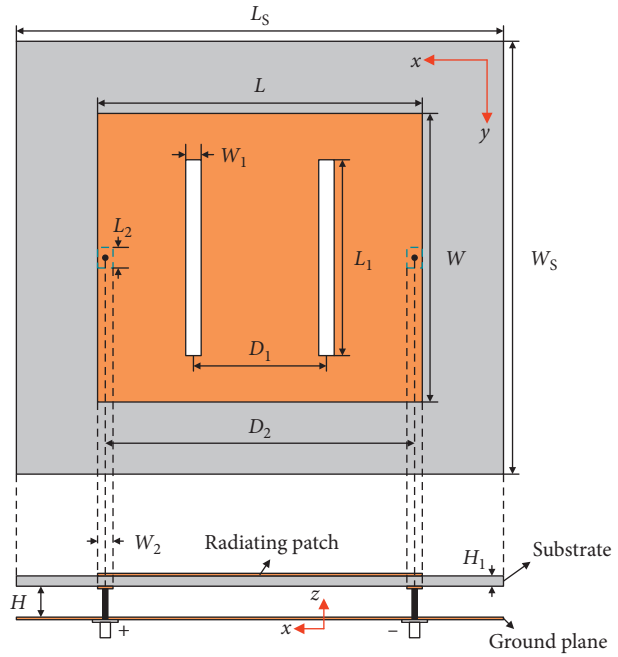

Figure 1: Geometry of the proposed wideband antenna.

It can be observed from Figure 4 that when slot length increases from 18 to 38 mm, the f_{slot} decreases from 7.2 GHz to 5.1 GHz clearly while f_{30} keeps constant at 6.24 GHz. Considering the whole performance, in this paper, $L_1 = 38$ mm is selected for the widest bandwidth.

3.2. Increasing the Frequency of TM_{12} Mode. To further extend the bandwidth, the TM_{12} mode is adjusted in proximity to slot and TM_{30} modes in this paper. According to the cavity model [12], the resonant frequencies (f_{mn}) of TM_{mn} modes in MPA can be expressed as follows:

$$f_{mn} = \frac{c}{2\sqrt{\varepsilon_r}} \times \sqrt{\left(\frac{m}{L}\right)^2 + \left(\frac{n}{W}\right)^2}, \quad (1)$$

where c is the light speed in the free space, ε_r is the dielectric constant of substrate, and $m = 1, 2, 3, \ldots$, and $n = 1, 2, 3, \ldots$

Based on formula (1), the patch width (W) plays an important role in the frequency of TM_{12} mode (f_{12}), yet has little effect on f_{30}. And the f_{slot} is mainly decided on the slot length, so the patch width also has little effect on f_{slot}. Therefore, when W is reduced, f_{12} will be increased

Table 1: Dimensions of the proposed antenna.

Parameters	L	L_S	L_1	L_2	W	W_S	W_1	W_2	D_1	D_2	H	H_1
Values (mm)	63	94.5	38	4	56	84	3	3	25.8	60	3	0.508

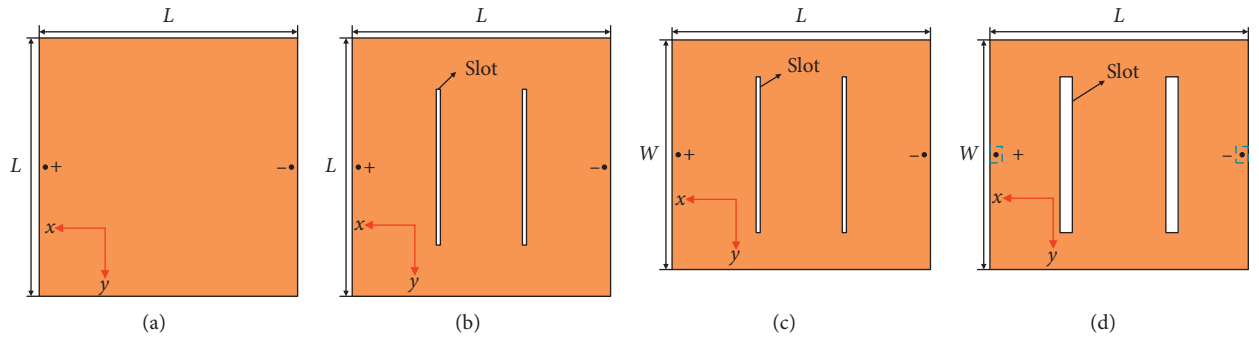

Figure 2: Design process of proposed wideband antenna. (a) Conventional MPA. (b) MPA with two slots. (c) MPA with two slots and shortened patch. (d) MPA with two slots, shortened patch and a pair of strips.

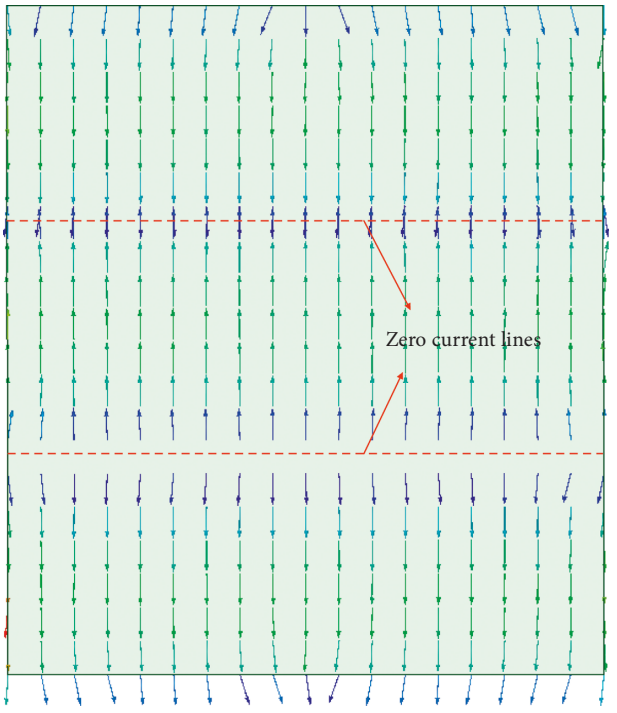

Figure 3: Current distribution of TM_{30} mode.

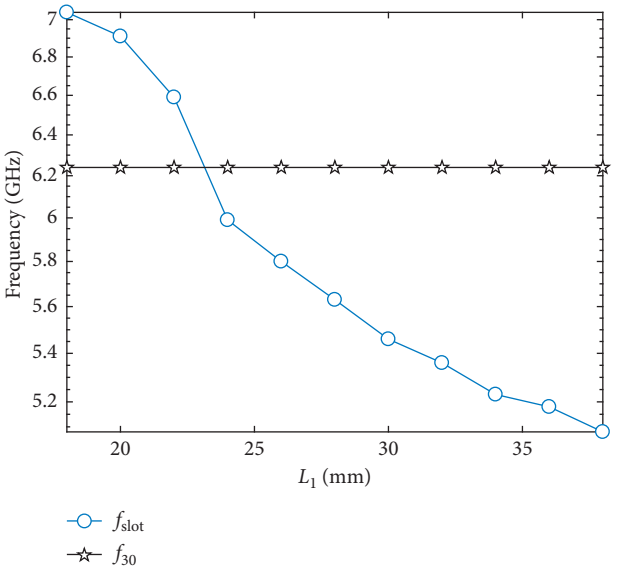

Figure 4: f_{30} and f_{slot} at different slots length L_1.

while f_{30} and f_{slot} keep constant. To better understand how the patch width influences f_{12}, f_{30}, and f_{slot}, Figure 5 plots f_{12}, f_{30}, and f_{slot} varying with patch width W. W_1, D_1, and L_1 are selected as 1 mm, 21 mm, and 38 mm, respectively.

We can see from Figure 5 that when W reduces from 63 to 56 mm, f_{12} increases from 4.18 GHz to 4.44 GHz while f_{30} and f_{slot} keep constant, which is consistent with the analysis above. Note that when $W = 56$ mm, the spacing of TM_{12} and slot modes is enough to form the wideband. Therefore, in this paper, we choose $W = 56$ mm for antenna design.

3.3. Impedance Matching. With the arrangements above, the TM_{12}, TM_{30}, and slot modes have been in proximity to each other. However, the input impedance is mismatch. To finally obtain a wideband MPA, the slot position (D_1) and width (W_1) are modified and a pair of small rectangular strips is adopted on the top of the feeding probes to achieve a good impedance matching. In this subsection, we analyze the effects of slots and rectangular strips on impedance matching. When one parameter is studied, the other parameters are fixed as listed in Table 1.

Figure 6 illustrates $|S_{dd11}|$ as a function of frequency at different slot position D_1. As can be seen from Figure 6, the slot position has great effects on impedance matching and bandwidth. Proper design of the slots position can achieve a better impedance matching and wider bandwidth. In this

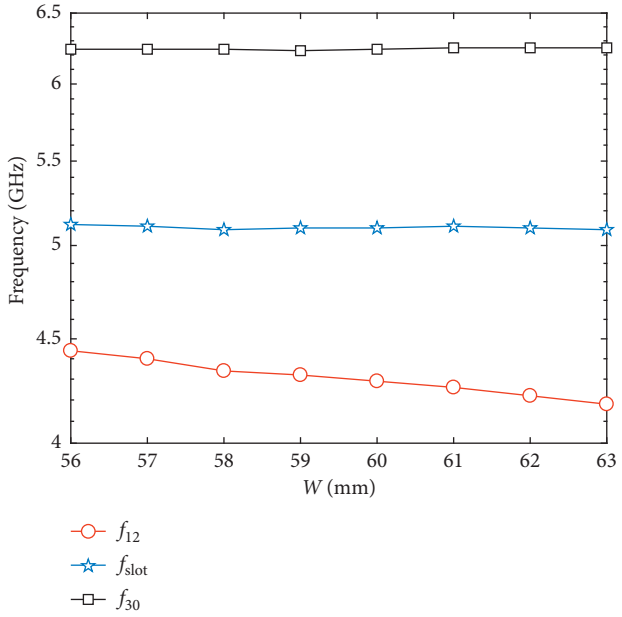

Figure 5: f_{12}, f_{30} and f_{slot} varies with patch width W.

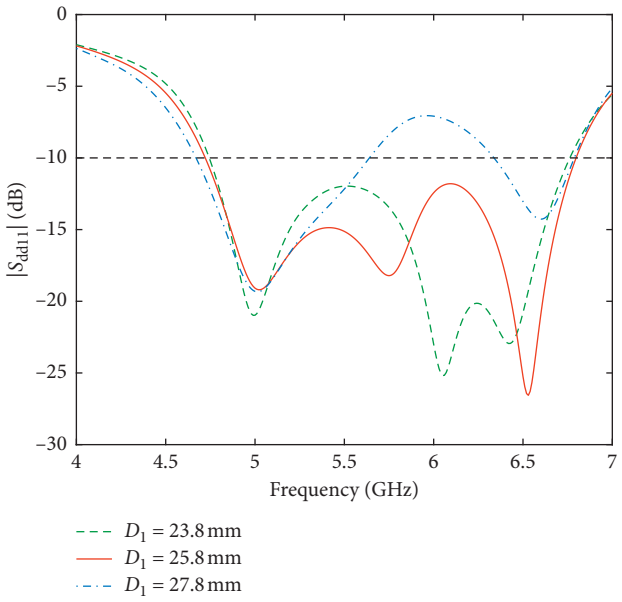

Figure 6: $|S_{dd11}|$ as a function of frequency at different slots position D_1.

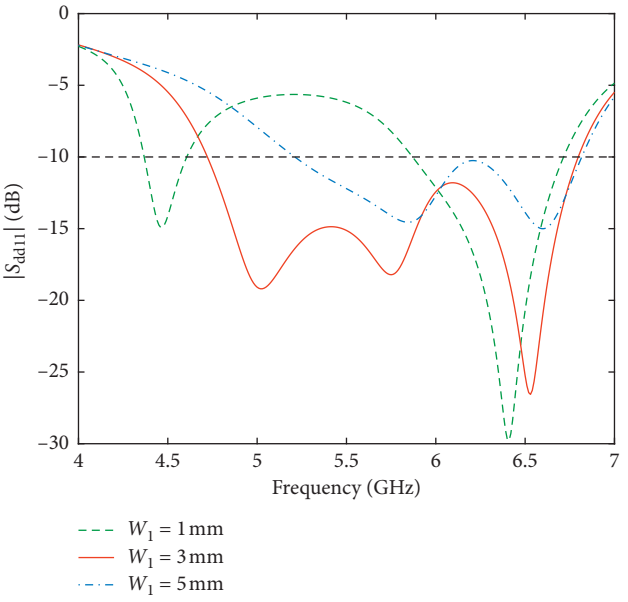

Figure 7: $|S_{dd11}|$ as a function of frequency at different slots width W_1.

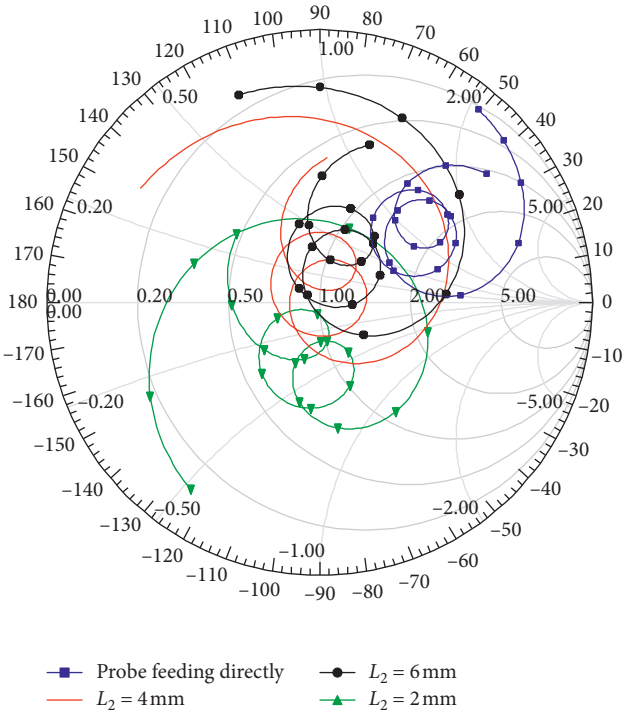

Figure 8: Smith chart of proposed wideband MPA at different L_2.

paper, considering the whole $|S_{dd11}|$ performance in Figure 6, the $D_1 = 25.8$ mm is selected for antenna design.

Figure 7 shows $|S_{dd11}|$ as a function of frequency at different slot width W_1. Like slots position D_1, the slots width W_1 also has large influences on impedance matching and bandwidth. Compare the whole $|S_{dd11}|$ performance at different slot width W_1, the best bandwidth is achieved at $W_1 = 3$ mm.

Besides, in this paper, a pair of small rectangular strips is adopted on the top of the feeding probes to eliminate the inductance introduced by probes for good impedance matching. Note that the value of capacitance introduced by the rectangular strips is mainly decided with the area of these rectangular strips. Therefore, we only modify the strips length L_2 to achieve impedance matching and keep W_2 as listed in Table 1. Figure 8 plots the Smith chart of proposed wideband MPA at different L_2.

From Figure 8, we can find that the input impedance is inductive as the probes connect radiating patch directly.

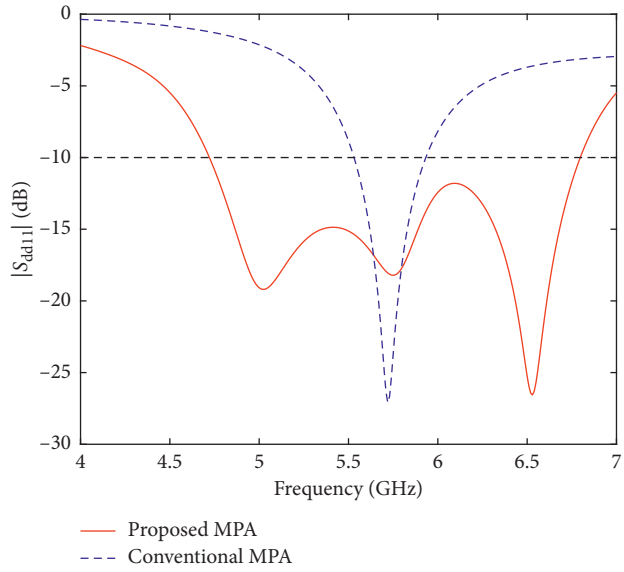

Figure 9: Reflection coefficient of proposed wideband MPA and conventional MPA.

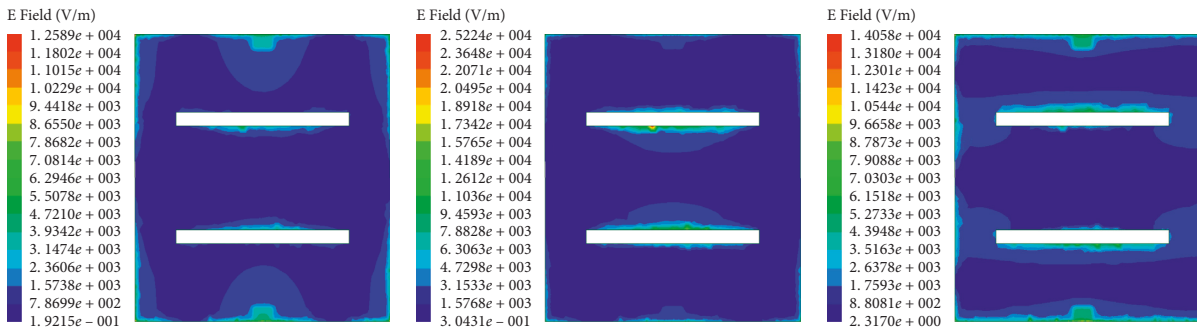

Figure 10: Electric field distributions underneath the radiating patch of proposed wideband MPA. (a) 5.02 GHz. (b) 5.75 GHz. (c) 6.53 GHz.

When a pair of rectangular strips is adopted on the top of the probes to capacitive-coupled feed and L_2 decreases from 6 mm to 2 mm, the input impedance gradually changes from inductive to capacitive. It can also be observed from Figure 8 that the best L_2 is 4 mm.

4. Results and Discussion

The reflection coefficient of proposed wideband MPA is plotted in Figure 9. It can be observed that the impedance bandwidth for $|S_{dd11}| < -10$ dB is 35.8%, covering from 4.72 to 6.79 GHz. Besides, there are three minima over the operating band, which is consistent with the three resonant modes mentioned above. Meanwhile, the reflection coefficient of conventional MPA at the same profile is also plotted in Figure 9. Compared with the traditional MPA, the impedance bandwidth of the proposed antenna has enhanced to more than three times, which indicates that the proposed antenna can extend the bandwidth distinctly.

Figure 10 plots the electric field distributions underneath the radiating patch at three minima of 5.02, 5.75, and 6.53 GHz. For the first minimum at 5.02 GHz, it can be found from Figure 10(a) that there are two vertical zero electric field lines and one horizontal zero electric field line, which is same as the electric field distributions of the TM_{12} mode of a conventional patch antenna. Thus, it is TM_{12} mode that works at 5.02 GHz. As for the second minimum at 5.75 GHz, the electric field is mainly distributed around two slots and is rarely around the radiative and non-radiative edges of the traditional microstrip antenna, which can be observed from Figure 10(b). This shows that the slot mode works at 5.75 GHz. While for the third minimum at 6.53 GHz, it can be clearly seen from the Figure 10(c) that there are three horizontal zero electric field lines, which indicates the proposed MPA resonates at the TM_{30} mode.

Figure 11 gives the normalized radiation patterns of the proposed wideband MPA at three minima of 5.02, 5.75, and 6.53 GHz. The copolarization radiation patterns are symmetric in both E-plane and H-plane and have the peaks in the broadside direction, which shows that the proposed wideband MPA maintains a stable radiation pattern over the operating band. Meanwhile, a good cross-polarization characteristic of lower than −25 dB is achieved.

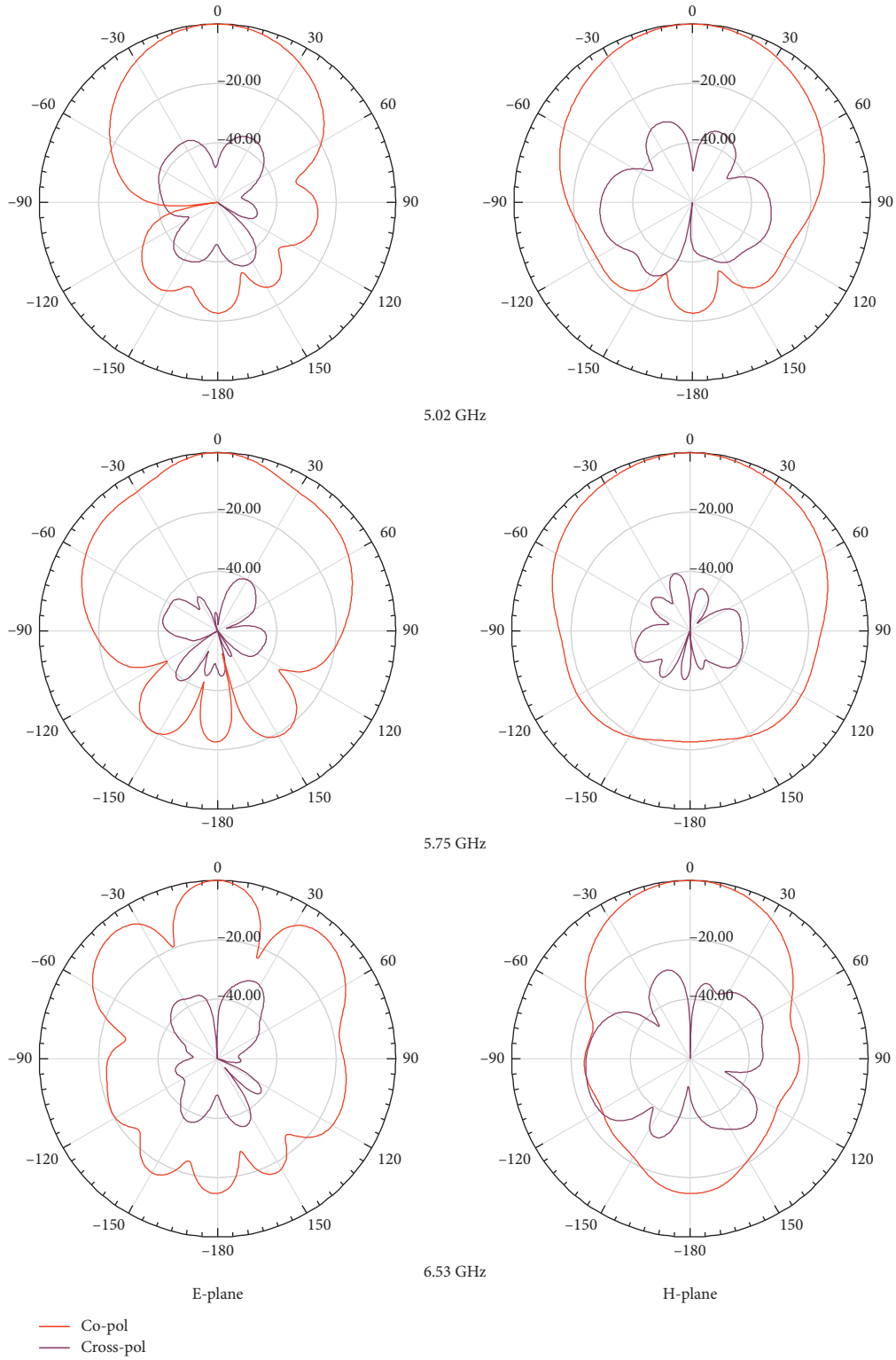

Figure 11: Normalized radiation patterns of proposed wideband MPA.

In addition, the gain, directivity, and efficiency as functions of frequency at broadside direction of the proposed antenna are illustrated in Figure 12. Over the operating band, the gain ranges from 8.8 to 13.24 dBi and the efficiency is above 90%. It can also be observed from Figure 12 that the gain is dropped at about 5.7-5.8 GHz. The reason is that for the proposed wideband antenna, the slot mode between TM_{12} and TM_{30} modes resonates in this band, and the gain of slot mode is lowest among three resonant modes.

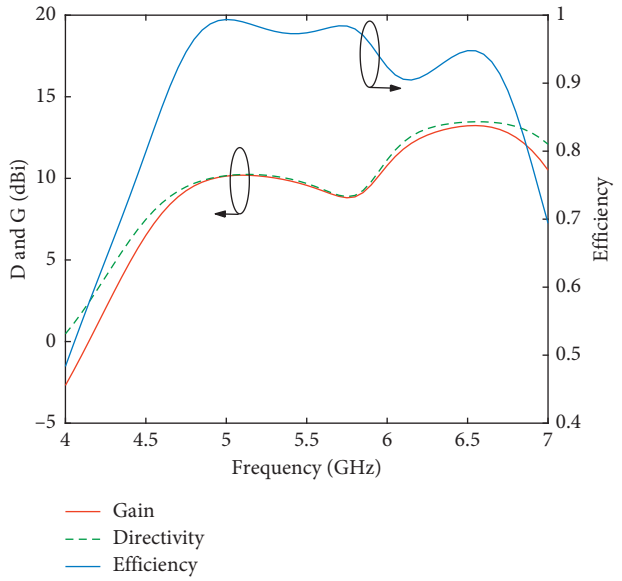

Figure 12: Gain, directivity, and efficiency as functions of frequency at broadside direction of proposed wideband MPA.

5. Conclusion

In this paper, a wideband differential-fed microstrip patch antenna based on radiation of three resonant modes of the TM_{12}, TM_{30}, and slot is proposed and analyzed. First, two symmetrical rectangular slots are cut on the radiating patch, which will excite another resonant slot mode near the TM_{30} mode to extend the impedance bandwidth. Second, to further expand the bandwidth, the width of the patch is reduced to increase the frequency of the TM_{12} mode with little effect on that of TM_{30} and slot modes. Moreover, a good impedance matching is achieved through adopting a pair of small rectangular strips on the top of the feeding probes. Finally, a wideband microstrip patch antenna with an impedance bandwidth of 35.8% is realized under a low profile of 0.067 λ_0. Besides, the proposed antenna maintains a stable radiation pattern and a good efficiency above 90% over the operating band. The proposed antenna is compact and has a wideband, it can be used for modern wireless communication systems.

Data Availability

The data in the HFSS used to support the findings of this study were supplied by Taohua Chen under license and so cannot be made freely available. Requests for access to these data should be made to Taohua Chen, 18813127085@163.com.

Conflicts of Interest

The authors declare that they have no conflicts of interest.

Acknowledgments

This work was supported by the National Science and Technology Major Project of China (no. 2017ZX03001021-005).

References

[1] W. Sun, Y. Li, Z. Zhang, and Z. Feng, "Broadband and low-profile microstrip antenna using strip-slot hybrid structure," *IEEE Antennas and Wireless Propagation Letters*, vol. 16, pp. 3118–3121, 2017.

[2] A. B. Constantine, *Antenna Theory: Analysis and design. Microstrip Antennas*, John Wiley & Sons, Hoboken, NJ, USA, 3rd edition, 2005.

[3] R. Bancroft, *Microstrip and Printed Antenna Design*, The Institution of Engineering and Technology, London, UK, 2009.

[4] S. W. Liao, Q. Xue, and J. H. Xu, "Parallel-plate transmission line and L-plate feeding differentially driven H-slot patch antenna," *IEEE Antennas & Wireless Propagation Letters*, vol. 11, no. 8, pp. 640–644, 2012.

[5] K. L. Chung and C.-H. Wong, "Wang-shaped patch antenna for wireless communications," *IEEE Antennas and Wireless Propagation Letters*, vol. 9, pp. 638–640, 2010.

[6] A. Singh and S. Singh, "Miniaturized wideband aperture coupled microstrip patch antenna by using inverted U-slot," *International Journal of Antennas and Propagation*, vol. 2014, Article ID 306942, 7 pages, 2014.

[7] F. Yang, X.-X. Zhang, X. Ye, and Y. Rahmat-Samii, "Wide-band E-shaped patch antennas for wireless communications," *IEEE Transactions on Antennas and Propagation*, vol. 49, no. 7, pp. 1094–1100, 2001.

[8] D. Wang, K. B. Ng, C. H. Chan, and H. Wong, "A novel wideband differentially-fed higher-order mode millimeter-wave patch antenna," *IEEE Transactions on Antennas and Propagation*, vol. 63, no. 2, pp. 466–473, 2015.

[9] N.-W. Liu, L. Zhu, W.-W. Choi, and X. Zhang, "A low-profile differential-fed patch antenna with bandwidth enhancement and sidelobe reduction under operation of TM10 and TM12 modes," *IEEE Transactions on Antennas and Propagation*, vol. 66, no. 9, pp. 4854–4859, 2018.

[10] N.-W. Liu, L. Zhu, W.-W. Choi, and G. Fu, "A low-profile wideband Aperture-fed microstrip antenna with improved radiation patterns," *IEEE Transactions on Antennas and Propagation*, vol. 67, no. 1, pp. 562–567, 2019.

[11] Y. P. Zhang and J. J. Wang, "Theory and analysis of differentially-driven microstrip antennas," *IEEE Transactions on Antennas and Propagation*, vol. 54, no. 4, pp. 1092–1099, 2006.

[12] R. Garg, P. Bhartia, I. Bahl, and A. Ittipiboon, *Microstrip Antenna Design Handbook*, Artech House, Norwood, Massachusetts, USA, 2001.